





Statens vegvesen

Ferry free E39 -Fjord crossings Bjørnafjorden

304624

Rev.	Publish date	Description	Made by	Checked by	Project appro.	Client appro.
0	15.08.2019	Final issue	MST	ANE	SEJ	
Client		 Statens vegvesen				
Contractor		Contract no.:				
		18/91094				

Document name:

Preferred solution, K12 - Appendix J
Ship collision

Document no.:

SBJ-33-C5-AMC-27-RE-110

Rev.:

0

Pages:

1227

CONCEPT DEVELOPMENT, FLOATING BRIDGE E39 BJØRNAFJORDEN

Preferred solution, K12

Appendix J – Ship collision

CLIENT

Statens vegvesen

DATE: / REVISION: 15.08.2019 / 0

DOCUMENT CODE: SBJ-33-C5-AMC-27-RE-110



 **AAS-JAKOBSEN**  **COWI**  **Multiconsult**



 **Aker Solutions**

 entail

 NGI

 **DISSING+WEITLING**
architecture als

 **mossmaritime**

REPORT

PROJECT	Concept development, floating bridge E39 Bjørnafjorden	DOCUMENT CODE	SBJ-33-C5-AMC-27-RE-110
SUBJECT	Appendix J – Ship collision – K12	ACCESSIBILITY	Restricted
CLIENT	Statens vegvesen	PROJECT MANAGER	Svein Erik Jakobsen
CONTACT	Øyvind Kongsvik Nedrebø	PREPARED BY	Martin Storheim
		RESPONSIBLE UNIT	AMC

SUMMARY

This report describes the status of ship collision analyses in the concept development work of a floating bridge over Bjørnafjorden. Both global and local effects are considered. The only damping sources that gives a significant contribution to the bridge response following an impact are viscous damping on pontoons and mooring lines, causing an improved response with more mooring. Comparison of global behavior in OrcaFlex and LS-DYNA reveal similar but not identical responses.

Local response was evaluated based on nonlinear finite element models with verified state-of-the-art material models following recommended guidelines for local response simulations. The resistance and resulting damage were investigated for pontoon, column and bridge girder. The most severe damage to the bridge occurs in the pontoons and columns. Pontoon damage is acceptable in the sense of flooded volume whereas column damage is more challenging. Deckhouse collisions to the bridge girder was found to cause limited damage to the bridge girder itself.

The bridge is compliant in the transverse direction, and pontoon impacts will yield increasing local deformation for increasing deviation in impact direction from the transverse direction. Up to 200 MJ is to be dissipated locally for the worst conditions, indicating significant damage to both pontoon and vessel. For pontoon collisions the energy dissipation through local plastic deformations are in the range of 40% of available kinetic energy for head-on, 60% for 45 degree offset and 80% for 80 degree offset, where offset is the angle from the bridge transverse axis (longest pontoon axis). Deckhouse collisions are not significantly different for head-on collision (0 deg) and at an angle (10 deg) in terms of energy dissipation. Mooring contributes significantly to energy dissipation, and a stronger decay of response is observed with more mooring lines. This does however not affect peak responses significantly, as the northern and southern end of the bridge are stiffness-dominated.

Pontoon collision and deckhouse collision cause a somewhat different response, with pontoon collisions giving higher torsional response in the bridge girder and deckhouse collisions a larger strong-axis bending moment response towards either end. For pontoon collisions the strong-axis bending moment is stiffness-dominated close to either end of the bridge, and there are only minor concept differences. For deckhouse collisions the southern scenarios are further out on the bridge, and the mooring stiffness contributes significantly to reduce peak loads towards the southern end. In the north high loads are observed for all concepts.

The bridge girder capacity is sufficient to avoid severe consequences of damage and has shown to be robust in the post-damage phase (see [1]). However, the torsional resistance of the columns (for all pontoons, all concepts) will be dimensioned by ship collisions and should be a point of focus in further design development. If the ship impact energy is reduced compared to the current level in the upcoming risk analysis a column with stiffness equal to the narrow column geometry with 40 mm plate thickness is enough to have a reasonable but high plastic utilization of the column. However, if the impact energy is not reduced it is recommended to introduce a slight increase in the torsional resistance and to include stiffening members that behave well in a scenario with torsional deformation.

0	15.08.2019	Final issue	M. Storheim	A. Nesteby	S. E. Jakobsen
REV.	DATE	DESCRIPTION	PREPARED BY	CHECKED BY	APPROVED BY

TABLE OF CONTENTS

1 Introduction..... 6

2 Methodology and assumptions..... 7

2.1 Setup and assumptions.....7

2.1.1 General7

2.1.2 Pontoon damping8

2.1.3 Mooring9

2.2 Collision scenarios and load modelling11

2.2.1 Scenarios.....11

2.3 Coupled local and global response11

3 Comparison between OrcaFlex and LS-DYNA 12

3.1 Setup.....12

3.2 Comparison of results for K11-0613

3.3 Comparison of results for K12-0414

3.4 Eigenmodes16

4 Local response evaluations 19

4.1 Ship bow vs. pontoon19

4.1.1 Scenarios.....19

4.2 Ship deckhouse vs. bridge girder20

4.2.1 Scenarios.....20

4.3 Material modelling.....22

4.3.1 Plastic work hardening.....22

4.3.2 Strain-rate dependence23

4.3.3 Fracture.....24

4.3.4 Verification of methodology28

4.4 Analysis setup28

4.4.1 Material strength28

4.4.2 Ship bows31

4.4.3 Ship deckhouse36

4.4.4 Pontoon38

4.4.5 Bridge girder41

4.4.6 Crane pedestal43

4.4.7 Boundary conditions43

4.5 Results collisions ship bow vs pontoon.....45

4.5.1 Head on 0 deg, centre line (Container_HeadOn_Centre_mean)52

4.5.2 Cruise 30 deg low (Cruise_30Deg_low).....58

4.5.3 Head on 0 deg, centre line + 2.5 m offset (Container_HeadOn_Centre+2_5_low)63

4.5.4 Runs with no centre bulkhead67

4.5.5 Sensitivity to super duplex material properties78

4.6 Results collisions ship deckhouse vs bridge girder.....78

4.6.1 Deckhouse collision with 0 degree angle, high impact78

4.6.2 Deckhouse collision with 0 degree angle, low impact81

4.6.3 Deckhouse collision with 10 degree angle, high impact84

4.6.4 Deckhouse collision with 10 degree angle, low impact87

4.6.5 Rigid crane pedestal collision90

4.7 Discussion93

4.7.1 Ship bows vs pontoon93

4.7.2 Ship vs bridge girder93

5 Global response evaluations 95

5.1 Selected scenarios95

5.2 Energy balance.....95

5.3 Bridge girder response.....97

5.4 Column response102

5.5 Mooring line response106

5.5.1 Quasi-static mooring line forces106

5.5.2 Evaluation of dynamic mooring line forces.....106

5.5.3 Discussion109

6 Consequence assessment 110

6.1 Pontoon damage..... 110

6.2 Column damage..... 112

6.2.1 Setup..... 112

6.2.2 Results (without reinforcements) 114

6.2.3 Results (with further reinforcements) 117

6.2.4 Discussion 118

6.3 Bridge-girder damage 119

7 Sensitivity checks..... 120

7.1 Reduction of impact energy..... 120

7.2 Increase of energy 122

8 Discussion and recommendations..... 124

9 References..... 125

10 Enclosures 126

1 Introduction

This report describes the work performed in consideration with resistance to ship collisions in the concept development work of a floating bridge over Bjørnafjorden. Both global and local effects are considered.

It is complicated to capture all relevant effects in a single simulation tool, and certain assumptions and limitations must be introduced. The AMC group believes that the present analysis setup and assumptions yields good estimates of the global dynamic response to ship collision events.

Some key points:

- The collision scenarios are based on the updated design bases as of February 2019 [2, 3], including a separation between bridge girder impacts on the southern and northern part of the bridge.
- Local force-displacement relations based on nonlinear finite element analysis of ship-pontoon collision and deckhouse-bridge girder collision
- Damping is included in the simulations as
 - Rayleigh stiffness damping
 - Viscous drag damping on pontoons
 - Heave potential damping calibrated to the measured heave periods
 - Viscous drag damping on mooring lines (simplified)
- Mooring stiffness is considered differently during the course of model and method development by either linear or nonlinear springs, the latter defined based on the actual mooring stiffness for each anchor group as defined in [4, 5].
- The hydrodynamic behavior of the global bridge model in LS-DYNA is verified against the OrcaFlex model both in time-domain and through eigenmodes, including modelling of idealized vs. full mooring system.
- The local capacity of the most critical component (columns with low torsional capacity) are simulated using a coupled approach with global and local damage to evaluate the complex interaction of the two processes properly.

2 Methodology and assumptions

2.1 Setup and assumptions

2.1.1 General

The LS-DYNA model is automatically generated based on the common listing files with model data used for OrcaFlex, Novaframe and RM-Bridge model generation. Hence, the models have the same basis of reference as for the other global models in the project, using the same discretization, mass and stiffness distribution. For details on the input to the models see [6] and [7].

The benefit of the LS-DYNA model compared to the OrcaFlex model for global collision evaluation is the possibility to utilize non-linear effects in both load and response, including using local shell element models to study the combined effects of internal and external mechanics of certain collision events.

LS-DYNA does not permit axis-dependent translational mass, hence only sway added mass is accounted for. Note that the transverse added mass is a small portion of the dynamic mass of the bridge system. Waterplane stiffness is accounted for by a draught-dependent buoyancy force applied in the VCB of each pontoon and rotational springs that represent the waterplane stiffness in pitch and roll ($\rho g I_{xx}$). The effect of dynamic location of buoyancy and vertical center of gravity is accounted for directly in the simulations. Gravity loading balance the buoyancy force.

The model is initialized for a period of 10 seconds in which stay-cable tension, static gravity and buoyancy forces are applied to the entire model. Compression of the bridge girder in the cable-stayed section is not compensated for, and as a result the floating bridge is pulled slightly out of the initial position. The magnitude of bridge response due to this is small compared to the ship collision response.

Comparisons between OrcaFlex and LS-DYNA for simplified load cases (Section 3) indicate that the LS-DYNA model behaves with acceptable accuracy compared to the level of uncertainty involved.

The bridge girder is supported a bit differently in the LS-DYNA model as opposed to the other global models as used by the project group (Figure 2-1). Compressive springs carry the transverse loads directly from the bridge girder to the bottom of the upper legs of the tower. Linear elastic springs support the weight of the bridge girder down to the outer ends of the cross beam elements. Rigid constraints are used to connect the different elements together (lower leg, upper leg, cross beam and the tower-end of connection springs).

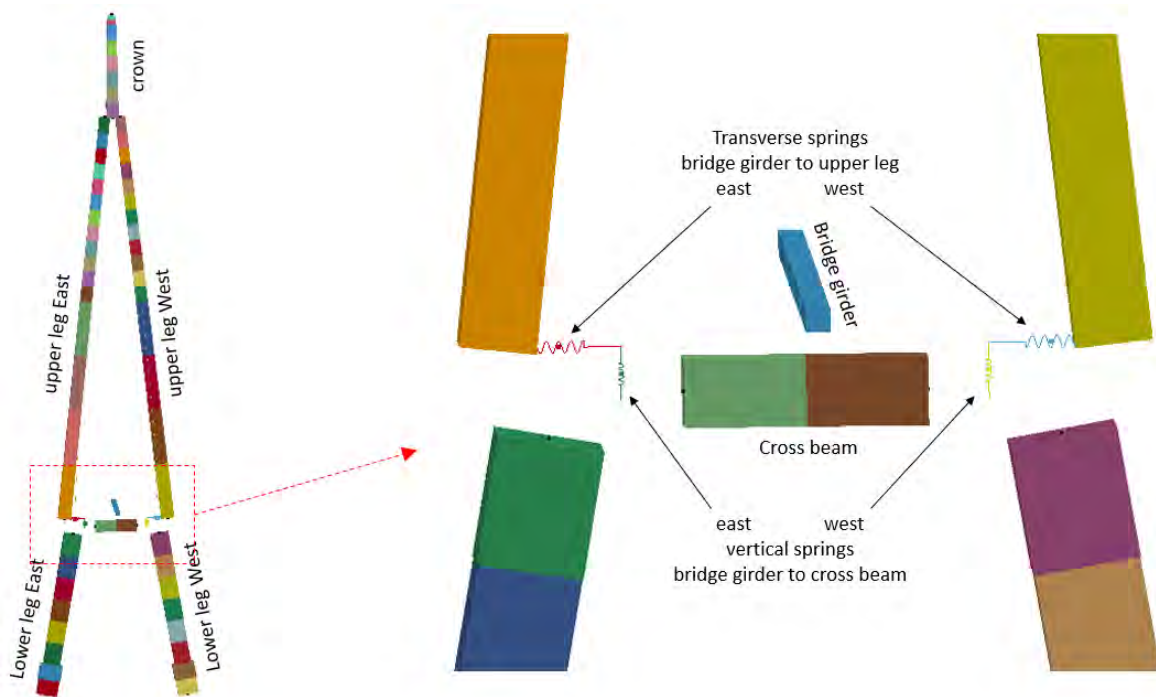


Figure 2-1 Illustration of tower and bridge girder support in tower as used for the collision simulations.

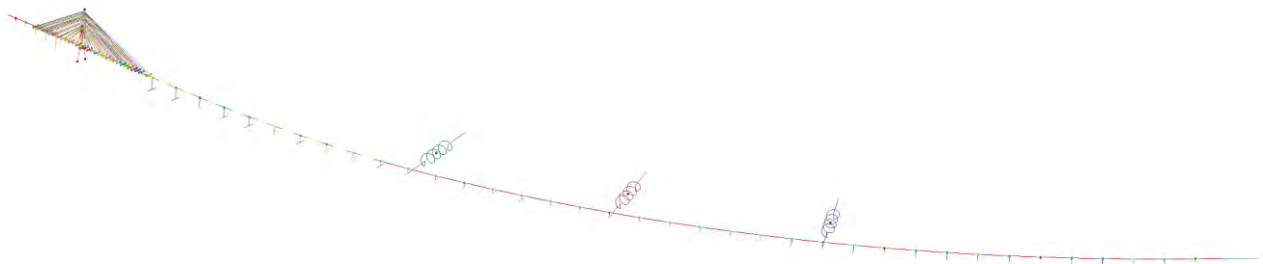


Figure 2-2 Global view of the K12_06 bridge model

2.1.2 Pontoon damping

Heave damping is accounted for by first running a simulation without heave in which the dominating vertical motion period is found, and second to add heave damping corresponding to the potential damping at this period for the individual pontoon types.

Viscous drag damping is included as a quadratic term with the pontoon velocity for sway and surge respectively. Mooring line damping is added as a linear damper element with a linear damping coefficient of 1000 kN/(m/s). This is lower than the mooring line damping found in [5], and gives a conservative estimate of the response of the moored concepts. Other hydrodynamic effects than viscous drag and heave potential damping was not accounted for. This will cause a high-frequency oscillation in LS-DYNA that is damped out under normal damping conditions, but this is not expected to influence the results significantly.

The viscous drag is a function of vortex shedding due to flow separation and the resulting turbulent fluid motion in the wake of the moving body. For transient effects the viscous drag will not be mobilized before the body has travelled a certain distance. The experiments of Sarpkaya (1966)

found this distance s to be a function of the size of the body (by radius R). For the pontoons this means that full viscous drag is not mobilized until a rather large transient motion has occurred but may be active in a steady-state current. Hence, the viscous drag coefficient used for ship collision simulations should be defined with this in mind and be significantly lower than that for a steady flow past the same pontoon.

The steady pontoon drag coefficient was estimated to be 0.3 at the time of simulation but later updated to 0.4 with CFD results (ref. [8]). As a pragmatic estimate for transient response in ship collision simulations the drag coefficient was set to 1/3 of 0.3.

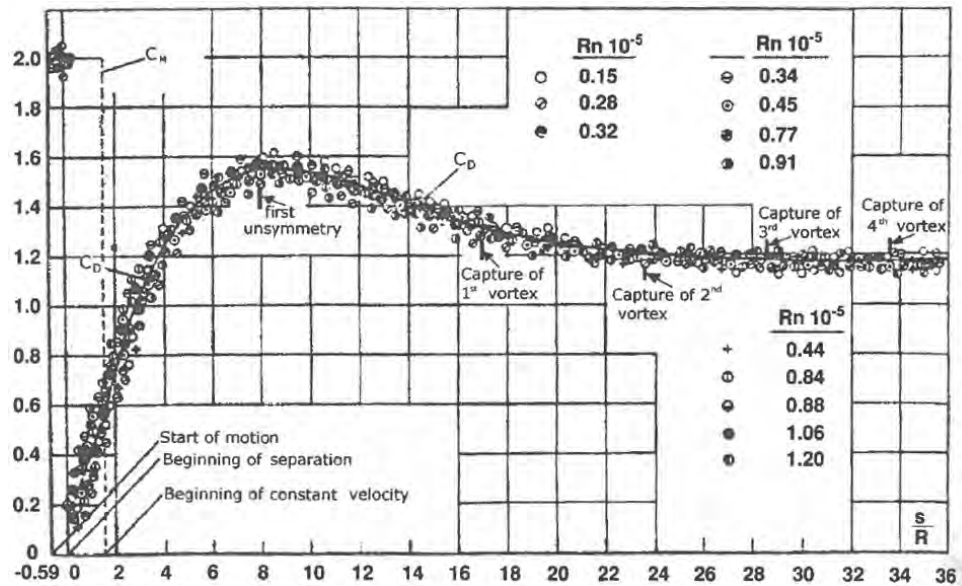


Figure 2-3 Transient drag coefficient C_d for a circular cylinder in nearly impulsively started laminar flow, from [9].

2.1.3 Mooring

Mooring is included as a combination of a spring and a dashpot representing the stiffness and viscous damping of the mooring system on a pontoon. The method of modelling of mooring stiffness in LS-DYNA has developed during the course of the analysis work, and the contents of this report contains several different mooring stiffness definitions:

- Early simulations used a linear spring, similar to the other global models [7]. These are the results in section 3. This is strictly only valid for transverse displacements of the moored pontoons of less than 3-5 m.
- The remaining simulations uses the actual mooring stiffness from the actual mooring clusters for each bridge.

Figure 2-4 shows the mooring characteristics from the Orcaflex model a linear assumption. For deflections greater than \pm 3-5 m the mooring stiffness is nonlinear. Further, there is a significant difference between the different mooring groups due to the anchor locations based on challenging seabed conditions. Figure 2-5 shows an example of resulting forces in each individual mooring line for a transverse offset from initial position. When the actual mooring stiffness is included for each pontoon the resulting mooring line tension can be found by interpolation for these curves, as done in section 5.5.

Mooring line damping was included based on a linear dashpot with a damping coefficient of 1 MN/(m/s). This is significantly below the damping values found from the Orcaflex model in [5] for moderate deformations, but as the mooring line damping decreases with increasing transverse deformation the estimate was considered reasonable.

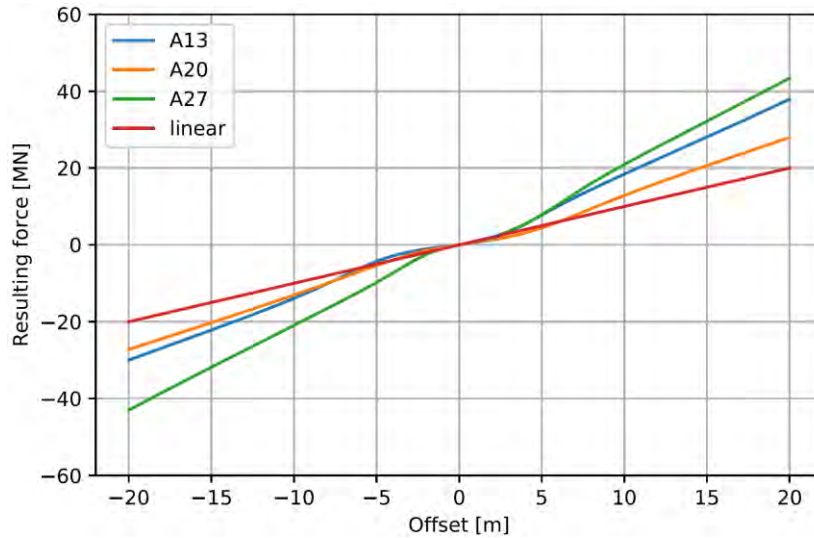


Figure 2-4 Nonlinear mooring stiffness from model K12-06 compared with a linear mooring of 1000 kN/m.

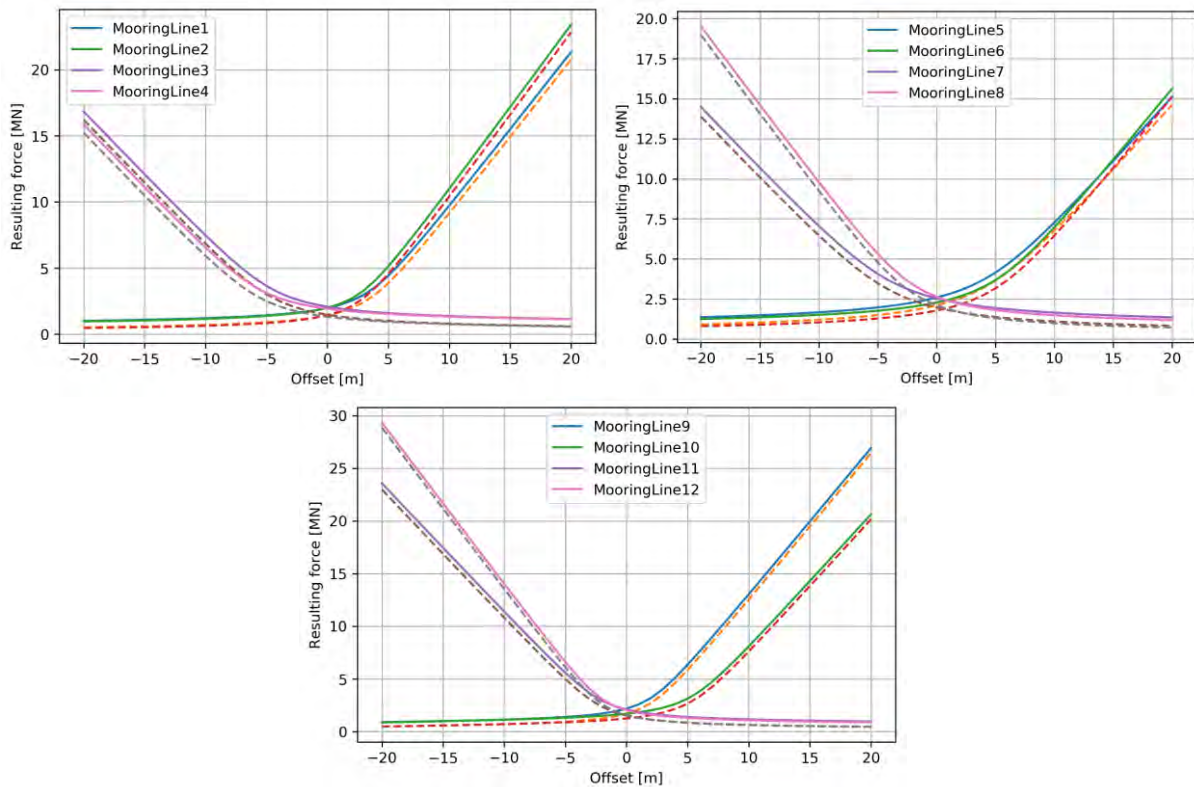


Figure 2-5 Individual mooring line force based on quasi-static transverse offset from initial position of the mooring cluster for K12-06 pontoon A13 (left top), A20 (right top) and A 27 (bottom). Continuous lines are for top of mooring line, dashed lines at the anchor end.

2.2 Collision scenarios and load modelling

2.2.1 Scenarios

The collision scenarios are defined based on the Design Basis [2, 3], as shown in Table 2-1. A 10% added mass in surge is included for the vessel. The data given in design basis separates between positions based on the axis numbers, a definition which is based on the straight bridge concept from phase 3. However, for the bridges with curvature the pontoon positions will change, and the defined split in energy based on pontoon positions will thus not be correct. This is not accounted for herein.

During the project phase a proposal was set forth to change the navigation channel on the west side of the bridge in a way that would prevent ships from under normal circumstances to head directly towards the bridge. This would significantly decrease the risk of a ship collision, and thereby reduce the energies in Table 2-1. Updated risk analysis were not available during this project phase, and this risk-reducing effect has thus not been explicitly considered.

Table 2-1 Ship collision scenarios from revised design basis [2].

CC 125m Element	Displacement [tonne]	Velocity [m/s]	LOA [m]	Energy [MJ]
Bridge girder North (of A23)	14855	5.8	138	275
Bridge girder South (of A23)	21123	6.2	206	447
Pontoon, Axis 3	14566	6.2	142	308
Pontoon, Axis 4-5	13851	6.2	140	293
Pontoon, Axis 6-23	13232	5.1	136	189
Pontoon, Axis 24-40	10662	5.1	122	153

In addition to the above, submarine collisions were mentioned in the design basis [2]. Currently the Norwegian Navy are considering the ThyssenKrupp U212 submarine as a replacement for the aging Ula-class submarines. The U212 submarines have a displacement of around 1500 tons. A typical cruising speed for such vessels is around 10 knots, resulting in 20 MJ of energy. If an impact were to occur close to maximum velocity (assumed as 22 knots) there would be around 100 MJ of energy.

If a submarine hits a mooring line it will likely shear the mooring line off. The bridge concepts are robust to loss of mooring [1]. The energy levels for a submarine impact to the pontoons is lower than those of the vessels in Table 2-1. The design vessels have narrow and strong bulbous bows, and their stiffness is sufficiently high to act as rigid towards the pontoon. Hence, submarine impacts will not be dimensioning for mooring lines or the pontoons, and is not considered further herein.

Similarly, smaller high-speed passenger crafts will with limited weight and high velocity not give higher impact energy than the larger slower ships in Table 2-1.

2.3 Coupled local and global response

Due to the global flexibility of the bridge the collisions considered herein, especially those not close to the tower or northern abutment, will be in disagreement with the assumptions and limitations used for the typical split between local and global collision response (internal and external mechanics). To mitigate this, checks with coupled local and global simulations were conducted. The time frame of the project limited the extent of these checks.

3 Comparison between OrcaFlex and LS-DYNA

NOTE : This chapter has not been updated with the latest model iterations. Its purpose is to show a comparison of response to illustrate that the main hydrodynamical aspects were covered in LS-DYNA, and this was considered adequately with simulations on old models. The section includes results for the end-anchored bridge concepts, first K11 to compare response when considering viscous effects on pontoons and then K12 for comparison with mooring line stiffness and damping.

The global dynamics simulations in the project are mainly carried out in the hydrodynamic analysis software OrcaFlex, as the sum of effects considered by the software is unrivalled compared to the alternatives when considering the important aspects affecting the global dynamic behavior. However, OrcaFlex has some limitations when it comes to modelling of inelastic behavior.

LS-DYNA was selected as the preferred tool for local ship collision simulations due to the availability of advanced fracture criteria applicable to collision evaluation of large stiffened panel structures such as ships and floating bridges. To bridge the gap between the global and local bridge response, a global model of the bridge was established in LS-DYNA. This model could then be used both for a direct evaluation of global dynamic response to a ship collision event and as a means of coupling the internal (local structural damage) and the external (global motion) mechanics of a ship collision event. The latter has not yet been performed.

3.1 Setup

It is of interest to verify the global dynamic behavior of the OrcaFlex model vs. the LS-DYNA model. For this purpose, a well-defined impulse load was considered in both softwares.

A force-time history (Figure 3-1) was applied to the A25 pontoon for the K11-06 and K12-04 bridge revisions, and the resulting response was compared. This load impulse roughly corresponds to a heavy vessel impacting with an energy in the range of 400 MJ to a pontoon.

The simulation duration was 200 s from onset of the force. A 0.05s time step was used in OrcaFlex (implicit) whereas explicit simulations were performed in LS-DYNA (time step in the range of 10^{-4} s).

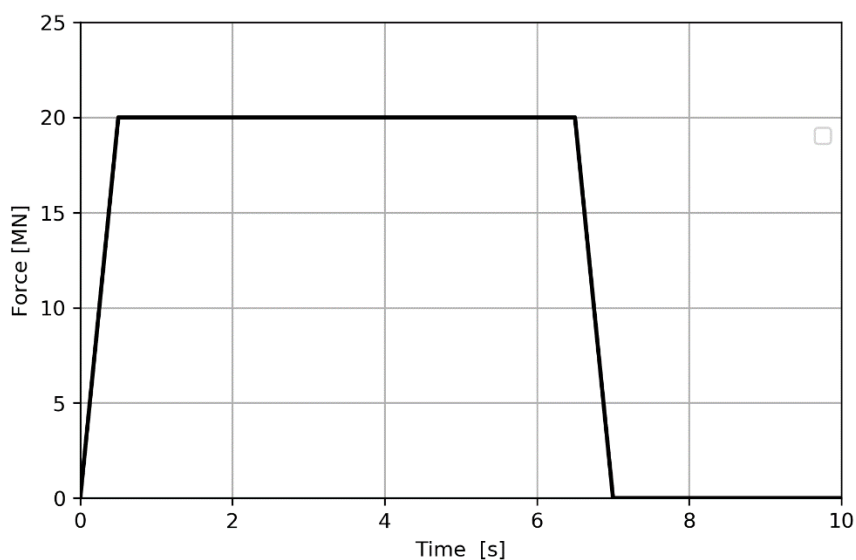


Figure 3-1 Force-time history used to describe a load impulse to the bridge.

3.2 Comparison of results for K11-06

A sensitivity check of damping effects (Figure 3-2) was performed.

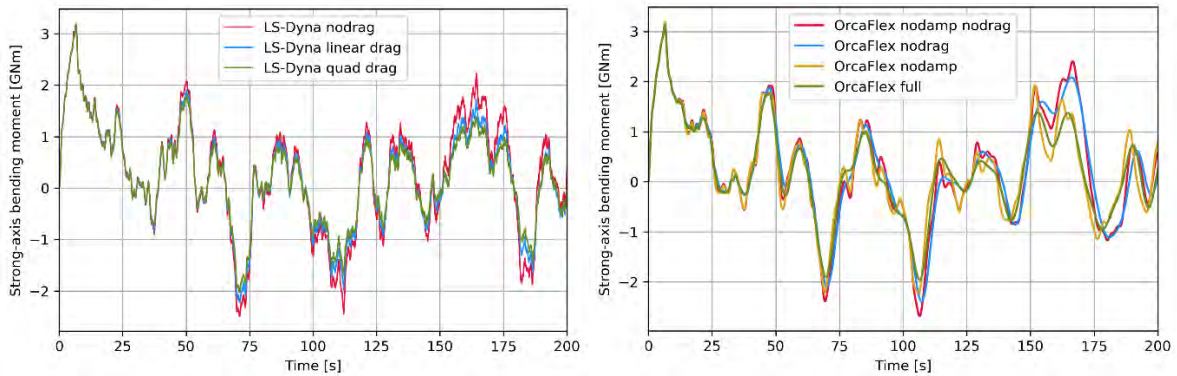


Figure 3-2 LS-DYNA (left) and Orcaflex (right) strong-axis bending moment in bridge girder around impact location with varying damping.

Next, the transverse displacement time history was compared at three locations: the impact location A25 and 1000 m to either side, shown in Figure 3-3. An adequate representation of the deflection-time history is shown in LS-DYNA compared to the OrcaFlex behavior, indicating that the major structural and hydrodynamic aspects are similar.

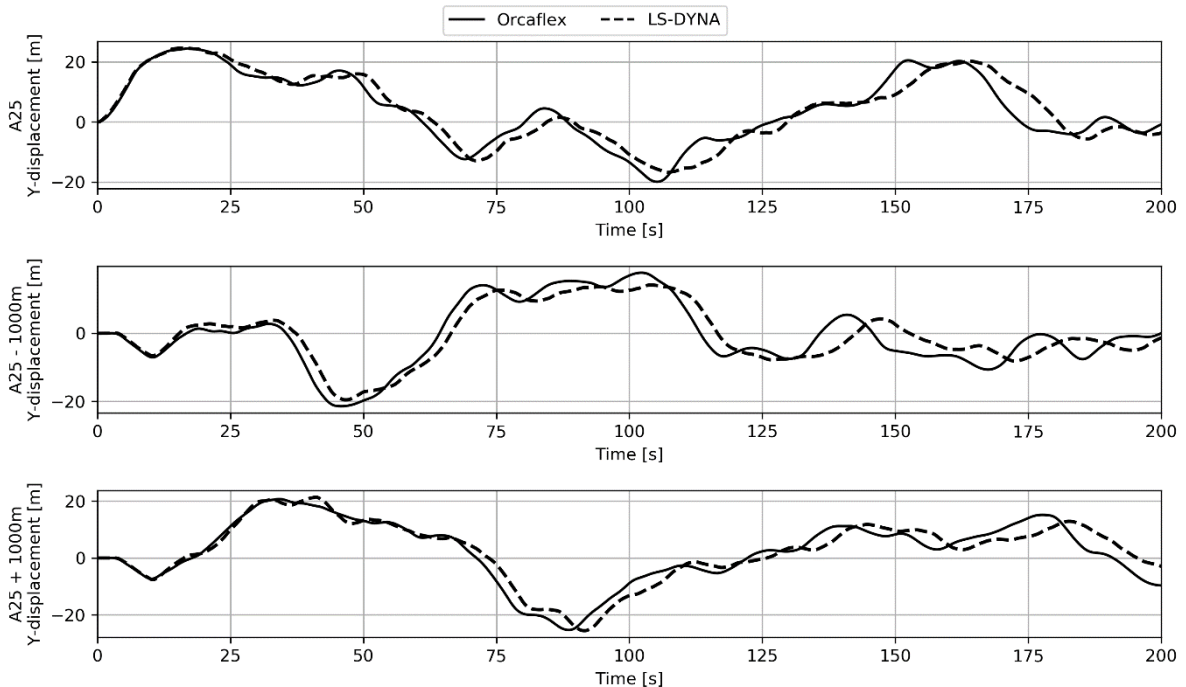


Figure 3-3 K11-06 : Time-history of transverse displacement of the bridge girder at three locations.

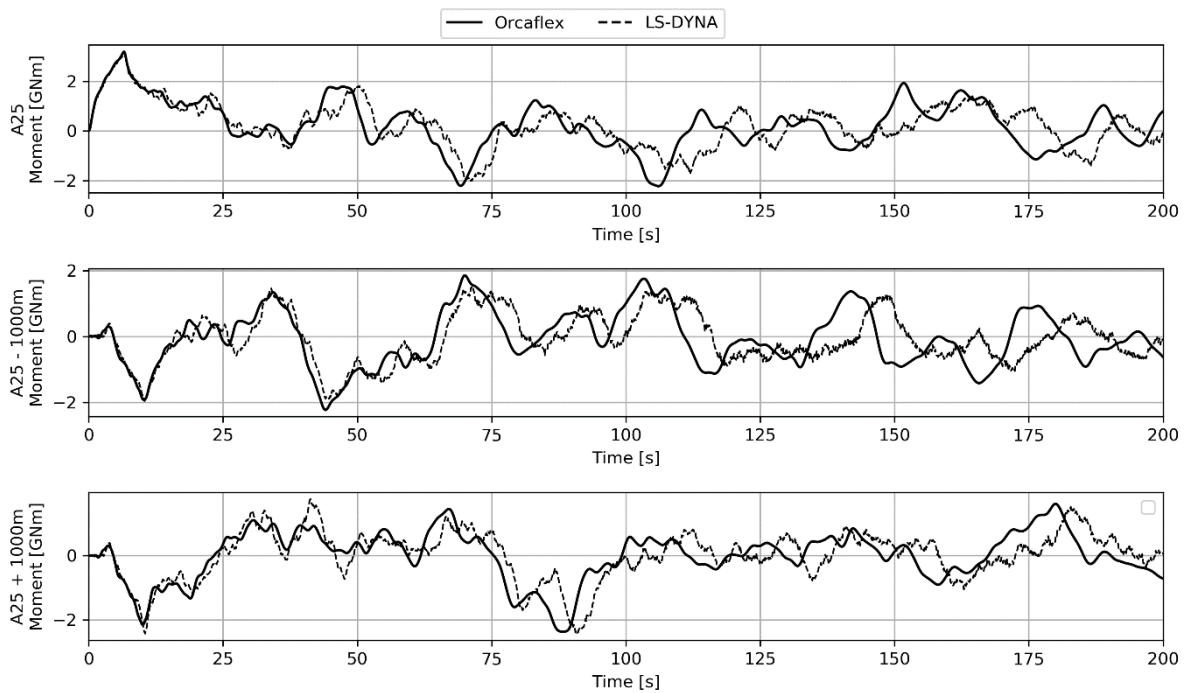


Figure 3-4 K11-06 : Time-history of strong-axis bending moment of the bridge girder at three locations.

3.3 Comparison of results for K12-04

Note : This simulations described in this section were from an earlier bridge model, and the method of using linear springs for mooring was later improved to a nonlinear spring. The comparison in this section was however not updated to reflect this.

The K12-04 model in OrcaFlex contains the full mooring system in actual configuration with nonlinear stiffness and full damping, whereas the LS-DYNA model contains linear springs with 500 kN/m spring stiffness and a mooring damping of 1 MN/(m/s) is specified for each moored pontoon. Hence, the two models do not represent the exact same physical condition, and an exact match is not expected when performing comparisons.

The time history of displacement at three locations are shown in Figure 3-5. OrcaFlex is run both with linear mooring springs (denoted *link mooring* in the figure) and with the full mooring system with and without damping on the mooring lines. With a linear spring the nature of the response is similar in both softwares. The large difference between the linear and full mooring indicate that the mooring response is not linear for the displacement amplitudes in a ship collision event. This should at a later stage also be included in the LS-DYNA model to improve the response.

The effect of mooring stiffness (dashed lines) and the effect of mooring damping (continuous lines) seems to be captured in a similar manner. The decay between load peaks seems to be consistent with the full mooring damping and with a linear damping of 1 MN/(m/s). Hence, the dissipation of energy due to mooring line damping is captured adequately in LS-DYNA.

It is of interest to include nonlinear stiffness and damping of the mooring system at a later stage to improve the (hydro)dynamic behavior of the LS-DYNA model.

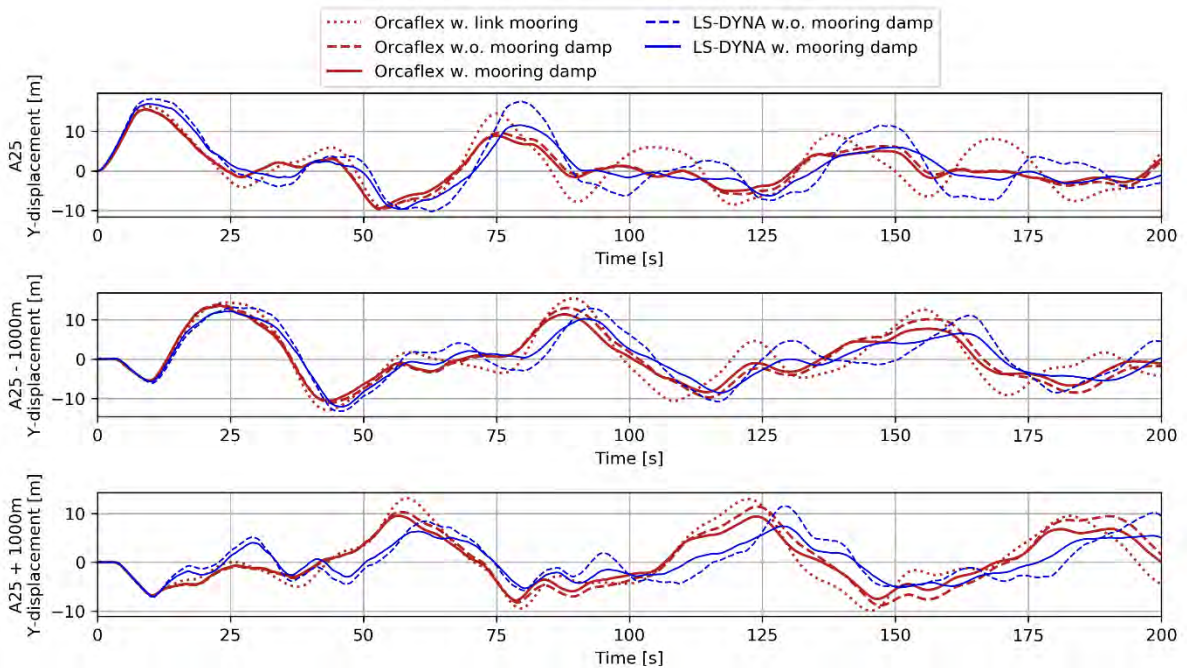


Figure 3-5 K12-04 : Time-history of transverse displacement of the bridge girder at three locations.

The resulting strong-axis bending moment is compared in Figure 3-6 for the same locations. The linear damping seems to also give an adequate behavior in the LS-DYNA model. It is to be noted that the moment-time history varies between the two models, and LS-DYNA have several short oscillations in the bending moment that is not present in OrcaFlex. The overall behavior and the peak values do however correlate fairly well.

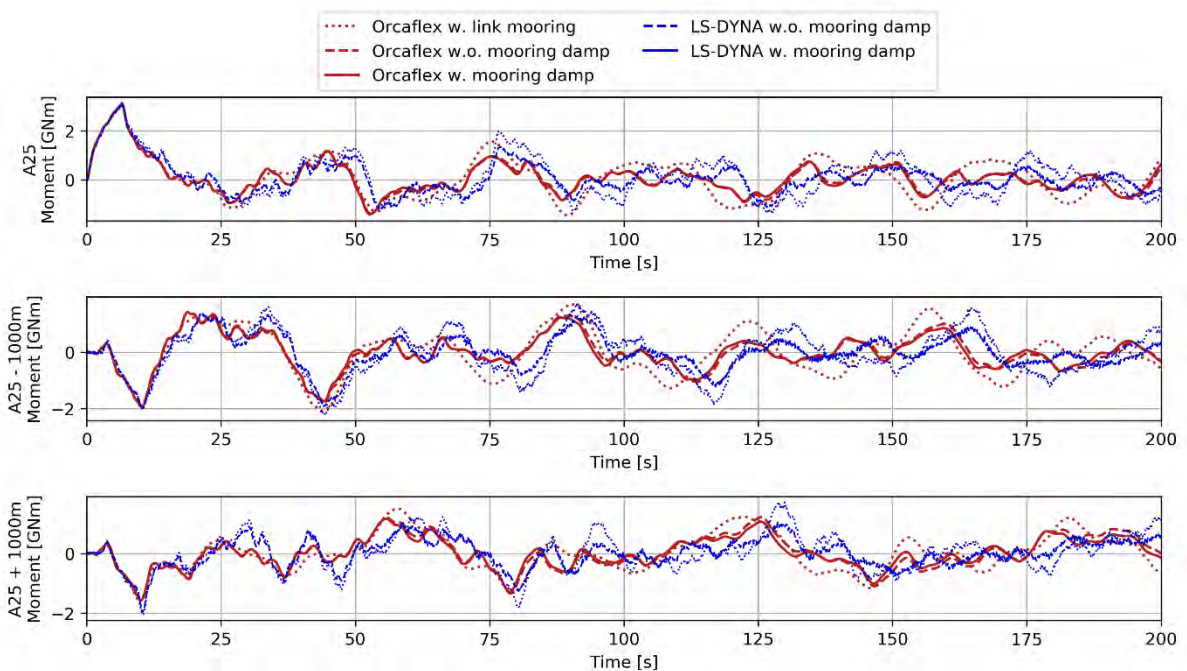


Figure 3-6 K12-04 : Time-history of strong-axis bending moment of the bridge girder at three locations.

3.4 Eigenmodes

NOTE : This chapter has not been updated with the latest model revisions for K12, but still shows the similarity between eigenmodes under similar assumptions for LS-DYNA and Orcaflex.

Eigenmodes were compared for the various concepts. In LS-DYNA, the added mass was not adjusted to match the frequency of the mode shape, rather the infinite value added mass was used. This results in an increasing mismatch between the modes as the frequency-dependent added mass changes for the various modes in OrcaFlex.

A key difference between the LS-DYNA model used for eigenvalue analysis and the LS-DYNA model used for collision simulations is that the eigenmode version of the model uses linear springs to represent the waterplane stiffness in heave whereas the collision version of the model used a buoyancy force dynamically dependent on each pontoons z-position. The latter is preferred for the collision simulations due to numerical stability, but prevents the vertical eigenmodes to be captured correctly.

For simplicity only the transverse mode shapes are compared in the following. A good agreement is found both in period and shape when considering the difference in added mass on the pontoons.

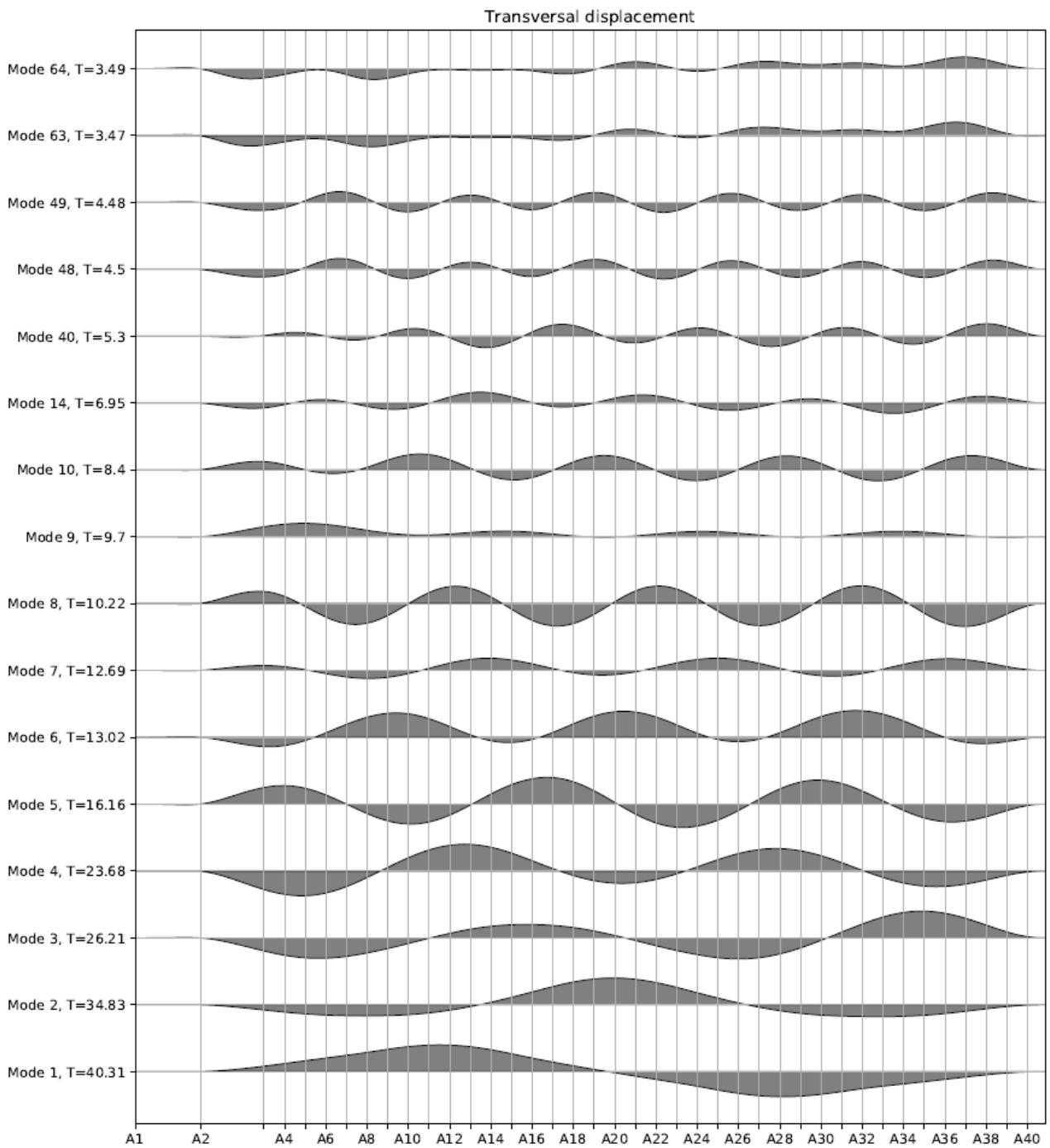


Figure 3-7 OrcaFlex transverse eigenmodes for K12_05

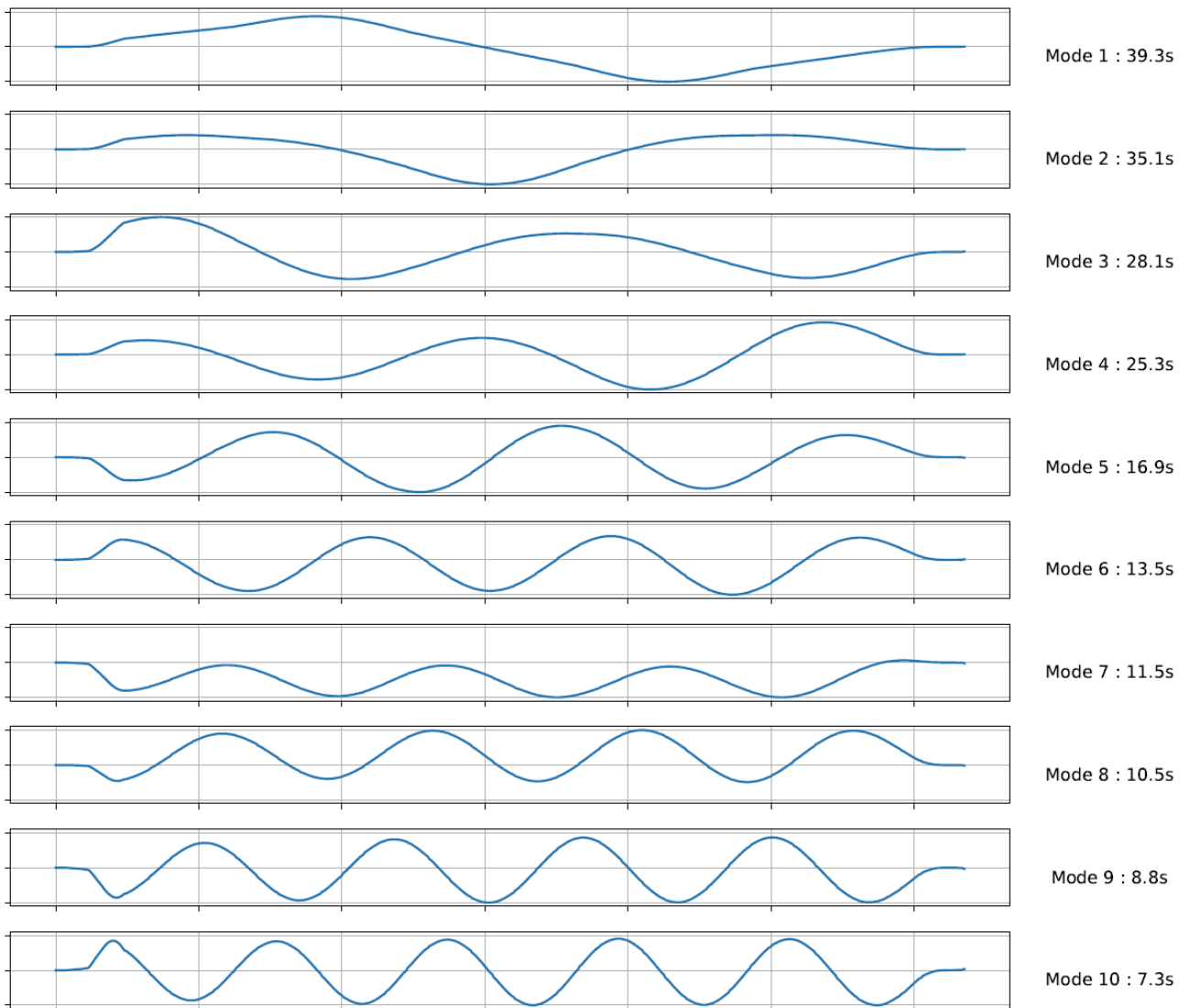


Figure 3-8 LS-DYNA transverse mode shapes for K12_05

4 Local response evaluations

The following sections presents results from the local collision analyses for

- Ship bows vs. pontoon
- Ship deckhouse vs. bridge girder
- Rigid crane pedestal vs. bridge girder (outside of design basis)

The collisions are performed by decoupling external and internal mechanics. Hence the results contain only the internal mechanics of the collision. The magnitude of the energy dissipation in the collision must be documented separately.

The analyses create envelope curves for the force displacement relationship for input to the global collision analysis. In addition, the damage from the collision is determined; how much of the structure is damaged, how many compartments are flooded etc.

4.1 Ship bow vs. pontoon

4.1.1 Scenarios

Three base case collision scenarios have been defined to create envelope curves for the force displacement relationship. The base cases are collisions at:

- Centerline bulkhead
- 2.5 m offset from the centerline bulkhead
- 30 degree angle with respect to pontoon longitudinal axis

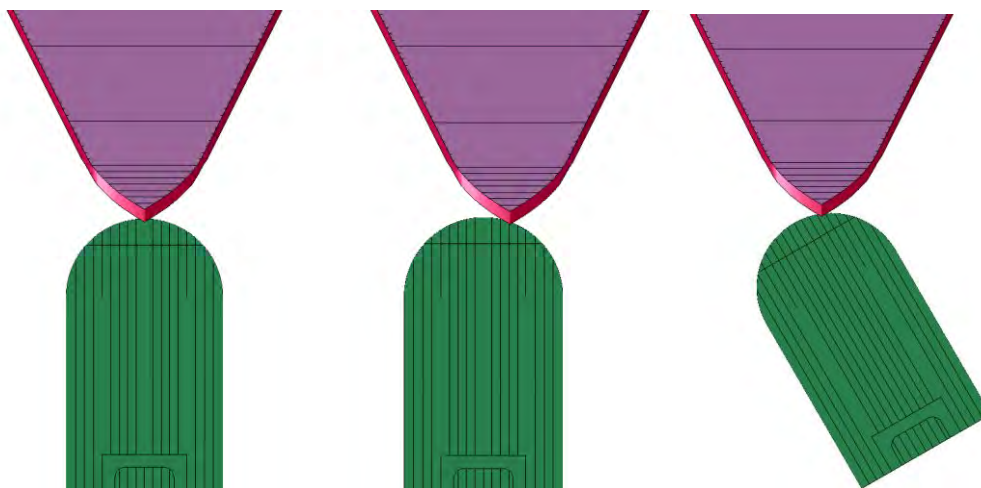


Figure 4-1 Collision scenarios, (a) left, (b) middle and (c) right

The energy levels to be dissipated by local plastic deformation are found in the global collision model and are listed in Section 5.2. For the pontoons up to around 200 MJ of energy is dissipated locally.

Note: The local collision simulations were performed up to about 150 MJ dissipated energy, whereas the latest global collision simulations show that up to 200 MJ may be dissipated locally. It was

assumed that the extrapolated force-displacement curve from the local collision simulations adequately describes the local behavior also for increased levels of indentation. The potential flooding of compartments is not expected to change with a small increase in local energy. Hence, the current values were considered acceptable irrespective of the mismatch in maximum dissipated local energy.

4.2 Ship deckhouse vs. bridge girder

Impacts to the bridge is simplified as deckhouse collisions in the design basis, and a deckhouse model was provided based on the work documented in [10].

4.2.1 Scenarios

In total four deckhouse vs. bridge girder collision scenarios were analyzed. Impact at two different angles to the bridge girder were considered; a 0 and a 10 degree relative angle between the ship and bridge transversal axis as shown in Figure 4-2. For each of the two angles, two collision heights were considered, as shown in Figure 4-3 and Figure 4-4.

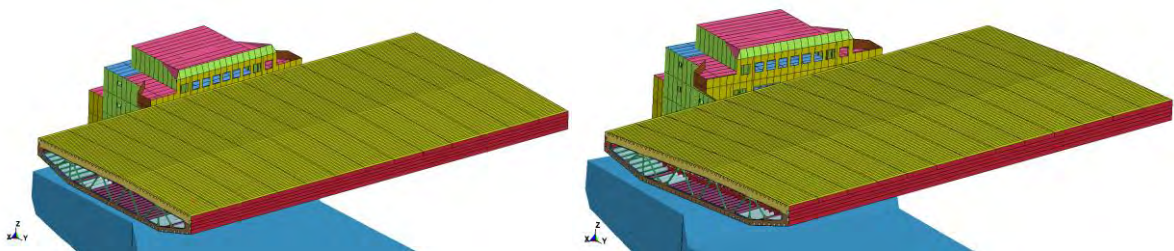


Figure 4-2 Deckhouse-bridge girder collisions with 0 degrees (left) and 10 degrees (right) relative angle between ship surge and bridge transversal directions.

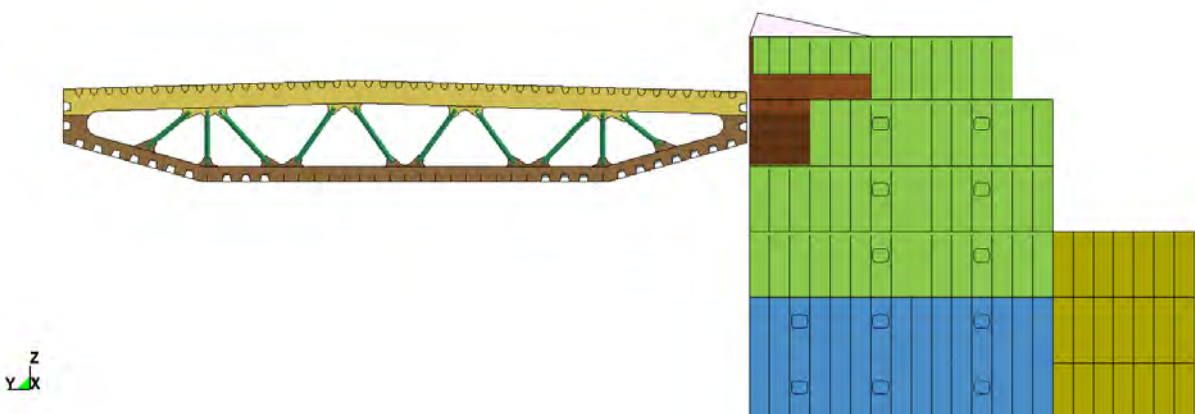


Figure 4-3 Deckhouse-bridge girder collisions, high impact, 0 degree collision angle

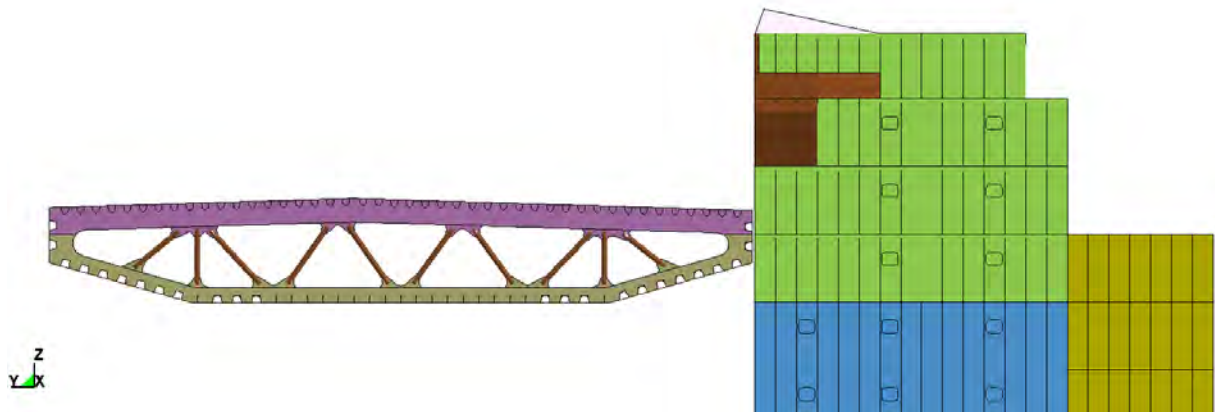


Figure 4-4 Deckhouse-bridge girder collisions, low impact, 0 degree collision angle

Additionally, a collision between the bridge girder and a rigid cylinder representing a typical crane pedestal is run to investigate the structural response of the bridge girder structure.

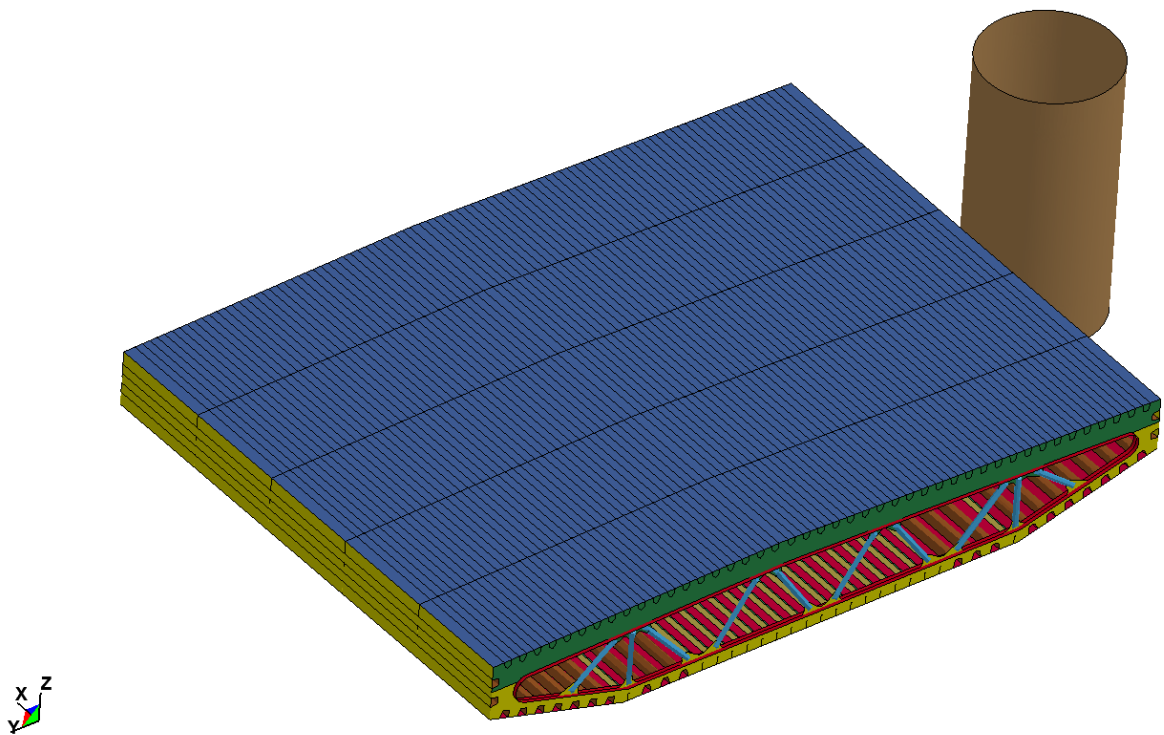


Figure 4-5 Rigid crane pedestal vs. bridge girder

Other impact scenarios that could occur to the bridge girder from vessels or objects with elevations above 14 m may be containers on the container vessel or a large cruise vessel with a bow significantly higher than the clearance below the bridge. These scenarios are not considered in this report.

The energy levels to be dissipated by local plastic deformation are found in the global collision model and are listed in Section 5.2. For the deck house to bridge girder collision up to around 200 MJ of energy is dissipated locally.

4.3 Material modelling

A realistic representation of the material response is important in order to obtain a realistic simulation outcome. For example, the slope of the stress-strain curve controls where strains will localize; a steep slope leads to more rapid strain concentrations with resulting fracture. Further, the onset of fracture marks a point of reduced resistance of the struck object, and a good prediction of the onset of fracture is required. A discussion of the material modelling for ship collision events is given in refs. [11], and more specifically towards the recommendations from DNVGL-RP-C208 [12] and in ref. [13].

The approach utilized in this report will in general follow the recommendations of DNVGL-RP-C208 using the option of a calibrated fracture criterion (Section 5.1.2 of the RP), in which well-known and proven fracture mechanics is used to describe the fracture locus. The approach was verified against a range of experimental tests in which the robust prediction of fracture was shown to be industry-leading both in accuracy and a low variability when applied to different structural problems with varying mesh discretization. Further, the plastic hardening parameters are adjusted compared to the recommended values in RP-C208, especially where the recommended values are not in line with DNVGL-OS-B101 [14]. The approach for material modelling is described in detail in the following.

4.3.1 Plastic work hardening

Structural steels commonly used in offshore rigs follow J2 flow theory, i.e., the von Mises yield criterion, the associated flow rule and isotropic hardening is adopted. The yield criterion is given by

$$f = \sigma_{eq} - \sigma_f(\varepsilon_p) = 0 \quad (1)$$

where σ_{eq} is the von Mises equivalent stress. The current flow stress σ_f is assumed as a function of the equivalent plastic strain ε_p via the Hollomon-type power-law hardening rule, i.e.,

$$\sigma_f(\varepsilon_p) = \begin{cases} \sigma_0 & \text{if } \varepsilon_p \leq \varepsilon_{plateau} \\ K(\varepsilon_{0,eff} + \varepsilon_p)^n & \text{if } \varepsilon_p > \varepsilon_{plateau} \end{cases} \quad (2)$$

where K and n are the power-law hardening parameters and σ_0 is the initial yield stress. To account for the existence of a strain plateau, the hardening is delayed until the plastic strain reaches the plateau strain $\varepsilon_{plateau}$. Thus, $\varepsilon_{0,eff}$ is defined by the relation

$$\varepsilon_{0,eff} = \varepsilon_0 - \varepsilon_{plateau} = \left(\frac{\sigma_0}{K}\right)^{\frac{1}{n}} - \varepsilon_{plateau} \quad (3)$$

where ε_0 is the strain at initial yield. The material response is plotted in Figure 4-6.

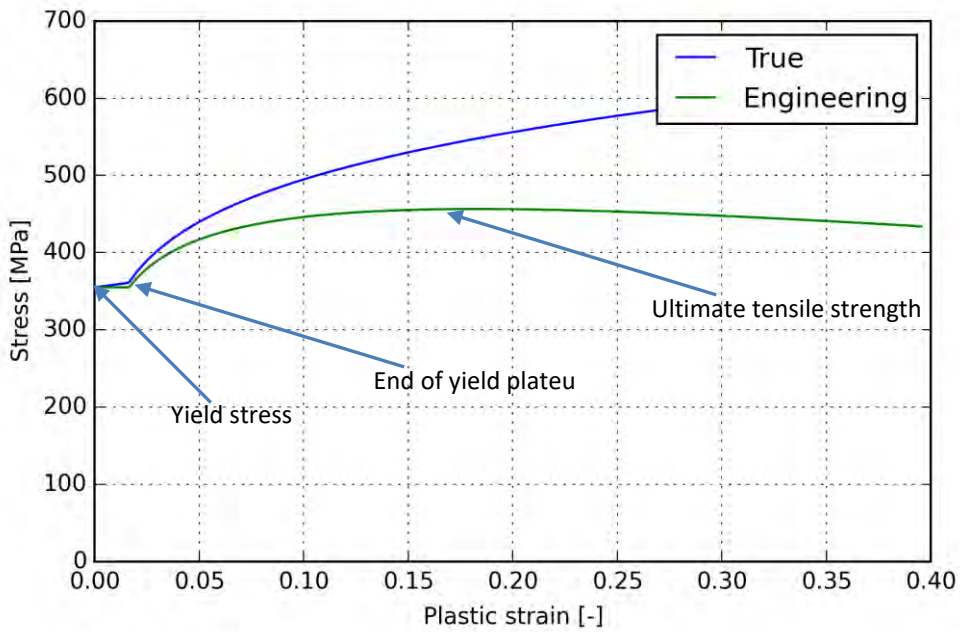


Figure 4-6 Example of stress-strain curve of a steel material, both for true and engineering values of stress and strain.

4.3.2 Strain-rate dependence

Collision simulations may yield high strain rates. Conventional steel materials show significant strain hardening for the initial yield stress (Figure 4-7a). However, for the plastic flow stress the strain hardening is considerably smaller (Figure 4-8b). As the critical aspect of a collision is to dissipate the strain energy, the most relevant part of the strain energy dissipation occur at large plastic strains. Hence, strain-rate hardening, if applied, must be calibrated to the flow stress and not to the initial yield stress.

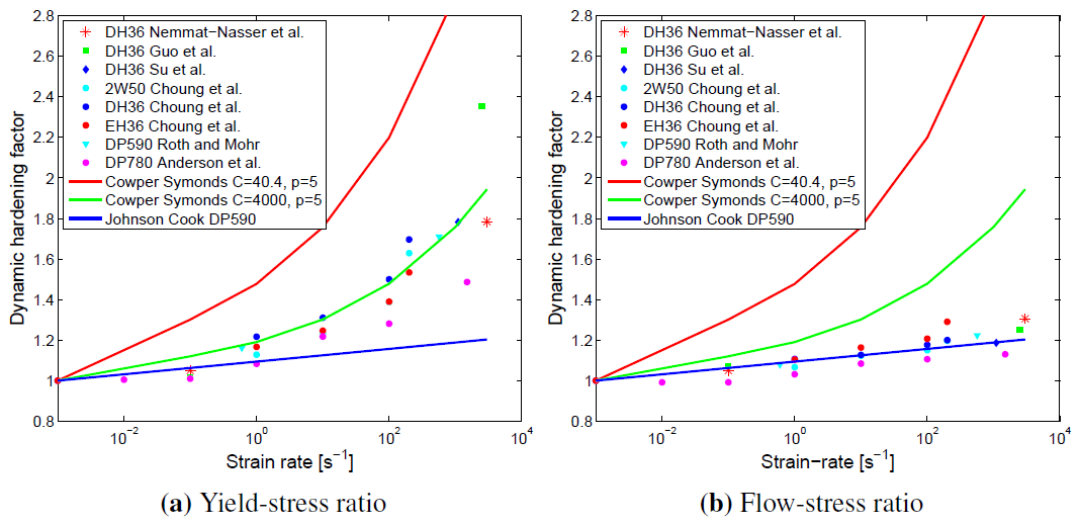


Figure 4-7 Experimental results of strain-rate hardening for initial yield stress and flow stress, figure from [15]

The experimental techniques for measuring strain-rate dependent response are challenging, and results vary between material batches and different testing facilities. Hence, the actual strain-rate hardening of the material used in a specific structure is difficult to guess using generic material data; experimental data from the actual material batch is required.

Ref. [11] evaluated the effect of strain-rate hardening in a ship collision scenario, and concluded that the actual contribution from strain-rate hardening was in the range of 10% to the energy dissipation. If strain-rate hardening was calibrated to initial yield stress rather than flow stress, the predicted effect of strain-rate hardening could be as high as 65%, i.e., an overestimation of the dissipated energy.

Considering the fact that strain-rate hardening will limit the indentation into the structure and acknowledging the uncertainty in actual strain-rate hardening parameters in lieu of material tests, it was decided to omit strain-rate hardening from the current assessment.

4.3.3 Fracture

Background

Fracture of steel plates is a complicated process, involving many different challenging aspects. The micromechanical process of fracture occurs at a length scale several orders of magnitude below the plate thickness. In comparison, the scale of the structural problem in a maritime collision event requires that the applied finite element length is between five to ten times the plate thickness. The micromechanical response governs the macromechanical response of the steel plate that can be simulated with the shell finite element model.

On a micromechanical level the fracture process is typically split in three phases; void nucleation, void growth and coalescence of voids. The level of plastic strain at which void nucleation occurs is strongly dependent on the strain-state of the material, i.e., the ratio at which the material is pulled in the different directions. The strain state is commonly described by stress triaxiality T as

$$T = \frac{\sigma_1 + \sigma_2 + \sigma_3}{3\sigma_{eq}} \quad (4)$$

where σ_i are the principal stresses and σ_{eq} the equivalent stress (herein the von Mises stress). The stress triaxiality describes the ratio between the volume change (hydrostatic) and the shape change (deviatoric) of the material. For plane stress states, as assumed with most shell elements, the strain-rate ratio β conveniently describes the strain state as

$$\beta = \frac{\dot{\varepsilon}_2}{\dot{\varepsilon}_1} \quad (5)$$

Where $\dot{\varepsilon}_i$ is the principal strain rates.

It is common to present results of the strain-state dependent fracture limit of materials in a forming limit diagram (FLD), such as in Figure 4-8. Typically, a decreasing critical fracture strain is found for decreasing absolute value of negative minor strains, whereas an increasing critical fracture strain is observed for increasing absolute value of positive minor strains.

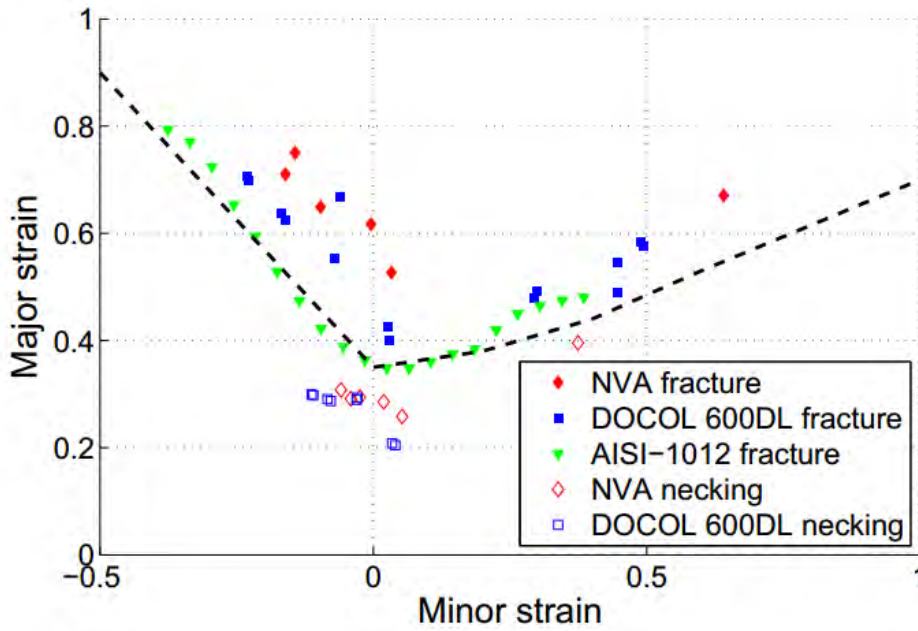


Figure 4-8 Typical strain-state dependent fracture response for common steels, from [15]

Pre-necking instability

The Bressan-Williams-Hill criterion, [16], is a theoretical fracture criterion that includes the commonly observed fracture behavior in Figure 4-8. The criterion predicts the onset of local instability in the form of either necking or a through-thickness shear failure. For reduced dependence of the strain path, the criterion was formulated in the principle stress space as

$$\sigma_1 = \begin{cases} \frac{2K}{\sqrt{3}} \frac{1 + \frac{1}{2}\beta}{\sqrt{\beta^2 + \beta + 1}} \left(\frac{2}{\sqrt{3}} \frac{\hat{\epsilon}_1}{1 + \beta} \sqrt{\beta^2 + \beta + 1} \right)^n & \text{if } -1 < \beta \leq 0 \\ \frac{2K}{\sqrt{3}} \frac{\left(\frac{2}{\sqrt{3}} \hat{\epsilon}_1 \right)^n}{\sqrt{1 - \left(\frac{\beta}{2 + \beta} \right)^2}} & \text{if } 0 < \beta \leq 1 \end{cases} \quad (6)$$

where K and n are the power law hardening parameters, $\hat{\epsilon}_1$ is a critical strain, β the strain-rate ratio and σ_1 the major (tensile) principal stress. For most materials, $\hat{\epsilon}_1 = n$ can be assumed with reasonable accuracy, thereby simplifying calibration of the criterion. A pre-necking mesh scaling can be included in the BWH instability criterion by scaling $\hat{\epsilon}_1$ as

$$\hat{\epsilon}_1 = \frac{1}{2} \left(\frac{t_e}{l_e} + 1 \right) n$$

where t_e/l_e is the initial ratio of element thickness to element length. This accounts for strain-concentrations not captured by coarse elements, e.g., due to out-of-plane bending of the plate close to stiffening members.

Post-necking response

The BWH criterion has been extended to include post-necking damage [17]. By considering the thickness reduction of a virtual neck inside the element (Figure 4-9), and adhering to the

experimental observation that the necking length at incipient necking is about the size of the plate thickness, a damage rule was formulated as

$$1 - D = \frac{\exp((1 - \langle -\beta \rangle) \Delta \varepsilon_1)}{1 + \frac{l_0}{t_0} [\exp((1 - \langle -\beta \rangle) \Delta \varepsilon_1) - 1]}$$

where D is the damage, $\Delta \varepsilon_1$ is the increase of major principal strain after onset of damage, l_0/t_0 is the ratio of element length to thickness at incipient necking and $\langle x \rangle = \max(x, 0)$. The damage is coupled to the element strength to achieve a decreasing element strength once local necking initiates. This damage function effectively accounts for the small local neck (with length equal to plate thickness) in a large element (five-ten times the plate thickness), and the strength reduction of the large shell element due to the small local neck inside the element.

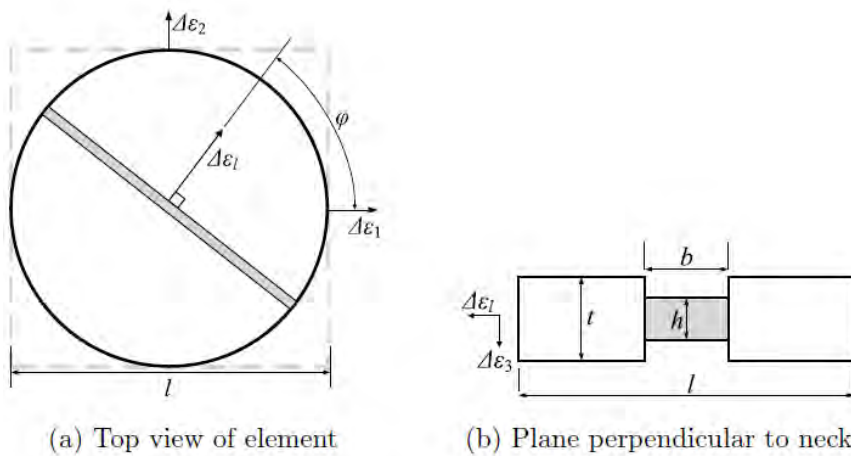


Figure 4-9 Material element with a local virtual neck.

The coupled damage reduces the element strength upon further deformation after incipient necking. At some point the element has to be removed from the simulation to allow the crack to propagate. In the coupled damage model, it was assumed that the element is removed once the thickness strain in the virtual neck reaches a critical value. The total thickness strain inside the virtual neck, $\tilde{\varepsilon}_3$, is now a function of the element strain and the damage D as

$$\tilde{\varepsilon}_3 = \varepsilon_3^0 + \Delta \tilde{\varepsilon}_3 = \varepsilon_3^0 + \Delta \varepsilon_3 + \ln(1 - D), l_0 \geq t_0$$

where ε_3^0 is the thickness strain at incipient necking (onset of BWH failure) and $\Delta \varepsilon_3$ the increase in thickness strain after virtual necking. To account both for reduced ductility and reduced post-necking mesh dependence at increasing triaxiality, the critical thickness strain in the virtual neck, $\tilde{\varepsilon}_{3,max}$, is defined as a ratio of the thickness strain at onset of necking, ε_3^0 , as

$$\tilde{\varepsilon}_{3,max} = \begin{cases} \varepsilon_3^0(1 + \xi) & \text{if } -1 < \beta \leq 0 \\ \varepsilon_3^0(1 + \xi(1 - \psi\beta)) & \text{if } 0 < \beta \leq 1 \end{cases}$$

where ξ and ψ are calibration parameters to the fracture model. Due to the damage coupling causing a reduction of the element strength, the dissipated energy to fracture is not that sensitive to the exact point of erosion. Hence, for most structural steels $\xi = 1$ and $\psi = 0.9$ can safely be assumed.

Discussion

The resulting instability and erosion model is visualized in a forming limit diagram in Figure 4-10. Combined, the BWH criterion with coupled damage captures the essence of the experimentally observed strain-state dependent behavior of steel plates, both prior to and after necking. Mesh-dependent behavior is adjusted for in a pragmatic way both for pre- and post-necking mesh dependence.

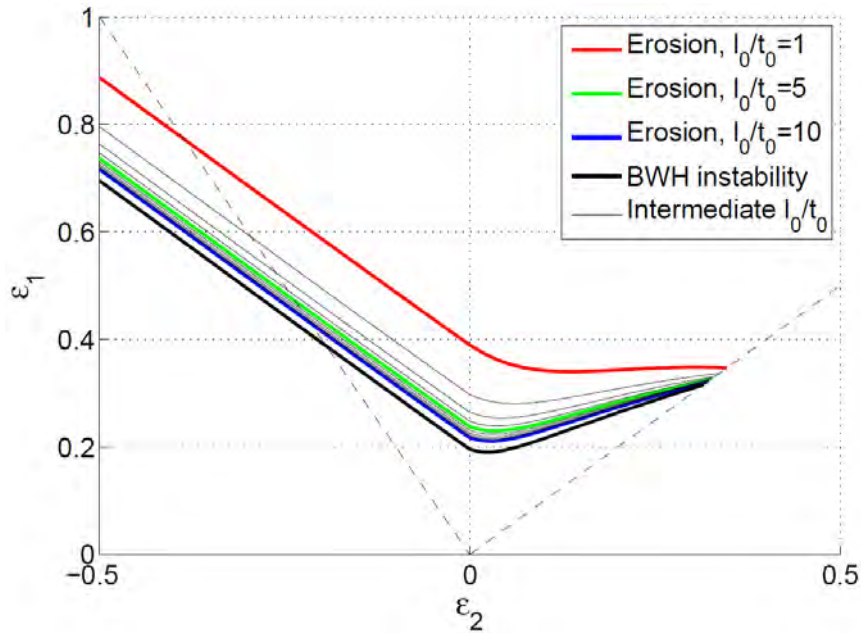


Figure 4-10 Visualization of onset of local instability (by the BWH criterion) and the mesh-dependent erosion limit from Eq. (10).

An appropriate method of adding a safety factor against the failure limit on the BWH criterion is to scale the $\hat{\epsilon}_1$ parameter in Eq. (6)). If not given directly, the parameter is taken similar to the power law exponent n . However, by defining $\hat{\epsilon}_1 = n/\gamma$ (with γ being the safety factor) the BWH criterion will trigger at a lower level of principal stress, thereby reducing the allowable straining. This scales effectively to different triaxial strain-states, and mesh scaling can be applied as before to ensure robust performance. The resulting strain-state dependent criterion is plotted in the principal stress space in Figure 4-11. It is to be noted that the assumption of a lower bound material strength directly introduce a safety margin on the fracture limit due to early strain localization, see [13] for discussion. Hence, an additional safety factor was not included herein.

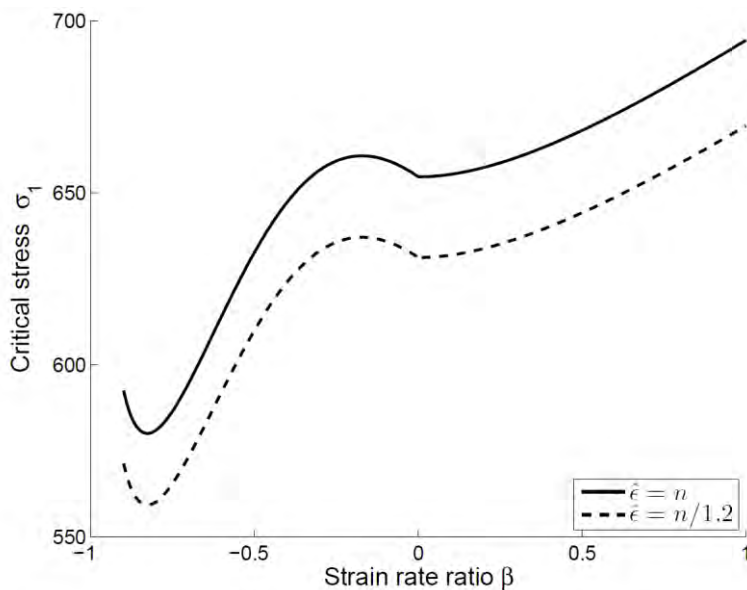


Figure 4-11 Critical principal strain from the BWH criterion, Eq. (6), with a safety factor on the fracture strain.

4.3.4 Verification of methodology

A large numerical benchmark study has been performed to document the fracture criterion. This revealed that the BWH criterion with coupled post-necking damage gave the best estimate of fracture limit with the least statistical variability compared to the commonly used fracture criteria for coarsely meshed shell structures. The verification work is shown in Enclosure 6, and most of it was also published in [15] and [18]. The same verification methodology was also applied to the proposed simplified fracture criterion in DNVGL-RP-C208 and the results were discussed in [13].

Based on the verification, it was decided that the use of the BWH fracture criterion with post-necking damage, lower bound material strength and no additional safety factor on fracture was the most appropriate method for accurate simulations of fracture in ALS scenarios; giving a lower bound but realistic estimate of fracture.

4.4 Analysis setup

4.4.1 Material strength

The material model consists of a linear elastic part up to yield followed by a yield plateau, and a power law hardening rule to simulate the strain hardening in accordance with typical material behavior (see ref. [11] for details). A BWH fracture criterion with post-necking damage was included to account for the strain-state dependent process of material fracture with low mesh dependency (ref. [17]).

For the normal steels used in the analysis the stress strain curves are based on a large number of material tests. It is therefore possible to use mean and lower bound values on the material properties.

The stress strain curves for the materials used in the collision analyses are shown in Figure 4-12. The input for the material curves is taken from DNVGL-OS-B101 [14], using a lower bound or mean ultimate tensile strength and elongation to failure.

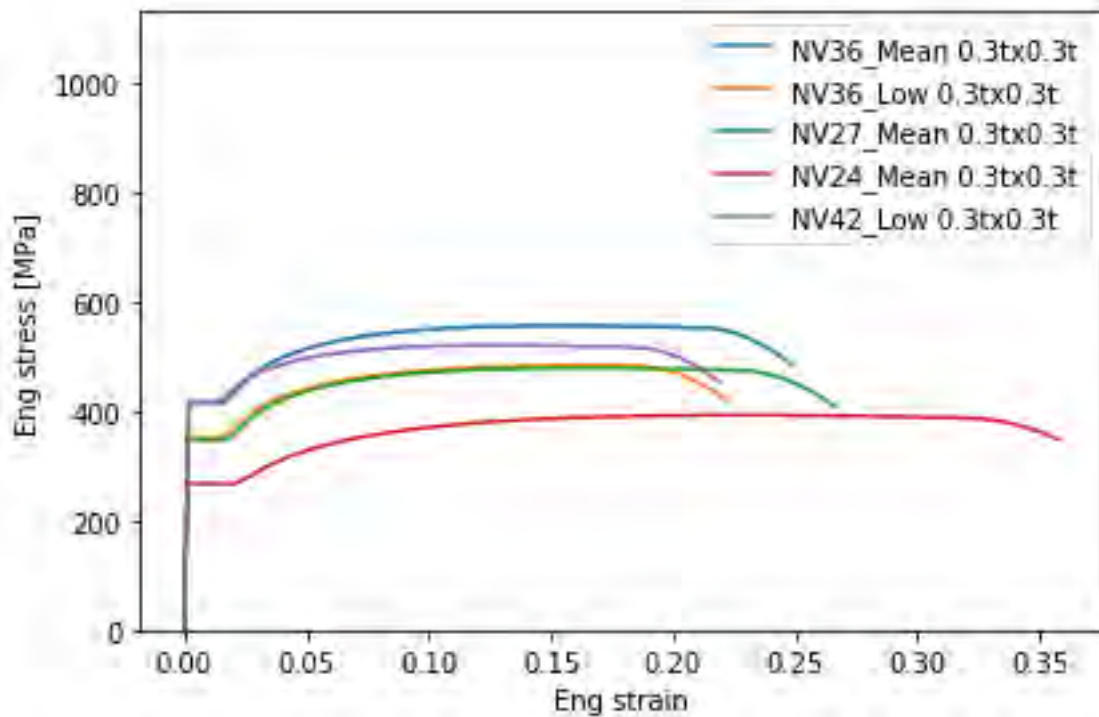


Figure 4-12 Material curves

Material data for the super duplex material used in the splash zone of the pontoon is limited, and the variability in the various data sources for this material is high. Here the material properties are tuned to match a tensile test from [19]. It is seen that there is a good correlation between the super duplex test from [19] and the strain-hardening model used in the analysis, reference made to Figure 4-13.

Note that the simulations have shown that the pontoon response is not very sensitive to the super duplex material strength as the main energy dissipation mechanism is plastic deformation of the bottom of the pontoon rather than membrane tension in the super duplex material.

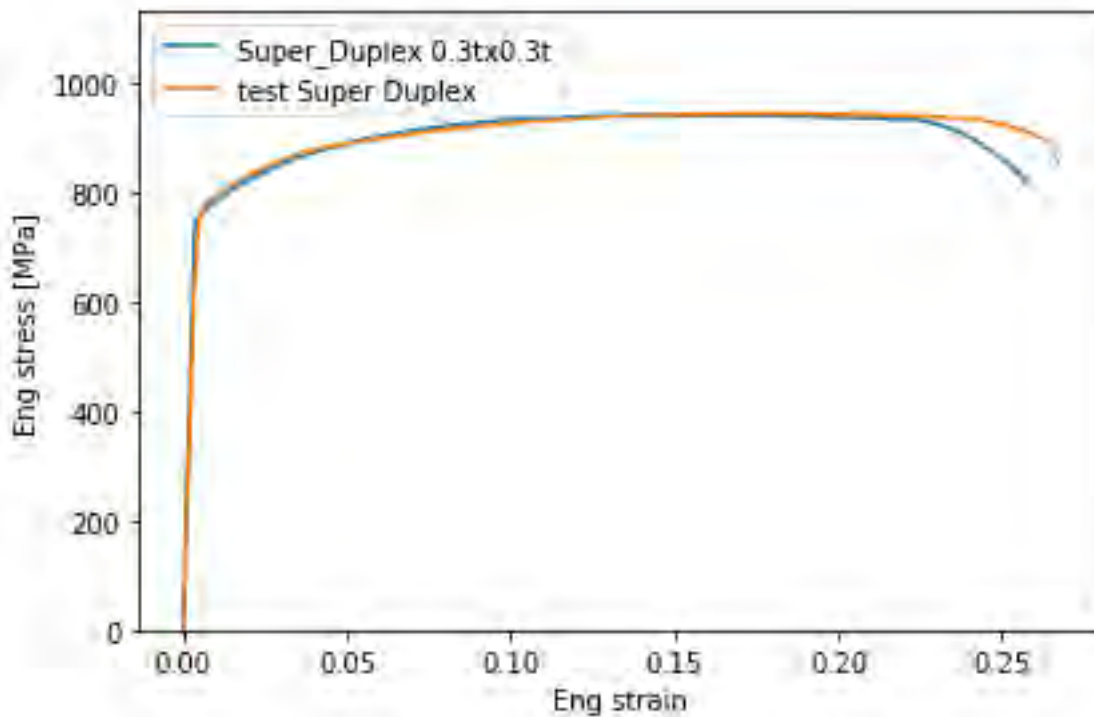


Figure 4-13 Material curve super duplex

Ship bows

The ships are analysed using mean strength of the material. The material strength of the ships should however not affect the results since the deformation will mostly occur in the pontoon due to its lower relative strength compared to the bulbous bow.

Deckhouse

Mean strength of the material is chosen for the deckhouse.

Pontoon

The material strength of the pontoon is chosen specifically for each run to create envelope force displacement curves as well as an upper and lower bound estimate of the pontoon damage. Mean strength is used for collisions analysis where the ship impacts the pontoon at strong points, such as bulkheads. Results from these runs will contribute to create an upper bound for the force displacement curve. A lower bound of the material strength is used for collisions analysis where the ship impacts the pontoon at weak points, e.g. hitting shell plate offset from bulkhead. Results from these analyses will contribute to create a lower bound for the force displacement curve and an upper bound for the pontoon damage.

Bridge girder

A lower bound of the material strength is used for the bridge girder.

Crane pedestal

The crane pedestal is modelled with a rigid material.

4.4.2 Ship bows

Three ship bows were provided by SVV as part of the design basis; a 7500 ton supply vessel, a container ship with around 180 m length over all and an ice-strengthened cruise vessel with 220 m length over all. NTNU [20] provides force-displacement relations for these vessels as shown in Figure 4-14 impacted against the phase 3-version of the end-anchored floating bridge pontoons. Note that the total contact force is the sum of the left and right figure.

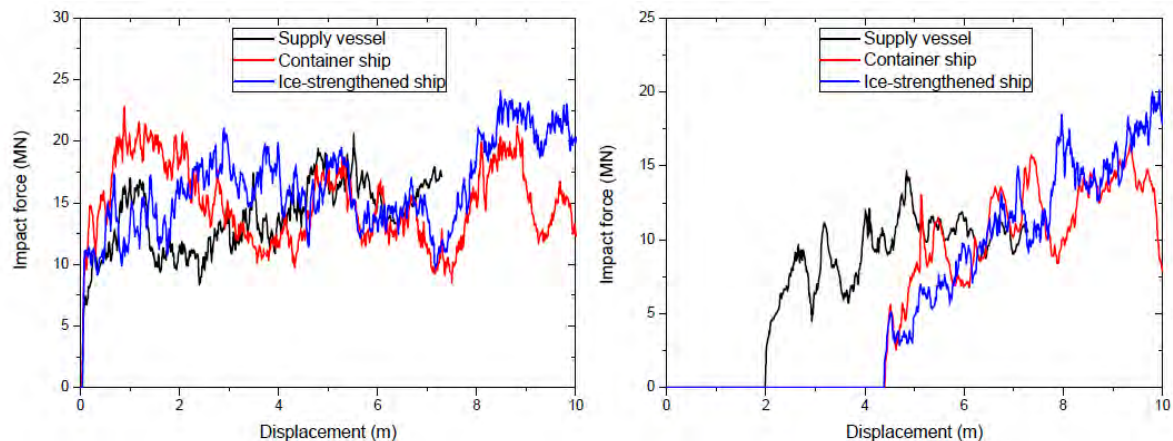


Figure 4-14 Force-displacement curves for the three ship bows, with bulb (left) and forecastle (right) response, Figure 10 from [20].

For the ships analysed in this phase of the project, the bulb will be the dominating member making contact. The bulb is for both the container and cruise ship much stronger than the pontoon. Hence, the deformation will occur in the pontoon. The model of the supply vessel is however much weaker and would result in a significantly different damage distribution with more deformation of the striking vessel.

Cruise ship

A model of a cruise vessel bow, was supplied by SVV, originating from NTNU. The vessel has a length over all of 223 m, a draught of 6.8 m and a beam of 35 m, and has an ICE-1B ice class, capable of independent navigation in 0.6 m thick ice. Hence, the bow is strong compared to conventional cruise vessels.

In phase 3 of the project (ref. [10]), the model as received from NTNU was very fine meshed, with more than 800 000 shell elements. Considering that the vessel bow only serve as a load, it was decided to re-mesh the model to achieve faster computational times so that the effort could be placed towards the response of the struck structure.

The re-meshed model has about 230 000 elements. The minimum time step was significantly increased (due to unnecessarily small elements in some details with the original mesh). Combining these effects, the simulation time for crushing of the bow model against a rigid plate decreased from 700 to 80 CPU-hours.

Further, the NTNU model was improved by a better modelling of the bulb tip so that it was in accordance with the structural drawings, see Figure 4-16.

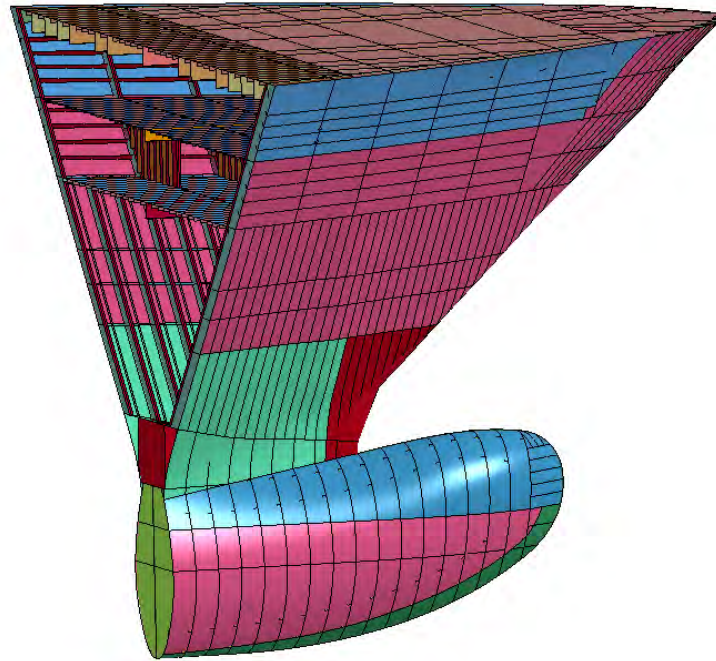


Figure 4-15 Cruise ship bow model

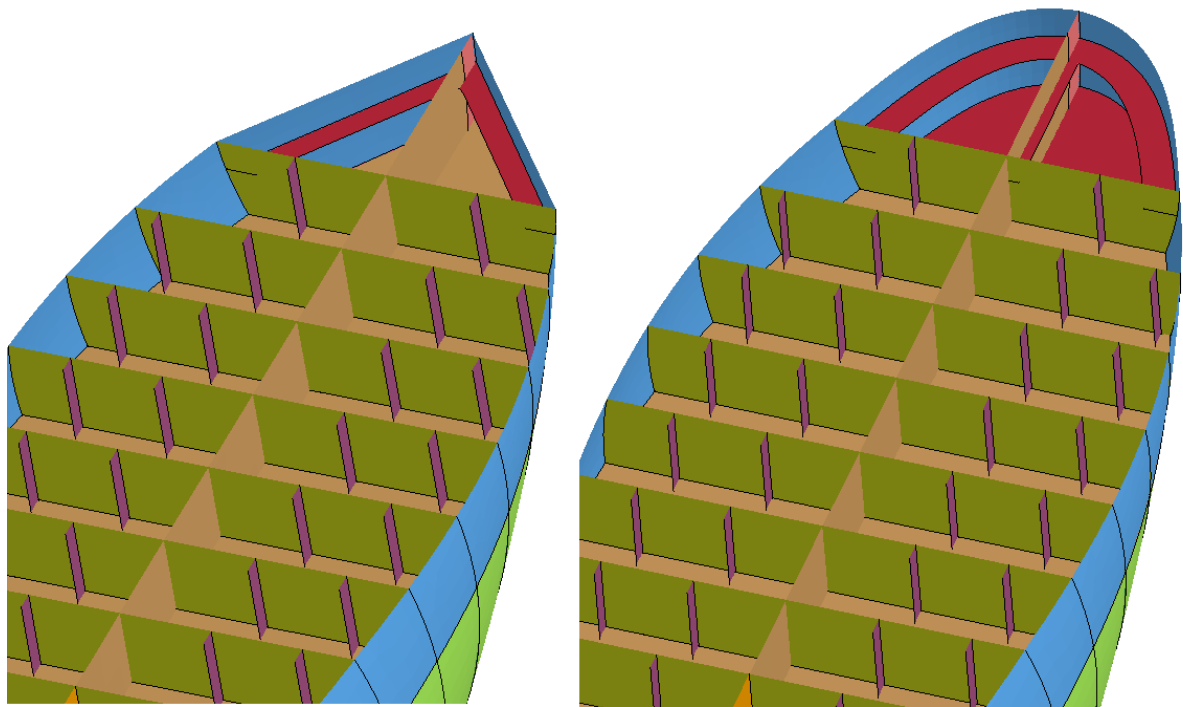


Figure 4-16 Bulb tip modification from NTNU simplification (left) to revised configuration in line with drawings (right).

The cruise ship bow is modelled with steel grade S355 with following material properties.

Steel material grade S355 (with mean material strength)

Modulus of Elasticity	2.10·10 ¹¹ N/m ²
Poisson`s Ratio	0.3
Yield Strength f _y	419 N/mm ²
G-modulus	8.0769·10 ¹⁰ N/m ²
B-modulus	1.75·10 ¹¹ N/m ²

The crushing force vs. indentation is shown in Figure 4-17 for collision with a vertical rigid wall. The re-meshing and bulb tip modelling have not caused a considerable difference in the contact force.

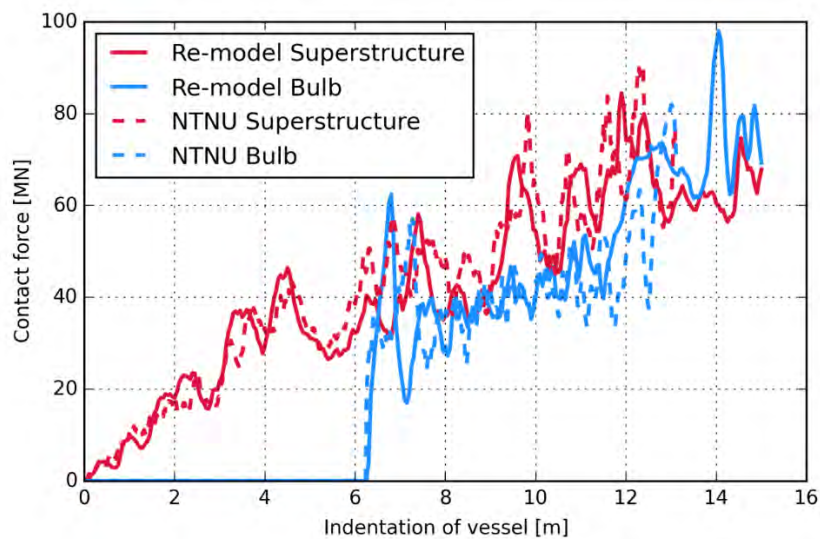


Figure 4-17 Crushing force for vessel superstructure and bulb compared with vessel displacement (indentation).

Container ship

The container vessel model was received from SVV (modelled at NTNU) and is more or less used as is. The model is shown in Figure 4-18, and is about 16 m high and 20 m long. Main particulars are given in Table 4-1. The ship has a design draught of 8.75 m and a scantling draught of 9.6 m. The draught in ballast condition is not known. A higher draught, such as for ballast conditions could endanger different parts of the bridge.

Based on experience from similar ships, the ballast draught for the current vessel is estimated to be just above the top of the bulb. Thus, in the current project stage and with the current bow model, it is acceptable to use only the design draught for simulation of the structural response. In the next project stage, different draughts could be included together with more vessel bows in order to evaluate the sensitivity of the bridge to collision events.

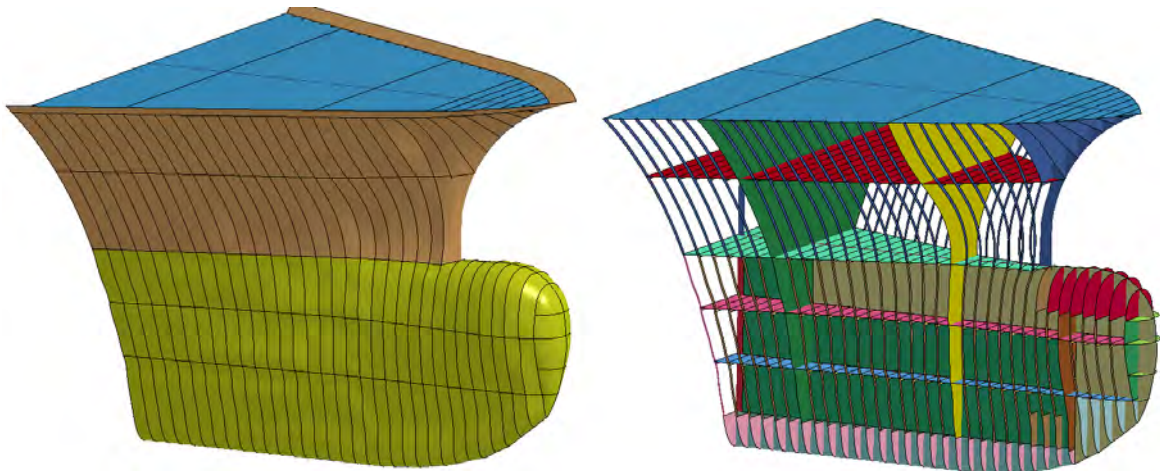


Figure 4-18 Container bow model, with outer plating (left) and showing internal structure (right).

Table 4-1 Main particulars of vessel.

Length over all	186 m
Breadth extreme	27.5 m
Gross tonnage	22900
Deadweight tonnage	28200 ton
Estimated displacement (=DWT/0.72)	39000 ton
Design draught	8.75 m



Figure 4-19 Container ship of similar size. Note the significant structure around anchors in the bow. Photo from marinetraffic.com.

The container ship bow is modelled with steel grade S275 with following material properties.

Steel material grade S275 (with mean material strength)

Modulus of Elasticity	$2.10 \cdot 10^{11} \text{ N/m}^2$
Poisson`s Ratio	0.3
Yield Strength f_y	352 N/mm^2
G-modulus	$8.0769 \cdot 10^{10} \text{ N/m}^2$
B-modulus	$1.75 \cdot 10^{11} \text{ N/m}^2$

Overall, the model is sufficient to represent a decent load for collision simulations. However, some minor issues were detected and described in the following. The hull surface is in areas quite rough (Figure 4-20), far beyond the tolerances of a ship structure. Such large imperfections may affect the crushing performance of the bow and initiate global buckling too early. However, the simulations show that this is not affecting the crushing response to a large degree.

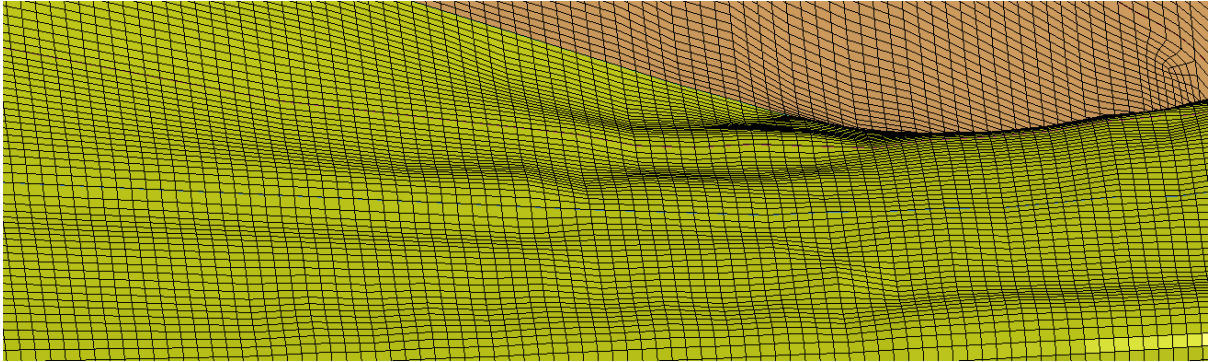


Figure 4-20 Rough surface of the bow model.

Some areas, like the transverse stiffening rings, are only meshed with one element over the height of the stiffener (Figure 4-21). This is acceptable for longitudinal crushing of the vessel, as the stiffener is not loaded in bending. However, for collisions at an oblique angle the stiffeners will behave too stiff.

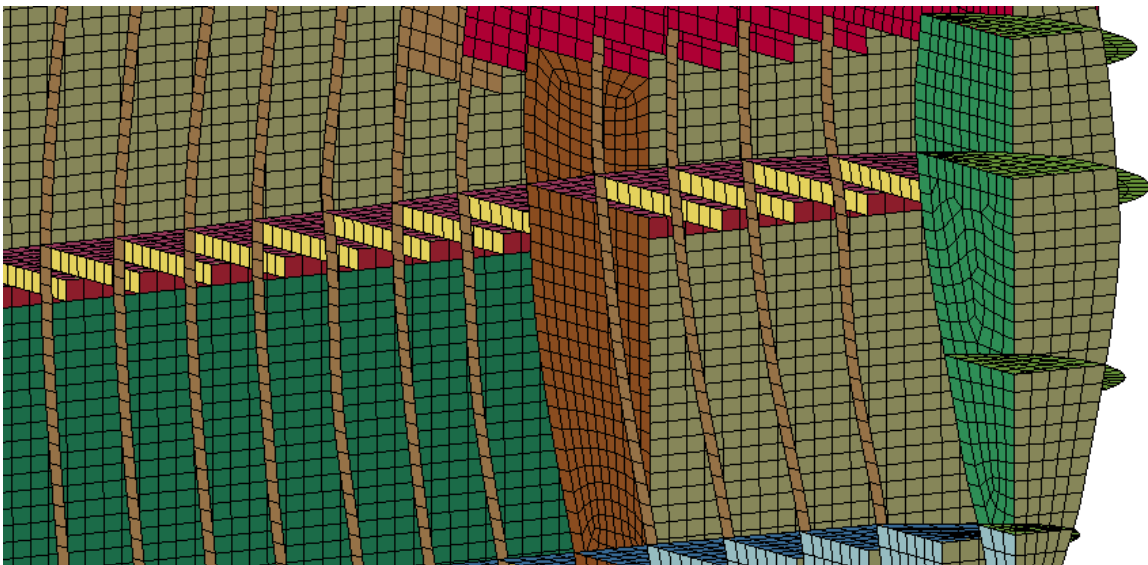


Figure 4-21 Transverse stiffening in the bulb area with very coarse mesh. View from below, looking to port and aft.

The lower parts of the model, including the bulb, were originally modelled based on available drawings. However, for the upper parts of the model relevant drawings were not available, and the model is thus based on an educated guess. Some simplifications are made in the upper structure that affects the crushing strength to a significant degree. Stiffeners are not modelled for deck 5 (uppermost deck). The bulwark (side of vessel above upper deck) is included as a 15 mm thick plate, but without relevant stiffening and hard points such as bollards, mooring pipes, fairleads and anchors (see Figure 4-19). Thus, both the crushing force of the upper structure and local hard points that may cause local damage to the bridge floater and pylon will not be correctly simulated. Updating the model to accommodate such features was not feasible at the current project stage, but is recommended for future stages of the project.

Hence, the bow model with the above mentioned corrections will give a decent load transferred to the floater structure in way of the vessel bulb, but underestimate the damage in way of the upper parts of the bow. The simulation results should be viewed with this in mind.

It is further emphasized that the bow model used in the current study represents only one possible vessel with one specific geometry. A slightly larger passenger vessel with a more protruding forecastle structure may cause larger damage to the connection between floater and bridge pylon. It is recommended that this is included in the assessments of local collision resistance in the next phase of the project.

Supply ship

Due to its weaker strength, the supply ship model provided by SVV has not been considered as it will result in a more favourable condition for the bridge

4.4.3 Ship deckhouse

The ship deckhouse provided by SVV was developed in phase 3 of the project [10] and based on a generic deck house design of a ship of similar size as the relevant design vessel for the Bjørnafjorden crossing. The deckhouse is modelled with steel with yield stress equal to 270MPa.

Steel material grade S270 (mean material strength)

Modulus of Elasticity	$2.10 \cdot 10^{11} \text{ N/m}^2$
Poisson`s Ratio	0.3
Yield Strength f_y	270 N/mm ²
G-modulus	$7.96 \cdot 10^{10} \text{ N/m}^2$
B-modulus	$1.73 \cdot 10^{11} \text{ N/m}^2$

The deckhouse model is shown in Figure 4-22. It can be seen that the windows are included with corresponding corner radius. Figure 4-23 show how the stiffeners are terminated at the girder web. It is also seen that the stiffeners are modelled with one element over the web height. Hence; if the stiffeners are subjected to bending, they will behave too stiff. Overall the response of the deckhouse model adequately represents a collision load to the bridge girder representative of a design ship collision scenario.

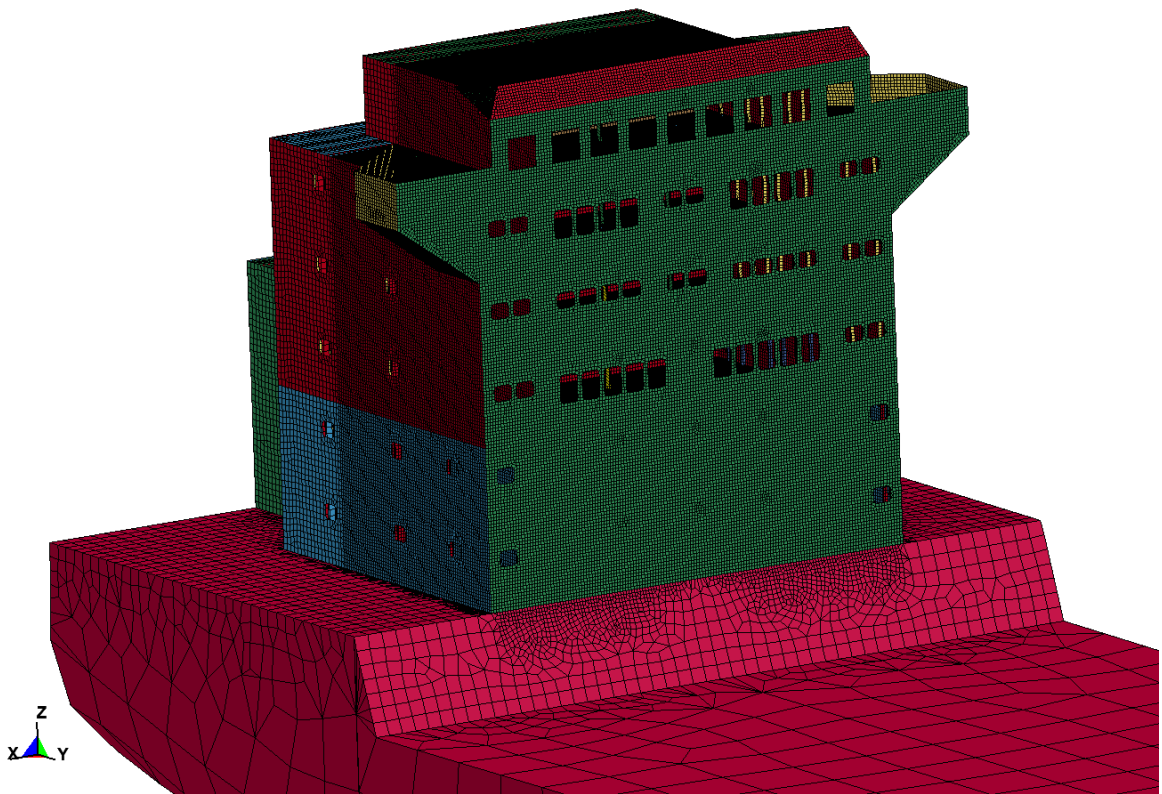


Figure 4-22 Element model of deckhouse

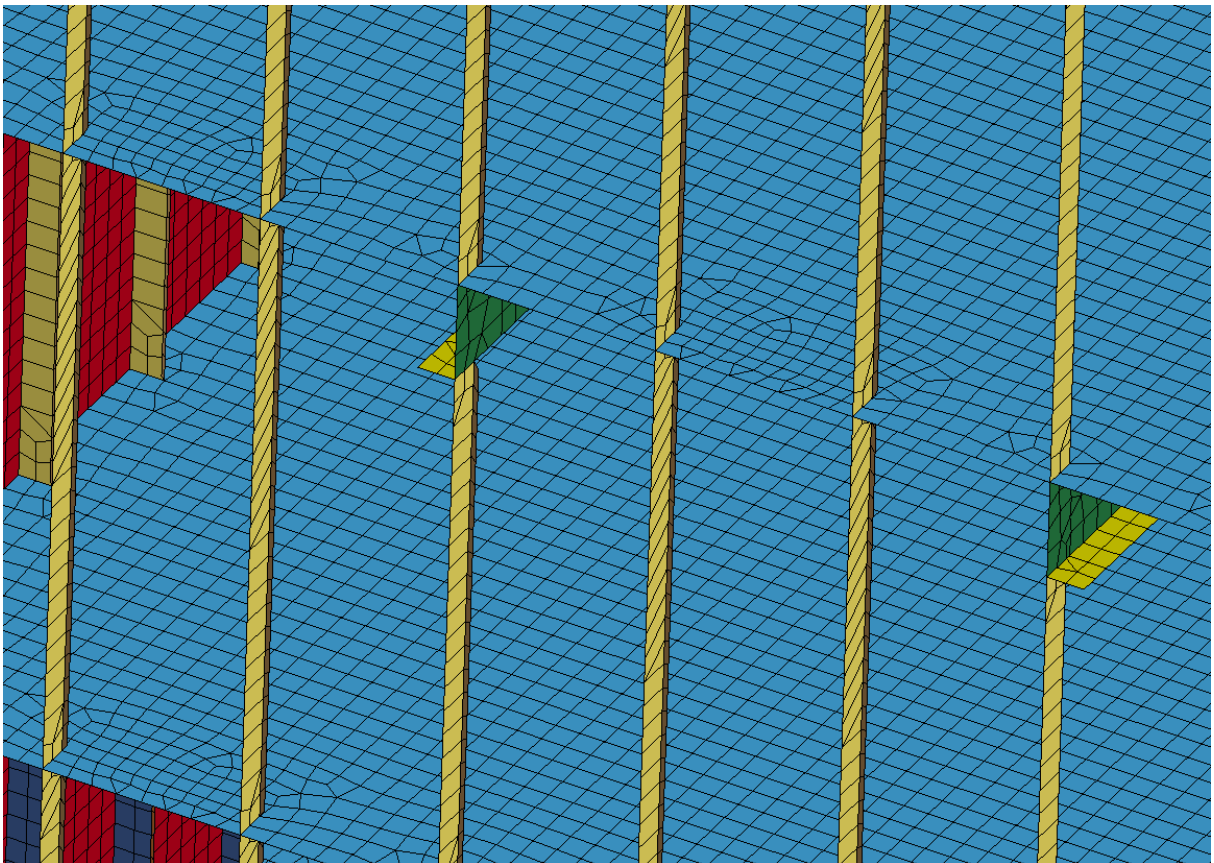


Figure 4-23 Mesh of stiffeners, deck and girders

4.4.4 Pontoon

The finite element model of the pontoon is shown in the following figures. The dimensions are taken from [21].

The pontoon consists mainly of steel with yield stress equal to 355MPa(S355). The material properties for steel material grade S355 are shown below.

Steel material grade S355 (with low material strength)

Modulus of Elasticity	$2.10 \cdot 10^{11} \text{ N/m}^2$
Poisson`s Ratio	0.3
*Yield Strength f_y	355 N/mm^2
G-modulus	$8.0769 \cdot 10^{10} \text{ N/m}^2$
B-modulus	$1.75 \cdot 10^{11} \text{ N/m}^2$

*When mean material strength is used, the yield stress equals 419MPa

In addition, all steel surfaces in the splash zone, reference made to Section 2.10 in [21], should be of super duplex steel. The super duplex steel used in the analyses has following material properties:

Steel material grade super duplex (2507 Outokumpu [19])

Modulus of Elasticity	$2.10 \cdot 10^{11} \text{ N/m}^2$
Poisson`s Ratio	0.3
Yield Strength f_y	750 N/mm^2
G-modulus	$8.0769 \cdot 10^{10} \text{ N/m}^2$
B-modulus	$1.75 \cdot 10^{11} \text{ N/m}^2$

Note that the extent of the super duplex zone (splash zone) was increased during design development after the local collision simulations were completed. This may have a minor influence on the results, but not considered significant enough to re-model and conduct new NLFEA simulations.

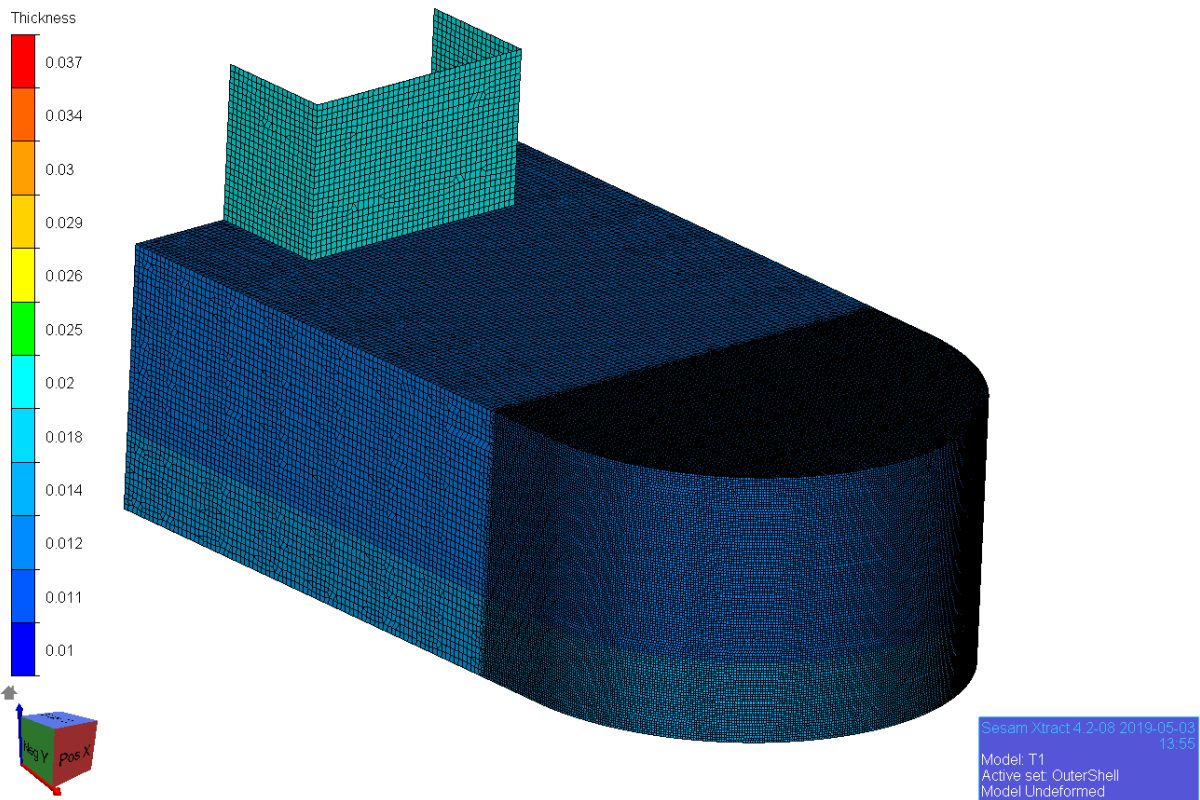


Figure 4-24 Thickness plot of pontoon

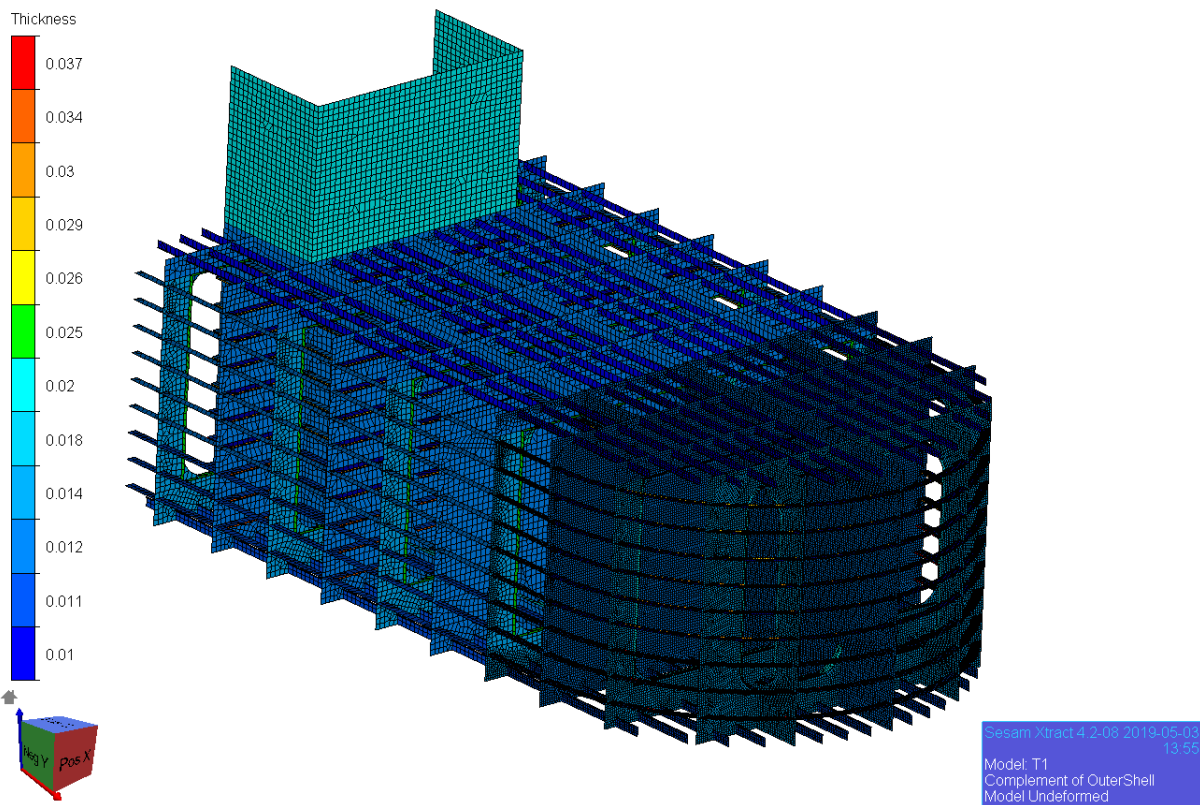


Figure 4-25 Thickness plot of pontoon, outer shell removed

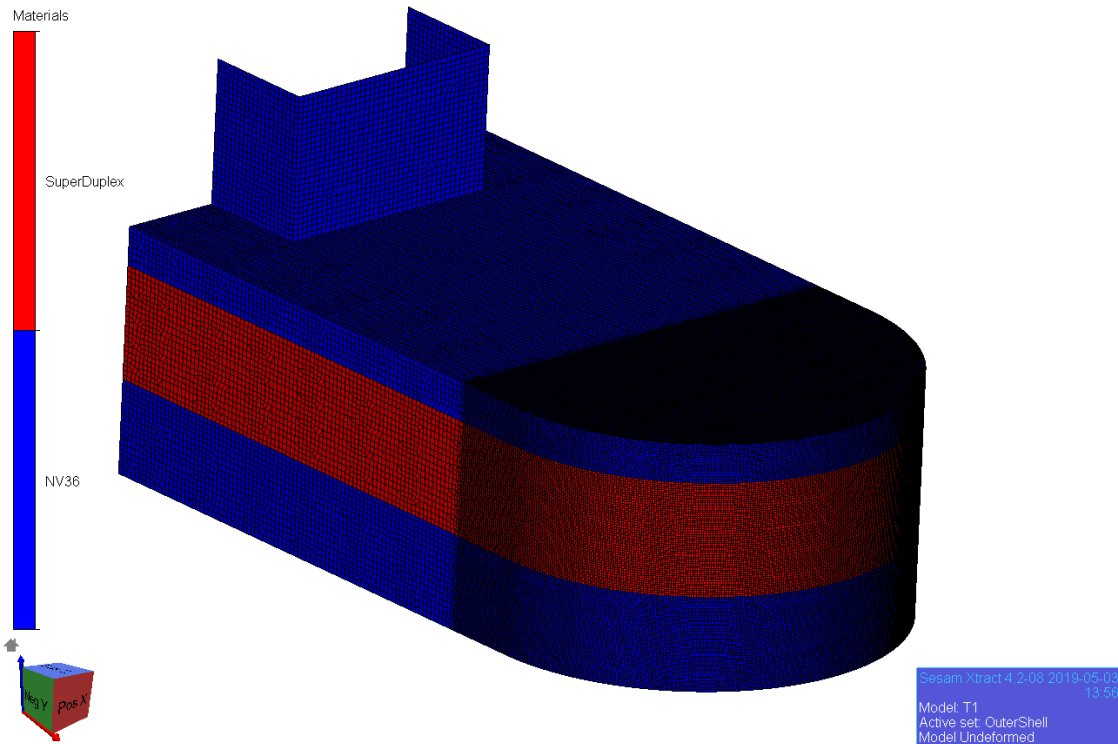


Figure 4-26 Pontoon materials

The portion of the pontoon that will experience deformation is meshed finely. The mesh size in the crushing area is 75 mm. It is ensured that all stiffeners have at least 3 elements over the stiffener height in the crushing zone as shown in Figure 4-27. The stiffener flanges on upper and bottom deck of the pontoon is sniped towards the outer shell.

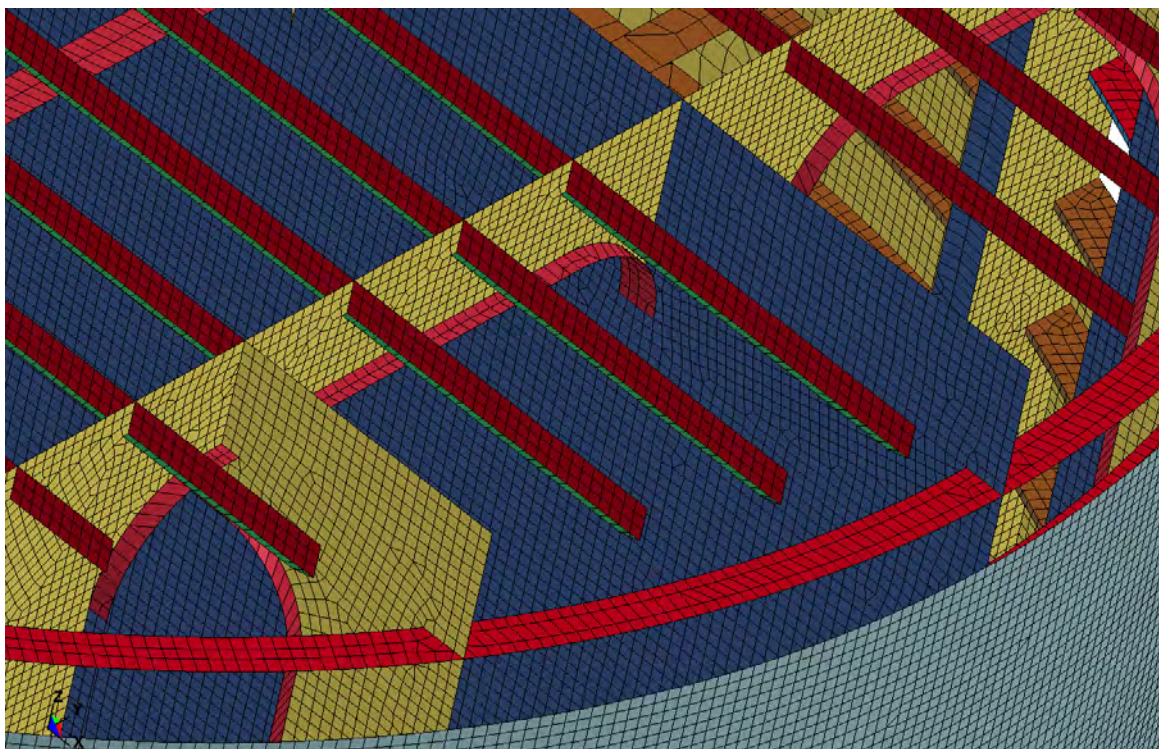


Figure 4-27 Mesh plot showing stiffeners in upper deck plate

Figure 4-28 show how the stiffener intersection between the stiffeners on the centre longitudinal bulkhead and the outer shell is modelled. It is seen that the flange on the bulkhead stiffener is sniped towards the flange of outer shell stiffener.

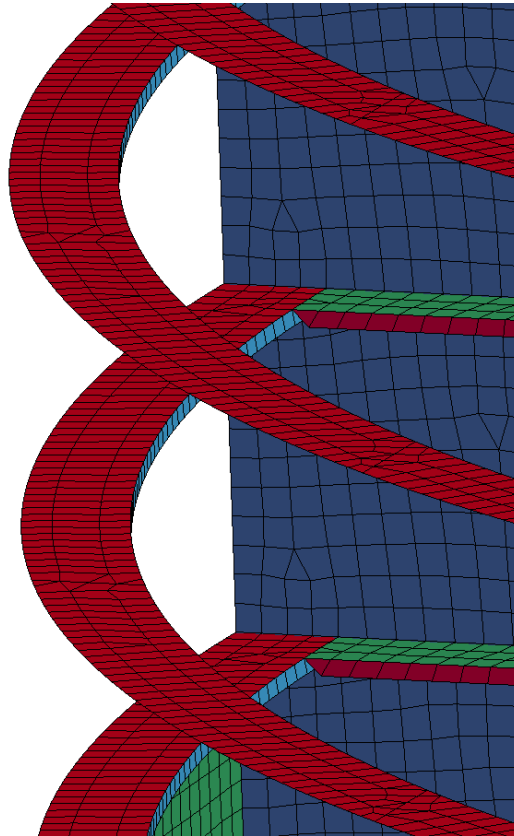


Figure 4-28 Mesh plot intersection between stiffeners on centre longitudinal bulkhead and outer shell

4.4.5 Bridge girder

The bridge girder consists of steel with yield stress equal to 420MPa (S420). The material properties for steel material grade S420 are shown below.

Steel material grade S420 (with low material strength)

Modulus of Elasticity	$2.10 \cdot 10^{11} \text{ N/m}^2$
Poisson`s Ratio	0.3
Yield Strength f_y	420 N/mm ²
G-modulus	$8.0769 \cdot 10^{10} \text{ N/m}^2$
B-modulus	$1.75 \cdot 10^{11} \text{ N/m}^2$

The finite element model is shown in Figure 4-29 which is a thickness plot of the model. Note that the bridge road, seen as the green 14mm plate below, has a density of 22 420 kg/m³ to account for the layer of asphalt.

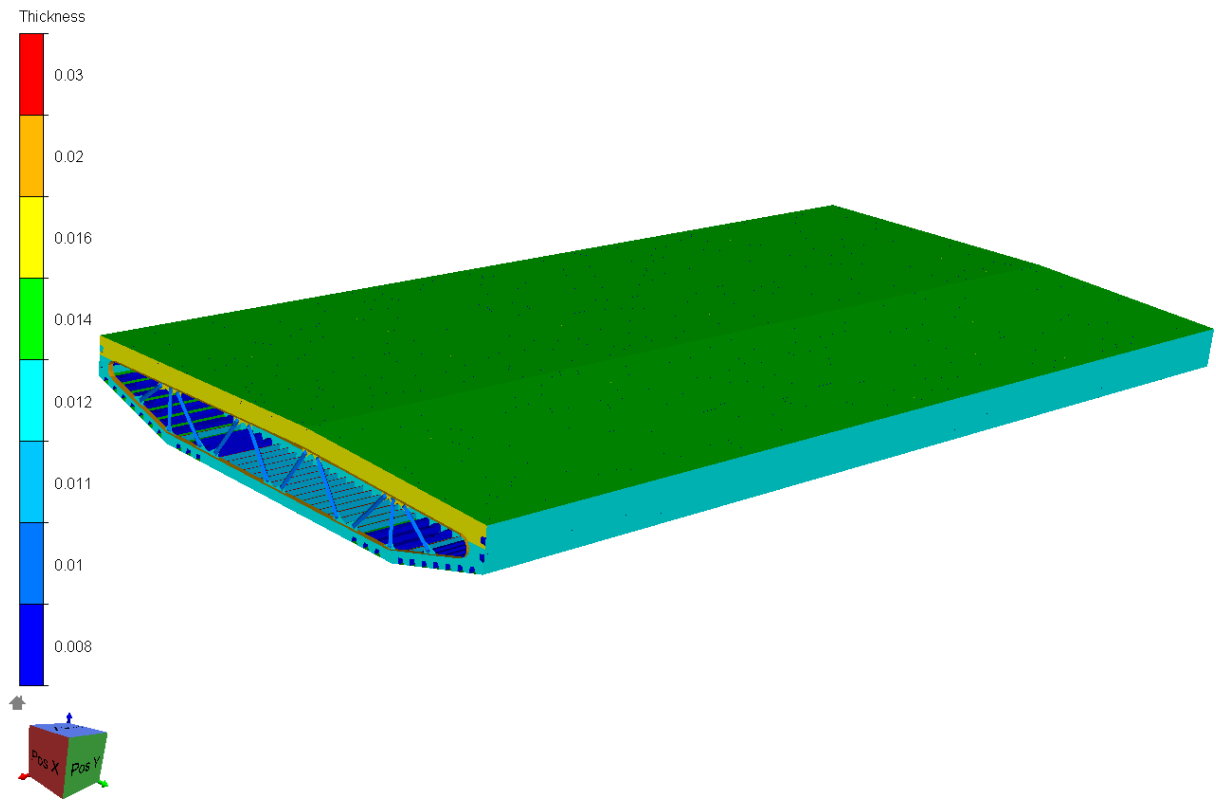


Figure 4-29 Finite element model of bridge girder showing thicknesses

Figure 4-30 shows the mesh of the bridge girder. The mesh is refined towards the expected contact zone in order to save calculation time. The transition in mesh size is approximately 8 m from the edge of the bridge.

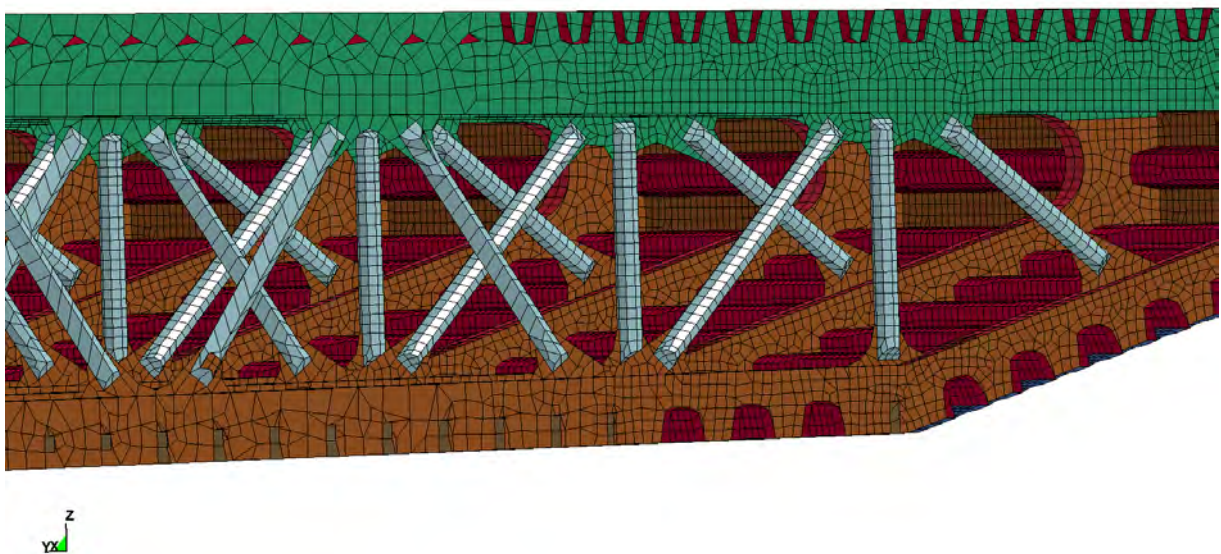


Figure 4-30 Mesh of bridge girder

4.4.6 Crane pedestal

To investigate the response to a sharp object protruding ahead of the deckhouse (currently not in the design basis) a crane pedestal was modelled. The accidental load scenario is outside of the design basis, but a relevant check in order to assess the possibility that a sharp object ahead of the deck house may tear the bridge girder in two.

The modelled crane pedestal has a diameter of 5 meter and is modelled with a rigid material. The mesh used is similar as for the bridge girder and shown in Figure 4-31. The assumption of a rigid response of the pedestal in a large impact event is not correct, but will represent an upper bound limit for damage to the bridge girder.



Figure 4-31 Mesh of crane pedestal

4.4.7 Boundary conditions

Ship bow vs. pontoon

The collision analysis is run by fixing the pontoon in the centreline and pushing the ship into the pontoon at a constant velocity of 5 m/s. Figure 4-32 shows the collision setup. The pontoon is fixed at the centreline as shown by the red line in the figure. The aft edge of the ship shown by the green line is pushed with a constant velocity directly into the ship. The aft part of the ship is fixed for motions in directions other than the direction of motion.

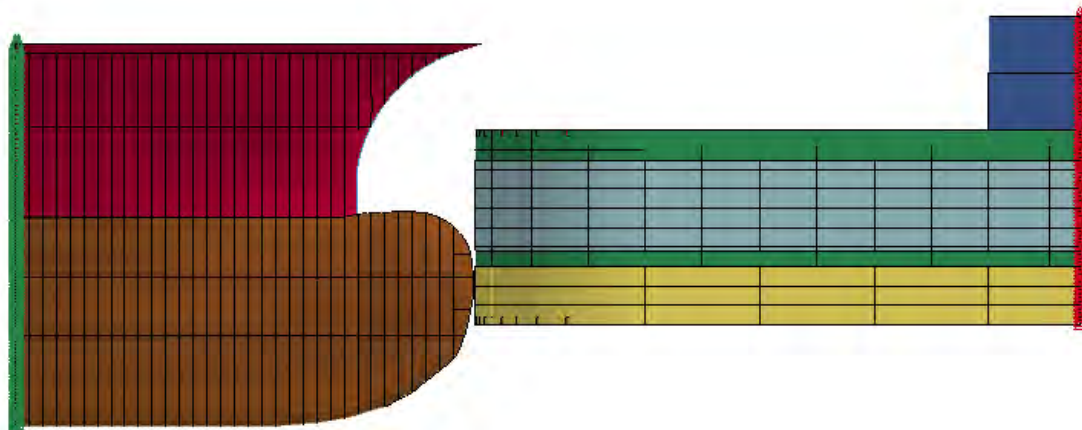


Figure 4-32 Collision set up.

The water line of the ship is assumed to be right above the top of the bulb. Only one collision height is considered. Varying the height may show slightly different capacities, but at this stage in the project it is not considered necessary to perform this variation. Due to the low draught of the pontoon most vessels will hit the bottom section of the pontoon, and the bottom plate will be mobilized in a similar manner even with small variations in the impact elevation.

Ship deckhouse vs. bridge girder

The collision analyses are run by pushing the ship into the bridge girder at a constant velocity of 5 m/s. The bridge girder is restrained against displacements, but by hinging the ends the bridge is free to rotate. The restrains are shown by the red and blue lines at the ends of the bridge girder in Figure 4-33.

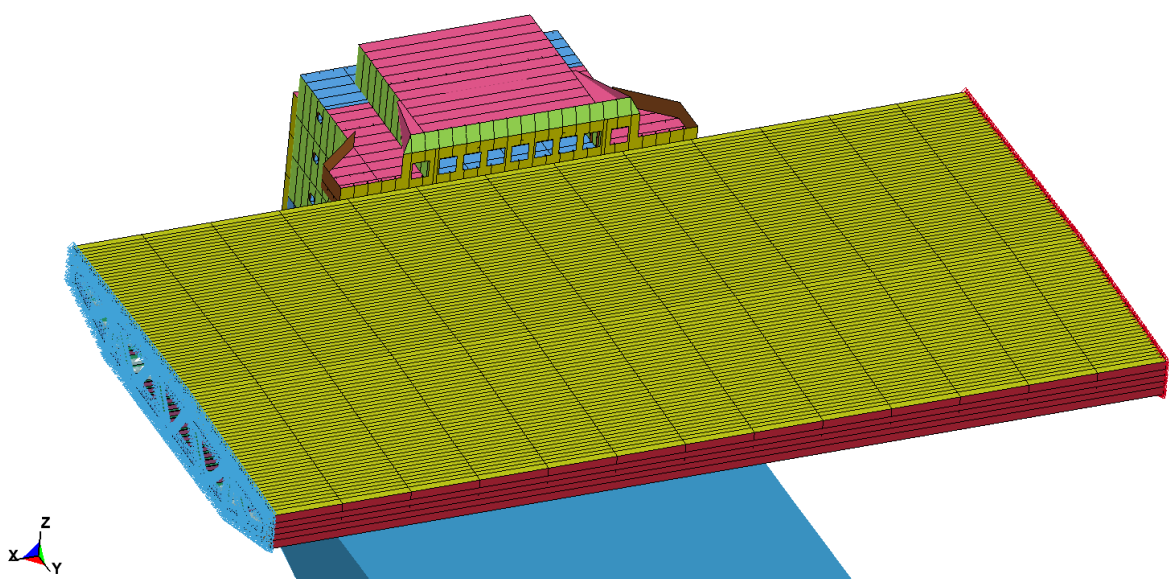


Figure 4-33 Collision setup deckhouse vs. bridge girder

For the collision between the rigid crane pedestal and the bridge girder, the bridge girder is restrained in the same manner as for the deckhouse collisions.

4.5 Results collisions ship bow vs pontoon

The results from the local pontoon collision are shown in this section. The force displacement curves and energy displacement curves are summarized in Figure 4-34 and Figure 4-35. Note that the results show the combined force-displacement relation for bulb and forecastle structure, not separately as those given in [20], Figure 4-14. A short description of the collision analyses is given in Table 4-2.

Table 4-2 Description of collision analyses, base case scenarios

Name	Material strength pontoon	Description
Container_HeadOn_Centre_mean	Mean	Collision in the global y-direction impacting the pontoon on the centre line with the container ship
Container_HeadOn_Centre+2.5_low	Low	Collision in the global y-direction impacting the pontoon 2.5 m off the centre line with the container ship
Cruise_30Deg_low	Low	Collision with the cruise ship with an angle of 30 degrees. The ship is aiming for the intersection between the longitudinal bulkhead and the first transverse bulkhead

It was suggested to replace the centre longitudinal bulkhead with a longitudinal girder. Hence, a set of sensitivity cases have been analysed. A description of the cases is found in Table 4-3.

Table 4-3 Description of collision analyses, sensitivity study scenarios

Name	Material strength pontoon	Description
Container_HeadOn_Centre_mean_NoBlkh	Mean	Collision in the global y-direction impacting the pontoon on the centreline with the container ship. The centre bulkhead is replaced with a longitudinal frame
Container_HeadOn_Centre+2.5_low_NoBlkh	Low	Collision in the global y-direction impacting the pontoon 2.5 m off the centreline with the container ship. The centre bulkhead is replaced with a longitudinal frame
Cruise_HeadOn_Centre_low_NoBlkh	Low	Collision in the global y-direction impacting the pontoon on the centreline with the cruise ship. The centre bulkhead is replaced with a longitudinal frame

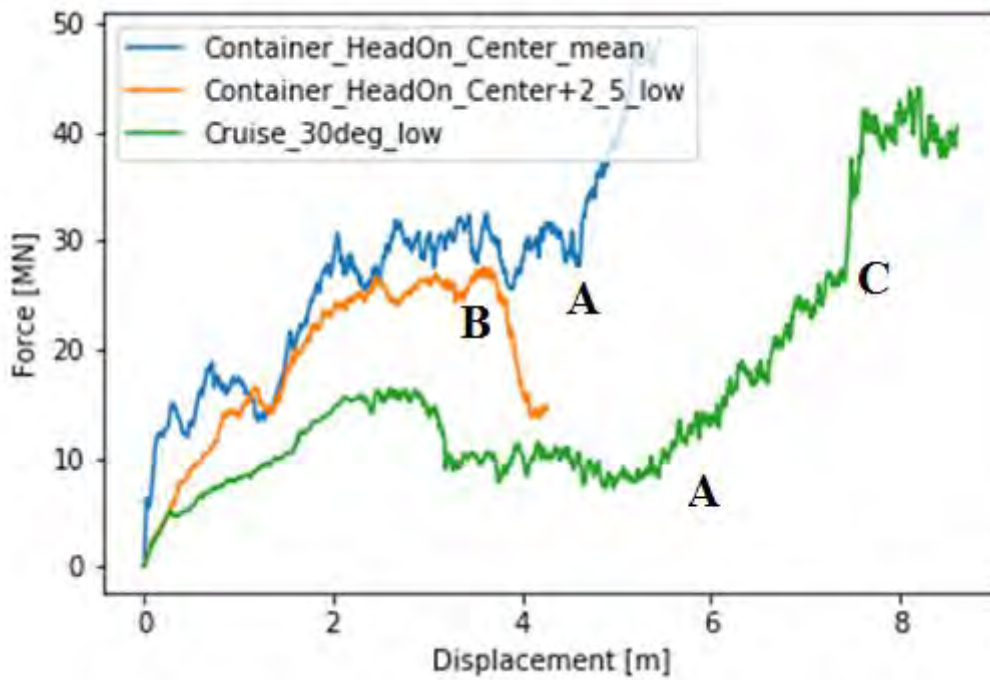


Figure 4-34 Force displacement curves for pontoon

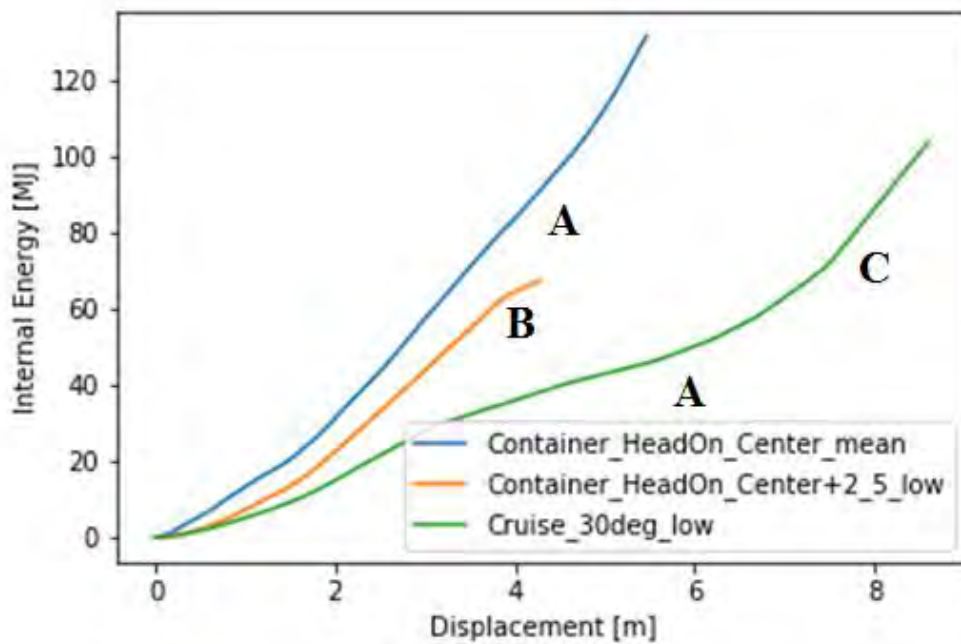
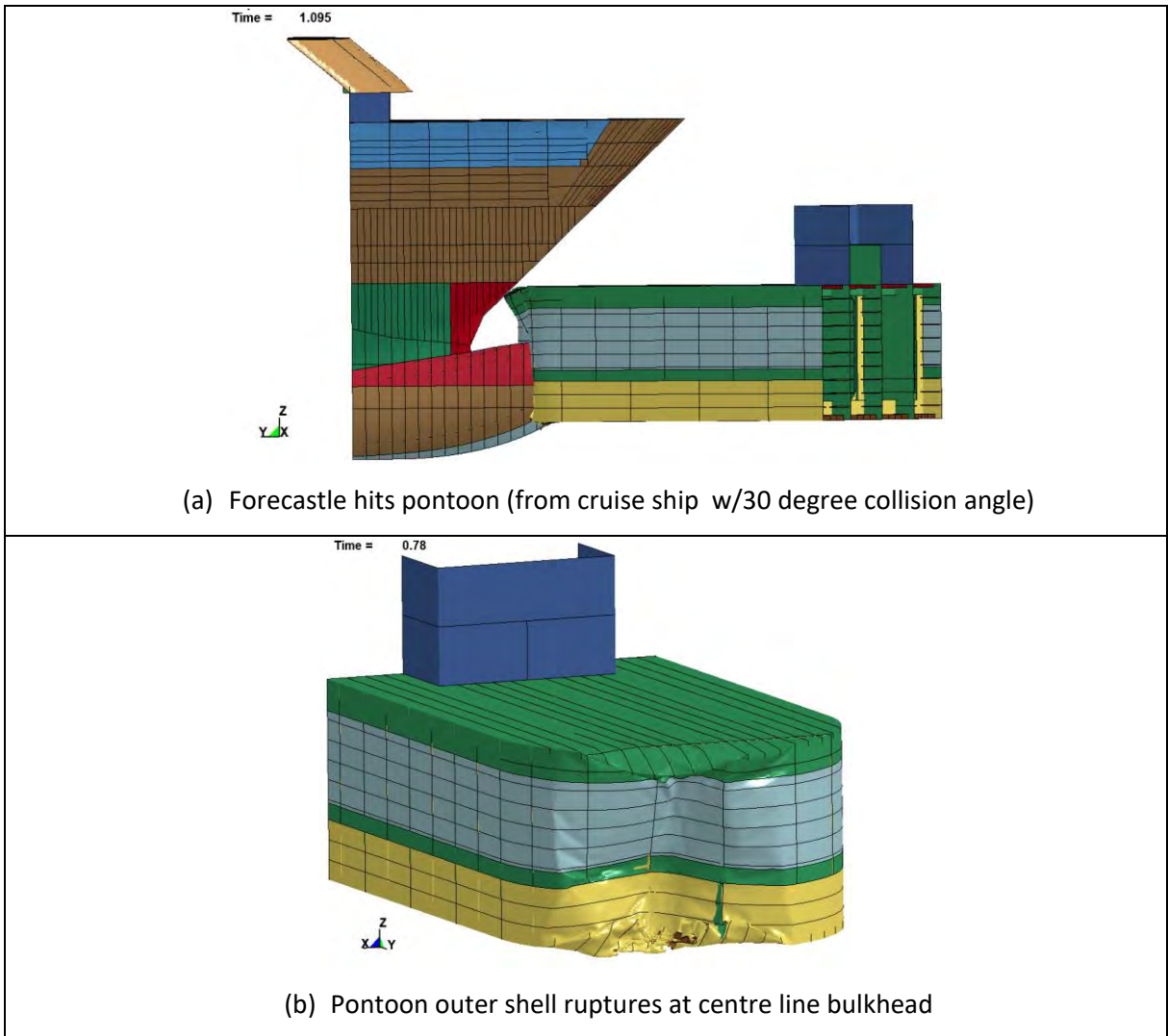


Figure 4-35 Energy displacement curves for pontoon

Figure 4-34 show force displacement curves for the three base cases. From the plot the following is observed:

- **A:** The forecastle hits the pontoon. This is seen in the force displacement curve as a significant increase in force. In addition, the slope of the internal energy displacement plot, Figure 4-35, increases.

- **B:** For the run with 2.5m offset from the centreline bulkhead the force displacement curve gets a significant drop when the outer shell of the pontoon ruptures. The rupture occurs at the centreline bulkhead, and propogates quickly.
- **C:** The bulb hits the first transverse frame which creates a significant increase in contact force. The force displacement curve flattens quite quickly which indicates that the bulb ruptures the bulkhead



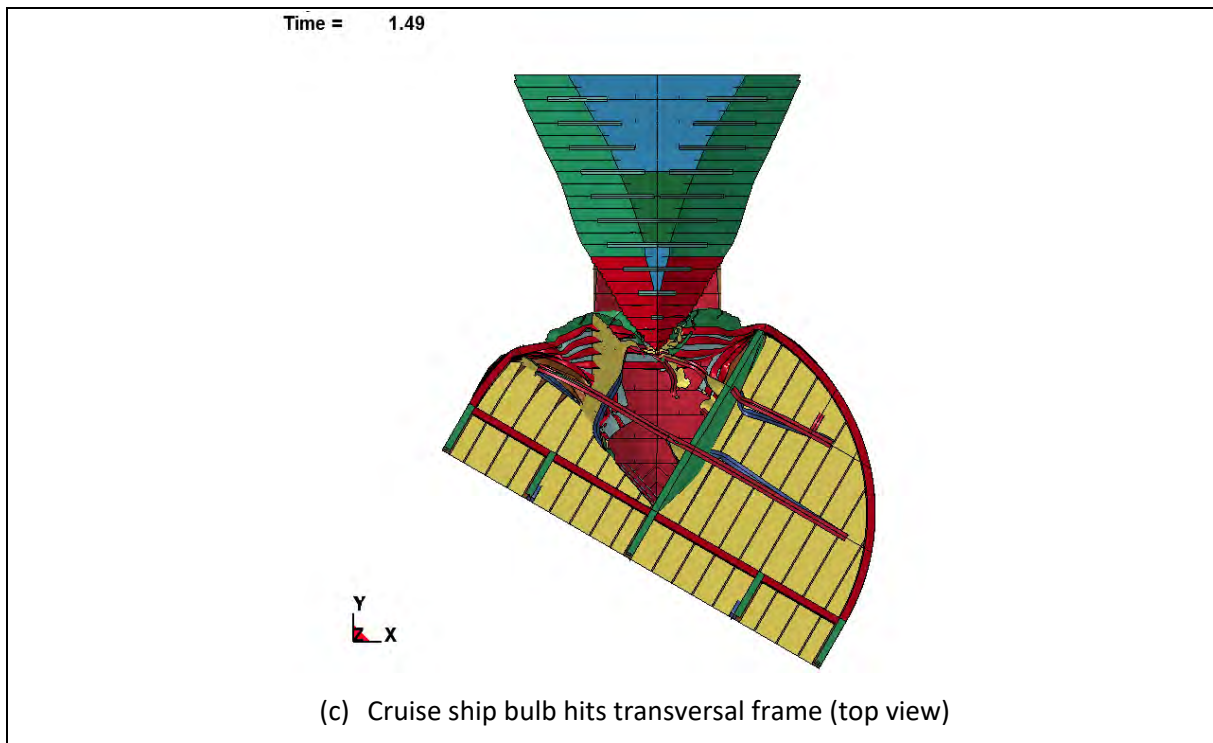


Figure 4-36 Figures showing different key points in analyses

Results from the sensitivity runs presented in Table 4-3 are shown below. It is seen that removing the centre bulkhead delays the peaks/ruptures in the force displacement curves for the initial indentation. With the bulkhead the upper deck plate is relatively intact and contacts the forecastle of the striking vessel after around 5 m displacement. With an open frame the upper deck support is reduced, and it is pulled down towards the bulbous bow. Hence, the contact with the forecastle is delayed to about 7 m displacement. The overall response with and without the bulkhead is quite similar except for the “delay”. Removing the bulkhead will cause a significant increase in deformation and is hence not recommended.

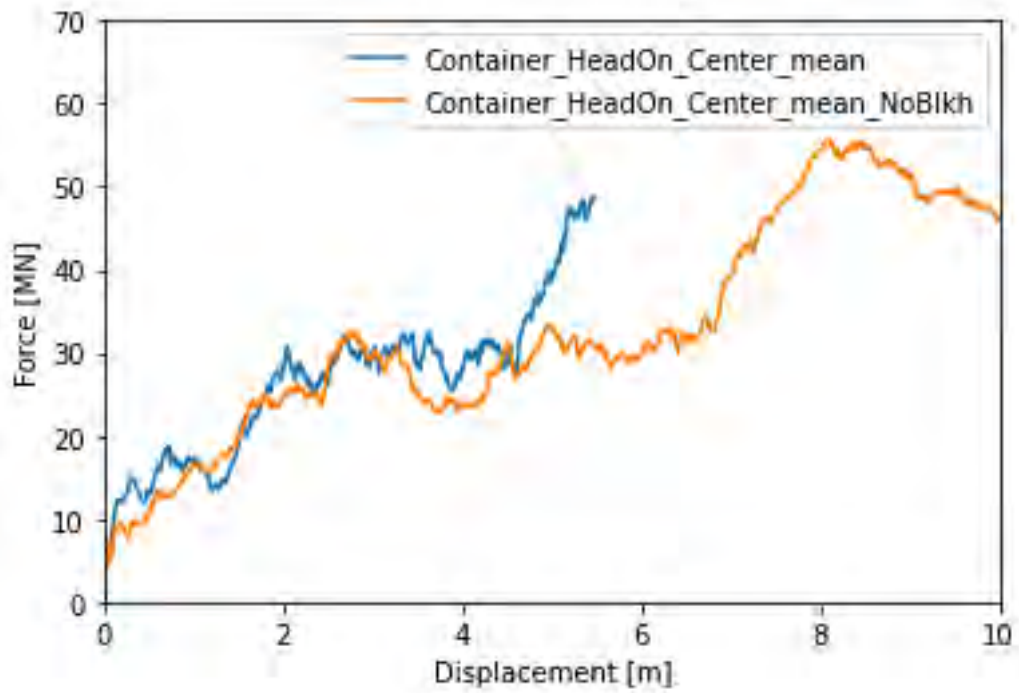


Figure 4-37 Comparison of force displacement curves with and without centreline bulkhead for container pontoon collision head on.

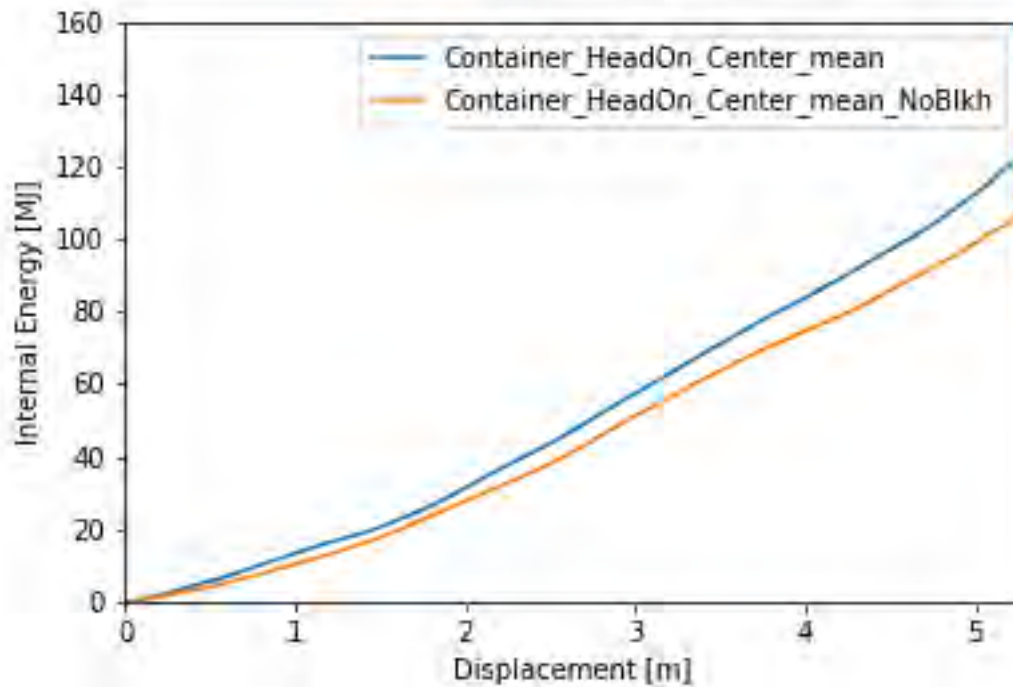


Figure 4-38 Comparison of energy displacement curves with and without centreline bulkhead for container pontoon head on collision

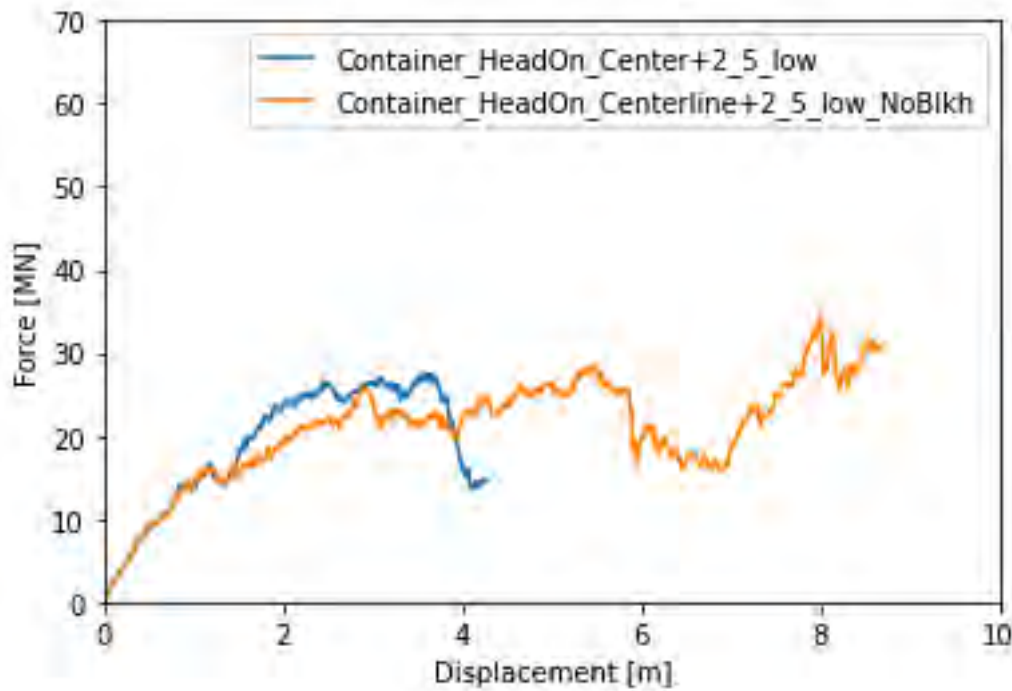


Figure 4-39 Comparison of force displacement curves with and without centreline bulkhead for container pontoon collision with 2.5m offset from centreline

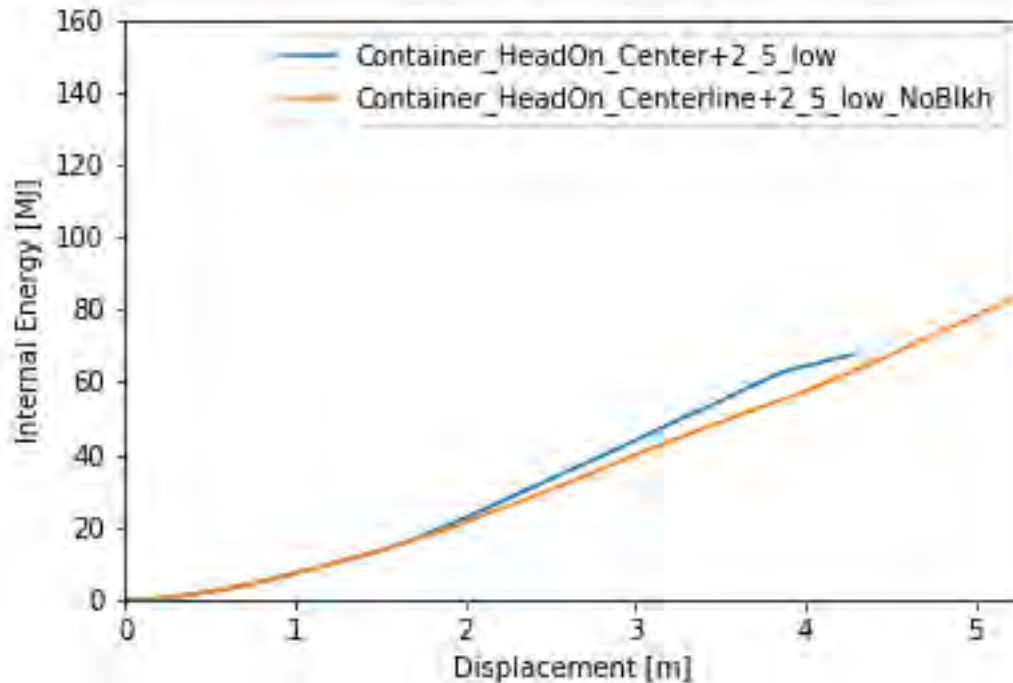


Figure 4-40 Comparison of energy displacement curves with and without centreline bulkhead for container pontoon collision with 2.5m offset from centreline

The compartment filling for each of the cases is quite similar. The maximum number of compromised compartments is 4. The compartments with names are shown in Figure 4-41.

Table 4-4 Summary of energy dissipation prior to rupture and number of filled compartments

Run	Energy dissipation at rupture [MJ]						No. Filled comp*
	C01	C02	C03	C04	C05	C06	
Container_HeadOn_Centre_mean	6	7	-	-	-	-	2 (130 MJ)
Container_HeadOn_+2_5_low	7	7					2 (110 MJ)
Cruise_30Deg_low	3	64	72	78			4 (105 MJ)
Container_HeadOn_+2_5_low_NoBlkh	5	5	-	120			3 (150 MJ)
Container_HeadOn_Centre_mean_NoBlkh	19	6	-	-	-	-	2 (67 MJ)
Cruise_HeadOn_Centre_low_NoBlkh	10	10	88	88			4 (144 MJ)

*Number in parenthesis is the energy dissipation at the end of the simulation



Figure 4-41 Compartment numbering in pontoon

Table 4-5 shows the potential flooded volume of the compartments for a pontoon with draught of 5 m. For the mooring pontoons a draught of 7.5 m was used, and the compartment volumes can thus be increased with 50% to account for this.

Table 4-5 Compartment volumes for a 5 m draught pontoon

	C01	C02	C03	C04	C05	C06	C07	C08
Volume [m ³]	371	371	318	318	318	318	318	318

Note that the tank arrangement has been changed after the analysis were performed, shown in Figure 4-42. By introducing manholes to the centre longitudinal bulkhead and making the longitudinal bulkheads located 4000mm off the centre line watertight, we now have three compartments over the pontoon width. The change will increase the pontoons robustness against collision scenarios where a ship hits the side of the pontoon with a small angle. By comparing Figure 4-42 with Figure 4-41 it can be assumed that the change will not have any negative effect on the results presented in Table 4-4.

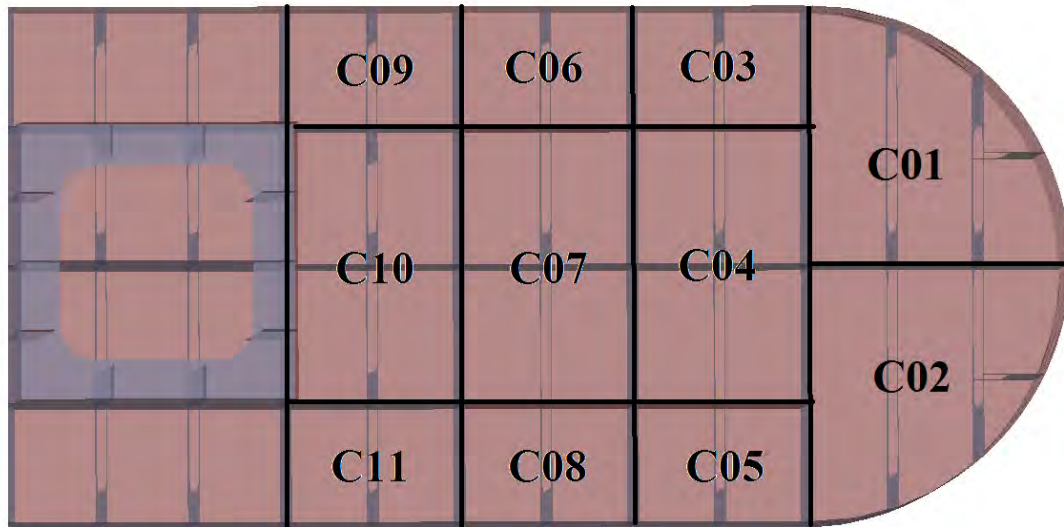


Figure 4-42 Updated tank plan

In the following sections the runs which give maximum indentation/compartament damage and collisions force is documented thoroughly. The remaining runs are also documented, but not on the same detail level.

4.5.1 Head on 0 deg, centre line (Container_HeadOn_Centre_mean)

Figures from the head on collision in the centre line are presented in this section.

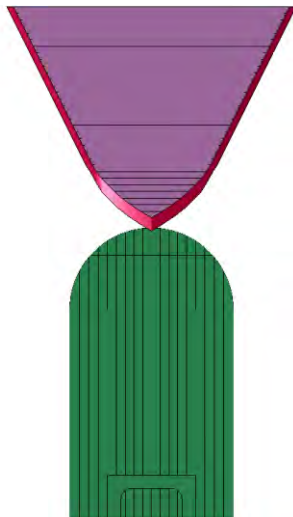


Figure 4-43 Collision scenario for HeadOn_Centre_mean

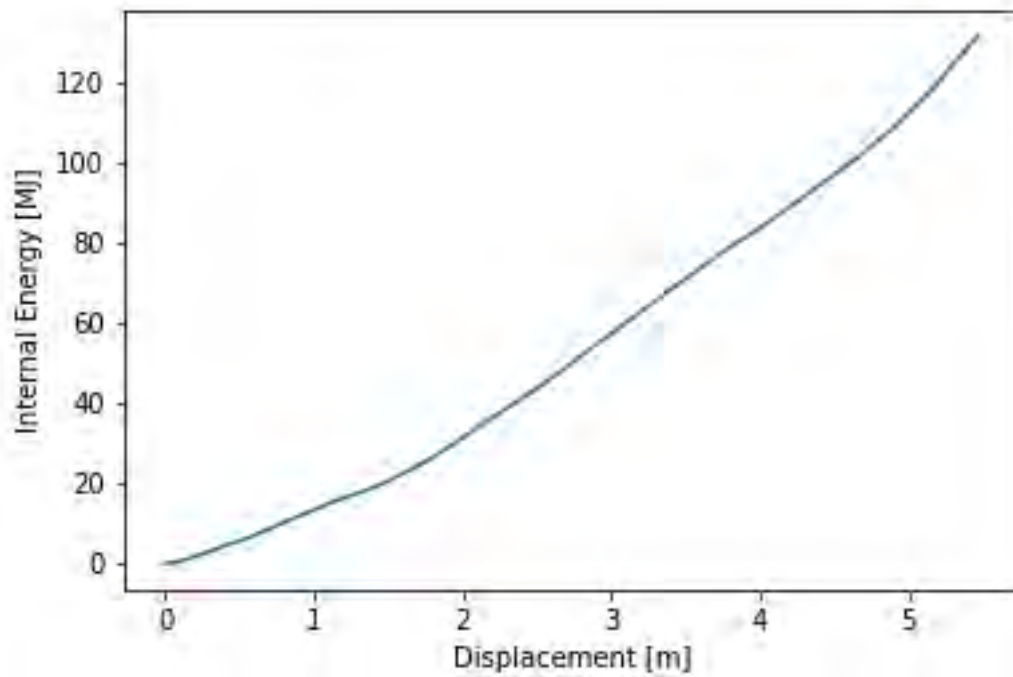


Figure 4-44 Energy displacement curve for "Container_HeadOn_Centre_mean"

From Figure 4-45 the force is plotted against the displacement. Note that the force for the bulb and forecastle is shown separately.

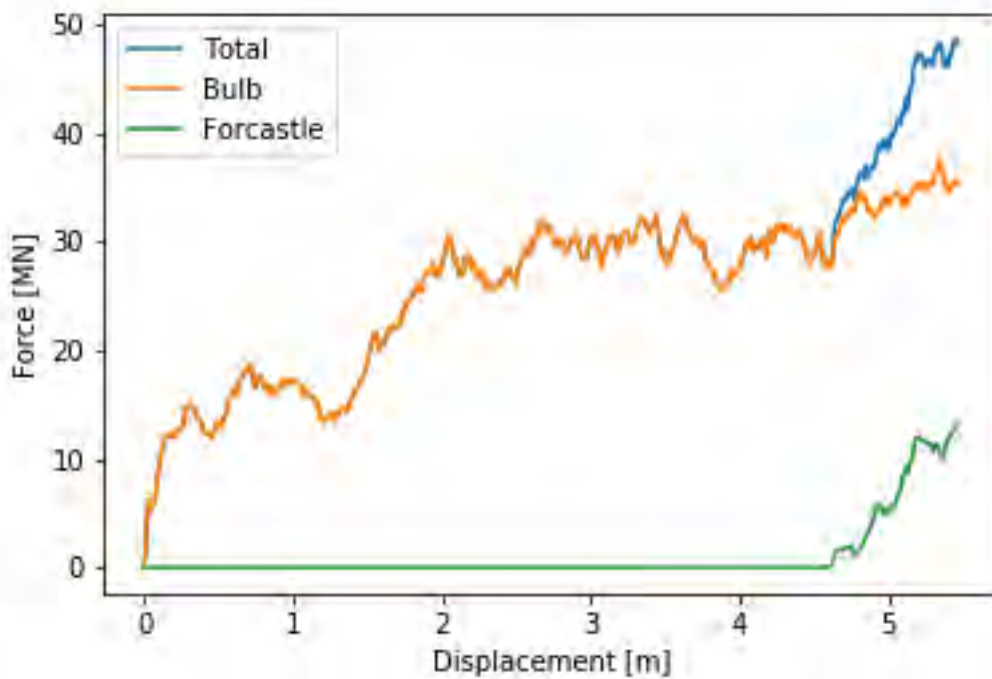


Figure 4-45 Force displacement curve for "Container_HeadOn_Centre_mean"

Figure 4-46 show the internal, kinetic and total energy from the analysis.

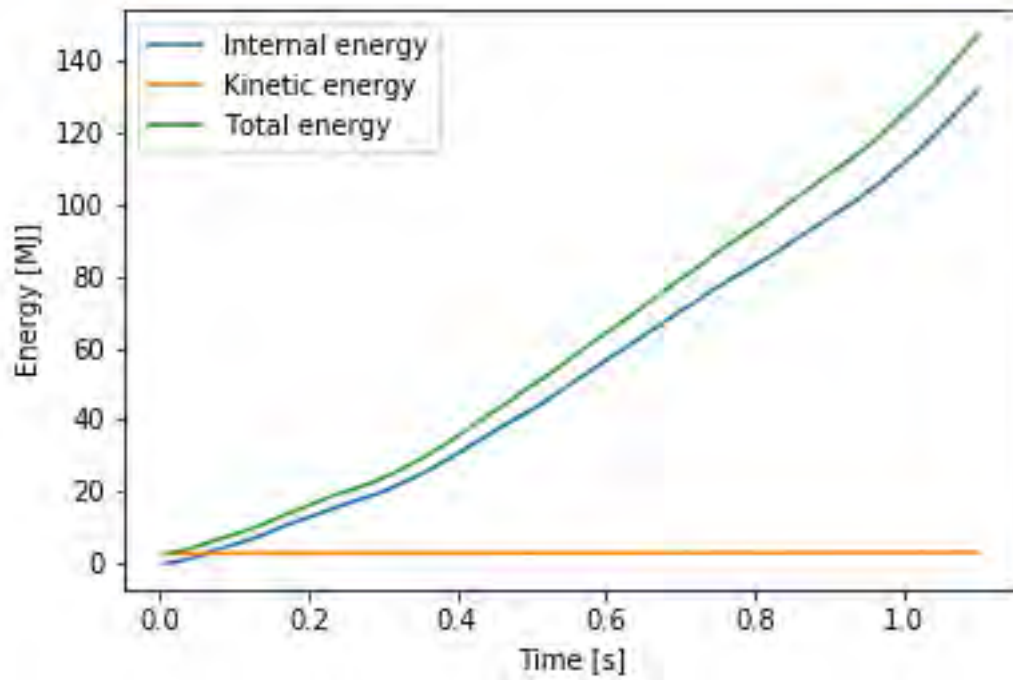


Figure 4-46 Internal, kinetic and total energy [MJ] vs time [s] for "Container_HeadOn_Centre_mean"

Figure 4-47 show the hourglass -and sliding energy from the analysis.

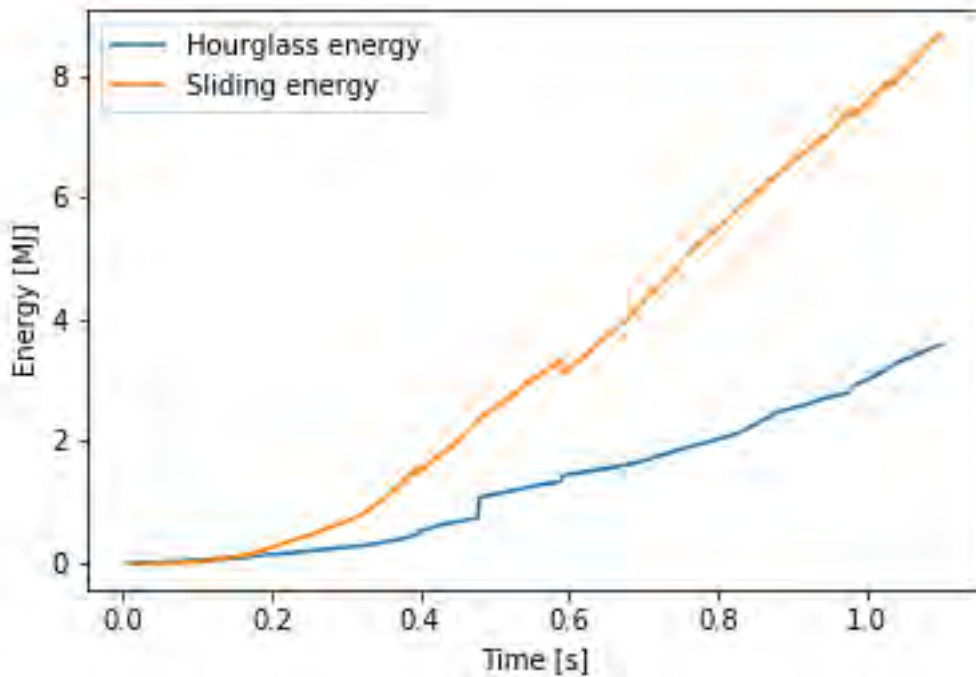


Figure 4-47 Hourglass and sliding energy [MJ] vs time [s] for "Container_HeadOn_Centre_mean"

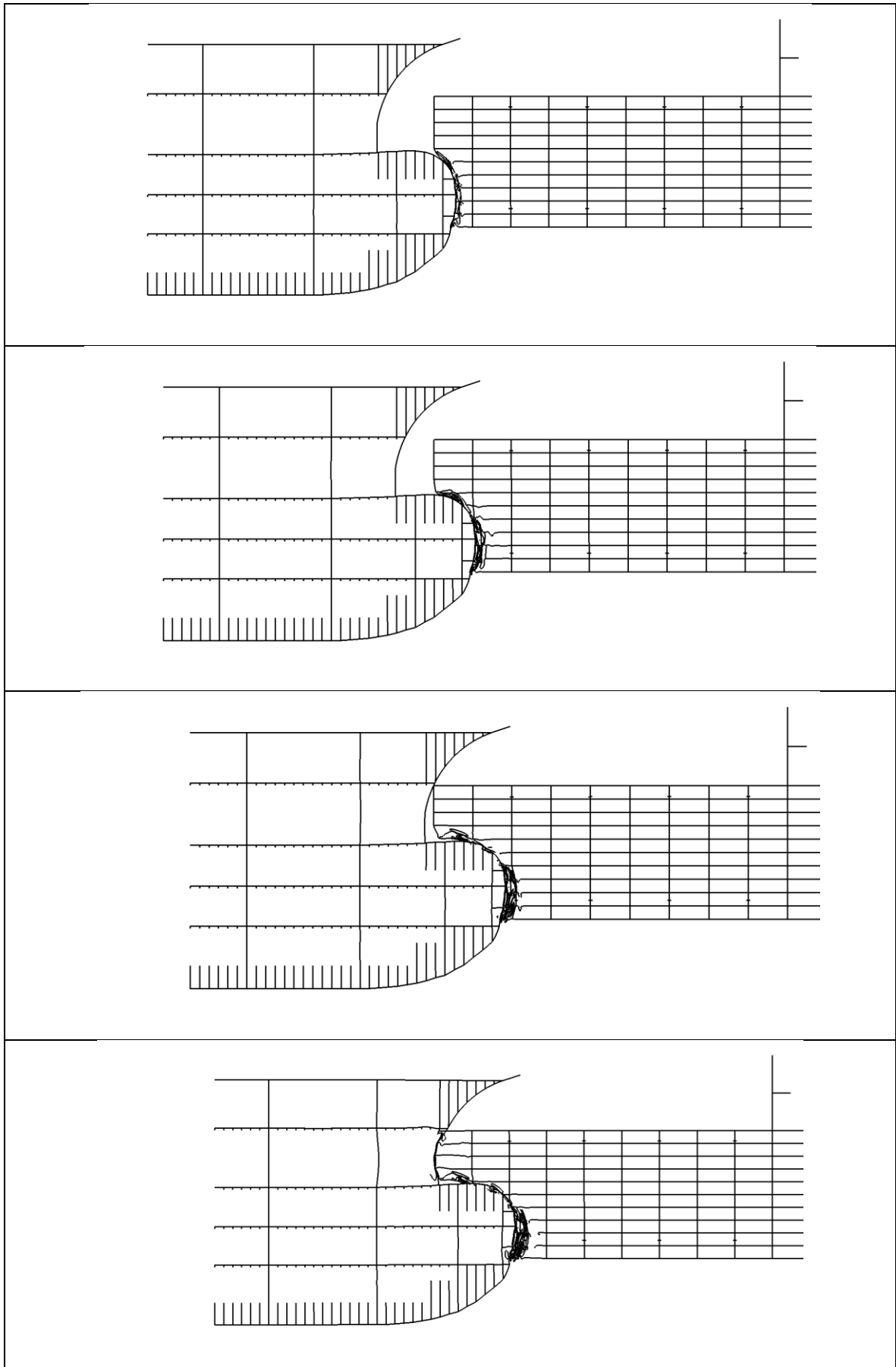


Figure 4-48 Deformation during collision. From above, 20 MJ, 50 MJ, 100 MJ and 130 MJ

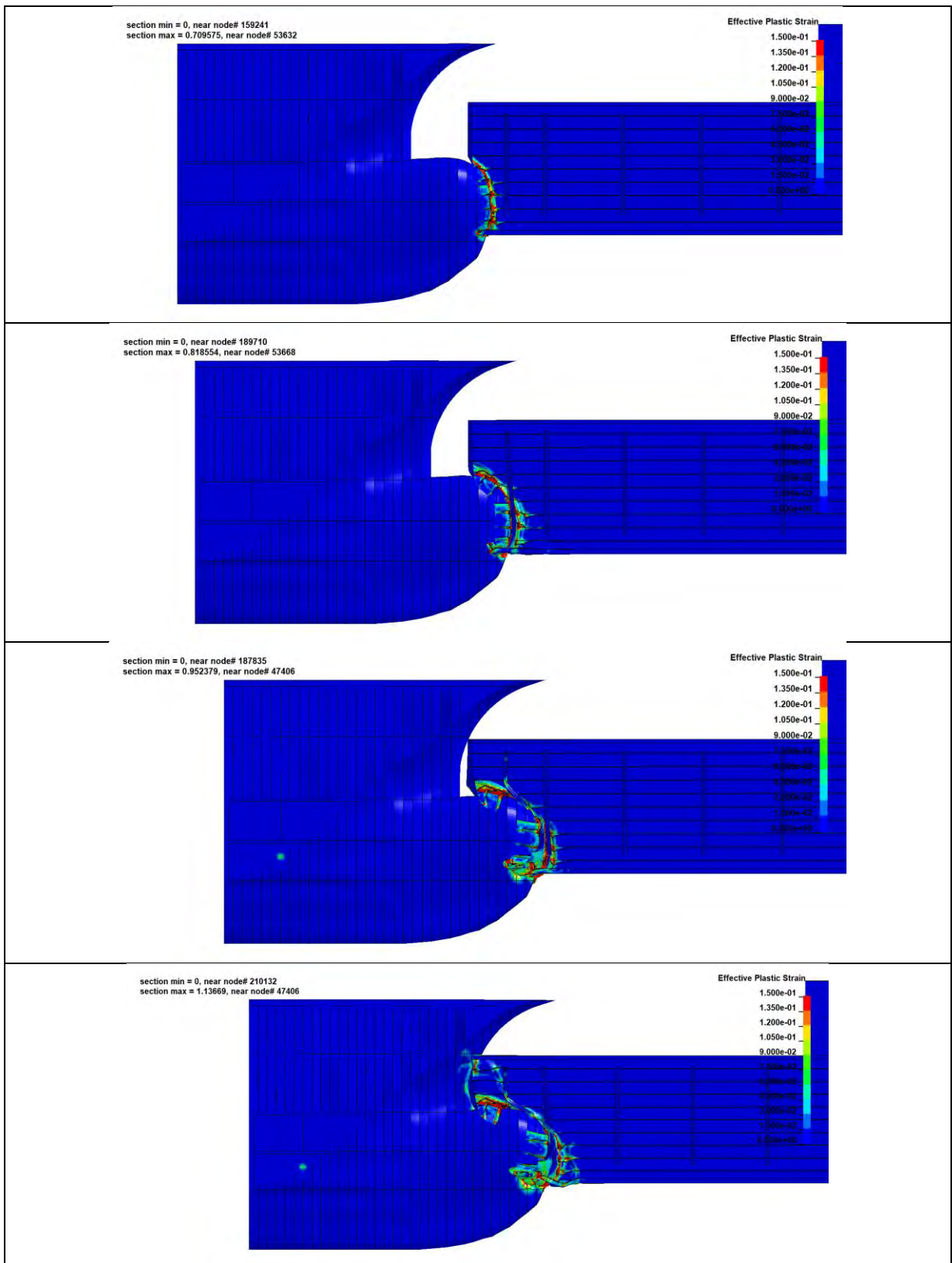


Figure 4-49 Effective plastic strain during collision. From above, 20 MJ, 50 MJ, 100 MJ and 130 MJ

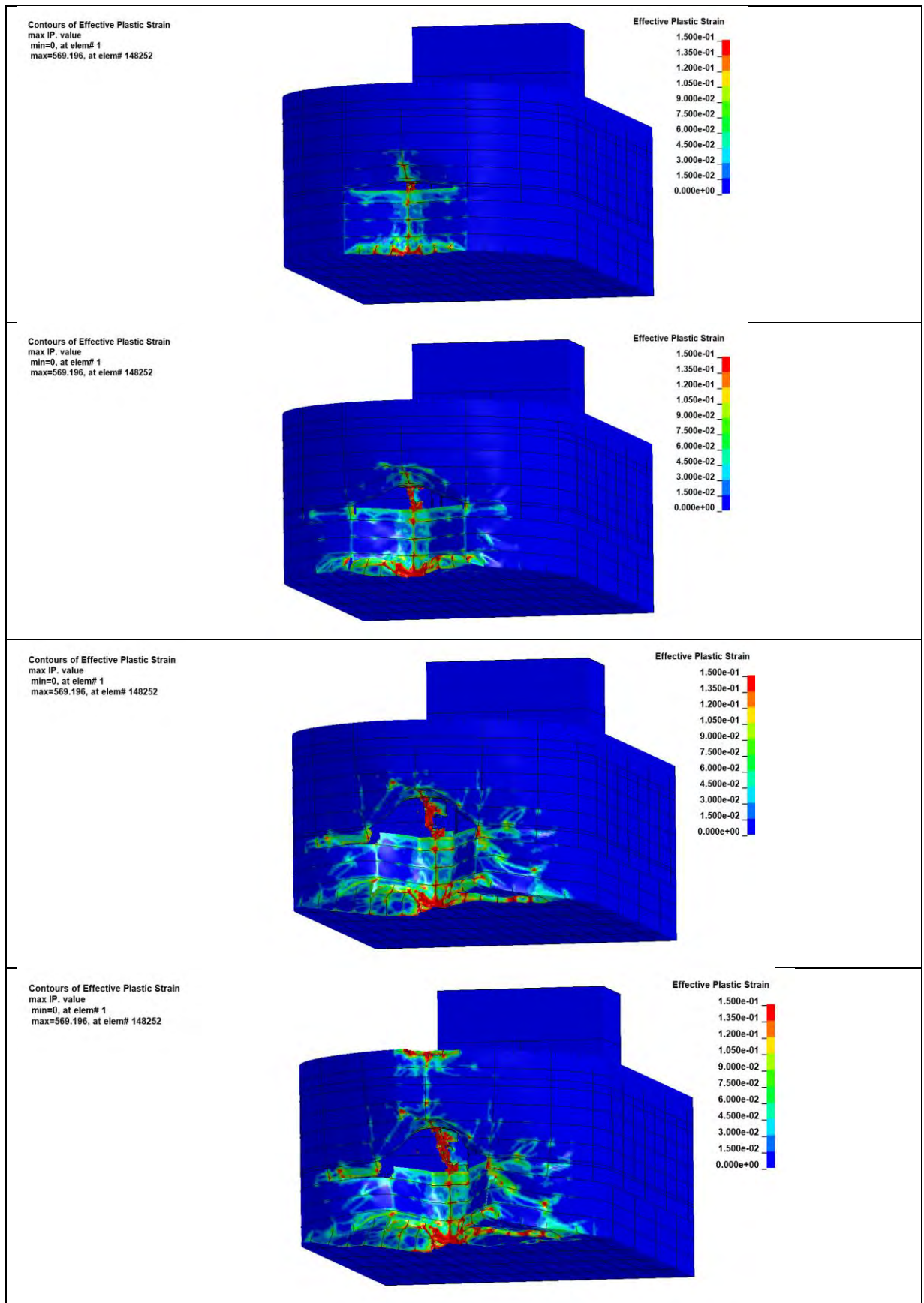


Figure 4-50 Effective plastic strain during collision. From above, 20 MJ, 50 MJ, 100 MJ and 130 MJ

4.5.2 Cruise 30 deg low (Cruise_30Deg_low)

Figures from the head on collision with a 30 degree angle are presented in this section.

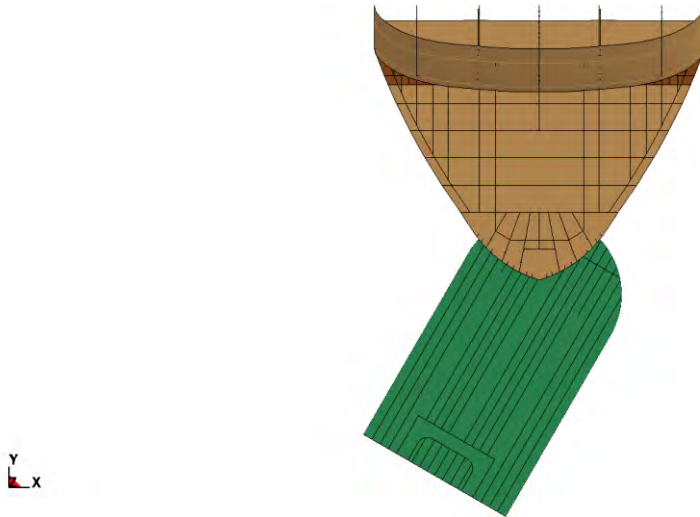


Figure 4-51 Collision scenario for Cruise_30Deg_low

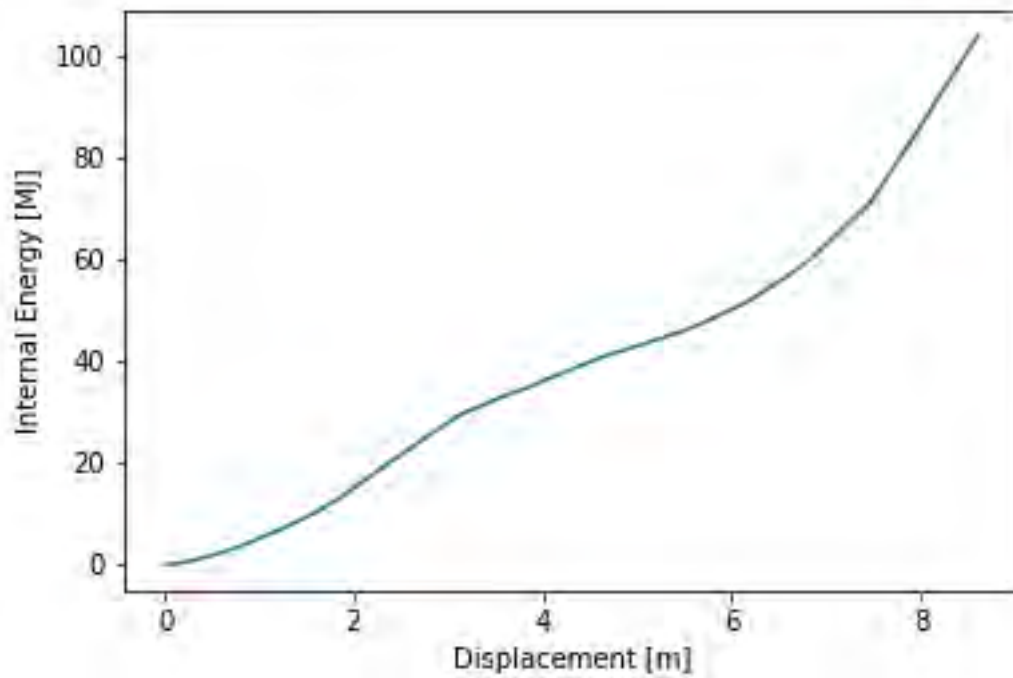


Figure 4-52 Energy displacement curve for "Cruise_30Deg_low"

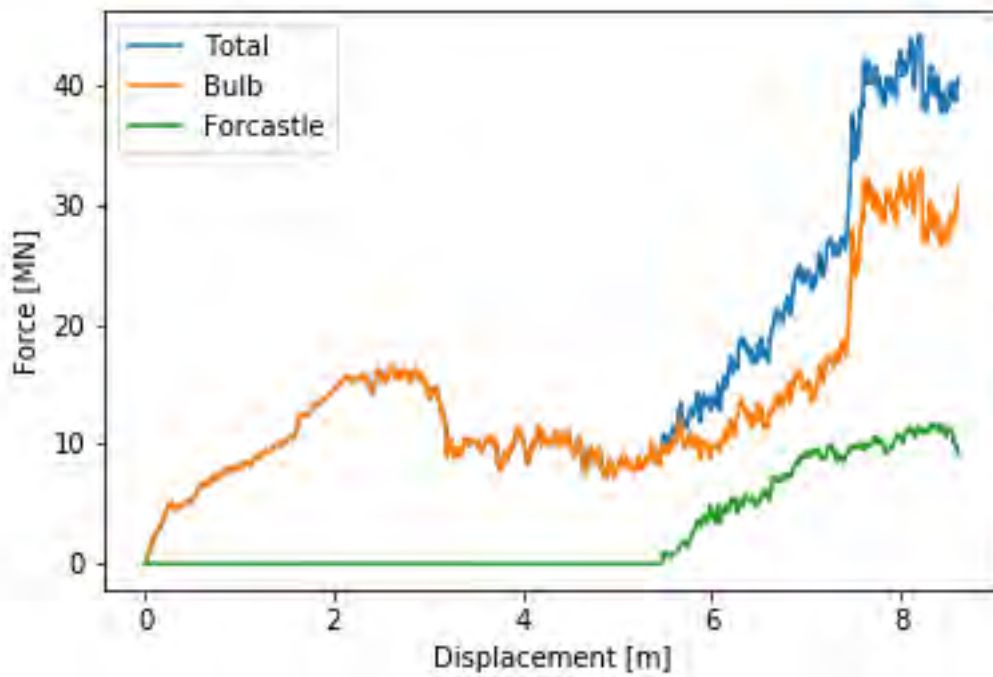


Figure 4-53 Force displacement curve for "Cruise_30Deg_low"

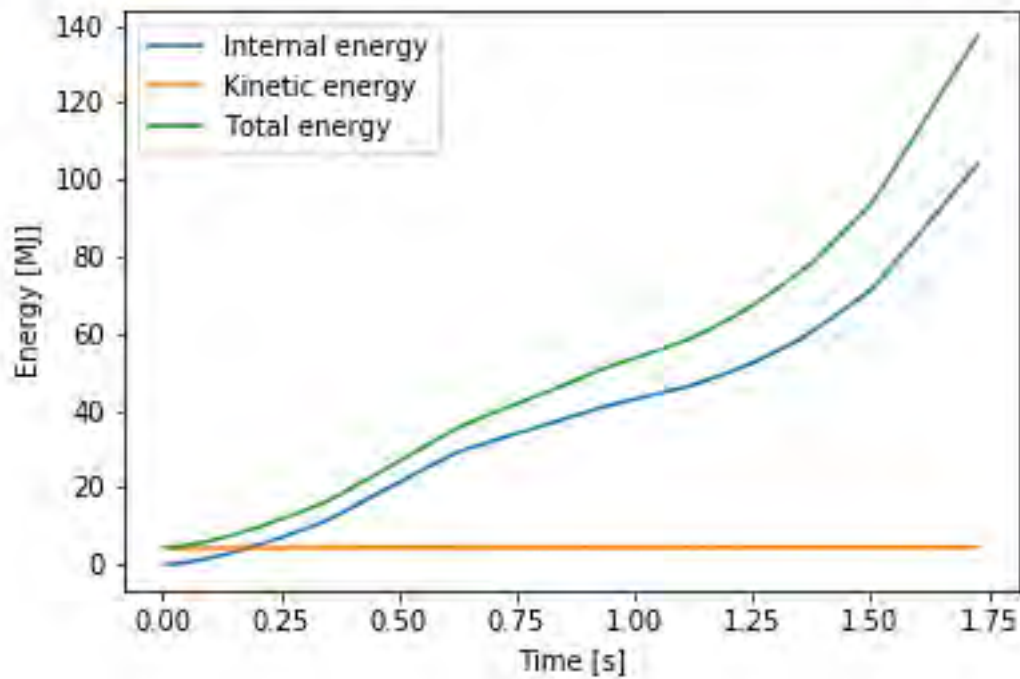


Figure 4-54 Internal, kinetic and total energy [MJ] vs time [s] for "Cruise_30Deg_low"

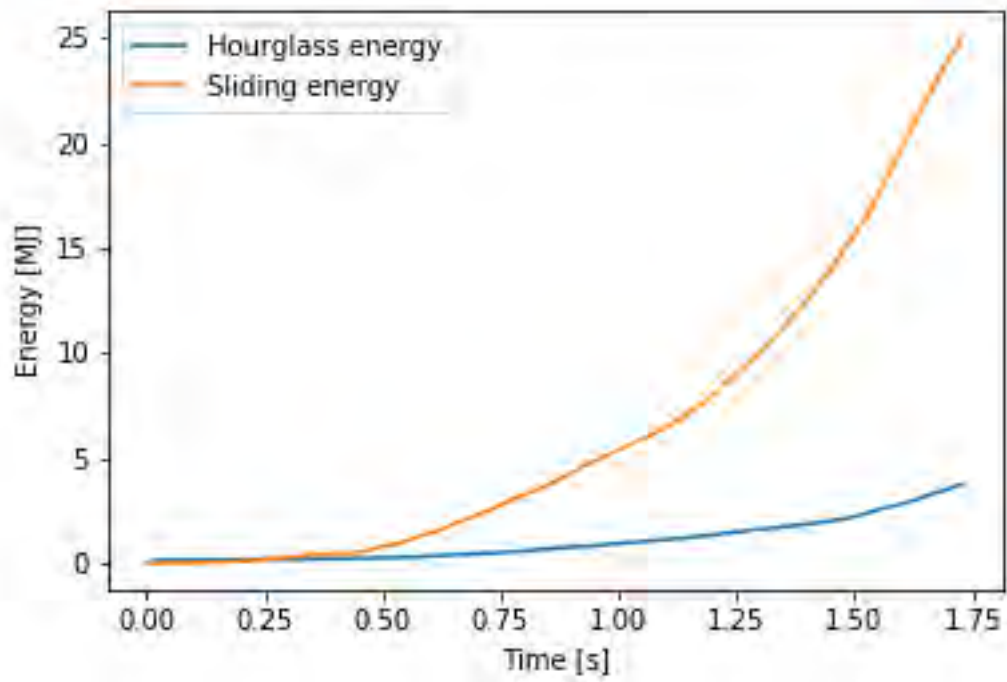


Figure 4-55 Hourglass -and sliding energy for "Cruise_30Deg_low"

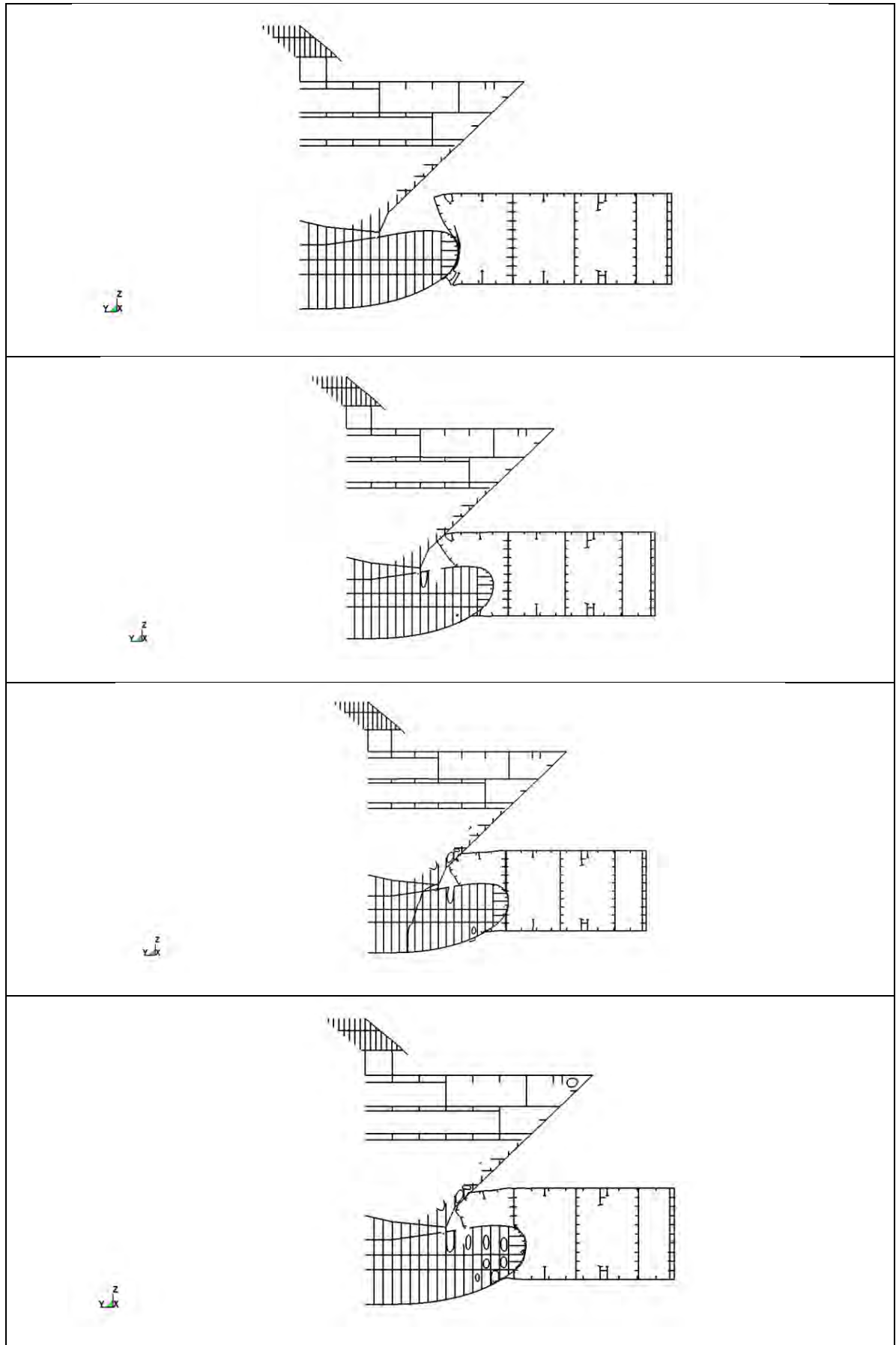


Figure 4-56 Deformation during collision. From above, 20 MJ, 50 MJ, 80 MJ and 105 MJ

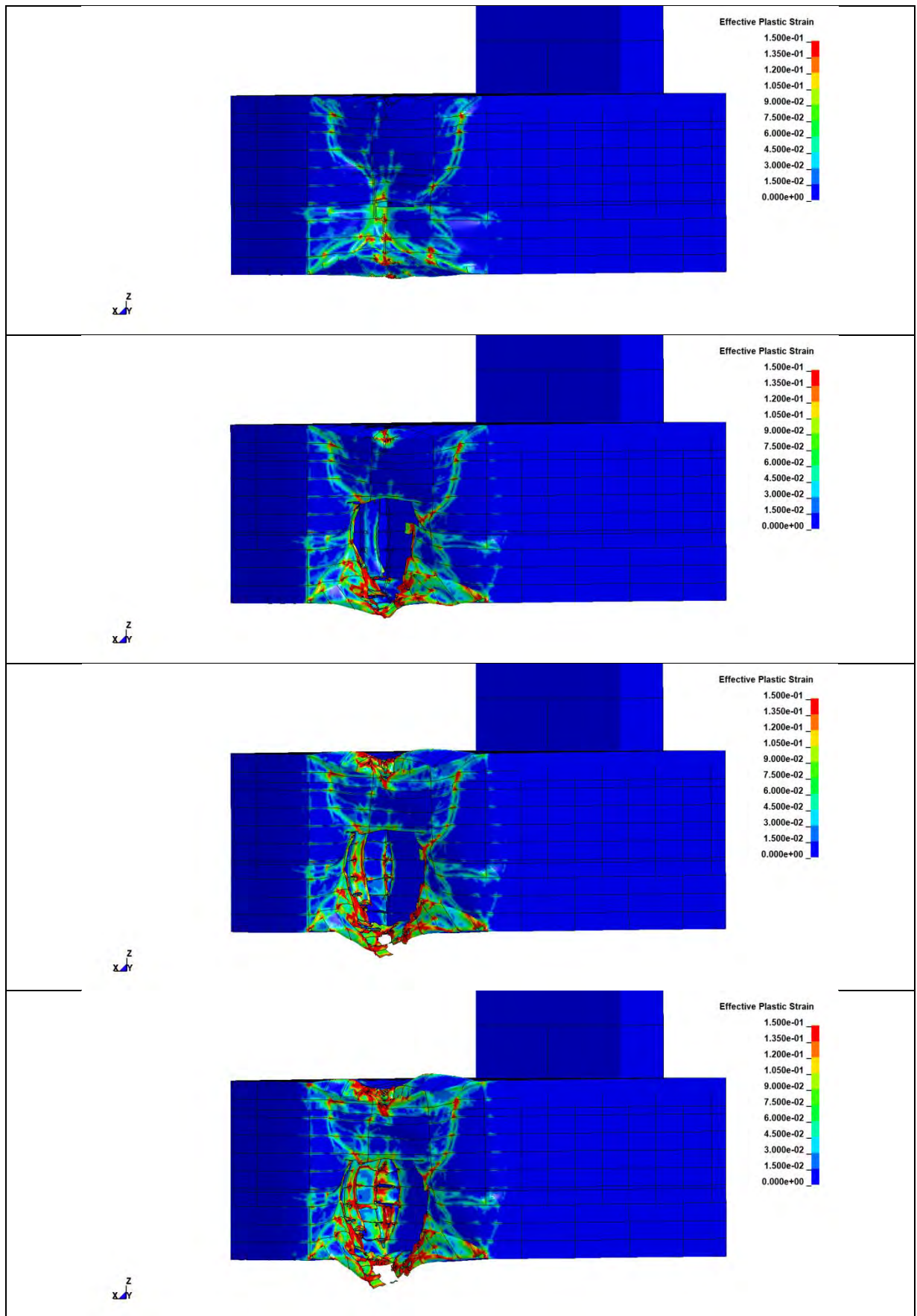


Figure 4-57 Effective plastic strain during collision. From above, 20 MJ, 50 MJ, 80 MJ and 105 MJ

4.5.3 Head on 0 deg, centre line + 2.5 m offset (Container_HeadOn_Centre+2_5_low)

Figures from the head on collision with a 2.5 m offset are presented in this section.

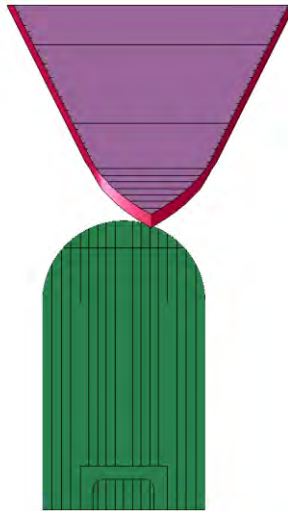


Figure 4-58 Collision scenario for HeadOn_Centre +2_5_low

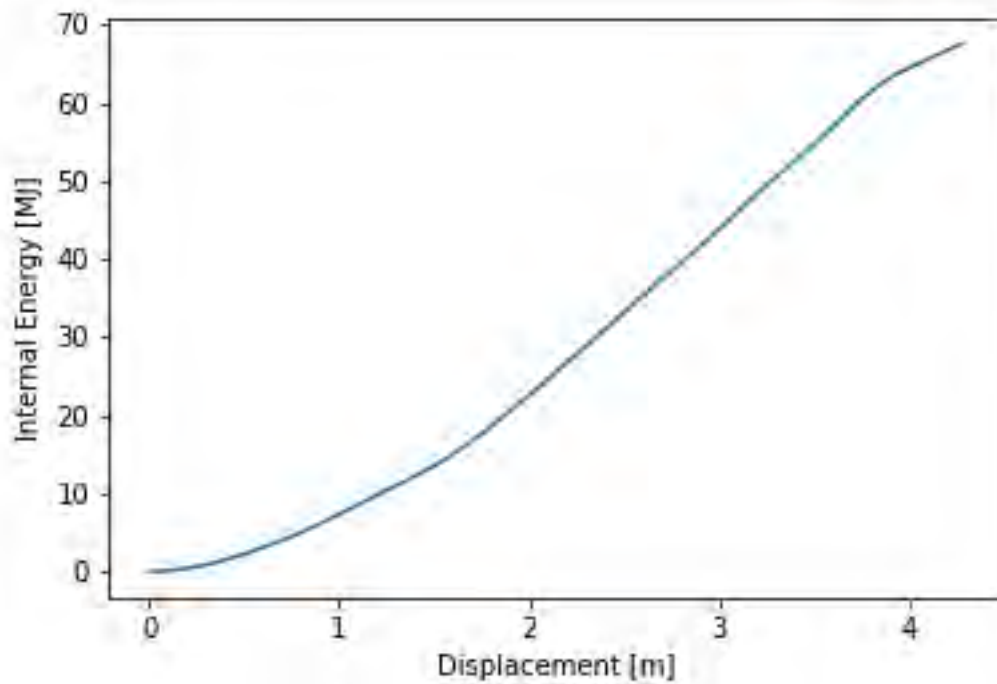


Figure 4-59 Energy displacement curve for "Container_HeadOn_Centre+2_5_low"

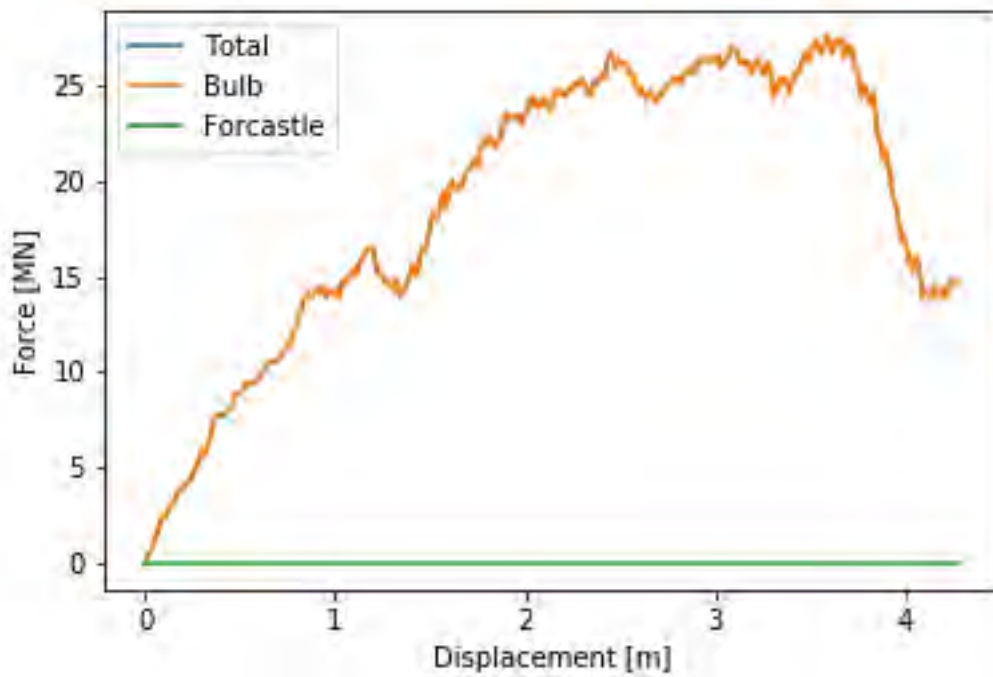


Figure 4-60 Force displacement curve for "Container_HeadOn_Centre+2_5_low"

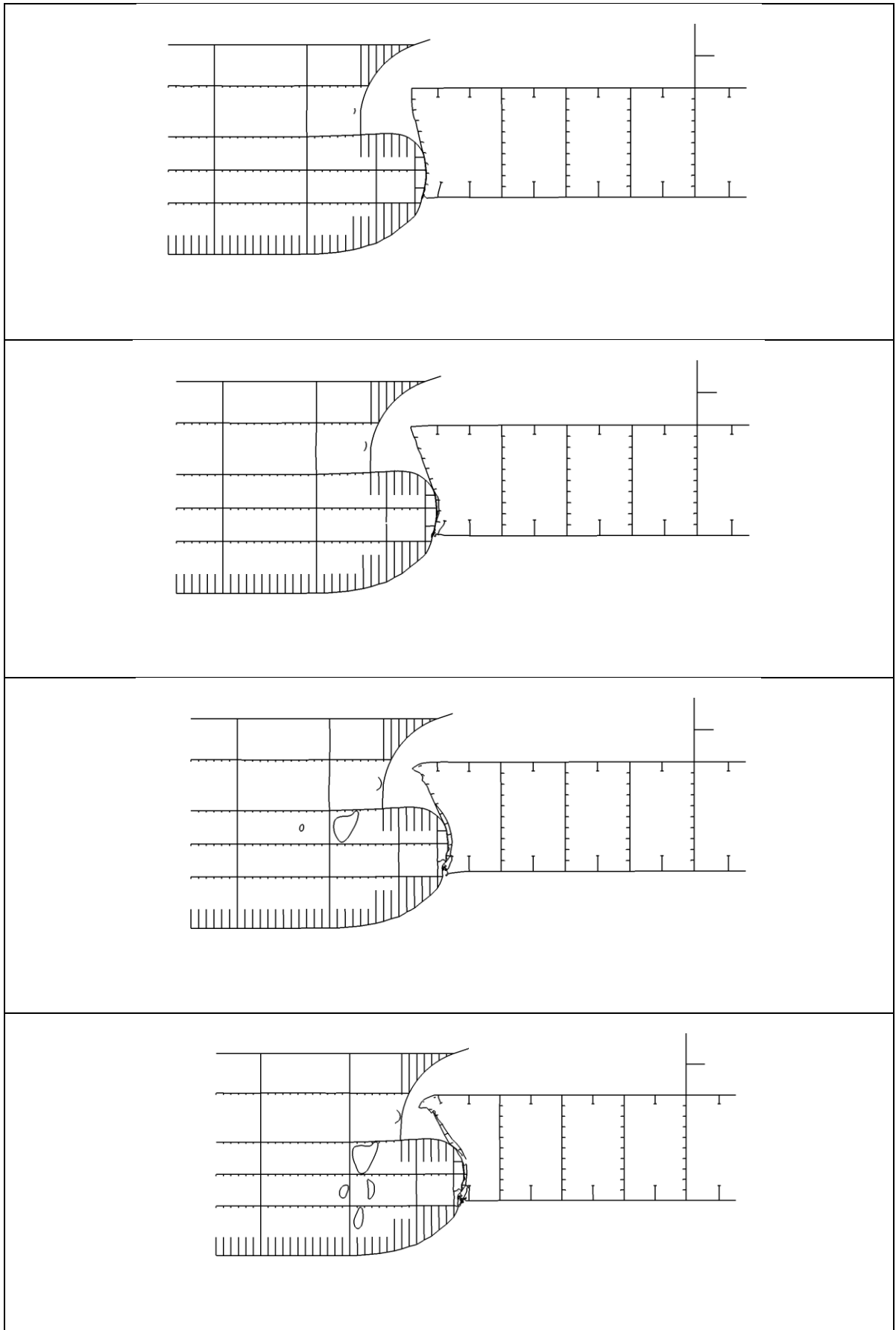


Figure 4-61 Deformation during collision. From above, 10 MJ, 25 MJ, 45 MJ and 67 MJ

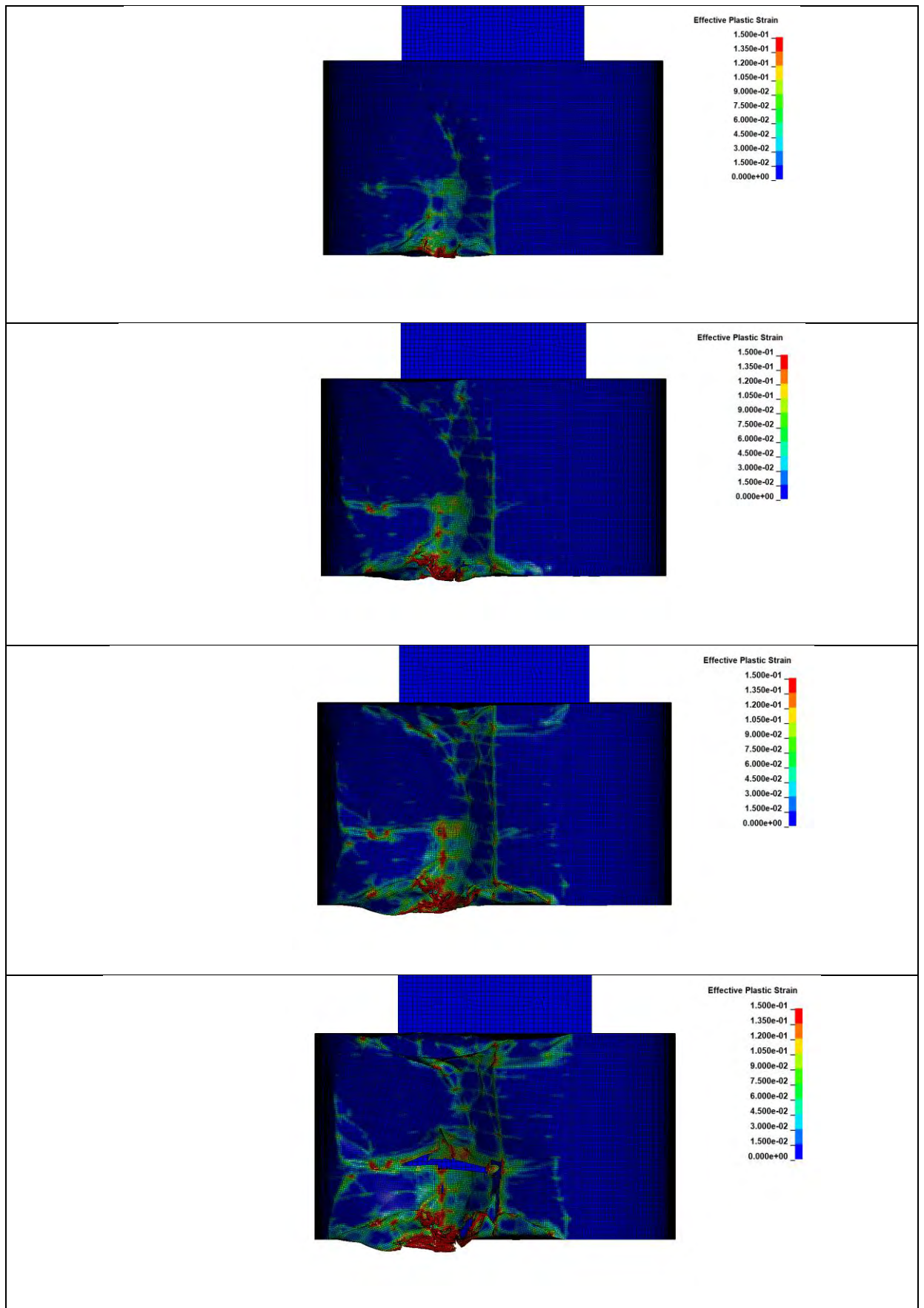


Figure 4-62 Effective plastic strain during collision. From above, 10 MJ, 25 MJ, 45 MJ and 67 MJ

4.5.4 Runs with no centre bulkhead

Head on 0 deg, centre line with no centre bulkhead (Container HeadOn Centre mean NoBlkh)

Figures from the head on collision without central bulkhead in pontoon are presented in this section.

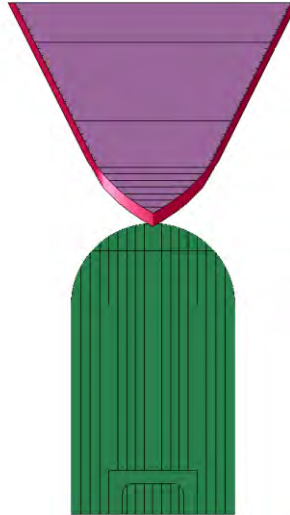


Figure 4-63 Collision scenario for HeadOn_Centre_mean_NoBlkh

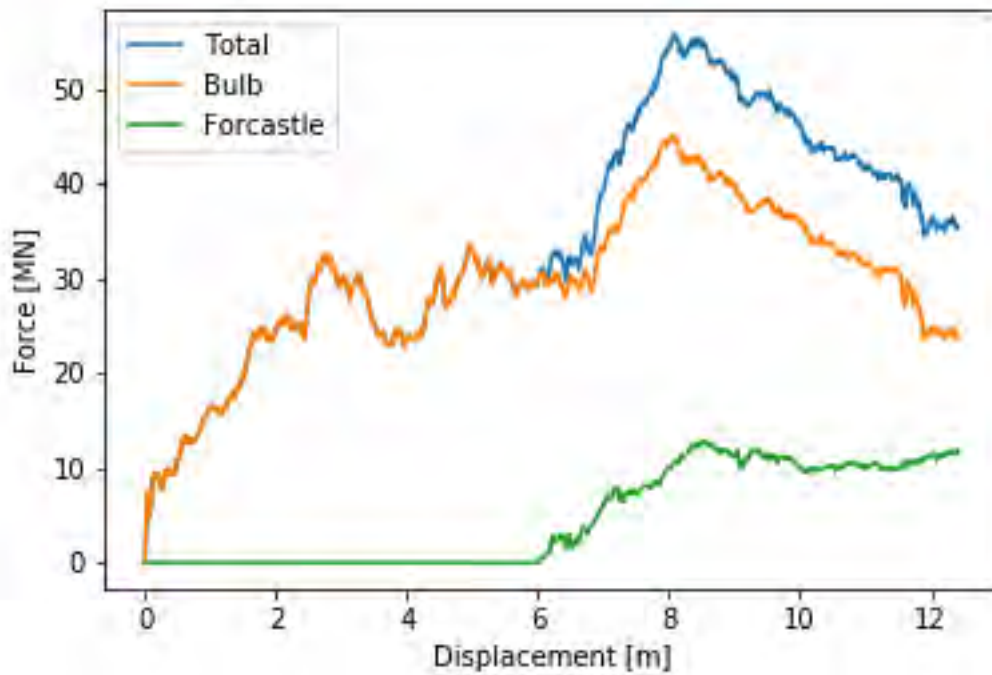


Figure 4-64 Force displacement curve for "Container_HeadOn_Centre_mean_NoBlkh"

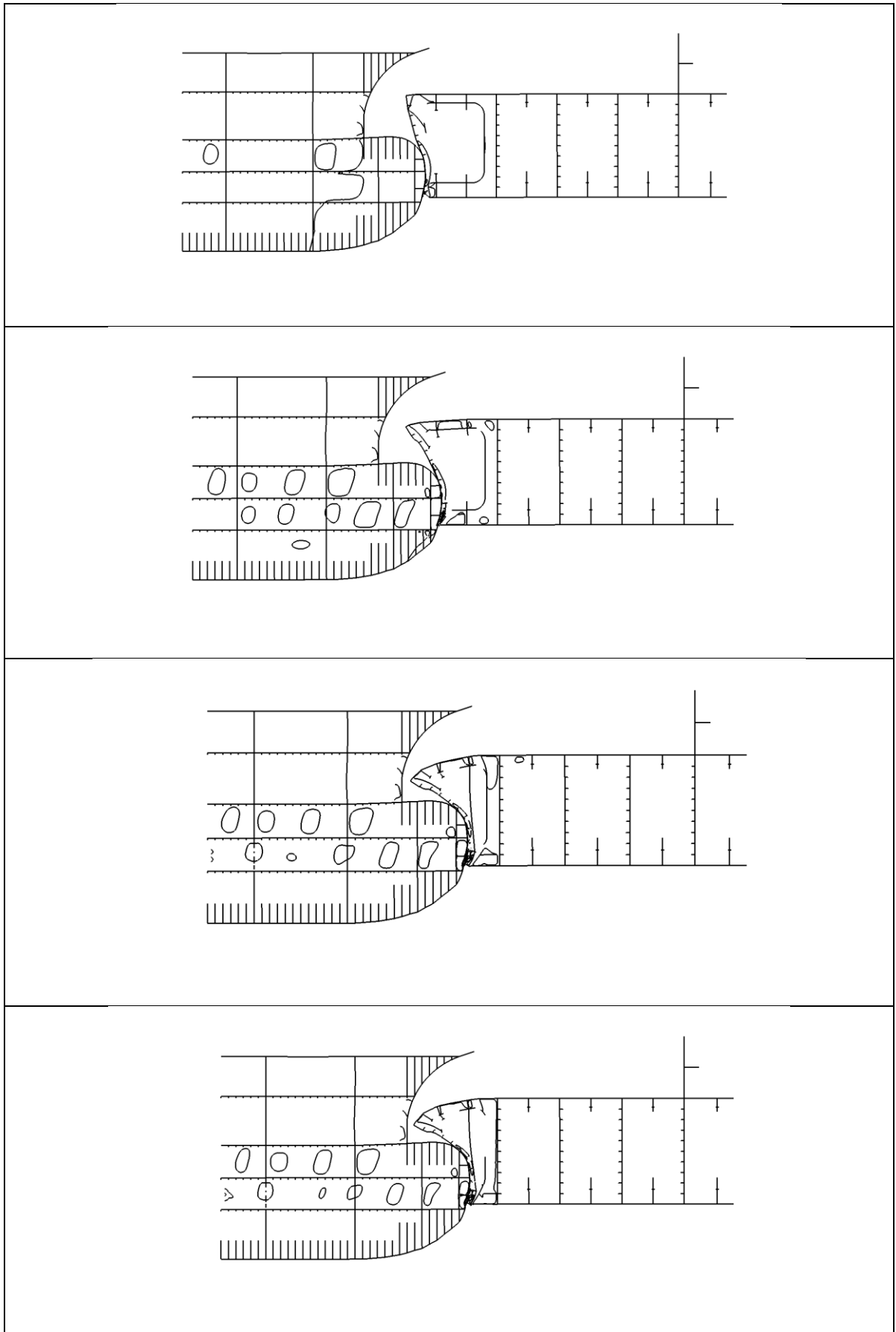


Figure 4-65 Deformation during collision. From above, 20 MJ, 50 MJ, 100 MJ and 110 MJ

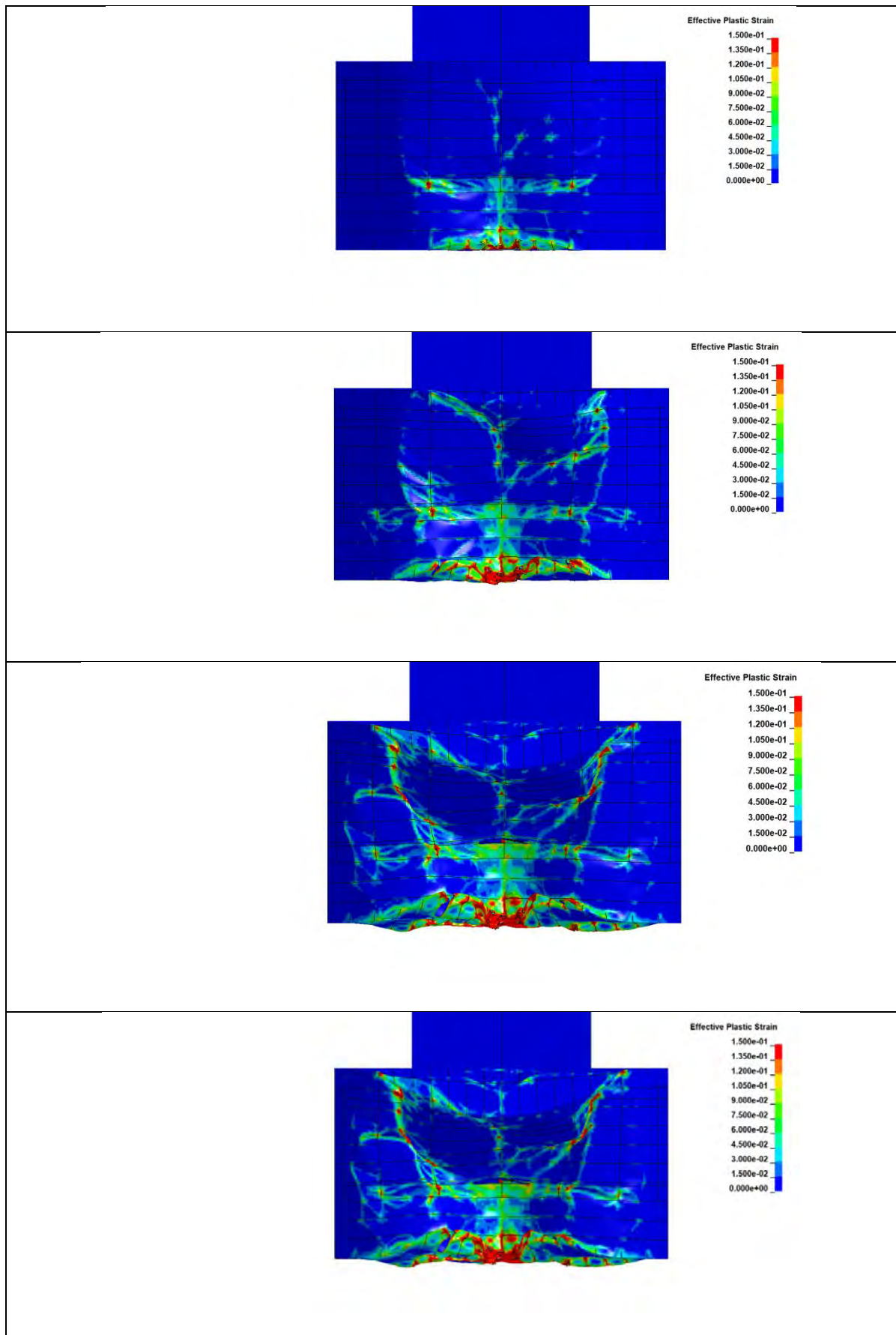


Figure 4-66 Effective plastic strain during collision. From above, 20 MJ, 50 MJ, 100 MJ and 110 MJ

Head on 0 deg, centre line + 2.5 m No bulkhead (Container HeadOn Centre+2.5 low Noblkh)

Figures from the head on collision with a 2.5 m offset with no centre bulkhead are presented in this section.

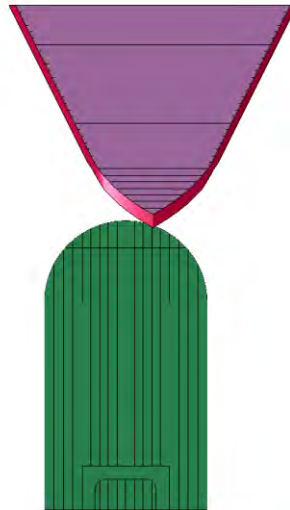


Figure 4-67 Collision scenario for Container_HeadOn_Centre+2.5_low_Noblkh

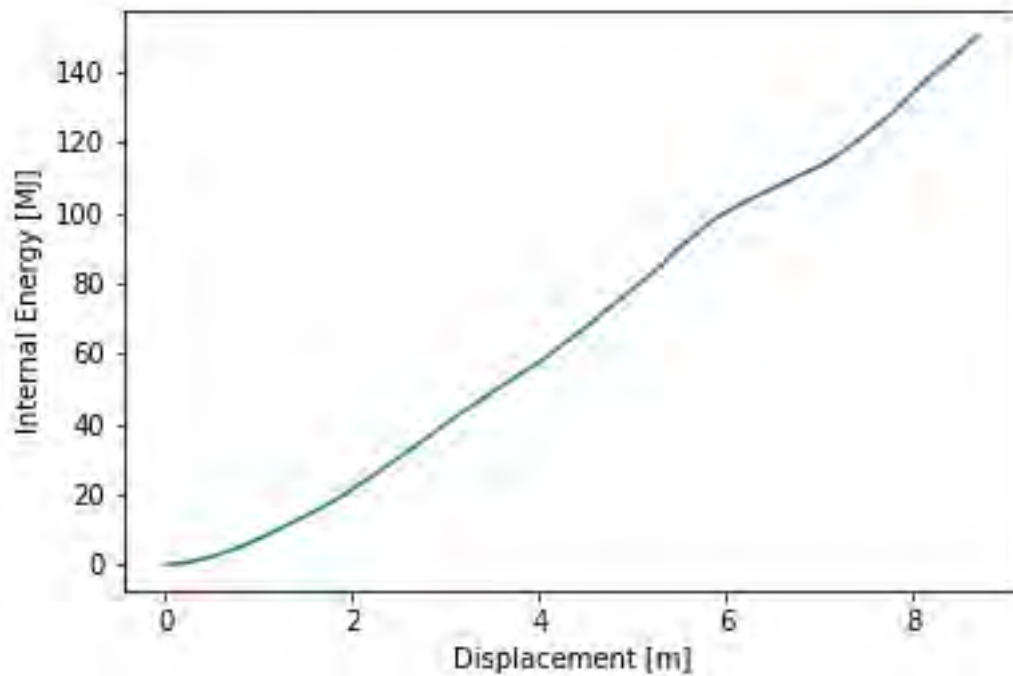


Figure 4-68 Energy displacement curve for "Container_HeadOn_Centre+2.5_low_Noblkh"

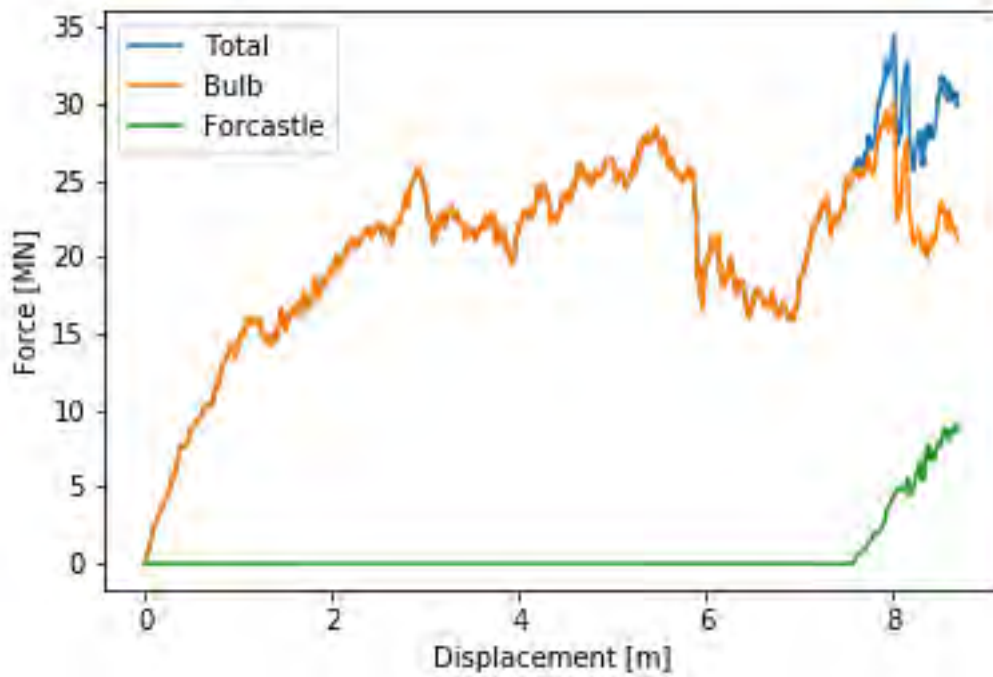


Figure 4-69 Force displacement curve for "Container_HeadOn_Centre+2.5_low_Noblkh"

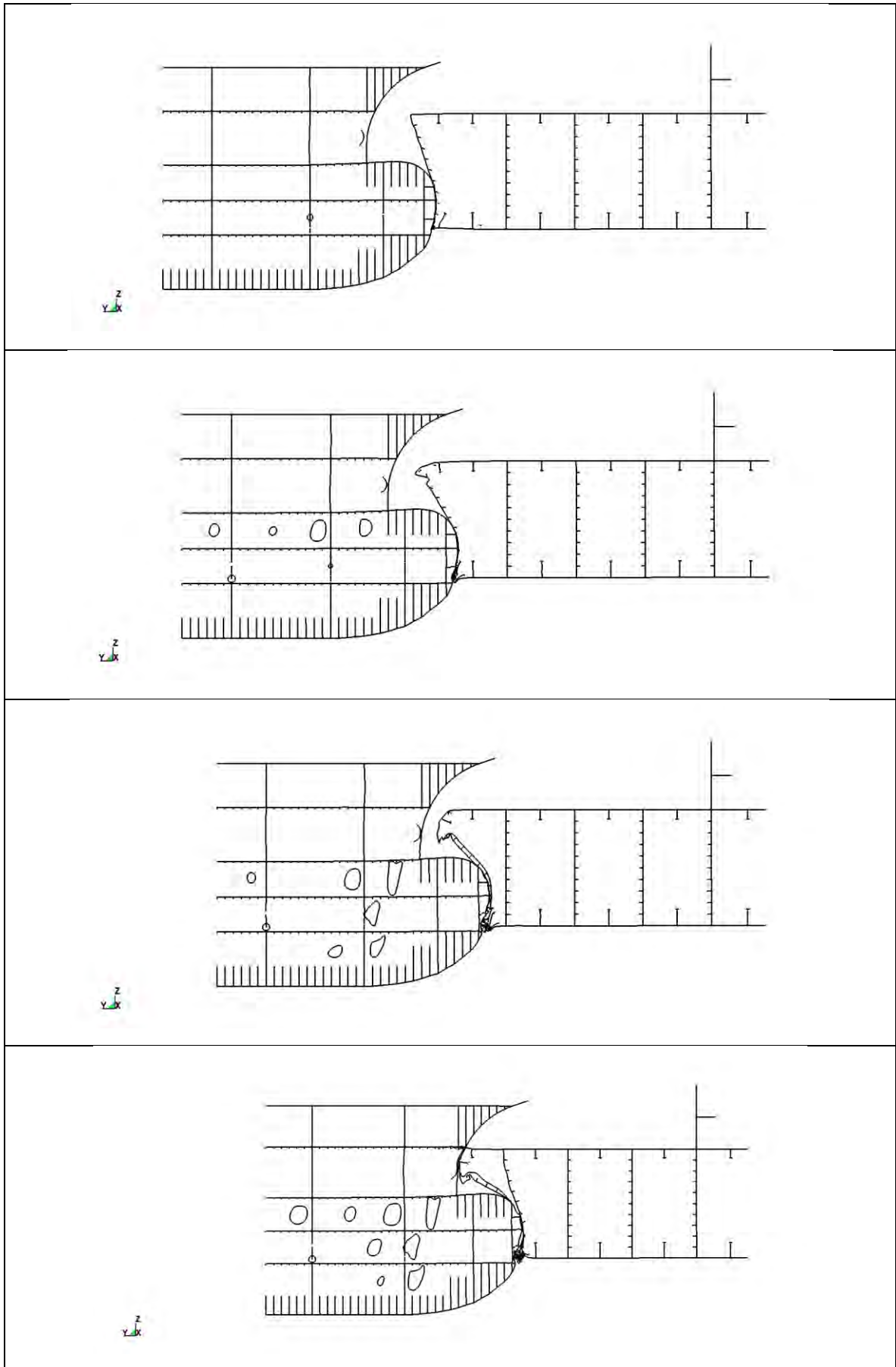


Figure 4-70 Deformation during collision. From above, 20 MJ, 50 MJ, 100 MJ and 150 MJ

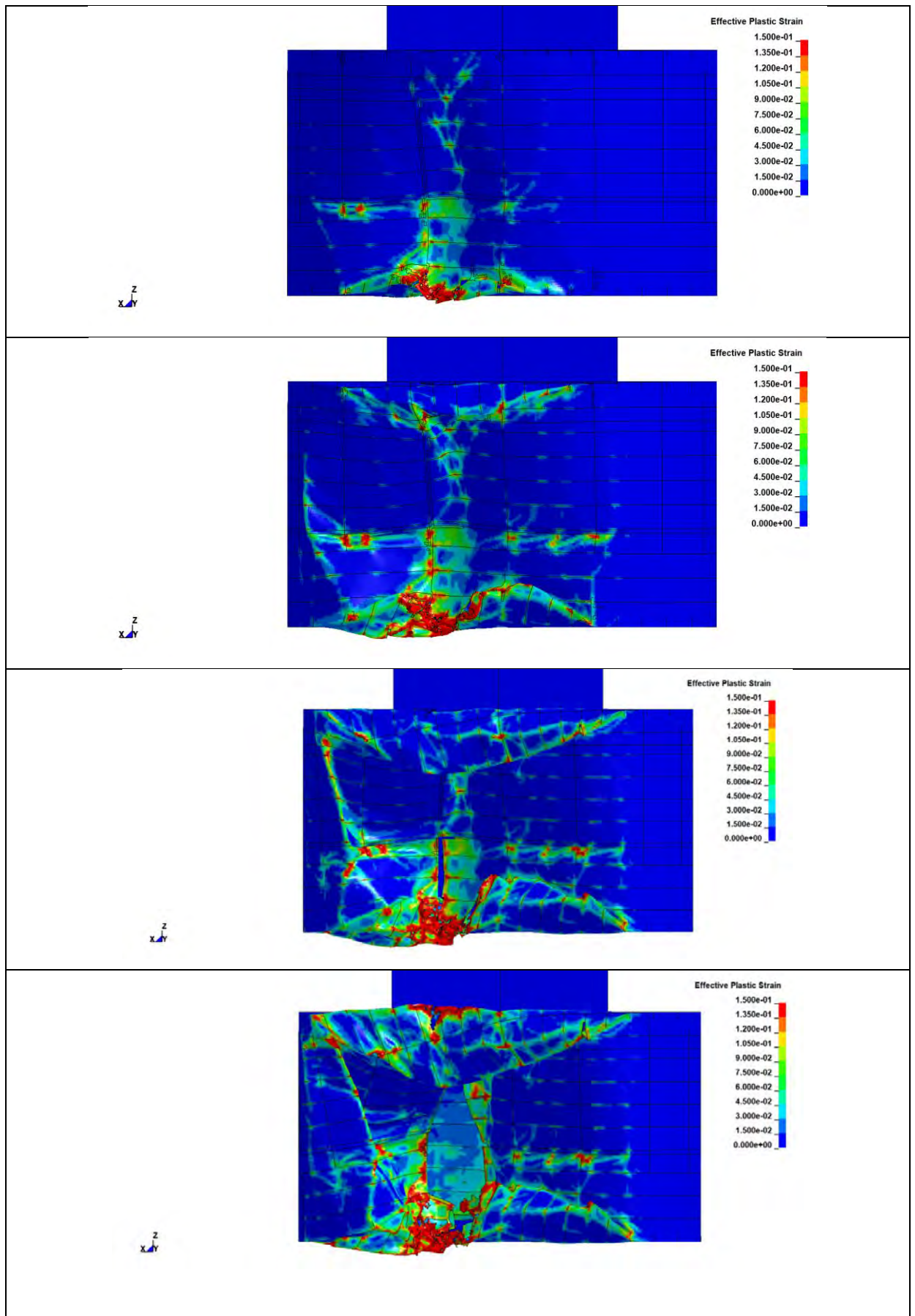


Figure 4-71 Effective plastic strain during collision. From above, 20 MJ, 50 MJ, 100 MJ and 150 MJ

Head on 0 deg, centre line No bulkhead (Cruise_HeadOn_Centre No bulkhead low)

Figures from the head on collision with no centre bulkhead are presented in this section.

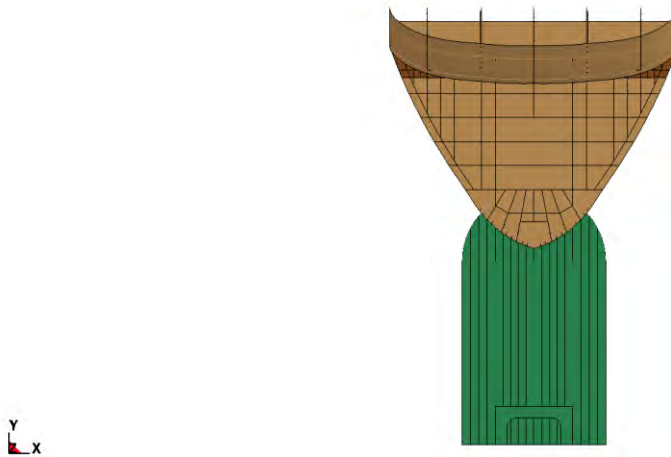


Figure 4-72 Collision scenario for Cruise_HeadOn_No centre bulkhed

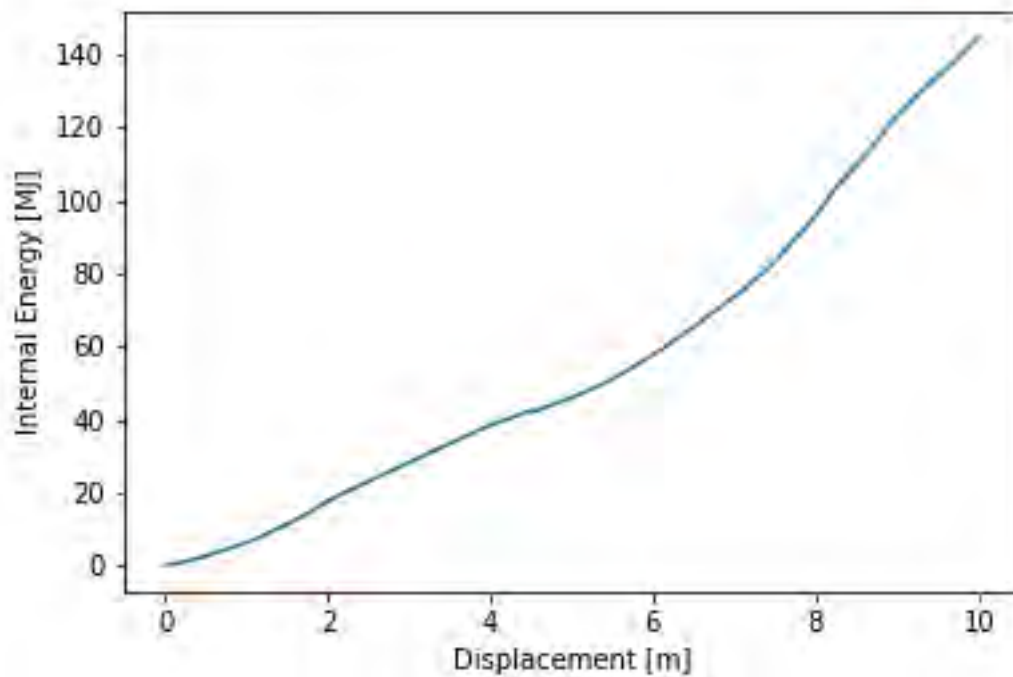


Figure 4-73 Energy displacement curve for " Container_HeadOn_Centre+2_5_low"

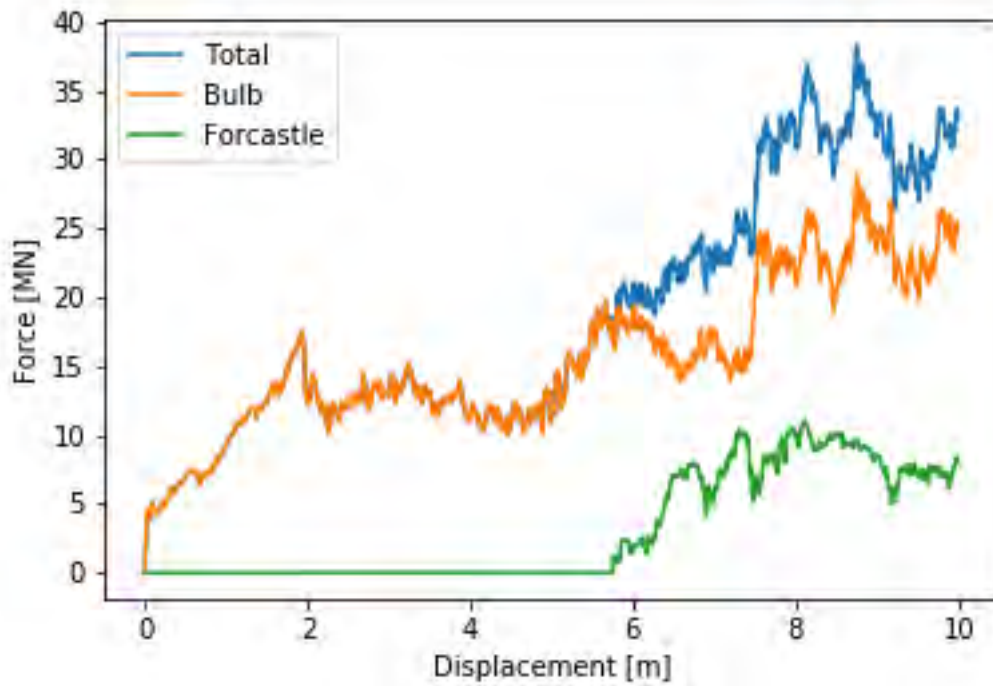


Figure 4-74 Force displacement curve for "Container_HeadOn_Centre+2_5_low"

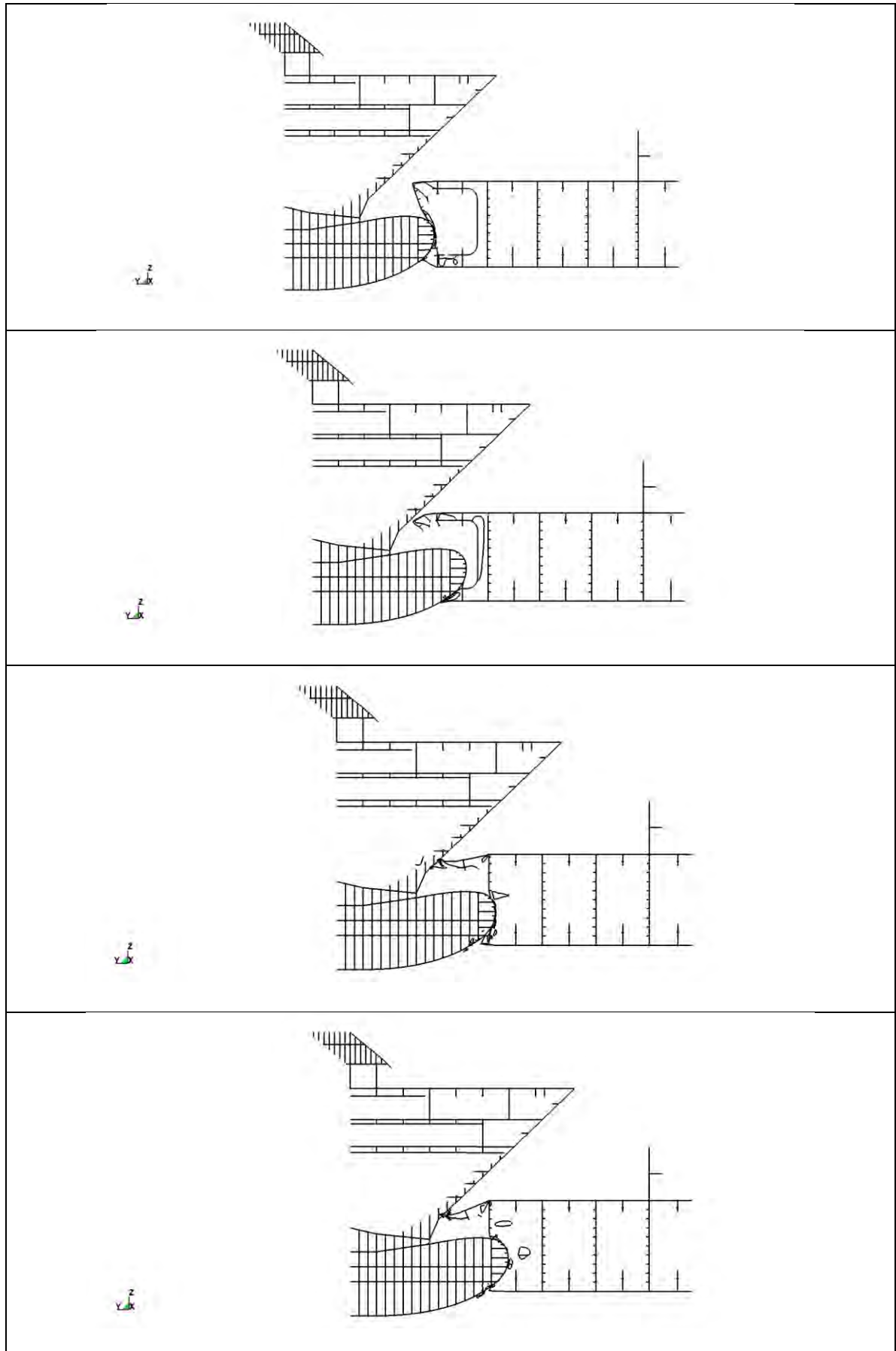


Figure 4-75 Deformation during collision. From above, 20 MJ, 50 MJ, 100 MJ and 130 MJ

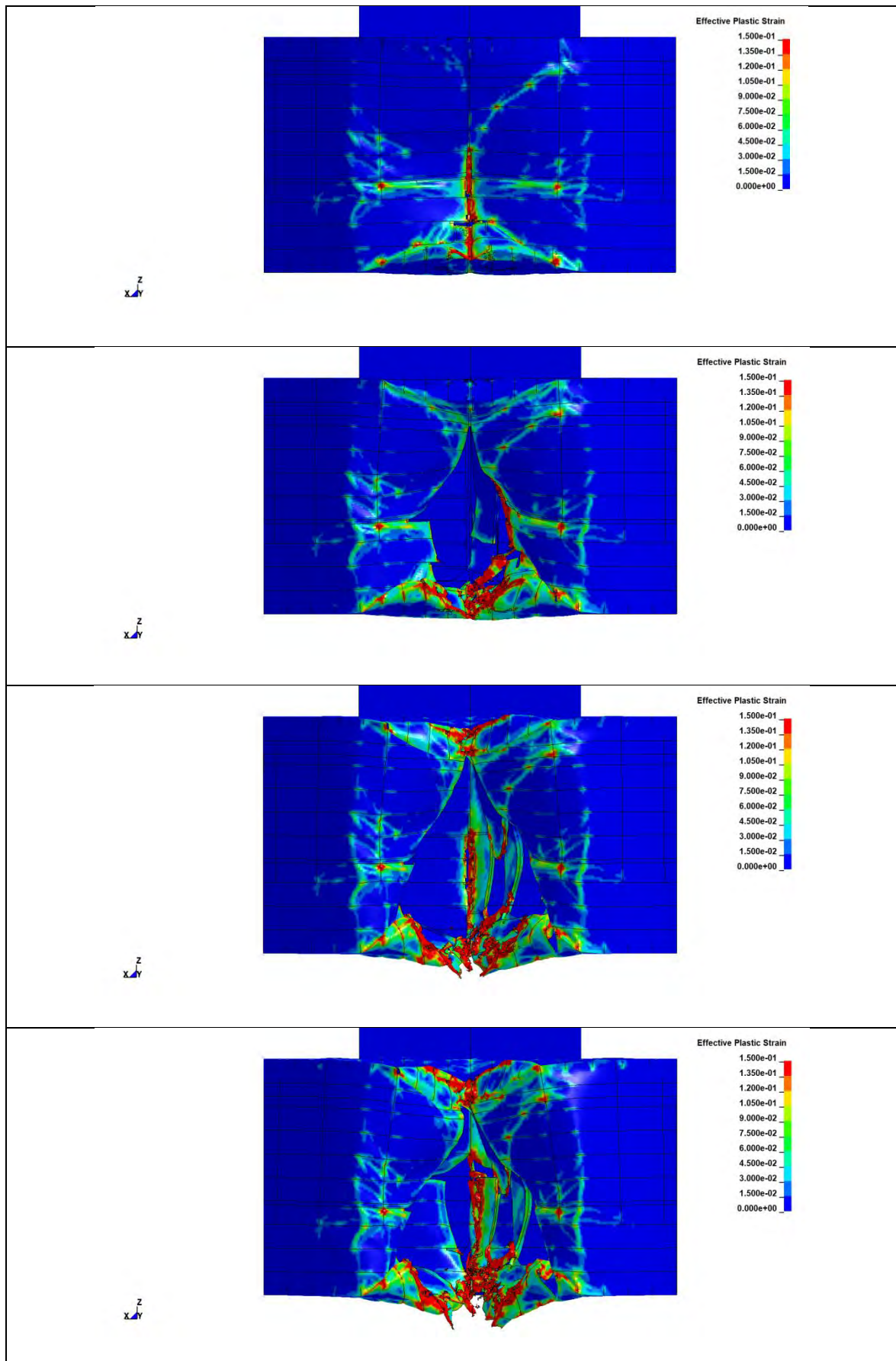


Figure 4-76 Effective plastic strain during collision. From above, 20 MJ, 50 MJ, 100 MJ and 130 MJ

4.5.5 Sensitivity to super duplex material properties

A simple sensitivity study was conducted on the effect of the increased material strength of the super duplex steel used in the splash zone. The study was performed on an early version of the pontoon model, and the absolute values are thus not directly comparable to the results presented above.

Figure 4-77 shows the resulting force-displacement curves for a head-on impact between the container vessel and the pontoon with either super duplex or NV36 steel in the splash zone. A minor strength increase is seen with super duplex on average, but the difference between the two is minimal w.r.t. energy dissipation for large deformation. Hence, the pontoon response is not very sensitive to the super duplex material strength.

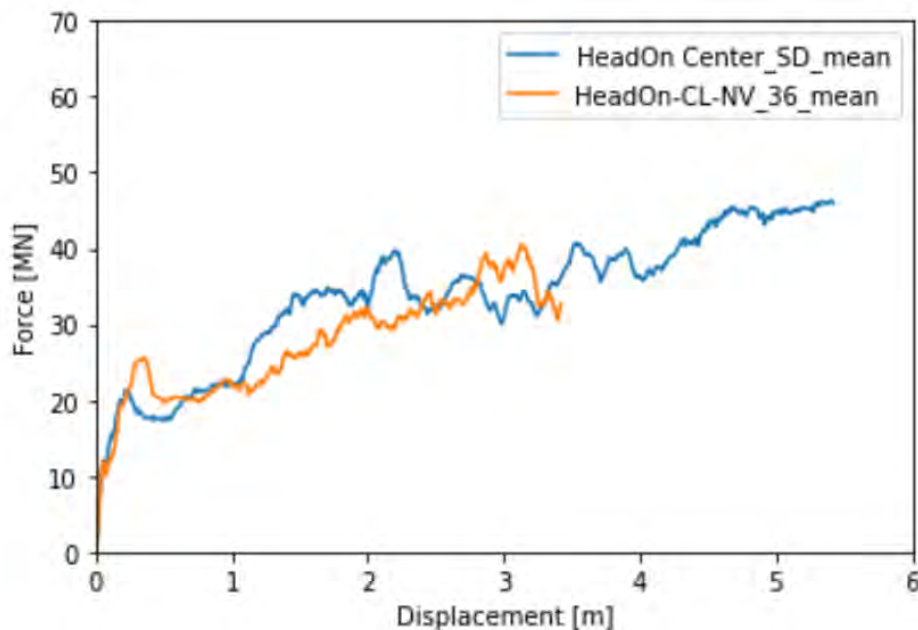


Figure 4-77 Sensitivity study for material strength in splash zone.

4.6 Results collisions ship deckhouse vs bridge girder

4.6.1 Deckhouse collision with 0 degree angle, high impact

The following figures present the results from the collision simulation between the container ship deckhouse and bridge girder for 0 degree collision angle and high impact location.

The side of the bridge girder is pushed approximately 1.4 meters inwards when 200 MJ energy is dissipated. Smaller ruptures in the side plates are observed at the periphery of the contact area and where the side plate is attached to the frames, as can be seen in Figure 4-81 and Figure 4-82.

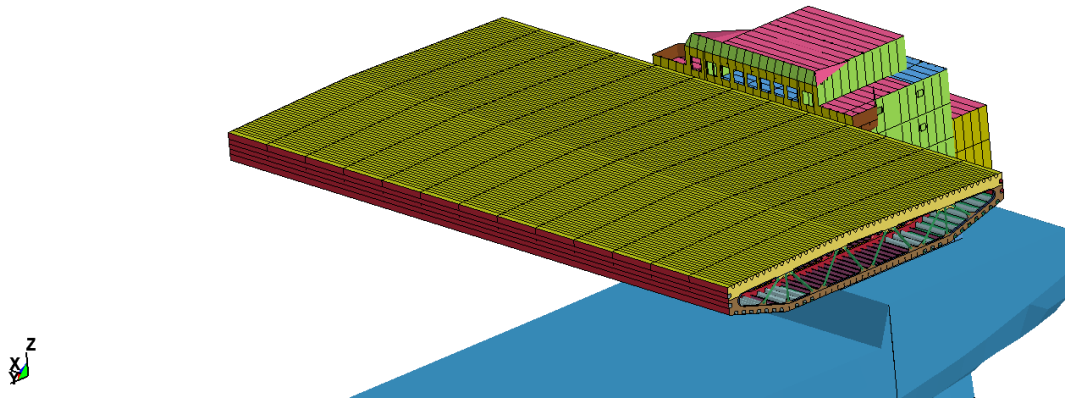


Figure 4-78 Deckhouse-bridge girder collision, 0 degree angle and high impact location

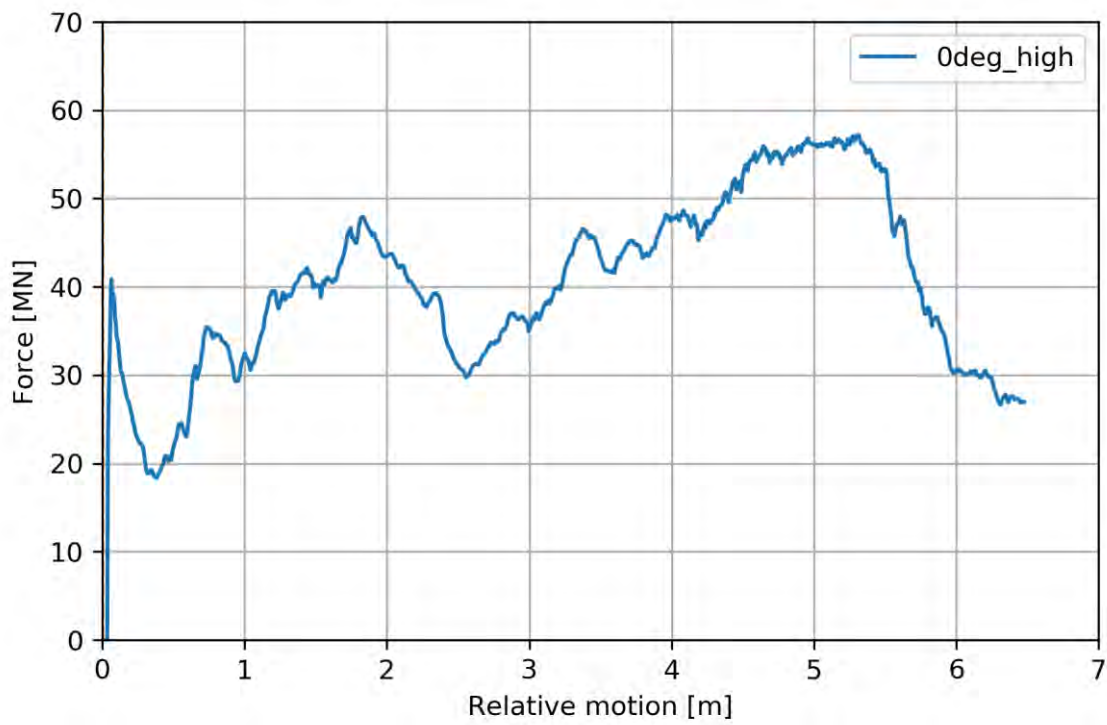


Figure 4-79 Force-displacement curve for deckhouse-bridge girder collision, 0 degree collision angle, high impact location

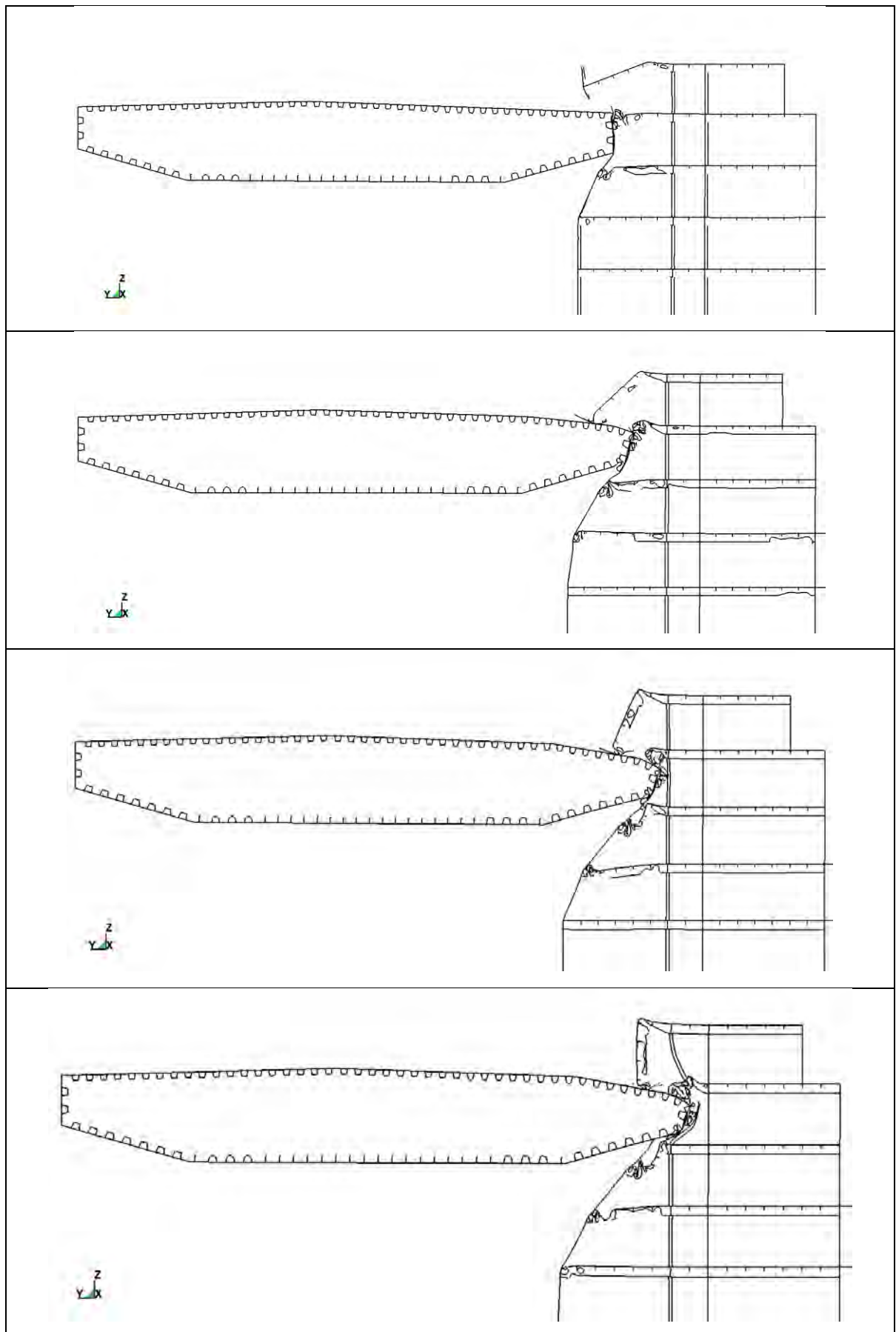


Figure 4-80 Deformation during collision. From above, 50 MJ, 100 MJ, 150 MJ and 200 MJ

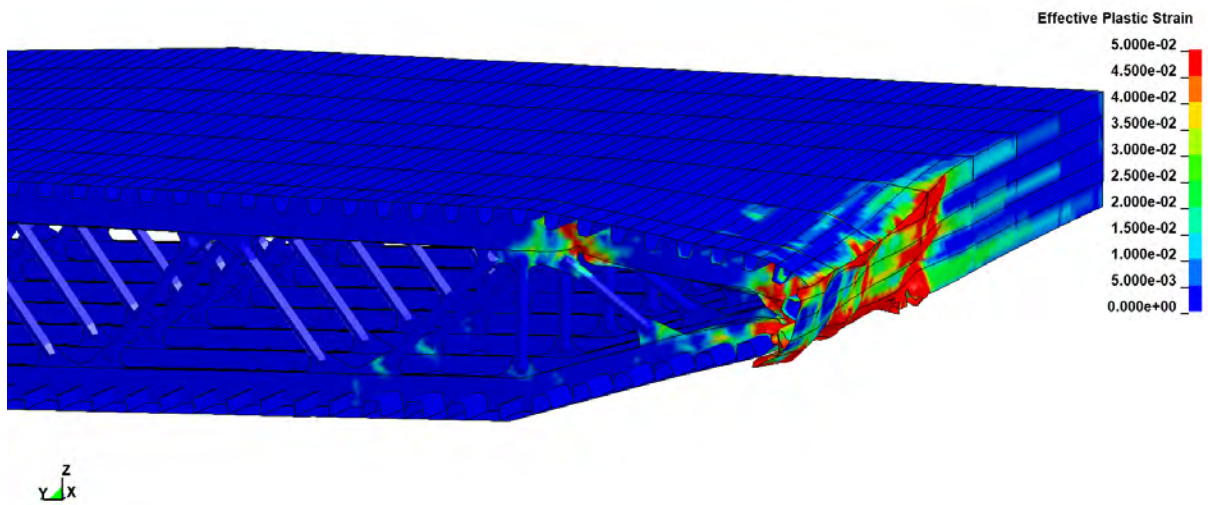


Figure 4-81 Effective plastic strains in the bridge girder after 200 MJ energy is dissipated. Only one half of the bridge girder model is shown.

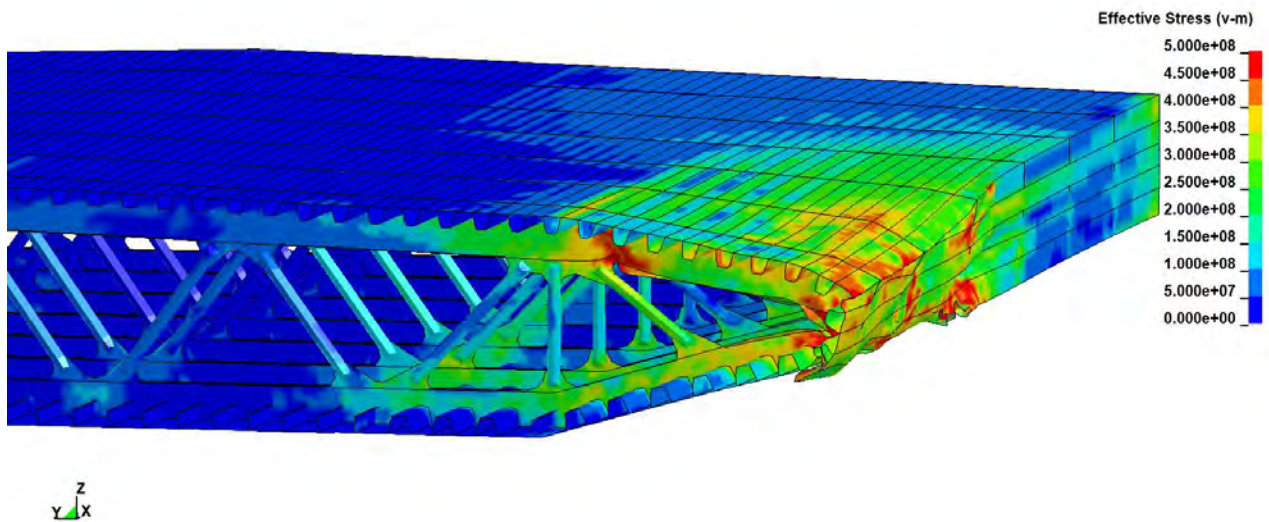


Figure 4-82 Von Mises stresses in the bridge girder after 200 MJ energy is dissipated. Only one half of the bridge girder model is shown.

4.6.2 Deckhouse collision with 0 degree angle, low impact

The following presents the results from the collision simulation between the container ship deckhouse and bridge girder for 0 degree collision angle and low impact location.

The side of the bridge girder is pushed approximately 0.6 meters inwards when 200 MJ energy is dissipated. Minor material ruptures in the side plates are observed at the periphery of the contact area, as seen in Figure 4-86 and Figure 4-87.

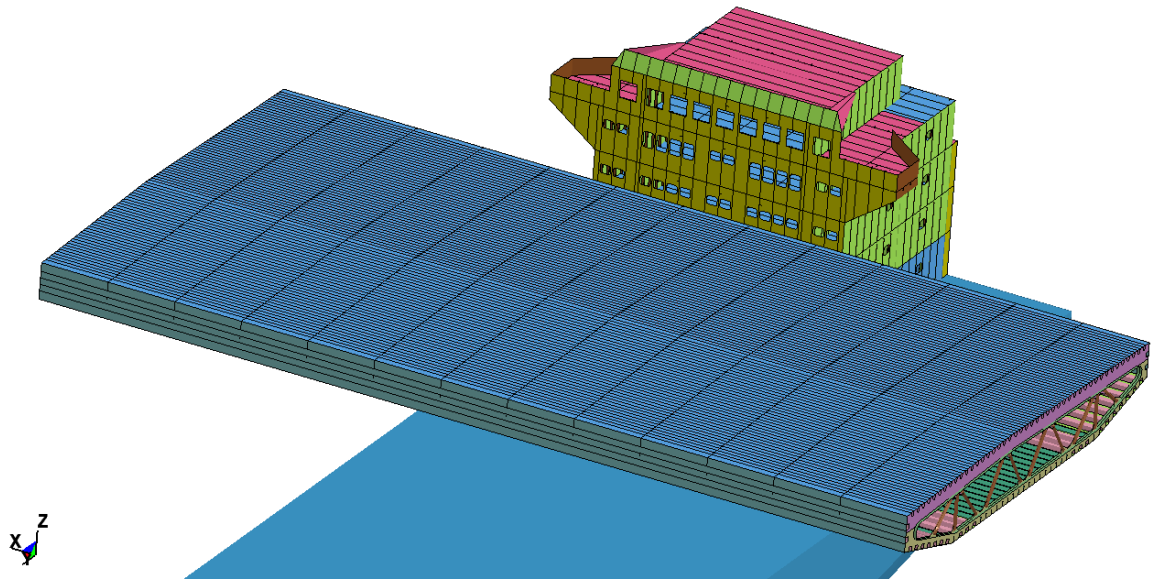


Figure 4-83 Deckhouse-bridge girder collision, 0 degree angle and high impact location

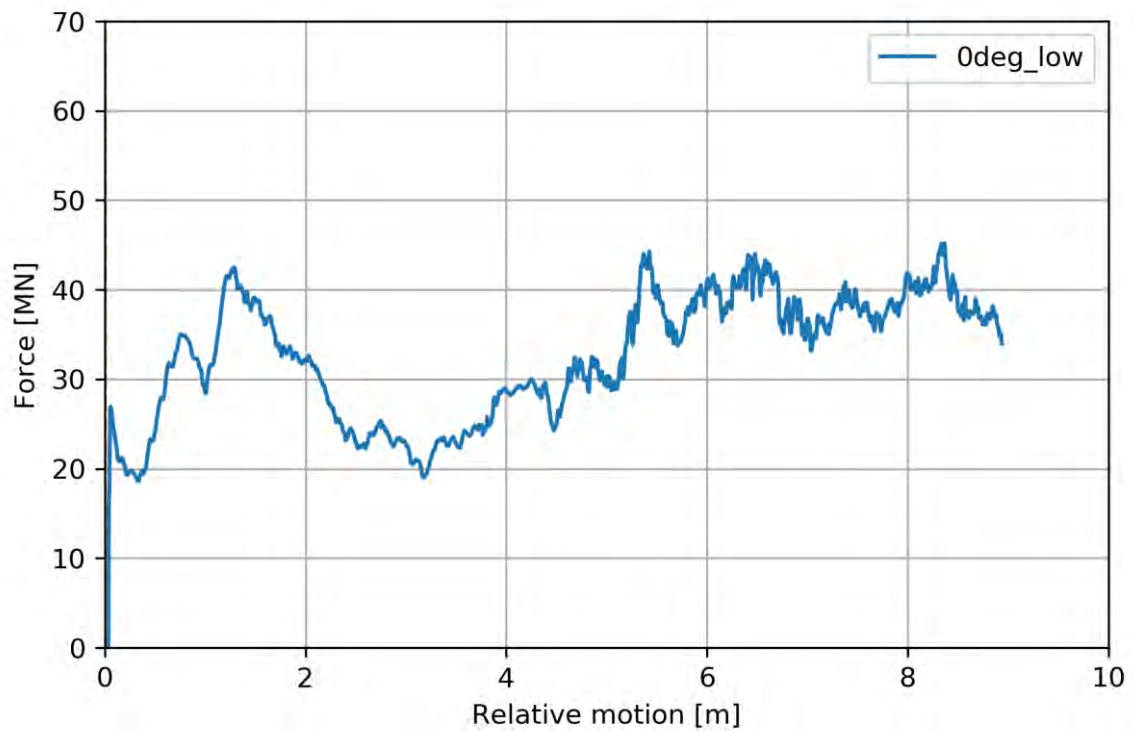


Figure 4-84 Force-displacement curve for deckhouse-bridge girder collision, 0 degree collision angle, low impact location

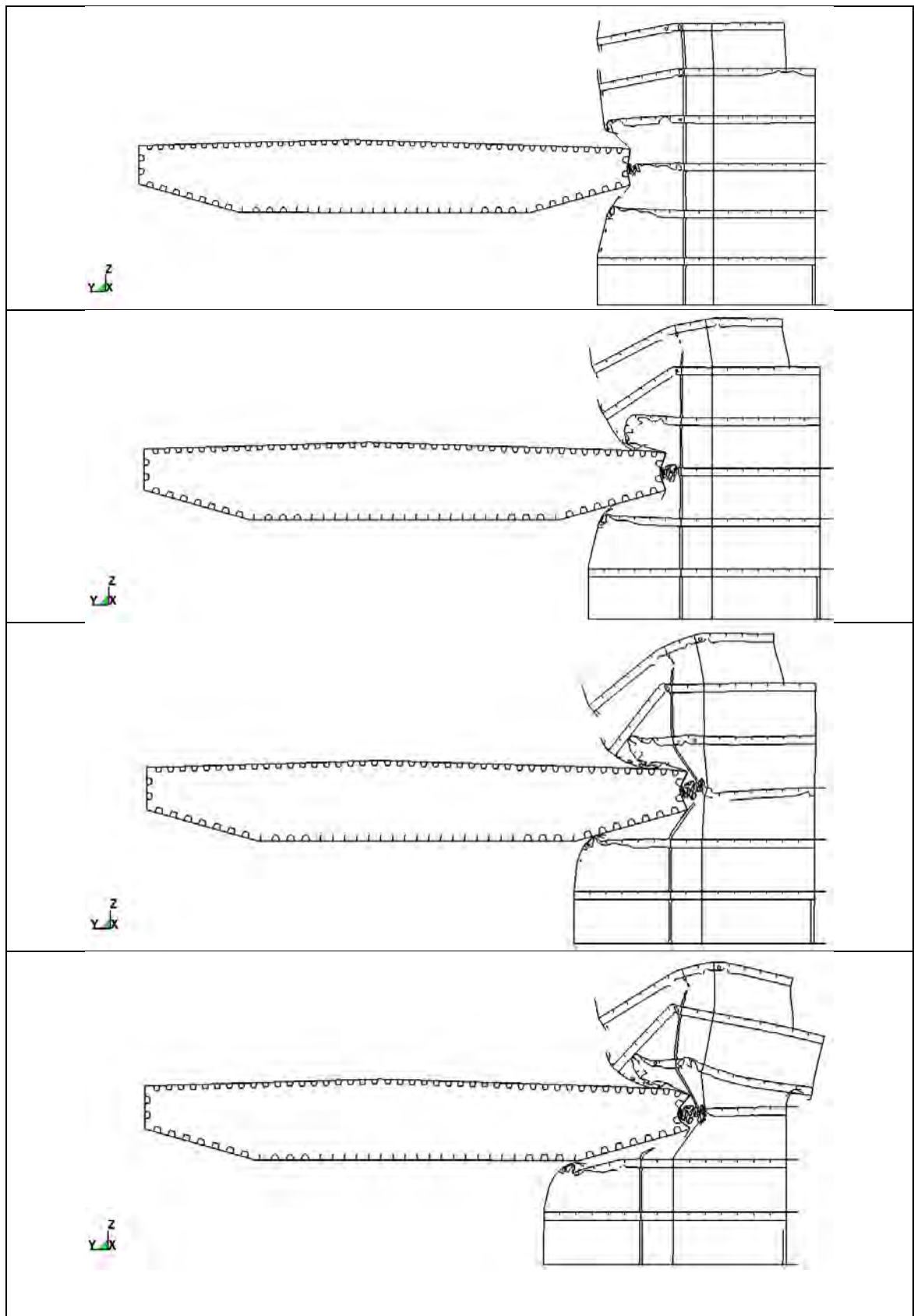


Figure 4-85 Deformation during collision. From above, 50 MJ, 100 MJ, 150 MJ and 200 MJ

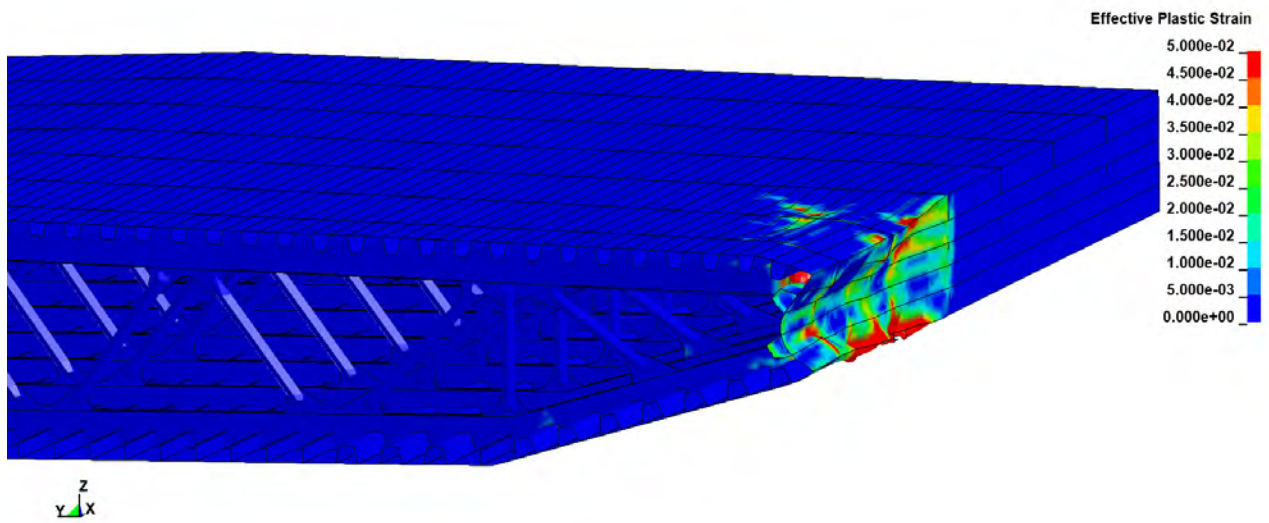


Figure 4-86 Effective plastic strain in the bridge girder after 200 MJ energy is dissipated. Only one half of the bridge girder model is shown.

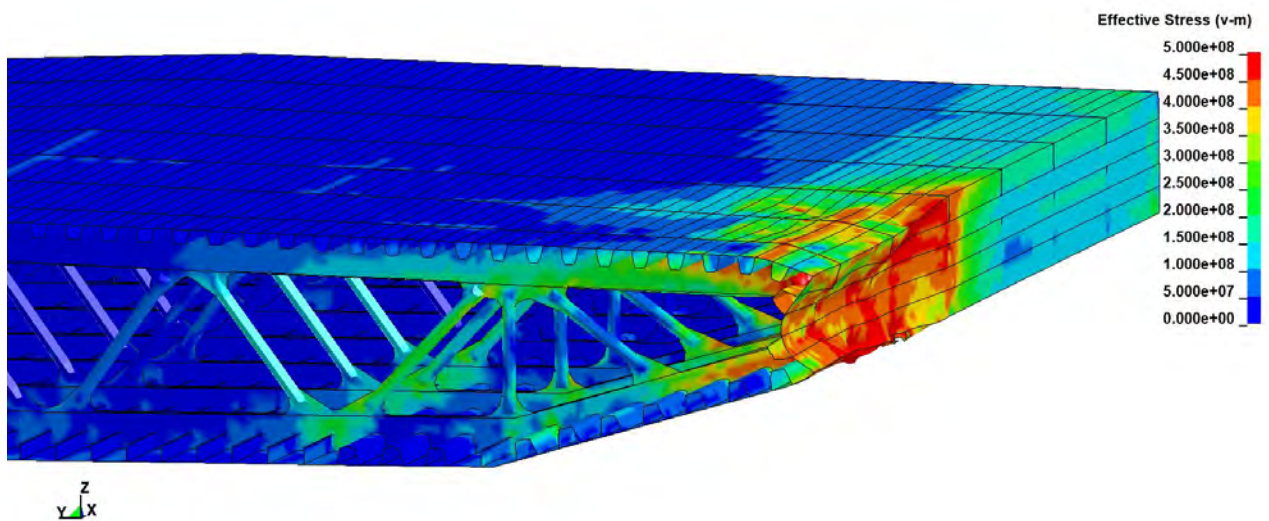


Figure 4-87 Von Mises stresses in the bridge girder after 200 MJ energy is dissipated. Only one half of the bridge girder model is shown.

4.6.3 Deckhouse collision with 10 degree angle, high impact

The following presents the results from the collision simulation between the container ship deckhouse and bridge girder for 10 degree collision angle and high impact location.

The side of the bridge girder is pushed approximately 0.15 meters inwards when 180 MJ energy is dissipated. No material failure is observed in the outer plates of the bridge girder.

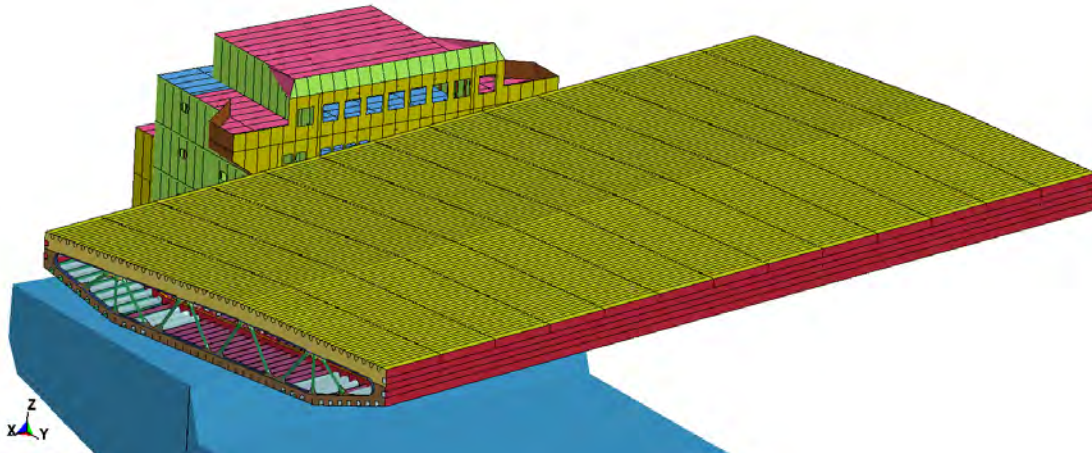


Figure 4-88 Deckhouse-bridge girder collision, 10 degree angle and high impact location

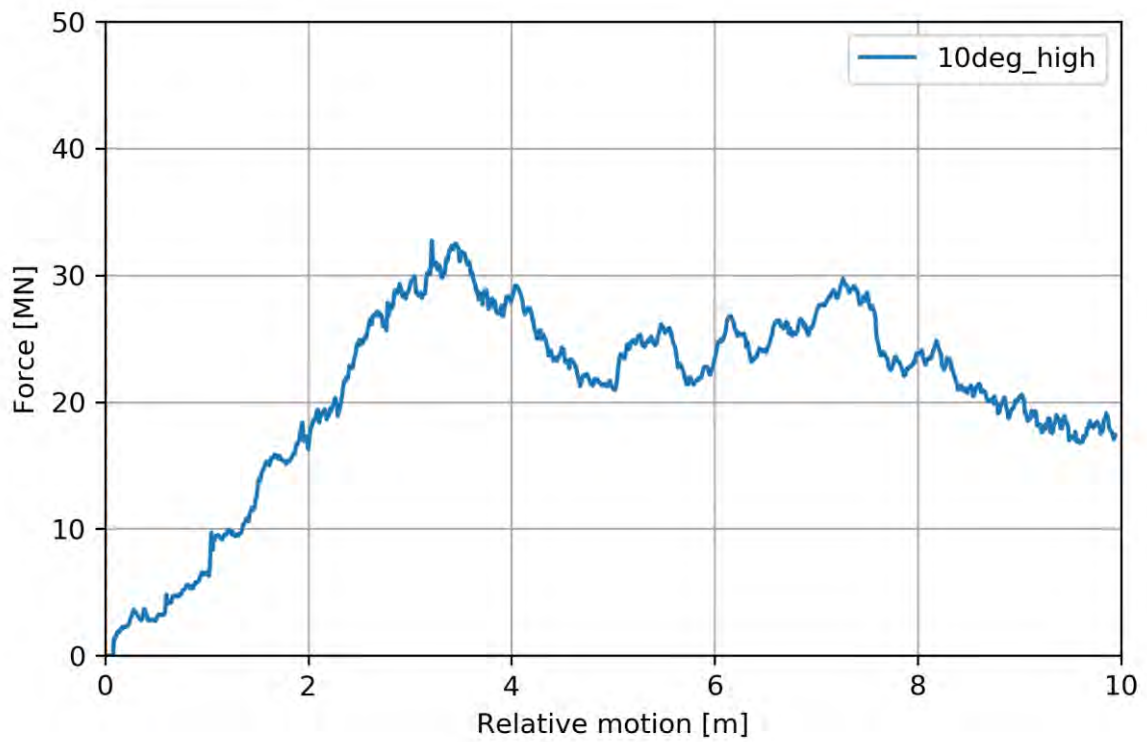


Figure 4-89 Force-displacement curve for deckhouse-bridge girder collision, 10 degree collision angle, high impact location

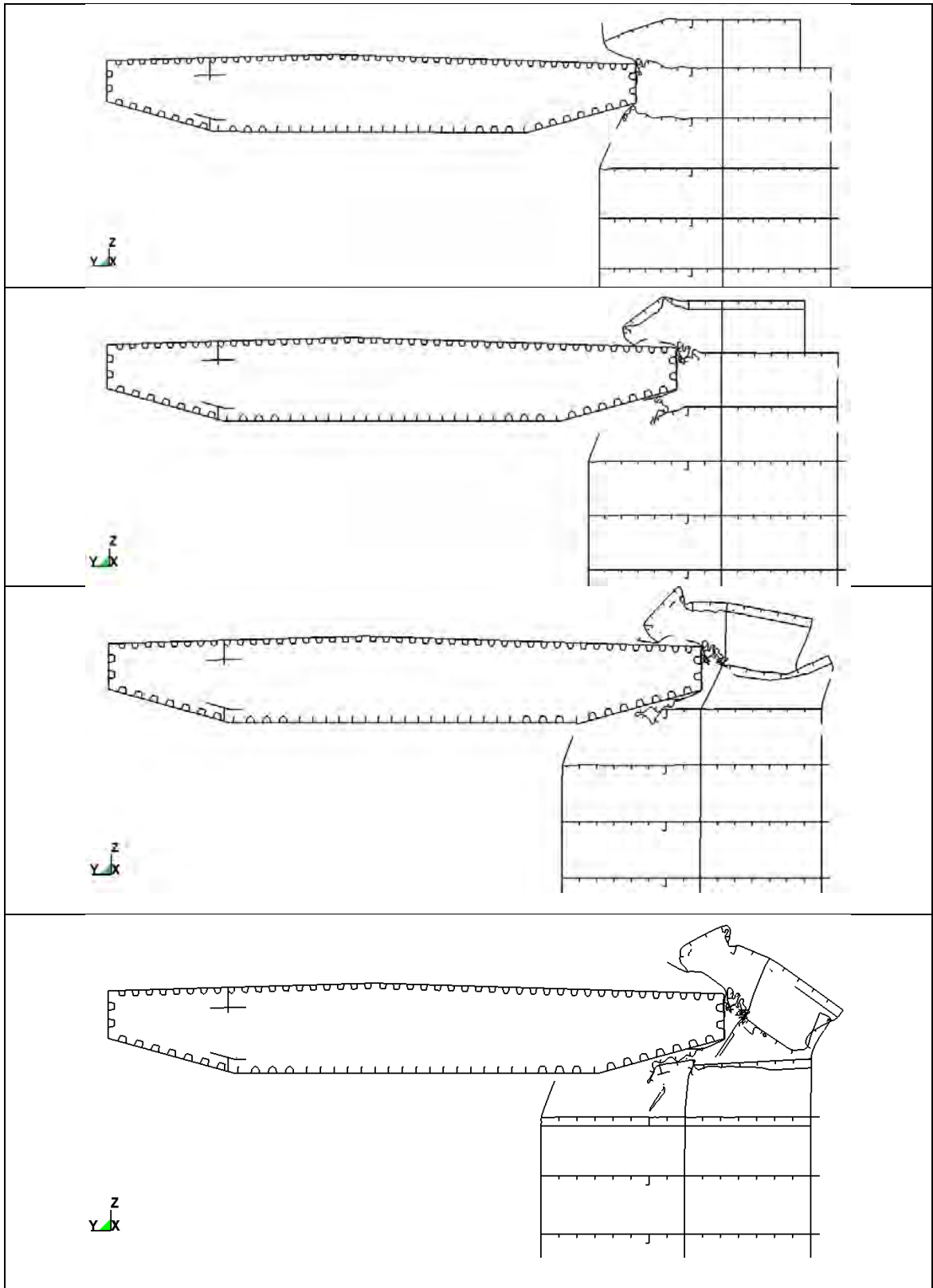


Figure 4-90 Deformation during collision. From above, 50 MJ, 100 MJ, 150 MJ and 180 MJ

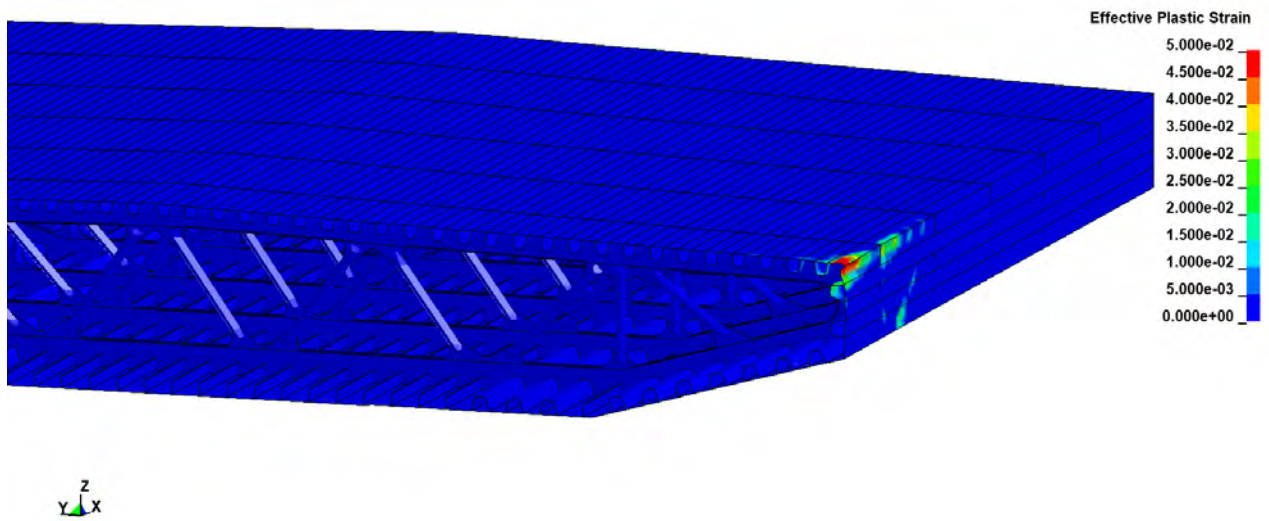


Figure 4-91 Effective plastic strain in the bridge girder after 180 MJ energy is dissipated. Only one half of the bridge girder model is shown.

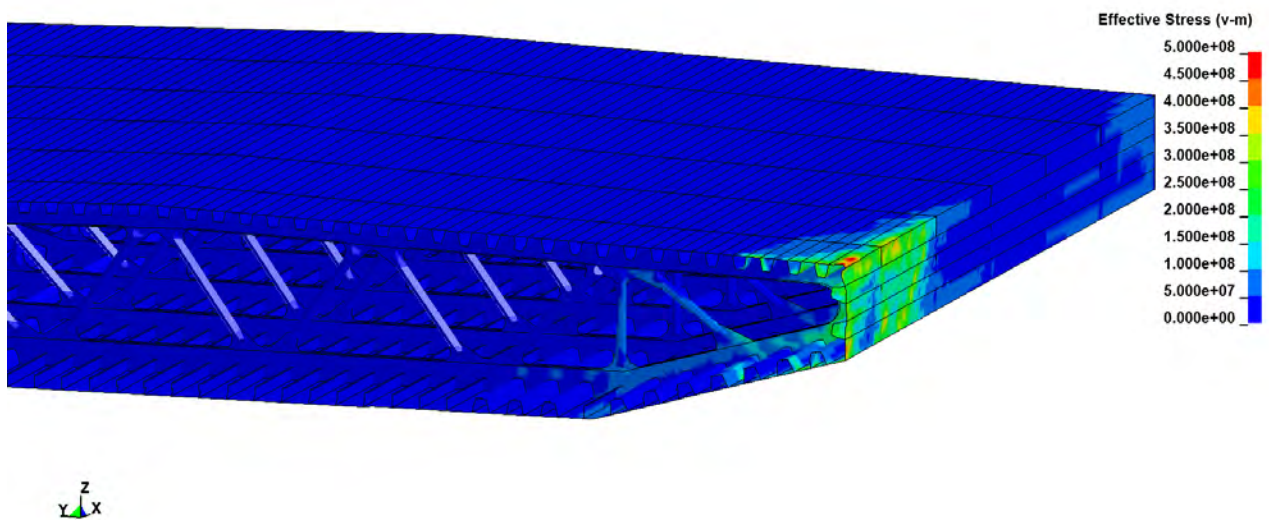


Figure 4-92 Von Mises stresses in the bridge girder after 180 MJ energy is dissipated. Only one half of the bridge girder model is shown.

4.6.4 Deckhouse collision with 10 degree angle, low impact

The following presents the results from the collision simulation between the container ship deckhouse and bridge girder for 10 degree collision angle and low impact location.

The side of the bridge girder is pushed approximately 0.4 meters inwards when 200 MJ energy is dissipated. A minor rupture in the side plate is observed at one location where at the outer plate meets a transverse frame.

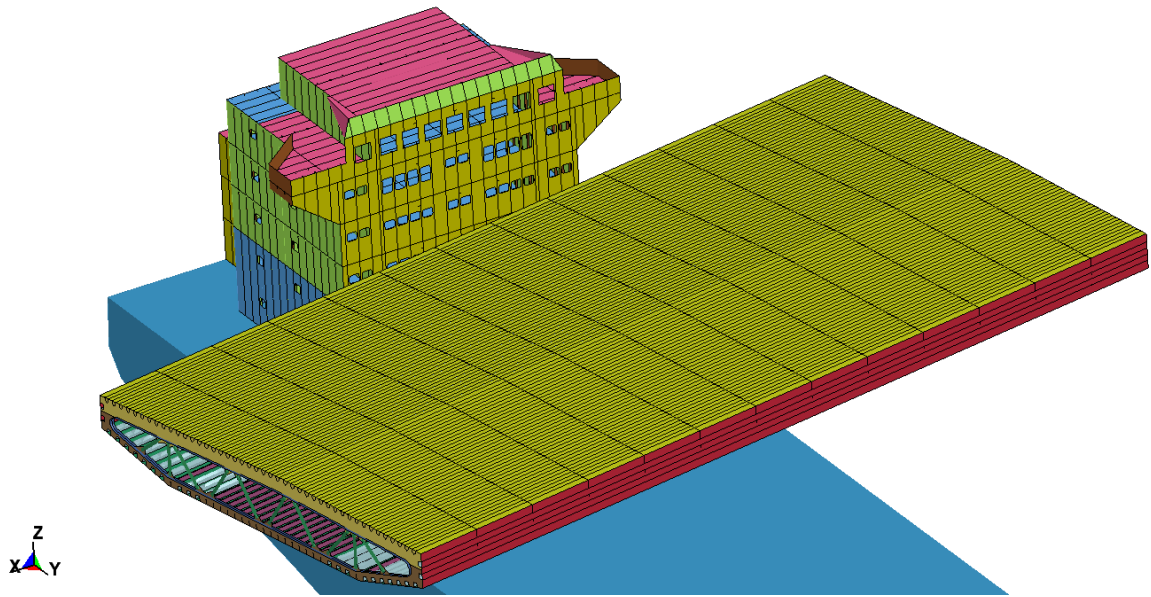


Figure 4-93 Deckhouse-bridge girder collision, 10 degree angle and low impact location

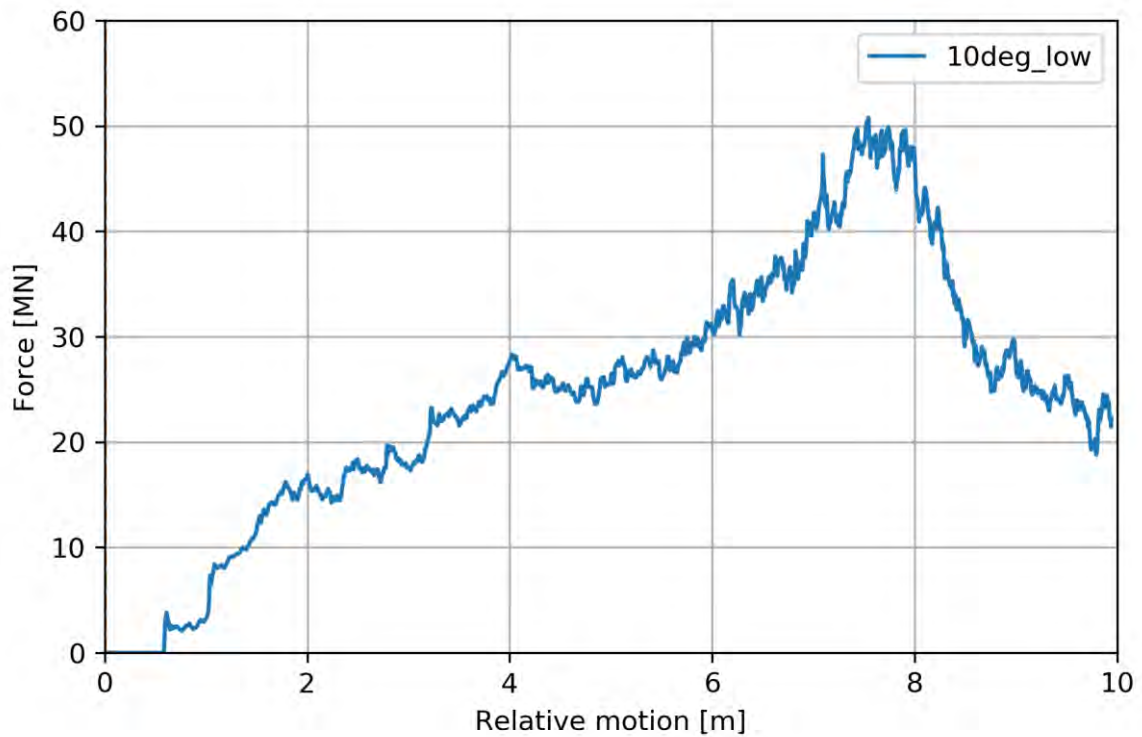


Figure 4-94 Force-displacement curve for deckhouse-bridge girder collision, 10 degree collision angle, low impact location

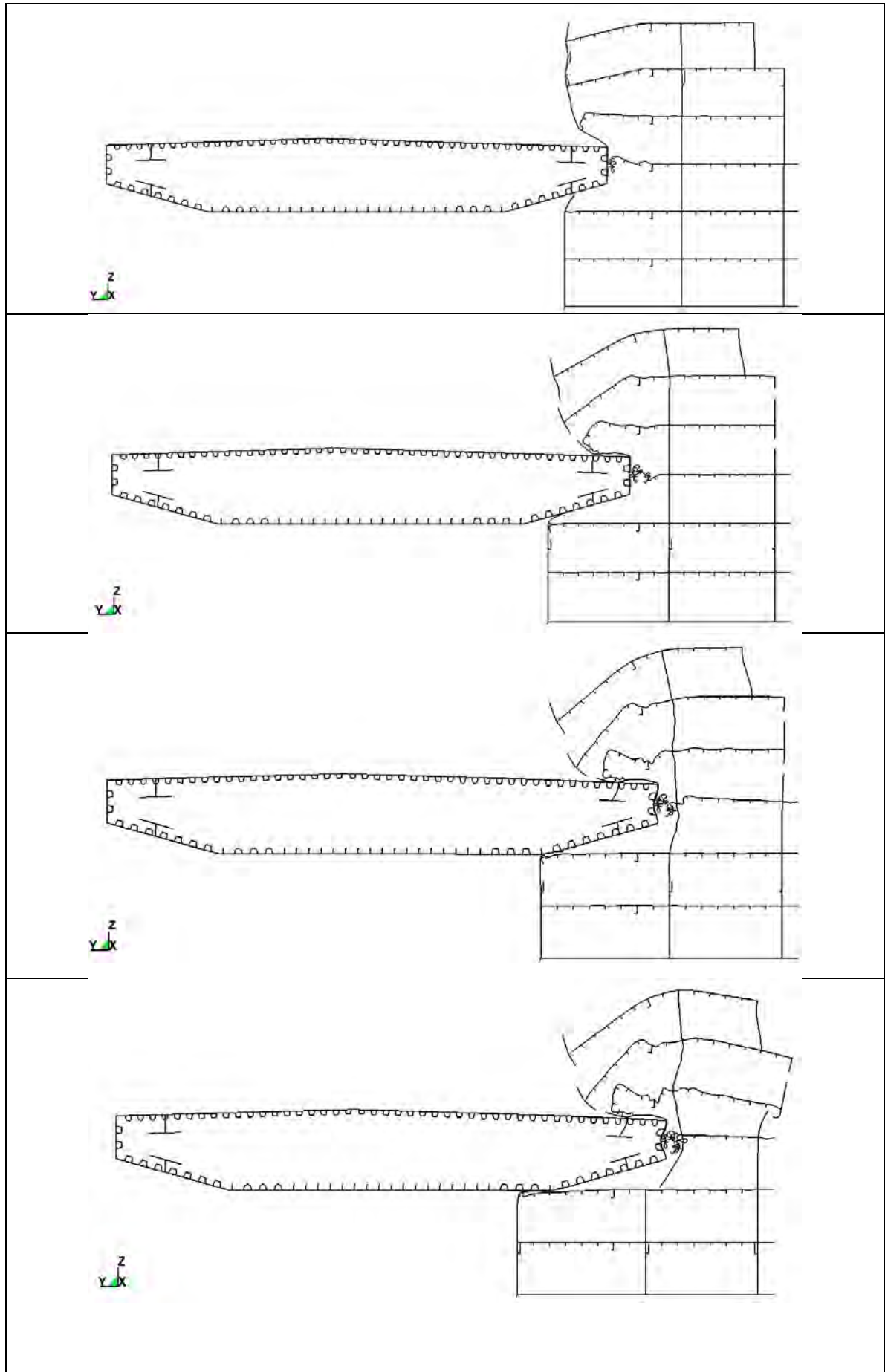


Figure 4-95 Deformation during collision. From above, 50 MJ, 100 MJ, 150 MJ and 200 MJ

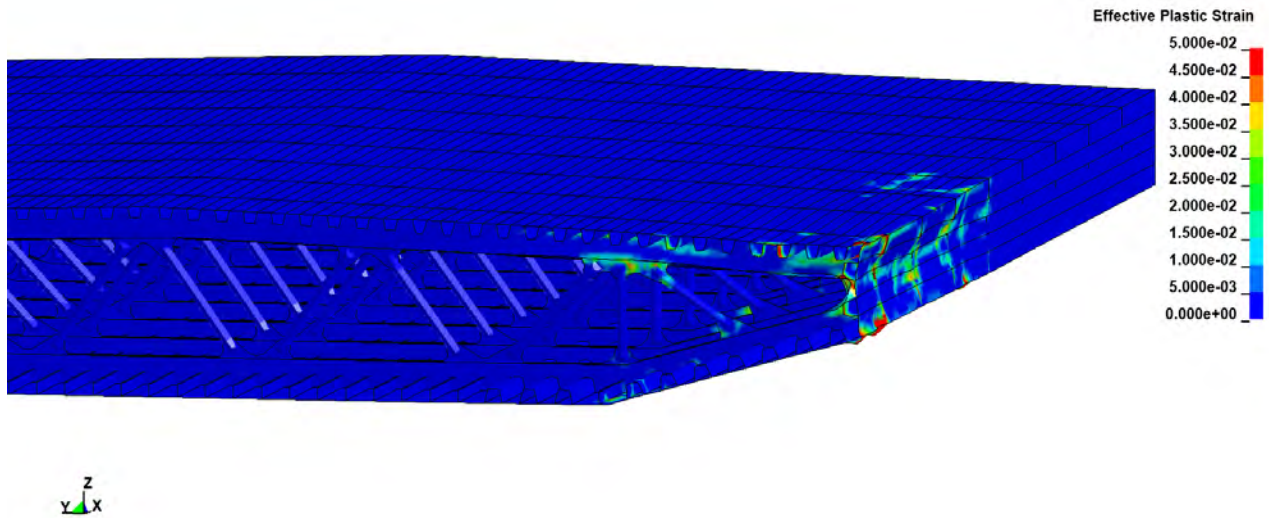


Figure 4-96 Effective plastic strain in the bridge girder after 200 MJ energy is dissipated. Only one half of the bridge girder model is shown.

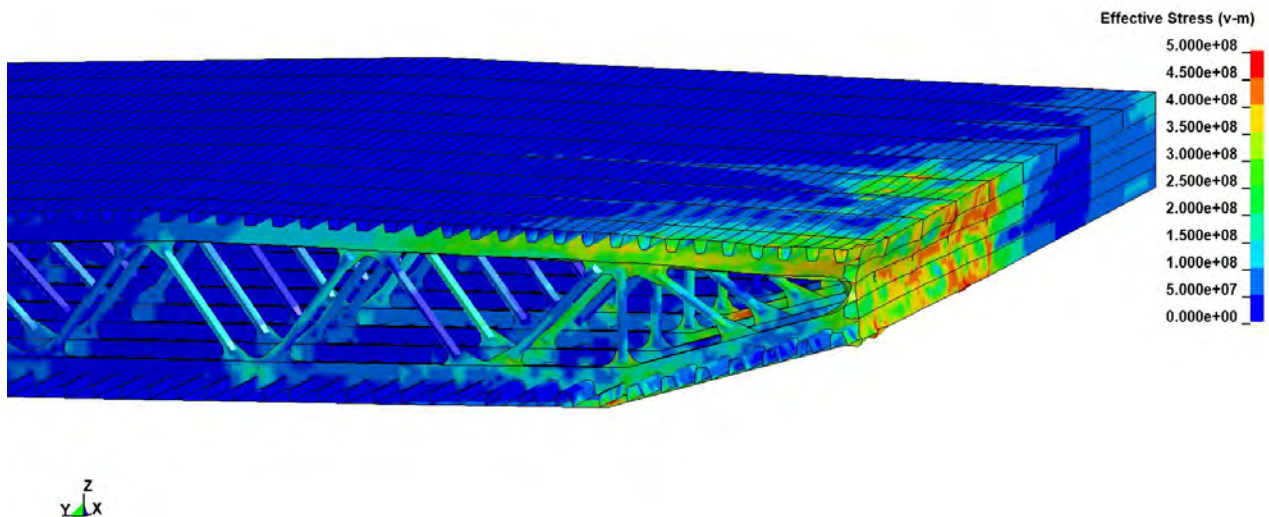


Figure 4-97 Von Mises stresses in the bridge girder after 200 MJ energy is dissipated. Only one half of the bridge girder model is shown.

4.6.5 Rigid crane pedestal collision

The results from the rigid crane pedestal-bridge girder collision are presented in the following. The force displacement curve in Figure 4-99 shows a relatively high contact force, leveling at around 35 MN. The corresponding damage in Figure 4-98 shows that the deformation is local and limited to tearing and folding in between the bridge girders transverse frames. The energy dissipation (Figure 4-100) is rather large, and a collision event involving energies in the range given in Table 2-1 will not be able to shear of the entire bridge girder even if the crane pedestal is rigid. This would allow for safe evacuation, but the bridge may not be able to sustain a 100-year environmental condition with such levels of damage.

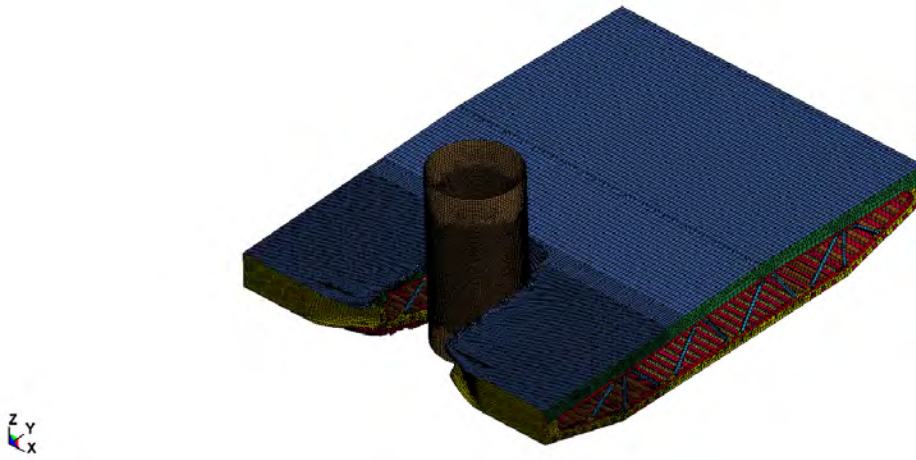


Figure 4-98 Deformation plot of rigid cylinder vs bridge girder collision at end of simulation.

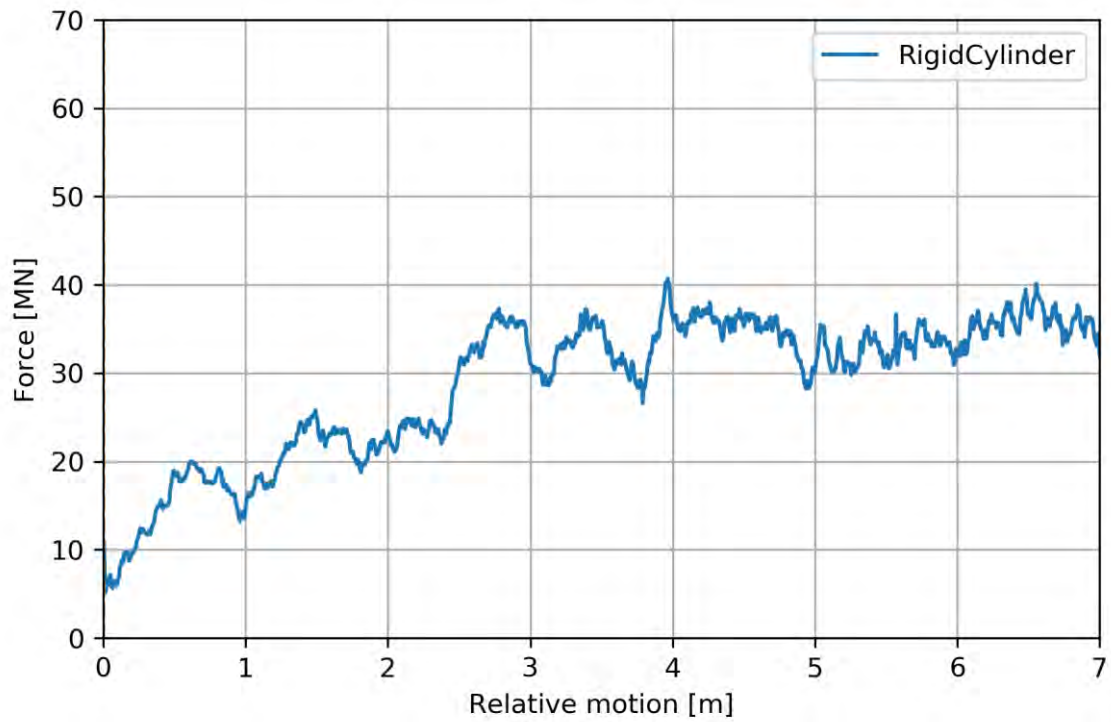


Figure 4-99 Force-displacement curve for rigid cylinder-displacement collision

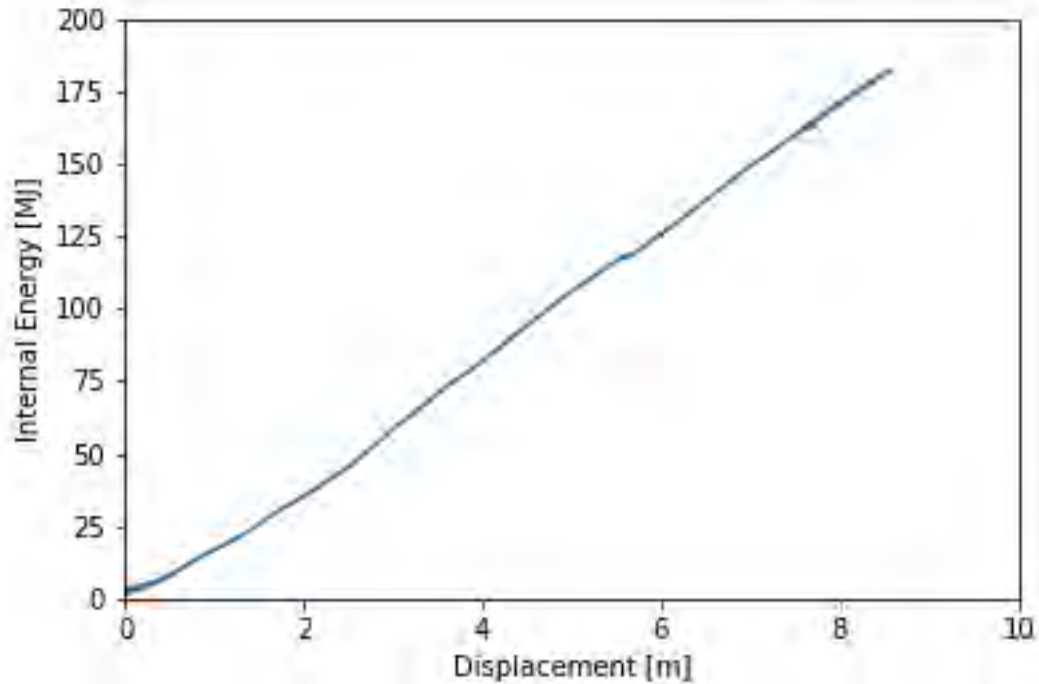


Figure 4-100 Energy-displacement curve for rigid cylinder-displacement collision

The validity of the assumption of a rigid crane pedestal can be checked by taking the maximum force from Figure 4-99 and calculating the required thickness in an event with no denting of the cylinder (from Equation 3.6 in [22]). R_c is the capacity taken as the maximum force from Figure 4-99.

$$R_c = f_y \cdot \frac{t^2}{4} \cdot \sqrt{\frac{D}{t}}$$

Solving the equation for t gives

$$t = \sqrt[3]{\frac{16R_c^2}{f_y^2 D}}$$

Assuming:

Yield stress, f_y	355MPa
D	5m
R_c	40MN

Gives a thickness equal to

$$t = \sqrt[3]{\frac{16R_c^2}{f_y^2 D}} = \sqrt[3]{\frac{16 \cdot (40MN)^2}{(355MPa)^2 \cdot 5m}} \cong 344mm$$

The crane pedestal must have an unrealistically high plate thickness, and it can be concluded that a typical crane pedestal will fail plastically and thereby give a significantly lower deformation compared to that shown in Figure 4-99.

If the impact to the bridge girder were from a high bow structure the increasing width of the bow as the indentation increases will yield a significant increase in dissipated energy. Hence, the damage from a bow striking directly to the bridge girder would be less than that from a rigid crane pedestal.

4.7 Discussion

4.7.1 Ship bows vs pontoon

The simulated ship collisions result in severe damage to the pontoon. The maximum compartment damage is from a cruise ship collision with a 30 degree angle. Here, four compartments are punctured at 78 MJ. With a 105 MJ of energy dissipation the indentation into the pontoon is 8.5 m.

The maximum collision force occurs for the head on collision in the centreline of the pontoon. The maximum collision force is approximately 50-55 MN, but this will increase for larger collision events as the forecastle structure of the striking vessel increases its contact area with the bridge.

The work performed on local pontoon response for this phase of the project gives a good basis for further design development of both the bridge and the pontoon. A few points are suggested for further study during detailed design:

- Evaluate new compartment layout in FE-model (should be more robust than the current model)
- Mesh a larger extent of the pontoon with fine mesh to simulate collisions with an even higher energy dissipation
- Perform collisions on the side of the pontoon for the maximum possible impact direction (60-80 deg)
- Perform a collision where the column will participate in the collision, both for local contact with the forecastle structure and for the sectional load resistance as a connection between the pontoon and the bridge girder.
- Perform more coupled global/local simulations in order to avoid the limitations of the internal/external mechanics split that strictly is not valid for the considered impact scenarios.

4.7.2 Ship vs bridge girder

The results from the collisions between the deckhouse and bridge girder yields a large contact force due to the vertical structural side walls of the bridge girder. The bridge girder has larger resistance than the deckhouse for most of the simulated impact, but with large energies the deckhouse will eventually cause some local buckling and fracture of the bridge girder. The interaction between the ship and the bridge girder varies somewhat depending on the impact location on the deck house. No large damage to the bridge girder is expected, and the post-impact strength is thus not largely

affected. Global simulations (ref. [1]) indicated that the global bridge response is not sensitive to minor strength reductions in the bridge girder.

Simulations of smaller objects impacting the bridge girder (outside of the design basis) show that the resistance is large and causes both high contact forces and energy dissipation. Hence, the local strength of the striking object will strongly influence the energy dissipation in a shared energy regime, and the bridge can safely be evacuated after a collision event. More work is needed in order to evaluate a realistic scenario and the post-damage resistance of the bridge.

5 Global response evaluations

The following section shows key results for selected components of the bridge concepts. A more complete listing of the individual response types for the different structural components can be found in Enclosure 1-4 to this report.

5.1 Selected scenarios

To get a reasonable amount of simulations the scenarios for pontoon collisions were selected as the first and last three pontoons as well as pontoons in A10, A20 and A30. For each of these, impacts at 0, 45 and 80 degrees were simulated. 0 degrees is defined transverse to the bridge, with central impact along the pontoon. 45 and 80 degrees were simulated relative to this direction, with impact on the pontoon tip. This is a conservative assumption as the torsional moment in the columns will be overestimated compared to a more realistic impact location closer to the bridge girder.

For deckhouse collisions impacts are defined mid-way between pontoons at selected locations, starting between A7-A8 and ending between the two northernmost pontoons. 0 and 180 degrees impact angle normal to the bridge girder was used (from East and West), with the force-indentation curves as in section 4.6. Note that the collision force level drops rapidly if the impact does not occur perpendicular to the bridge girder. However, it was found in [23] that the global bridge girder response was similar for 0 and 10 degrees impact, and the latter was thus not assessed further herein.

Impact scenarios in this section are simulated from the West (termed 180 deg) and East (termed 0 deg). Pontoon impacts also include oblique impacts at 45 and 80 degrees to the transverse bridge axis. Impacts to the pontoon with more than 80 degrees from the transverse axis were not considered feasible due to the proximity to neighboring pontoons.

5.2 Energy balance

The energy balance for a scenario with impact to pontoon A20 are shown in [Figure 5-1](#). A significant part of the available kinetic energy is quickly dissipated by plastic deformation in the local collision zone (in pontoon and vessel), while the bridge is equally excited for kinetic and internal (elastic) energy. After the initial phase the bridge energy is gradually dissipated by viscous damping; some in the pontoons but mostly by the mooring lines.

The individual energy contributors are termed as follows:

- Kinetic ship : Instantaneous kinetic energy of the ship during the collision (starting as the available kinetic energy for collision).
- Kinetic bridge : Instantaneous kinetic energy in the bridge (all structural components except for mooring lines)
- Internal bridge : Instantaneous stored elastic energy in the bridge (all structural components except for mooring lines)
- Local collision : Energy dissipated by plastic deformation in the local deformation in the collision zone (i.e., area under the nonlinear collision spring force-displacement curve).
- Viscous damping : Energy dissipated by viscous drag on the pontoons
- Mooring damping : Energy dissipated by viscous drag on mooring lines
- Mooring stiffness : Instantaneous stored elastic energy in the mooring lines

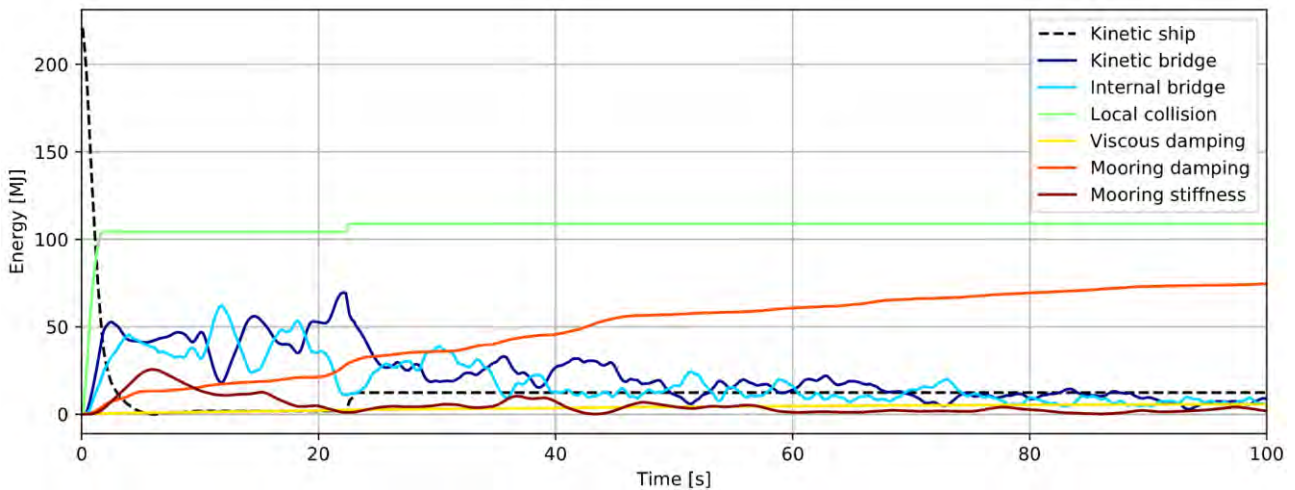


Figure 5-1 Energy balance for K12-05, impact on pontoon A20 0deg.

Table 5-1 shows key aspects of the energy balance in the collisions. Note that the values are not occurring simultaneously. Some observations to be made:

- The bridge is stiffness-dominated when struck towards either end (see Figure 5-8), whereas it is inertia-dominated when struck in the central portions. Local plastic damage will be worse for the stiffness-dominated global response.
- The bridge is compliant in the transverse direction, and pontoon impacts will yield increasing local deformation for increasing deviation in impact direction from the transverse direction. Up to 208 MJ is to be dissipated locally for the worst conditions, indicating significant damage to both pontoon and vessel. No big differences in the response is observed between the concepts.
- Deckhouse collisions give significant elastic and plastic energy dissipation. Global elastic deformation is largest for K11 due to the lack of mooring. Local plastic deformational energy is not significantly different for the four concepts.
- Mooring contributes significantly to energy dissipation compared to viscous drag on the pontoon. The elastic energy stored in the bridge drops by 30% for deckhouse collisions for K12-06 compared to K11-07. This does however not affect peak responses significantly, as the northern and southern end of the bridge are stiffness-dominated. Some effect is seen as a reduction of average response in the low bridge, see section 5.3.

Table 5-1 Summary of energy dissipation components.

			Pontoon	Deck house
Kinetic energy	Ship	Max	260	447
		End	24	323
	Bridge	Max	89	184
		End	25	34
Internal energy	Global	Max	120	182
		End	25	49
	Local	End	202	166
Damping energy	Pontoon	End	10	20
	Mooring	End	99	180

5.3 Bridge girder response

The following shows envelopes of all the global response variables of the bridge girder. Detailed results in which each simulated scenario is plotted can be found in the Enclosures to this report. Deckhouse collisions are governing for the bridge girder except for small areas in the transition between the high- and low-bridge.

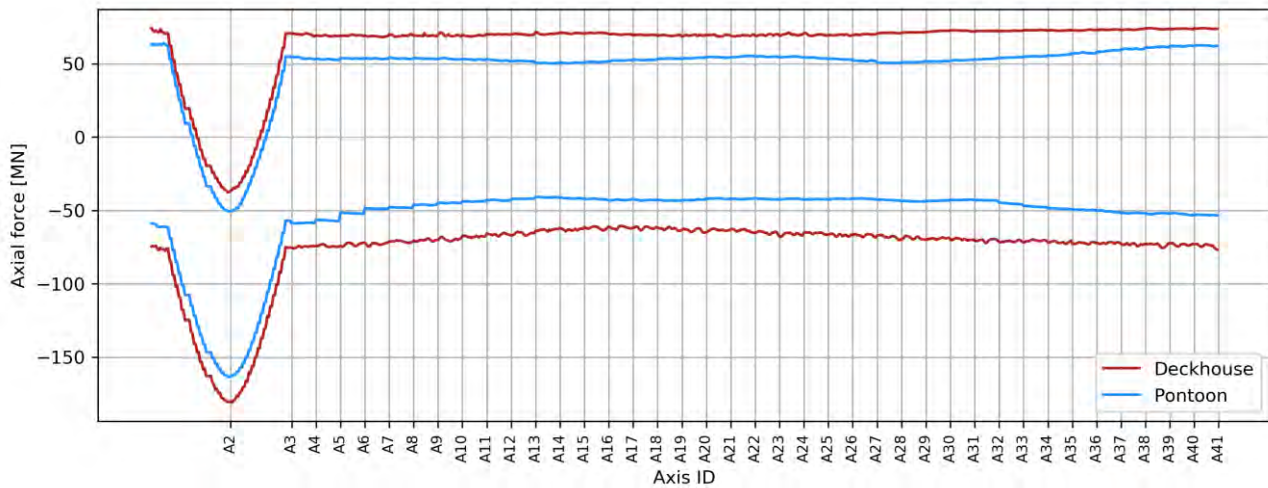


Figure 5-2 Axial force envelopes for the bridge girder.

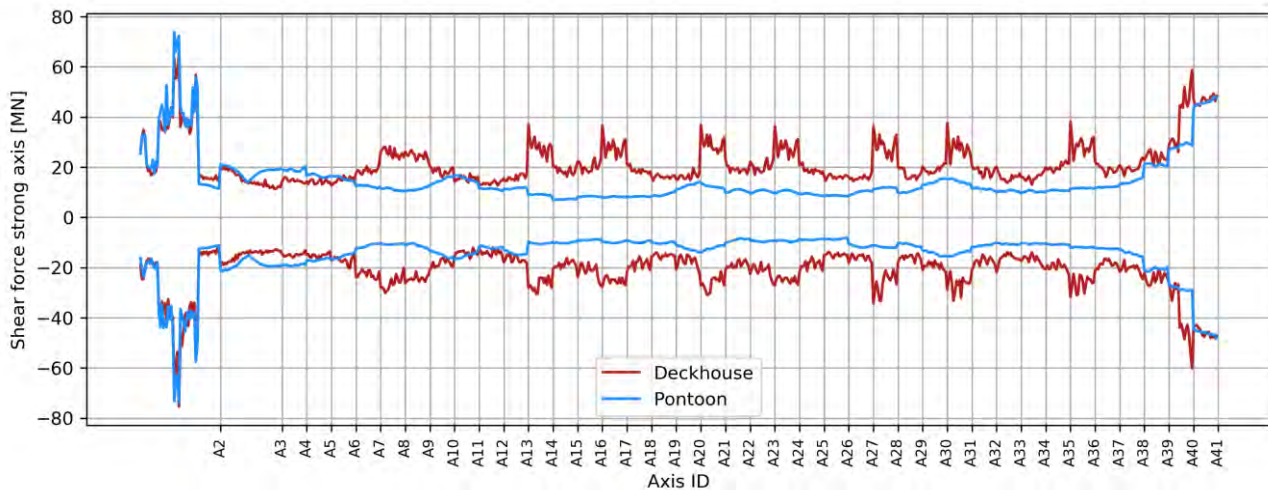


Figure 5-3 Strong-axis shear force envelopes for the bridge girder.

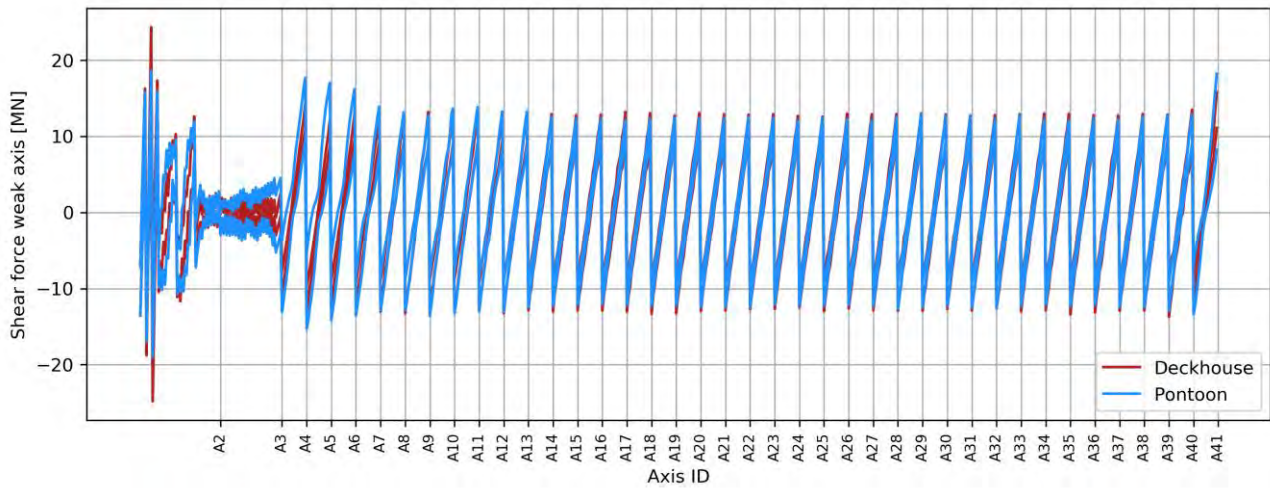


Figure 5-4 Weak-axis shear force envelopes for the bridge girder.

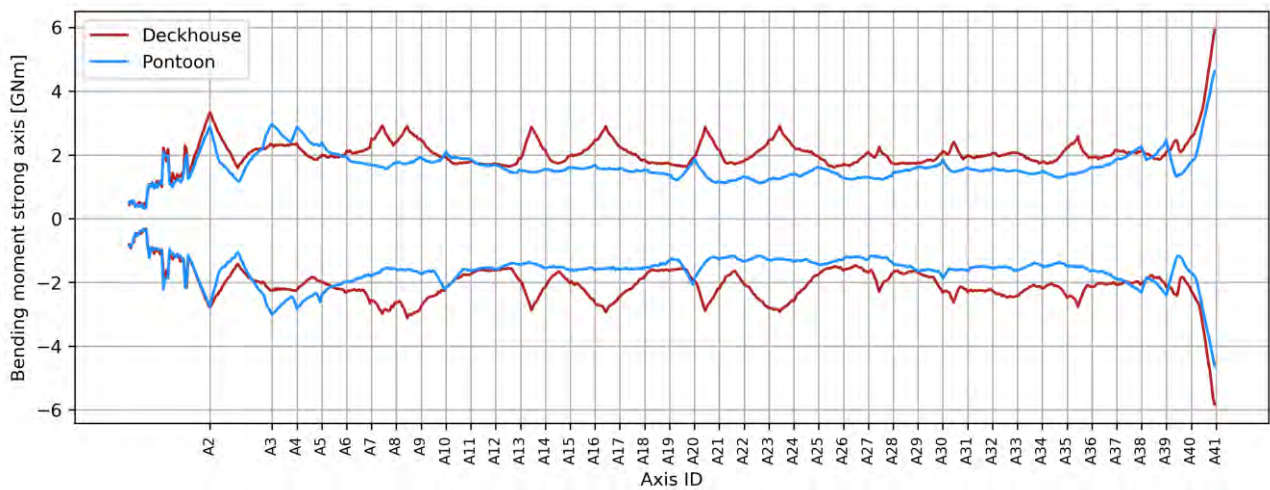


Figure 5-5 Strong-axis bending moment envelopes for the bridge girder.

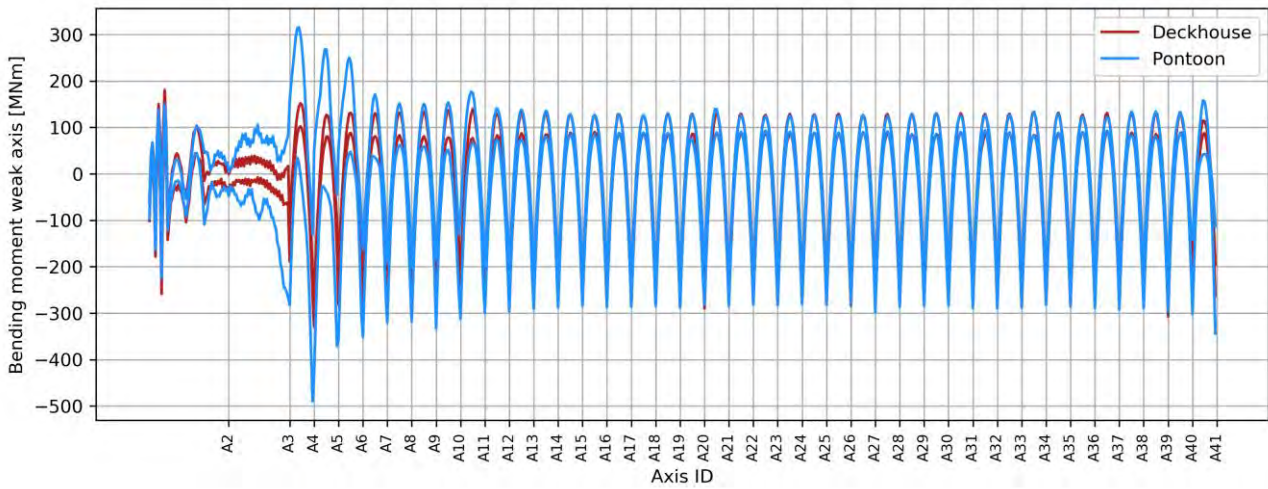


Figure 5-6 Weak-axis bending moment envelopes for the bridge girder.

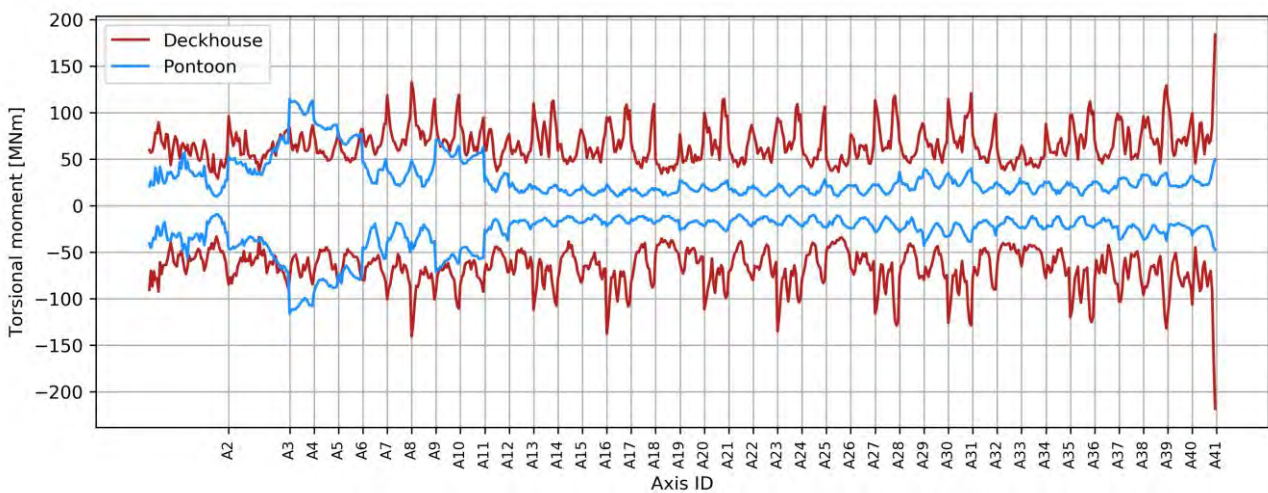


Figure 5-7 Torsional moment envelopes for the bridge girder.

Figure 5-8 shows the strong-axis bending moment for deckhouse collision close to the Northern abutment at various time steps. The stiffness-dominated behavior is clear with very high loads at the initial time steps in which the collision force is highest.

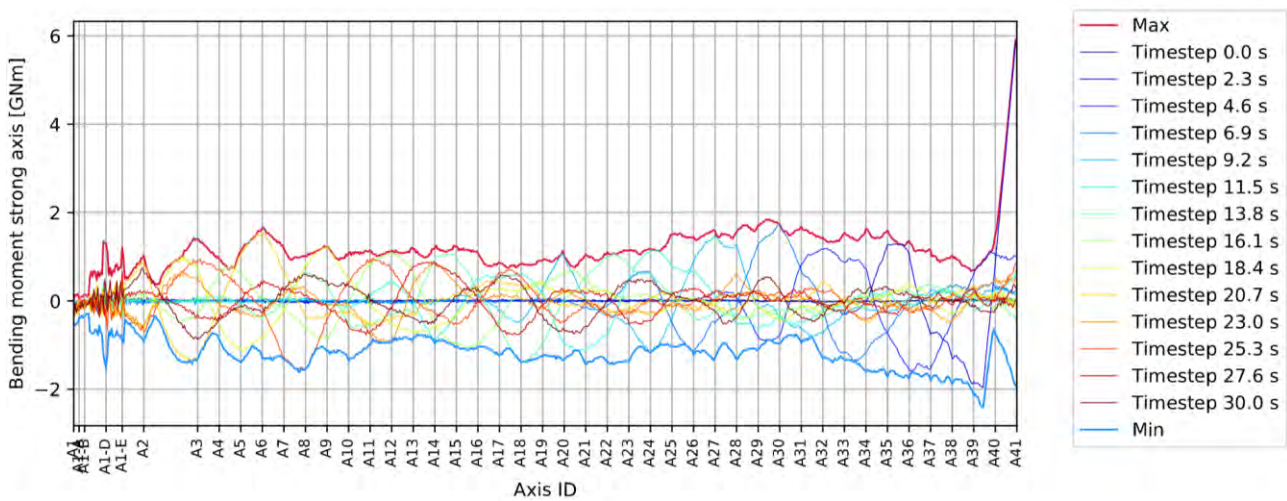


Figure 5-8 Detailed plot of strong-axis moment for deckhouse impact between A39 and A40, 0 deg, with envelopes and at specific time steps.

The resulting von mises stresses in the bridge girder are shown in Figure 5-9, calculated using the same stress evaluation points as those used in Appendix G [1]. Figure 5-10 to Figure 5-12 shows stress results for a few selected impact scenarios. The bridge response is within the elastic range for most parts, but plastic utilization is shown for the following locations:

- Locally around the impact zone, in which plastic deformations occur in many structural components. Local simulations in section 4 shows that these responses are acceptable.
- Towards the Northern abutment, before reaching the reinforced cross-sections. Mitigating measures may be to evaluate the local effect of the plastic utilization (believed to yield acceptable results) and to optimize the reinforcements towards the Northern abutment, with somewhat increased strength over a larger span.
- Above the first pontoons for impacts to pontoon A3, primarily governed by strong-axis moment.

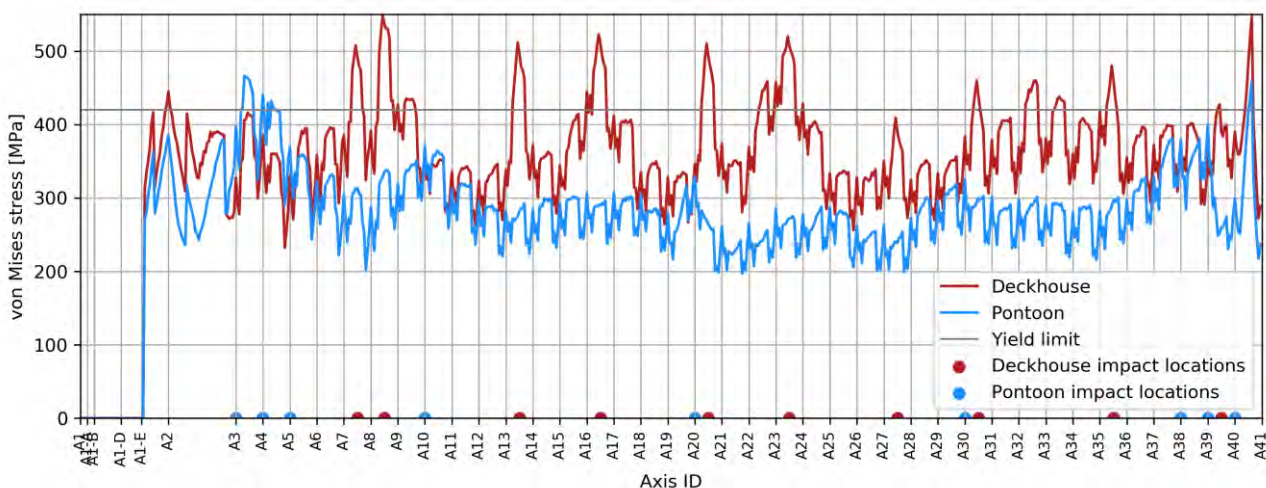


Figure 5-9 Envelopes of von Mises stress for the K12_06 bridge. Lines represent stresses, dots show the simulated impact locations.

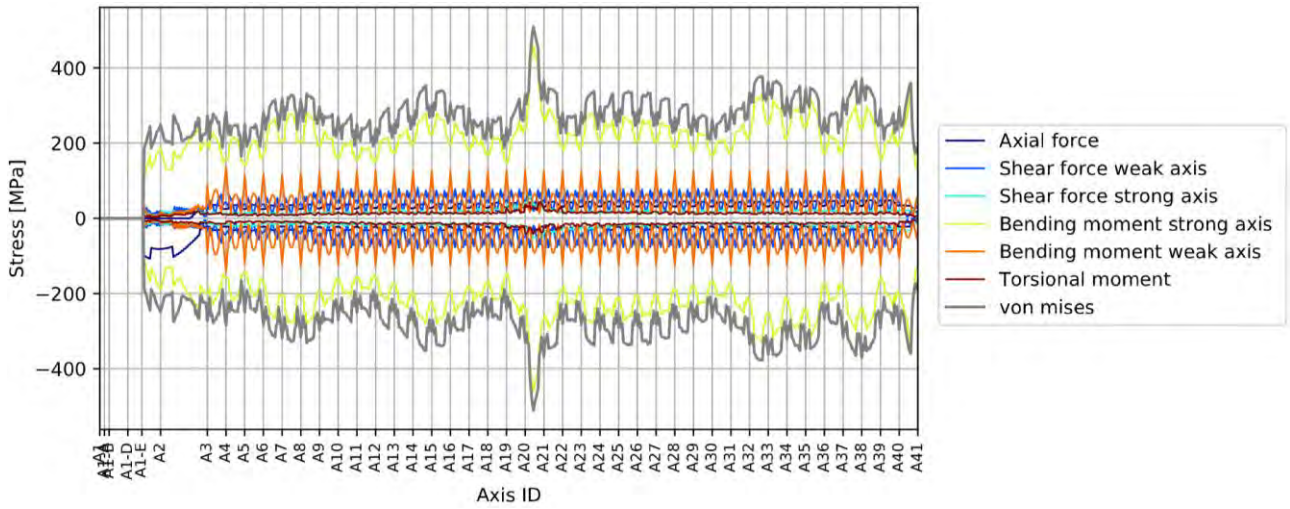


Figure 5-10 Envelopes of von Mises stress for the K12_06 bridge with contribution from the various sectional load components, deckhouse impact between pontoons A20 and A21, 0 deg.

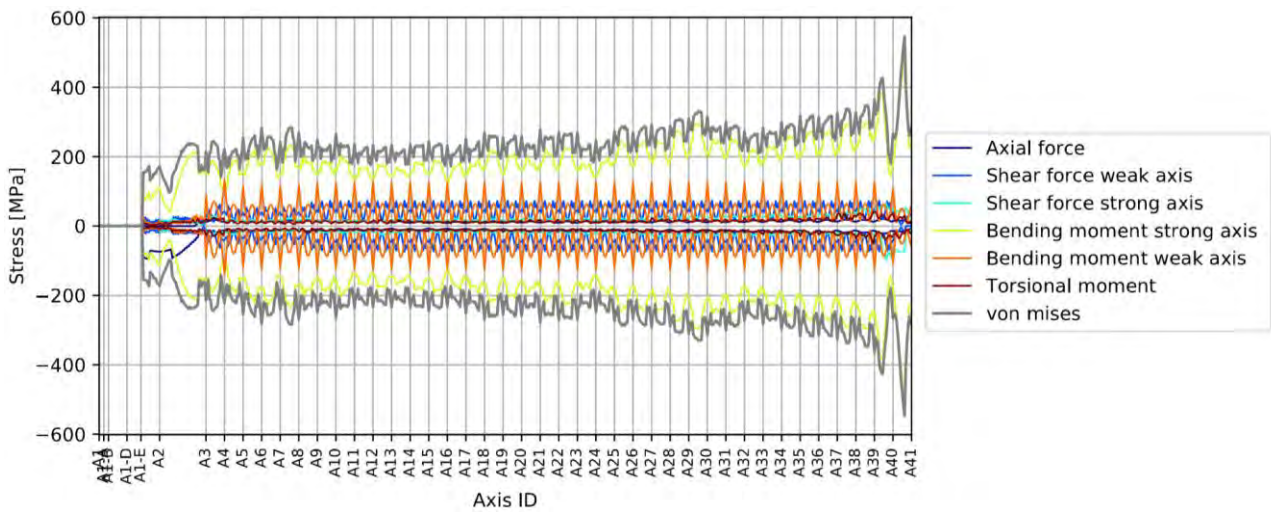


Figure 5-11 Envelopes of von Mises stress for the K12_06 bridge with contribution from the various sectional load components, deckhouse impact between pontoons A39 and A40, 0 deg.

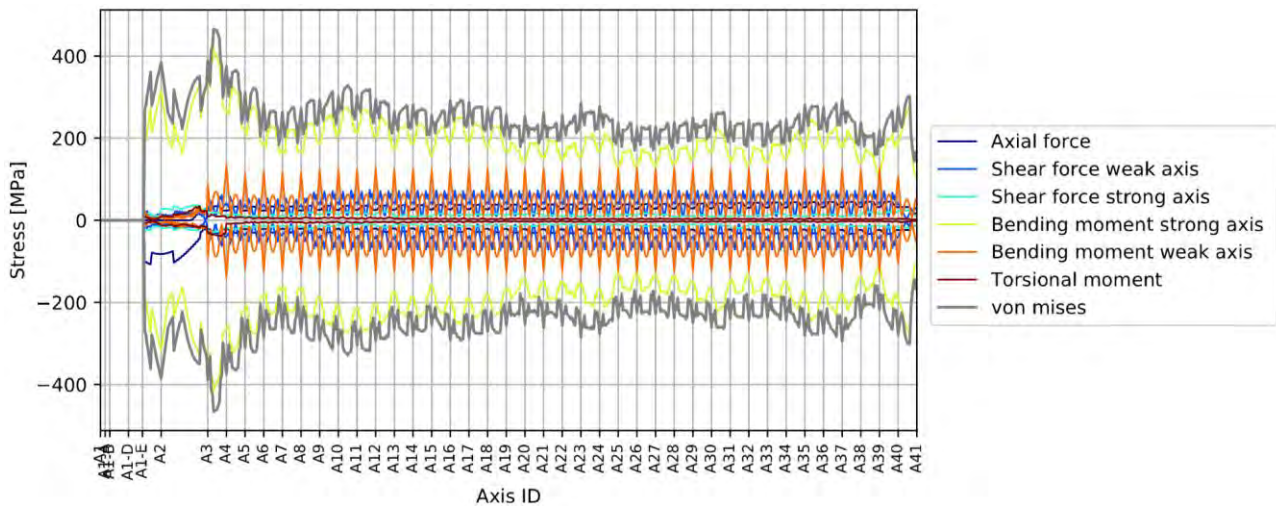


Figure 5-12 Envelopes of von Mises stress for the K12_06 bridge with contribution from the various sectional load components, pontoon impact on A3, 0 deg.

5.4 Column response

Figure 5-13 to Figure 5-15 show the torsional moment in columns for impact to pontoon A3 at varying impact directions. Columns in the back span are termed *BCEi*, whereas columns in the floating bridge are termed *Ai*, both counting from south to north. A significant increase in torsional moment is observed as the direction deviates from the transverse direction of the pontoon. The design basis [2] specifies impacts from all possible directions, and this seems like a reasonable estimate considering that most of the ship collision events as pr. the risk analysis report are from vessels passing along the bridge rather than under the bridge. This will be dimensioning for the columns along the entire bridge.

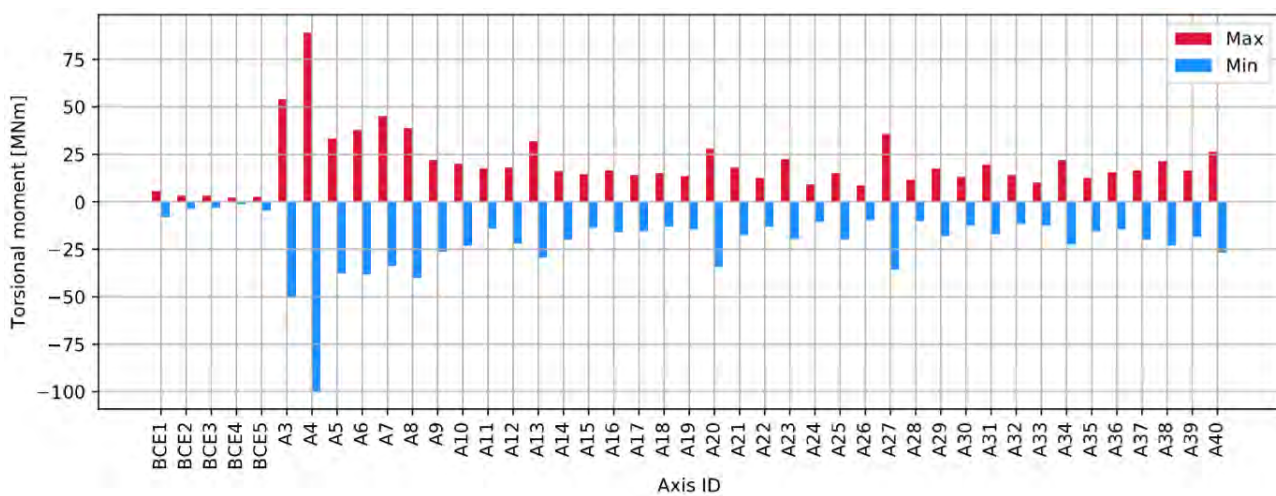


Figure 5-13 Torsional moment in columns for concept K13-06 impact to pontoon A3, 0deg.

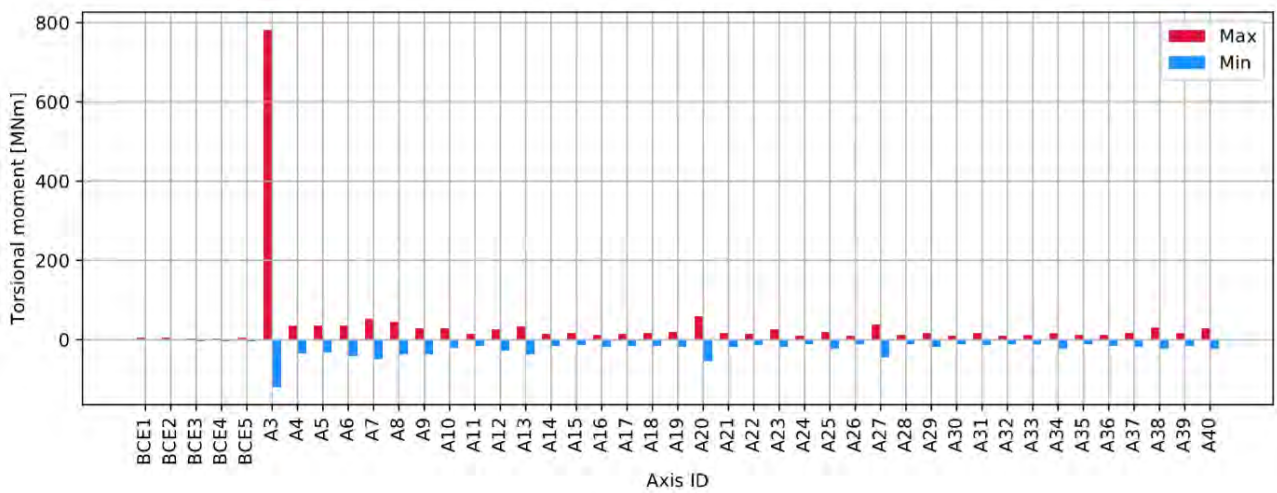


Figure 5-14 Torsional moment in columns for concept K13-06 impact to pontoon A3, 45deg.

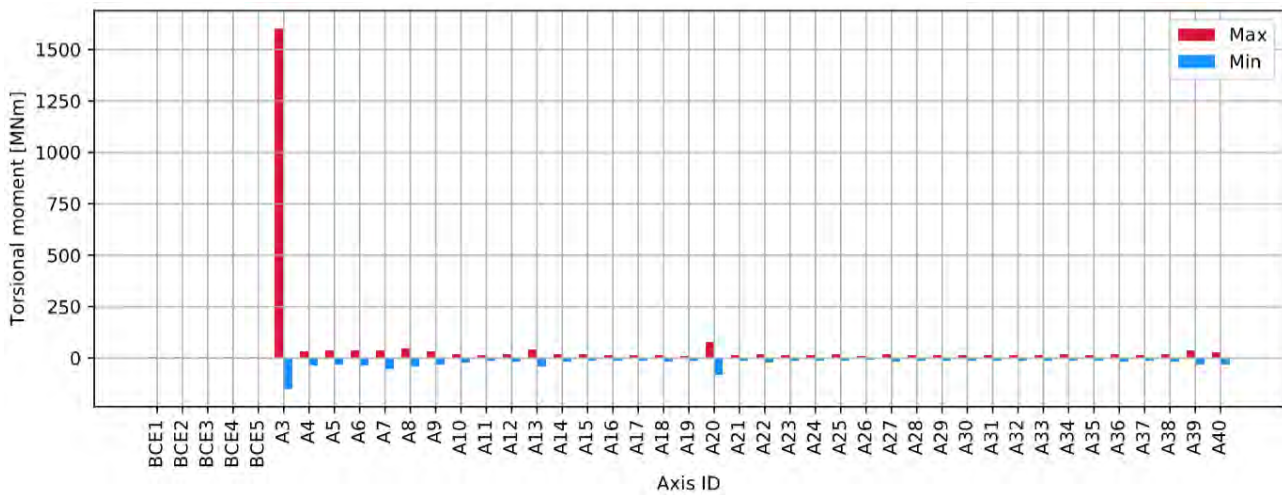


Figure 5-15 Torsional moment in columns for concept K13-06 impact to pontoon A3, 80deg.

Figure 5-16 to Figure 5-20 show key column responses enveloped over all simulated scenarios. A step in torsional response is found north of axis 23, related to the difference in collision energy north of this limit as defined in [3].

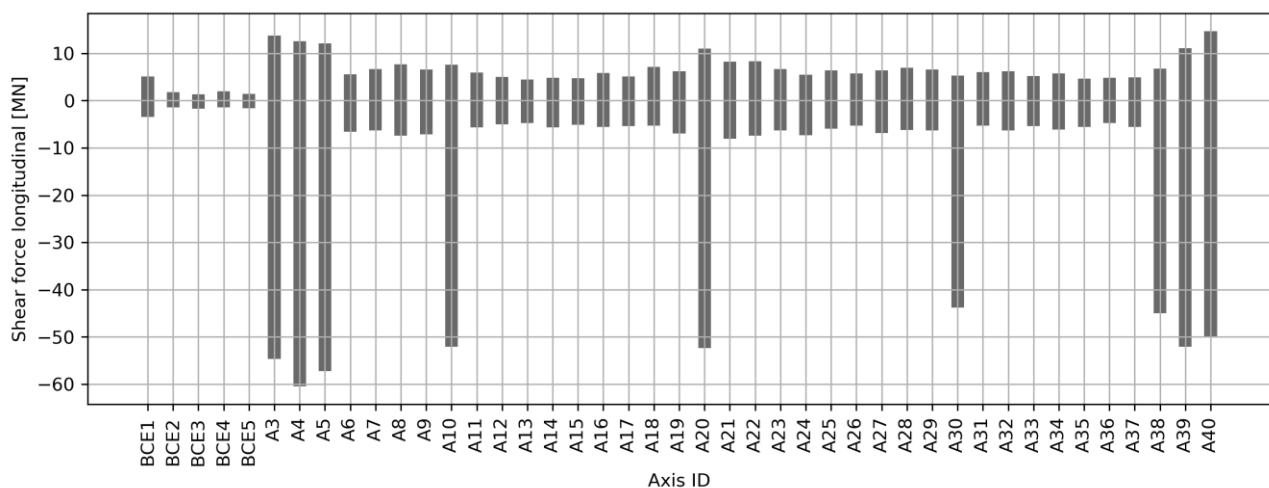


Figure 5-16 Comparison of longitudinal shear force response for K12_06, top of column

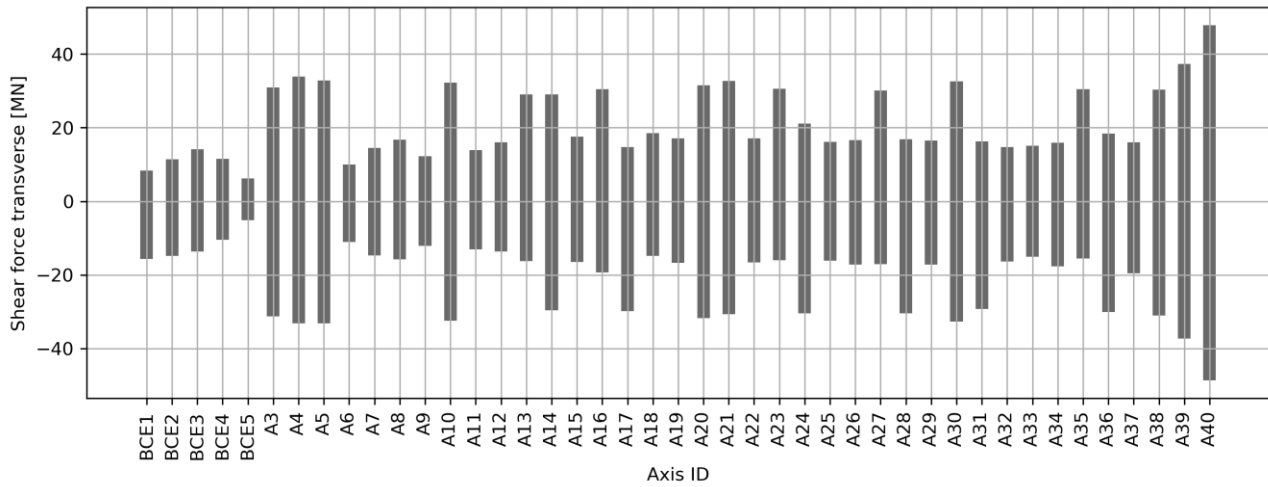


Figure 5-17 Comparison of transverse shear force response for K12_06, top of column

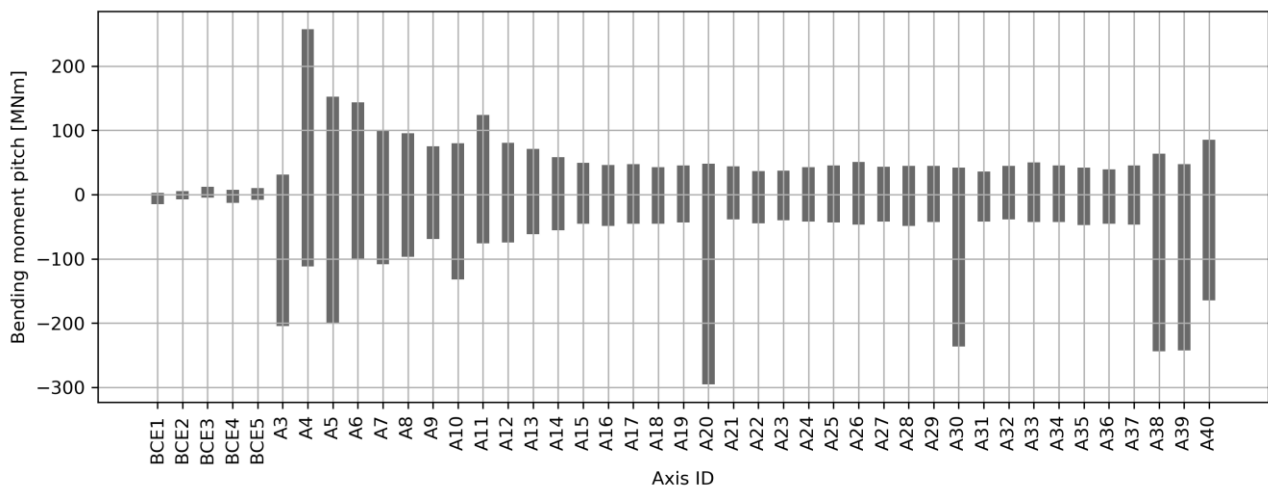


Figure 5-18 Comparison of pitch moment response for K12_06, top of column

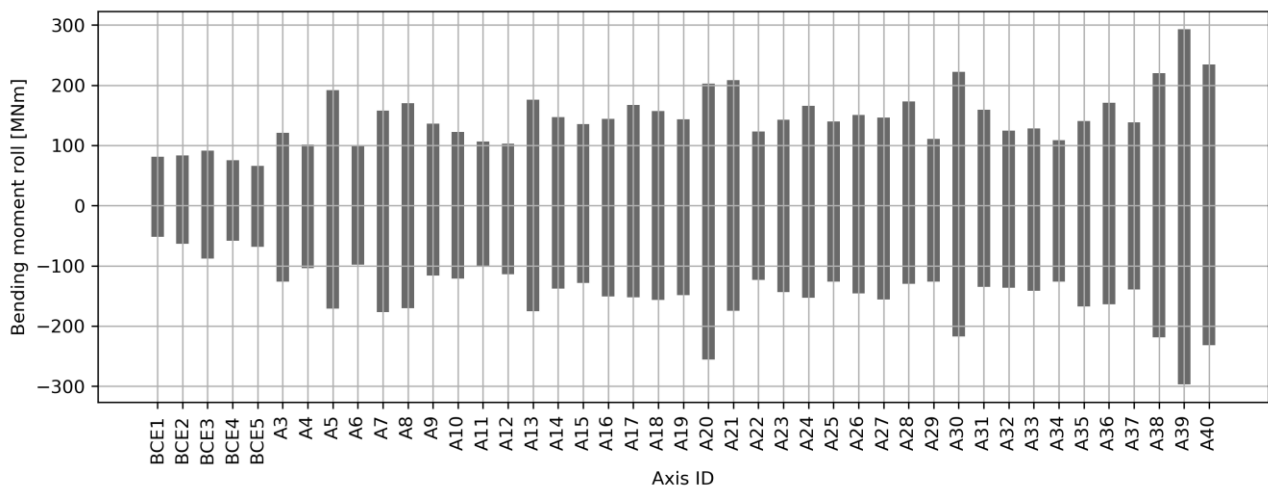


Figure 5-19 Comparison of roll moment response for K12_06, top of column

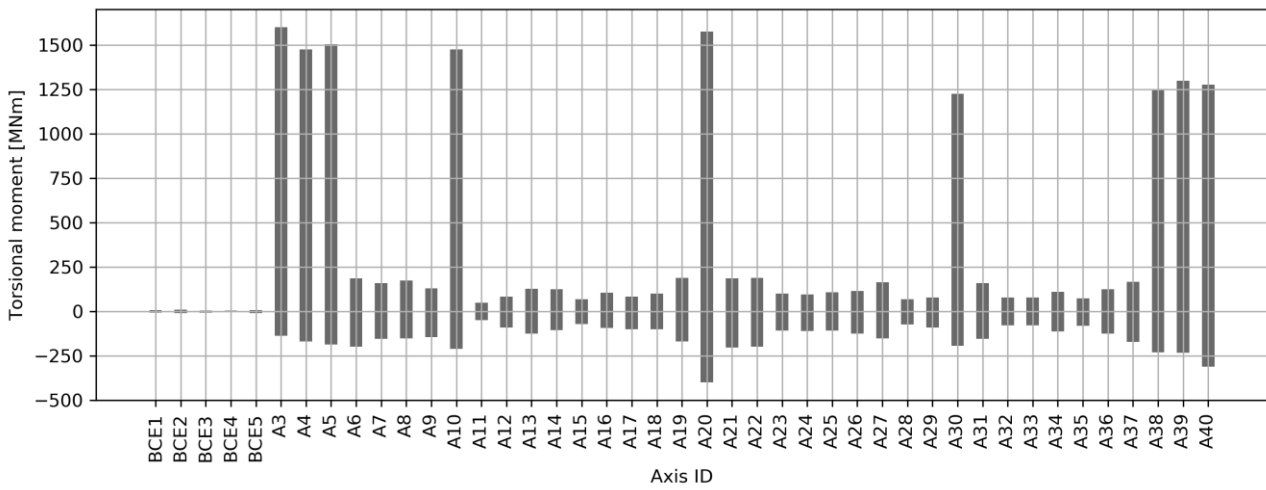


Figure 5-20 Comparison of torsional response for K12_06, top of column

5.5 Mooring line response

5.5.1 Quasi-static mooring line forces

The mooring line response was evaluated in more detail based on simulations with nonlinear mooring stiffness calibrated to each mooring cluster’s nonlinear stiffness properties. Both pontoon- and deckhouse collision were considered, but deckhouse collisions dominate the mooring forces as the transverse bridge deflection is larger the larger the available energy. Impacts are considered only normal to the local bridge axis from either East or West side.

The forces are found by a quasi-static assumption, the mooring line force from a static displacement of the pontoon (*Figure 2-5*) is evaluated based on the dynamic pontoon displacement as found in LS-DYNA.

Table 5-2 the maximum displacements of the moored pontoons and Table 5-3 the maximum mooring line forces. The forces are well below the breaking strength of the mooring line, and ship collisions are thus not dimensioning for the anchor line strength. They may however be dimensioning for the anchor design.

Table 5-2 Maximum pontoon displacements for the deckhouse collision scenarios.

Ship impact (m)		Cluster 1	Cluster 2	Cluster 3
K12	from West	-10.8	-10.7	-6.6
	from East	9.4	10.3	6.7

Table 5-3 Peak mooring line forces [MN] during all simulated collision scenarios on deckhouse collisions.

	Top	Bottom
Mooringline1	9	8.5
Mooringline2	10.3	9.7
Mooringline3	8.2	7.6
Mooringline4	7.3	6.6
Mooringline5	7.5	7
Mooringline6	7.2	6.7
Mooringline7	7.6	7
Mooringline8	10.5	9.9
Mooringline9	8.6	8.1
Mooringline10	4.5	4
Mooringline11	7.4	6.8
Mooringline12	8.9	8.4

5.5.2 Evaluation of dynamic mooring line forces

A check of the quasi-static mooring line response was performed by extracting the force-time-history for the local collision from LS-DYNA and applying it directly to the same location in the Orcaflex

model. The force-time-history includes external and internal mechanics, plastic energy dissipation in local deformation and viscous energy dissipation. Figure 5-21 shows the force-time-history, showing that the main collision is over in about 8 seconds, but due to bridge vibrations contact forces arise in shorter time periods after this. After around 18 seconds the ship is pushed away from the bridge.

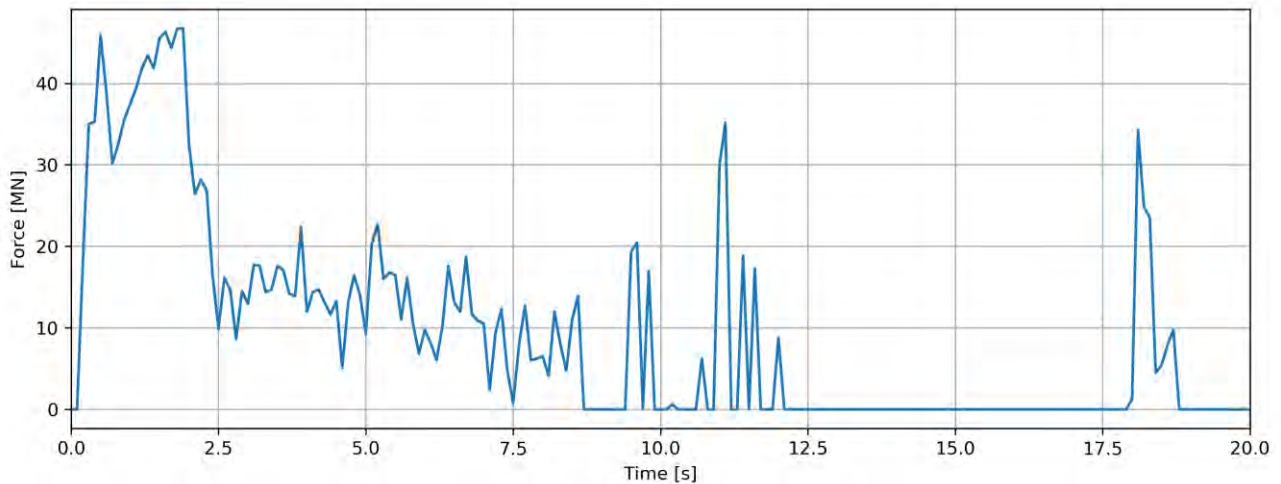


Figure 5-21 Force-time-history from LS-DYNA for deckhouse collision between axis A13 and A14, 0 deg.

Figure 5-22 compares the transverse deflection of pontoon A13 from the two simulations. It is seen that the Orcaflex simulations yields a somewhat larger deflection than the LS-DYNA model. Investigations of the Orcaflex results revealed that this is partly related to the amount of viscous damping on mooring lines and partly to the vertical force component in the mooring lines (a horizontal spring is assumed in LS-DYNA). The vertical force component in the mooring line results in increased roll motion of the pontoon (not captured in LS-DYNA).

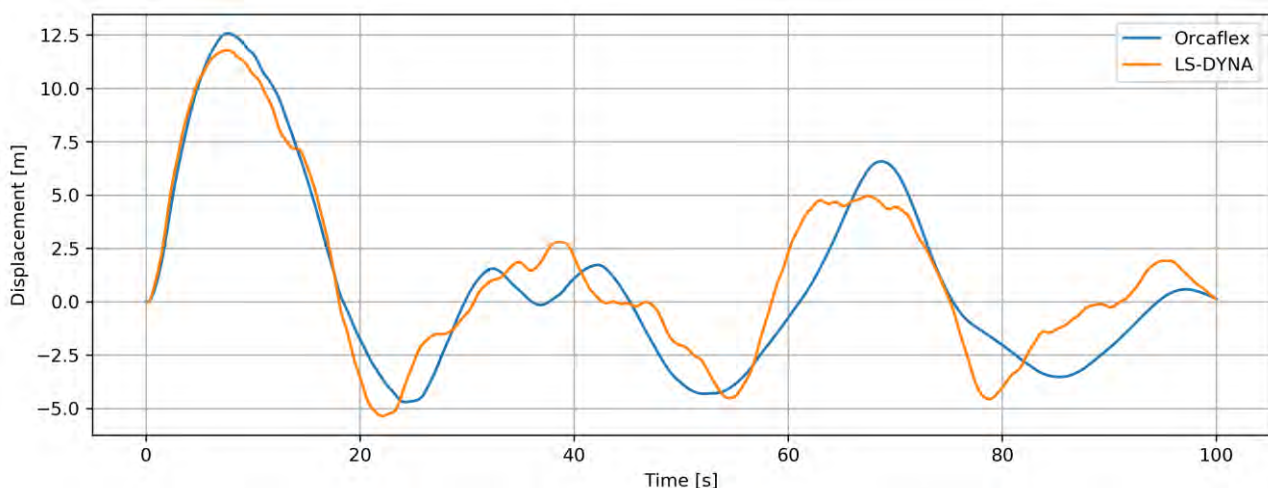


Figure 5-22 Resulting displacement of pontoon A13 for the force-time-history in Figure 5-21.

Figure 5-23 shows the corresponding dynamic mooring line forces. The peak forces are somewhat above those from the quasi-static approach in Table 5-3. Pontoon displacements (as discussed

above) partly explains the differences. However, investigation of the dynamic Orcaflex mooring line forces compared with a quasi-static mooring line force calculated from the same pontoon deflection reveals that there was a dynamic amplification of the mooring line force of about 13%.

Mooring line 1 and 2 (east side of the mooring cluster on A13) are especially taught due to the anchor position (Figure 5-24). During a ship collision with energy as in the design basis the lines are almost fully stretched out, giving a large gradient of the force vs. displacement curve (Figure 2-5). The mooring line response is thus very sensitive to the exact displacement of the moored pontoon.

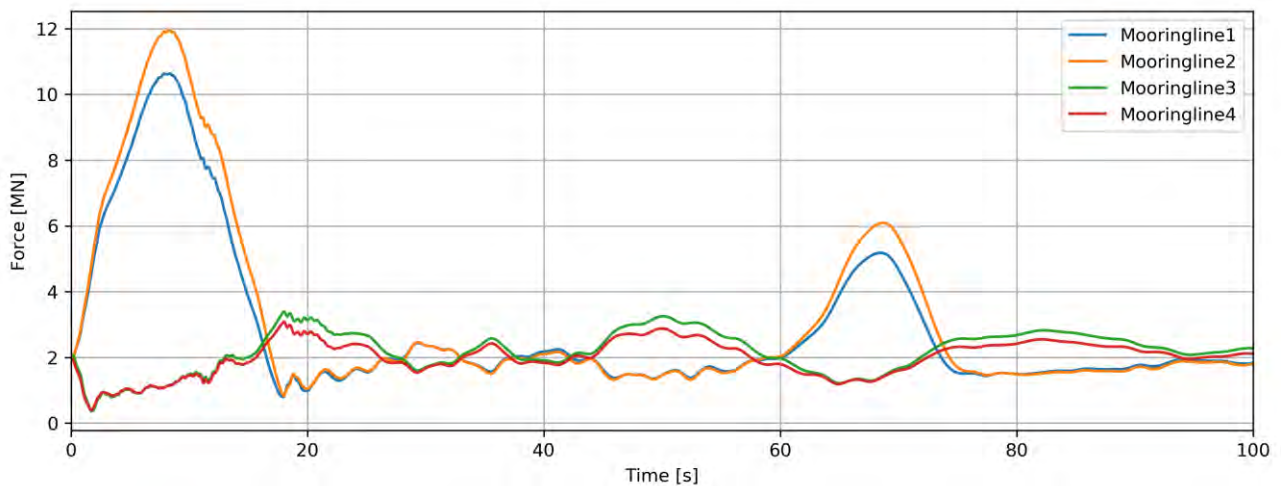


Figure 5-23 Resulting mooring line forces on pontoon A13 for the force-time-history in Figure 5-21.

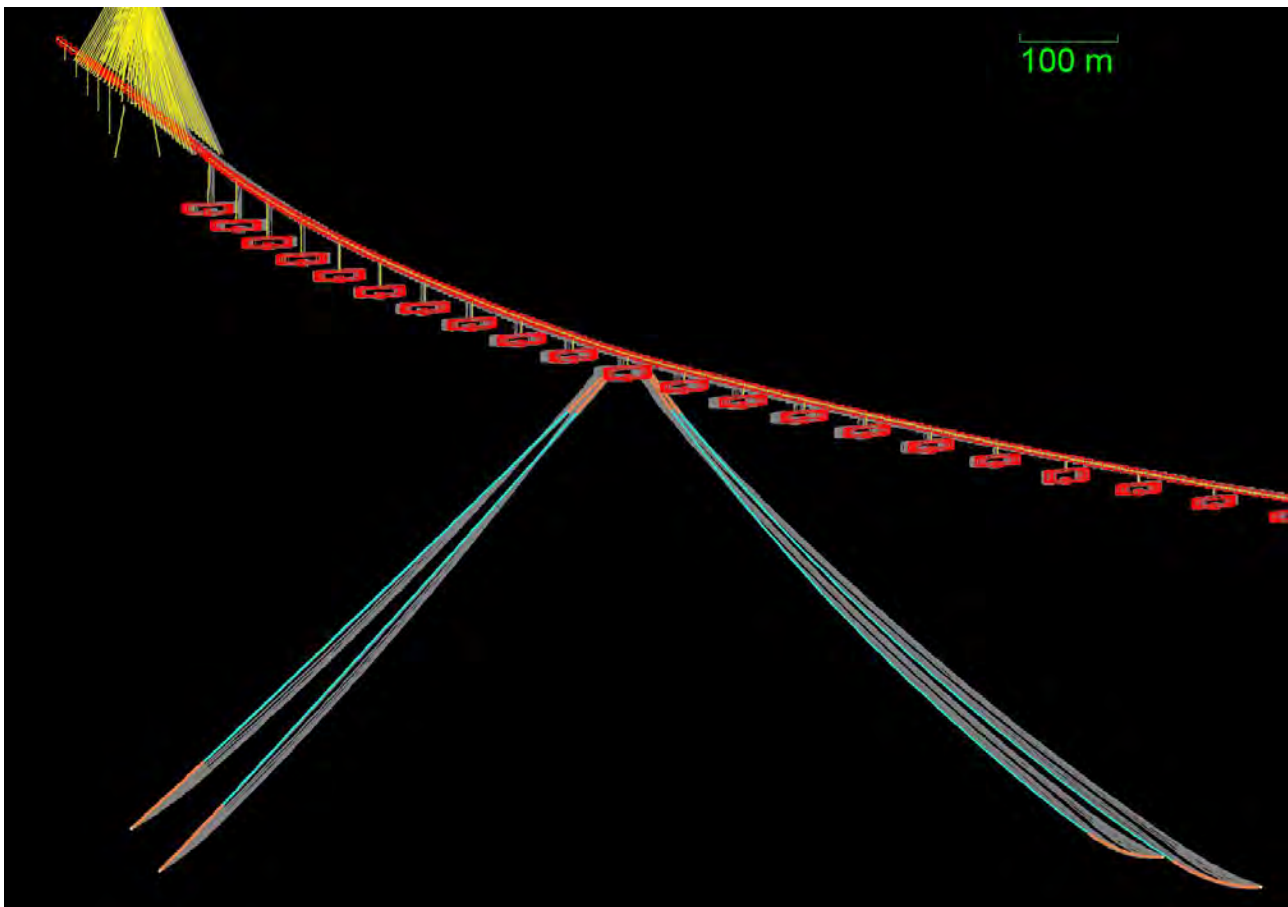


Figure 5-24 Visualization of the peak mooring line force for the force-time-history in Figure 5-21. Grey indicate previous positions up to peak load.

5.5.3 Discussion

The quasi-static approach for evaluation of the mooring line forces from a dynamic model that only consider a nonlinear mooring cluster stiffness was shown to underestimate the mooring line forces. For detailed design it is recommended to include a more comprehensive modelling of the mooring system also in the collision simulations, including the actual force directions and viscous damping. This can be achieved by modelling the mooring lines with rope elements and applying the viscous drag loads by a user-defined load model.

For use of the quasi-static results presented in Table 5-3 it is recommended to include a load factor of 1.16 to account for dynamic amplification of the mooring line and differences in how viscous energy dissipation is accounted for in the two solvers.

6 Consequence assessment

The bridge response to collision events may exceed the ULS capacity significantly and cause permanent damage to structural elements outside of the local collision zone. This section gives some considerations as basis for evaluation of the local damage and post-collision capacity (which are outside the scope of this document).

6.1 Pontoon damage

The pontoon damage is limited to local damage in way of the bulb and forecastle structure. Up to four compartments may be flooded, with a total volume of 1300 m³. The bottom plate structure of the pontoon will be fully or partially mobilized, thereby dissipating energy. Figure 6-1 shows a typical deformation behavior when struck by a cruise vessel with a strong but slender bulbous bow.

Note that collision to a moored pontoon will have a different local response due to the increased draught of the pontoon (thereby less mobilization of bottom plate capacity) and due to local reinforcements around the anchors. The volume of flooded compartments will be 50% higher due to the increased draught, and about 2000 m³ could be flooded.

As input for a global integrity check of the bridge, impact to a moored pontoon is assumed, with four-compartment damage. This gives loss of buoyancy and a loss of waterplane stiffness in heave, roll and pitch. See [1] for details.

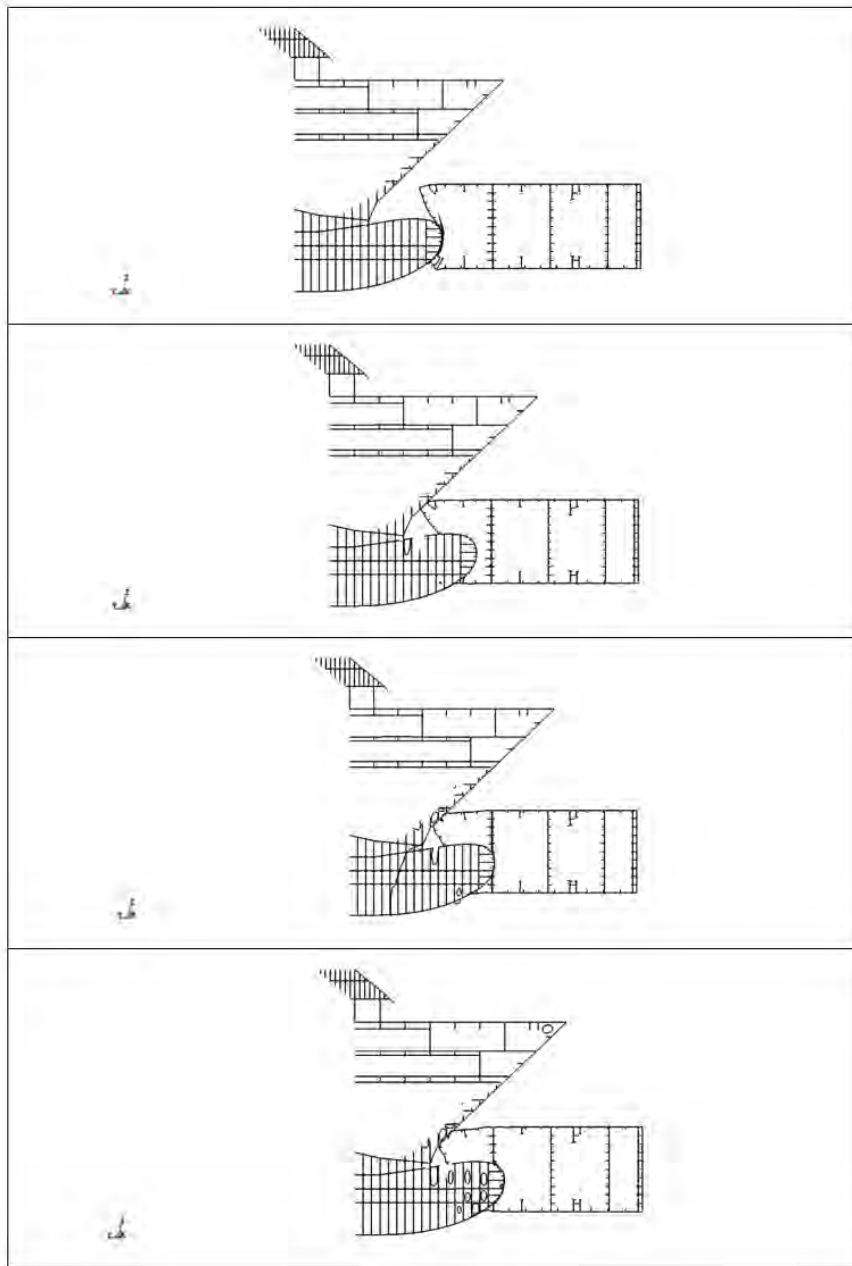


Figure 6-1 Deformation during collision between cruise vessel and pontoon. From above, 20 MJ, 50 MJ, 80 MJ and 105 MJ

6.2 Column damage

The global ship collision simulations reveal very large torsional utilization if the pontoon is struck by a vessel travelling nearly parallel to the bridge. The likelihood of such a scenario can be questioned, but it is covered by the requirements in the design basis. The current column design is rather slender, and the torsional load is above the elastic capacity. Hence, an evaluation of the local response of the column was performed in a coupled global/local response model.

6.2.1 Setup

A FE model of the current proposal for column design was established, in which all relevant structural members were modelled with refined shell elements (Figure 6-2 and Figure 6-3). A constant outer shell thickness was assumed, and variations of this thickness was used to study the effect of increasing torsional resistance of the column. No imperfections were included in the model, which is considered an acceptable assumption for large deformations (the exact onset of plastic buckling capacity at cannot be evaluated directly from the results). The material behavior was modelled using the lower bound properties of NV36 steel from DNVGL-OS-B101 [14] by means of a power law hardening model including a yield plateau and the BWH fracture criterion including post-necking damage, similar to the simulations in Section 4.

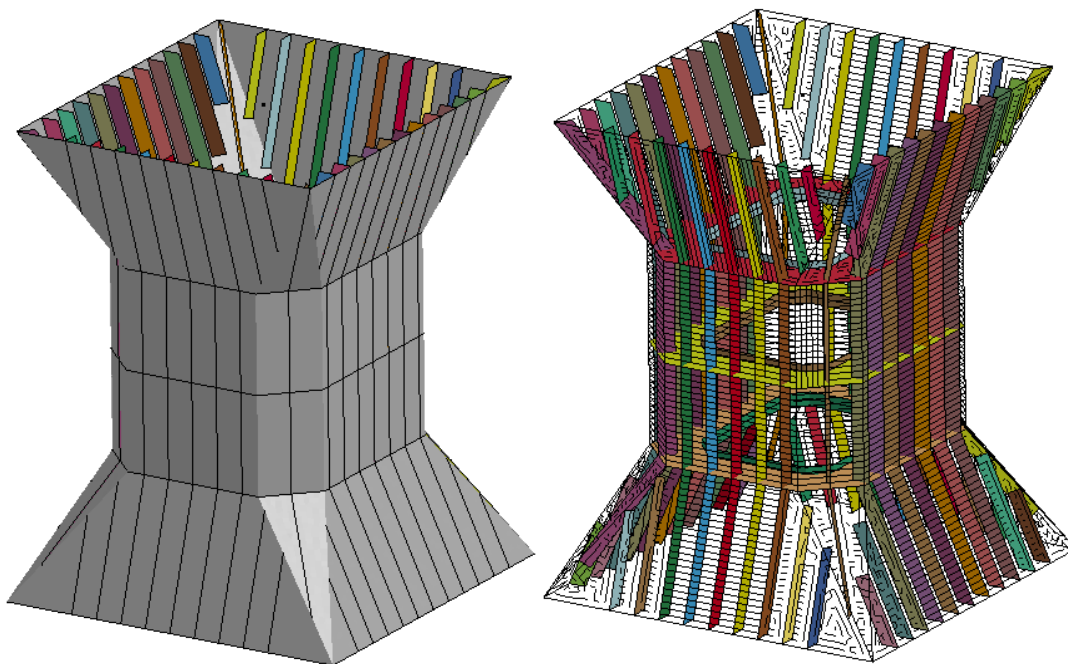


Figure 6-2 Local shell model of the column with and without the outer shell.

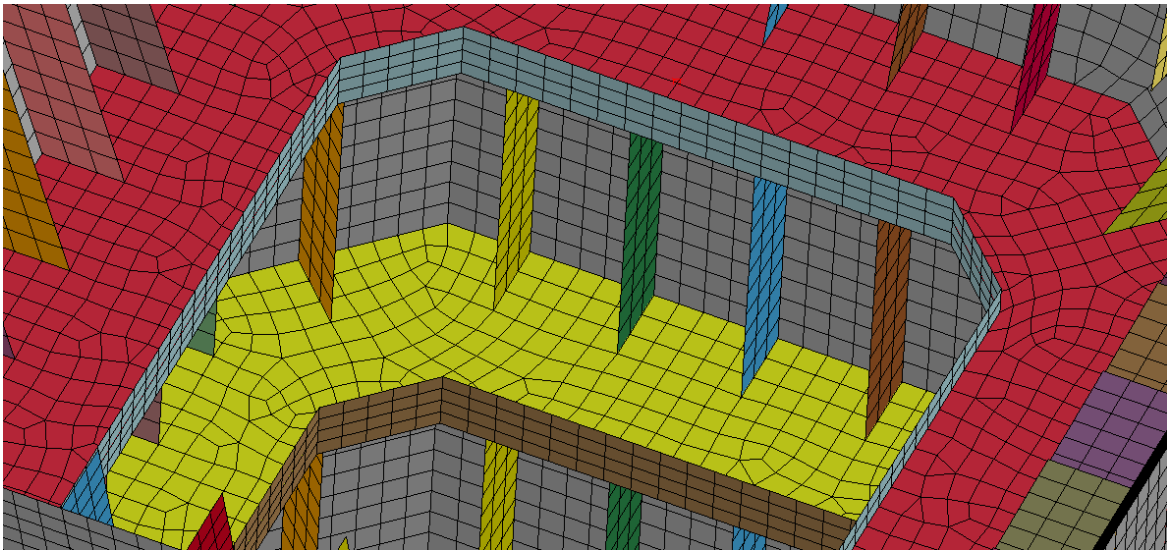


Figure 6-3 Discretization example from the column model.

The column model is merged into the global beam model of the K12-05 bridge concept at axis A20, and rigid multipoint constraints are used to connect the column model to the pontoon and bridge girder. Figure 6-4 and Figure 6-5 shows parts of the combined global/local model (MPCs not shown).

The considered scenario for simulation was a ship impact to the pontoon at an angle of 80 degrees from the transverse bridge axis impacting at the pontoon tip (thereby significantly overestimating the maximum obtainable torsion). The force-deformation curve of the local ship-pontoon collision and the mass and velocity of the impacting ship were selected according to Table 2-1.

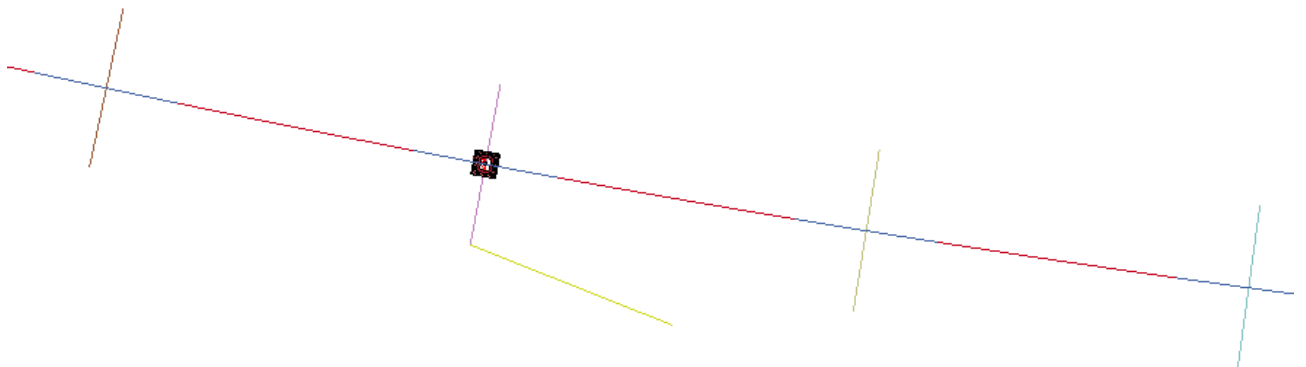


Figure 6-4 Top view of collision scenario, with impact direction and location indicated with a yellow line.

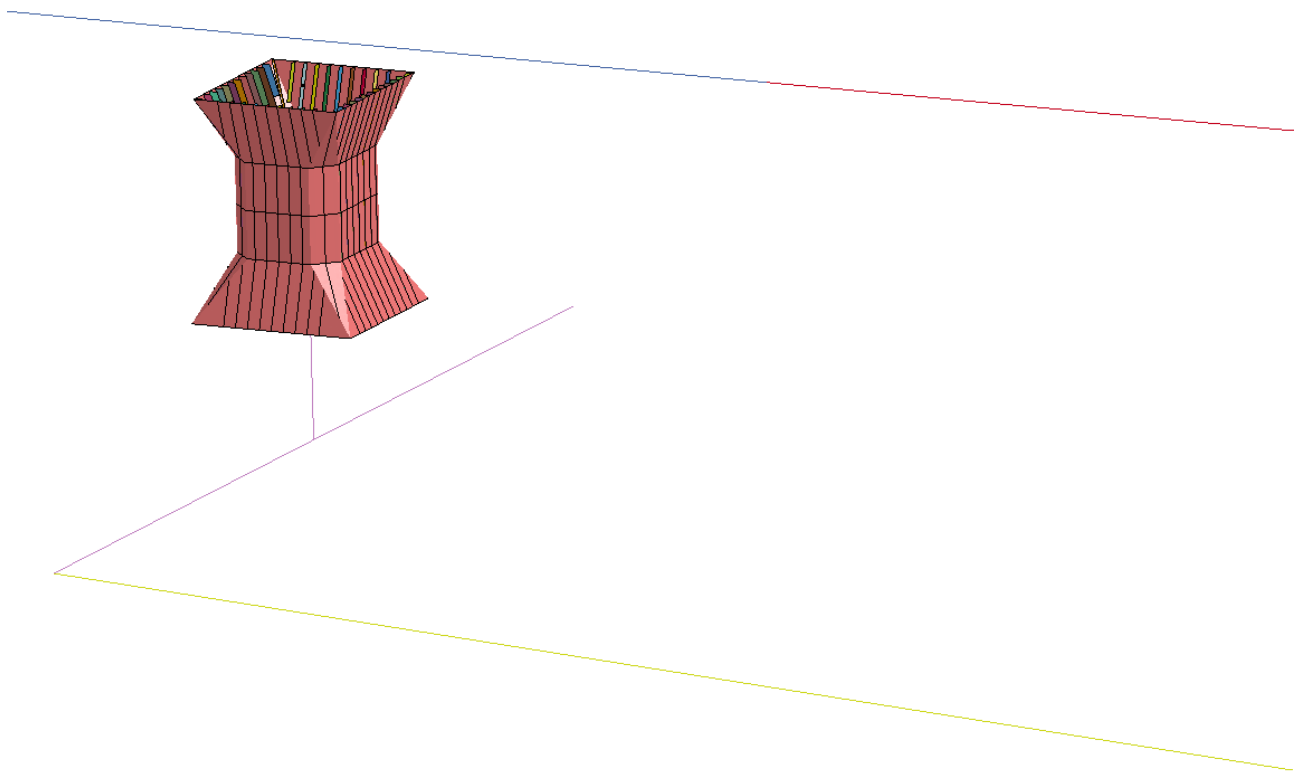


Figure 6-5 Local view of column and pontoon

Thickness variations of the outer shell plate of 25, 40, 50, 60 and 80 mm were simulated, along with a scenario with 40 mm plate but with only 50% of the kinetic energy. 25 mm was initially the base case for the column design and was sufficient to withstand the ULS load requirements.

6.2.2 Results (without reinforcements)

Figure 6-6 shows the deformation history of the 25 mm column (the column design as proposed in March 2019 [24]) when subject to an impact at the pontoon tip with an angle of 80 degrees from the transverse bridge axis. The column has insufficient resistance and is not able to withstand the torsional load on the column. Hence, a rotation of more than 90 degrees occurs without the striking vessel being stopped. Severe fracture is observed, and the column is completely destroyed. Figure 6-7 shows the response of the bridge girder due to the shortening of the column. A weak-axis bending moment of more than 800 MNm is observed at the neighbouring pontoons (from an elastic beam response).

The 25mm column is clearly not sufficient to withstand the design impact loads, and reinforcements are necessary.

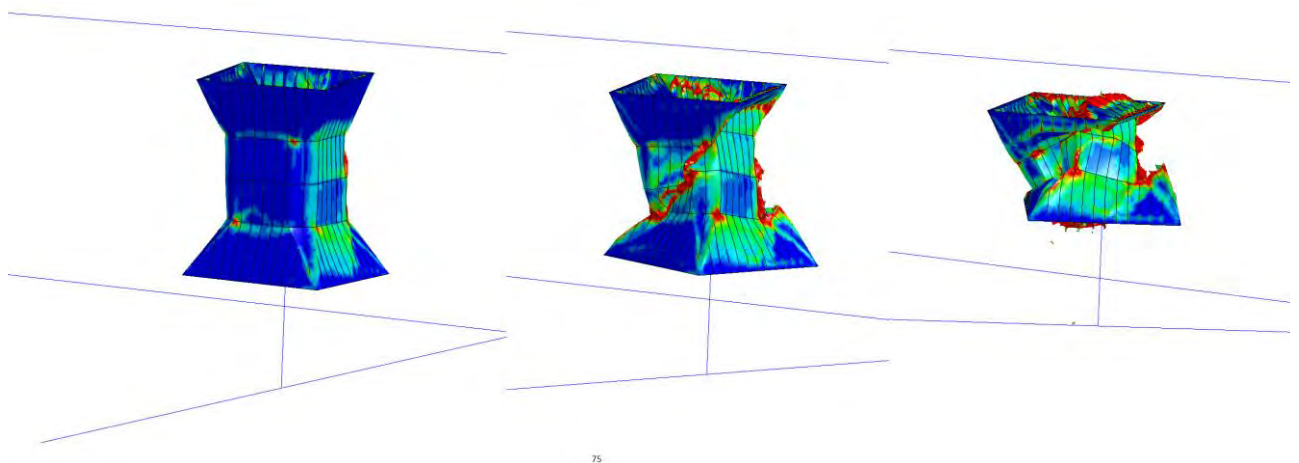


Figure 6-6 Deformation of 25mm column during a ship collision event

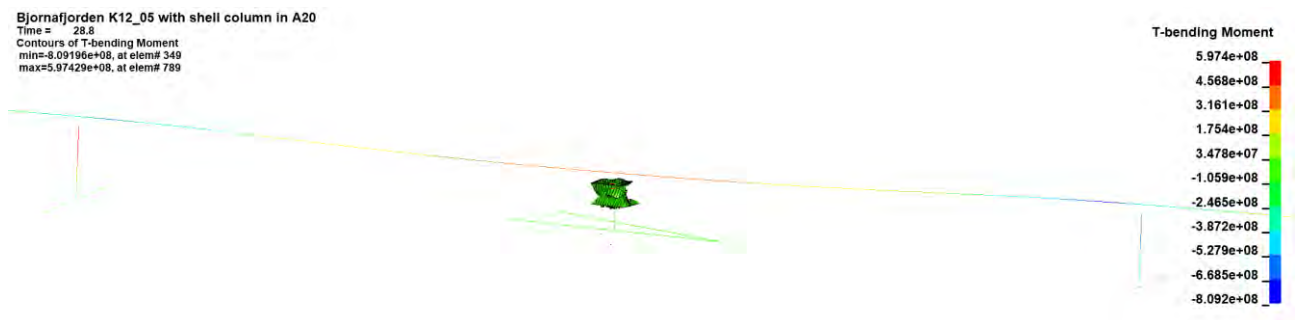


Figure 6-7 Weak-axis bending moment in the bridge girder due to column contraction during rotation for the 25mm thick column model.

A new base case was suggested as a strength increase equivalent to a 40 mm thick shell plate using the same geometry and structural layout as for the 25 mm column. Figure 6-8 and Figure 6-9 shows the response of the new column with 40 mm shell thickness to the selected impact scenario. A significant torsion of the column is observed, with around 40 degrees rotation which shortens the column by approximately 2 m. The lateral displacement of the lower part of the column is slightly above 1 m. Fracture occurred in the intersection between the narrow section and the transition to larger cross-sectional area, directly outside of the internal ring girder. The energy dissipation (Figure 6-10) shows that the main part of the impact energy is transferred to plastic strain energy in the column.

With the level of deformation, fracture and the shortening of the column it is not safe to assume that the column will have a residual capacity to survive a 100-year storm after the impact. However, as the ship collision energy is expected to decrease towards the next phase of the project due to the re-routing of the nearby navigational channel, the column with stiffness equal to a 40 mm shell plate is selected as the recommended design for this phase of the project.

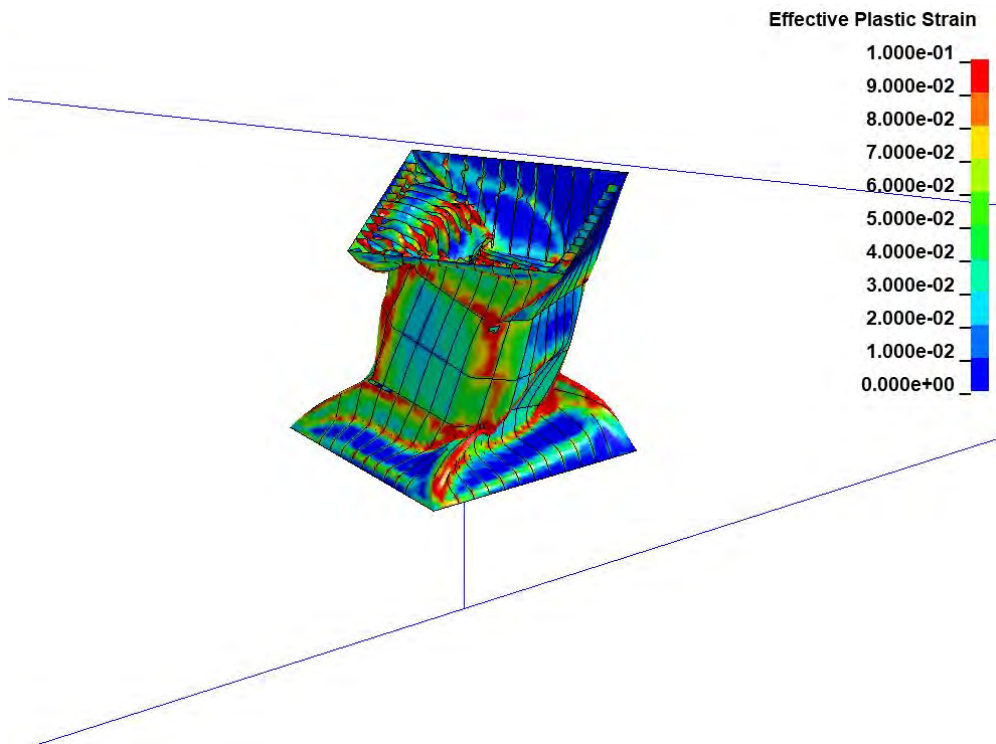


Figure 6-8 Resulting deformation and plastic strain at end of impact for the non-reinforced column.

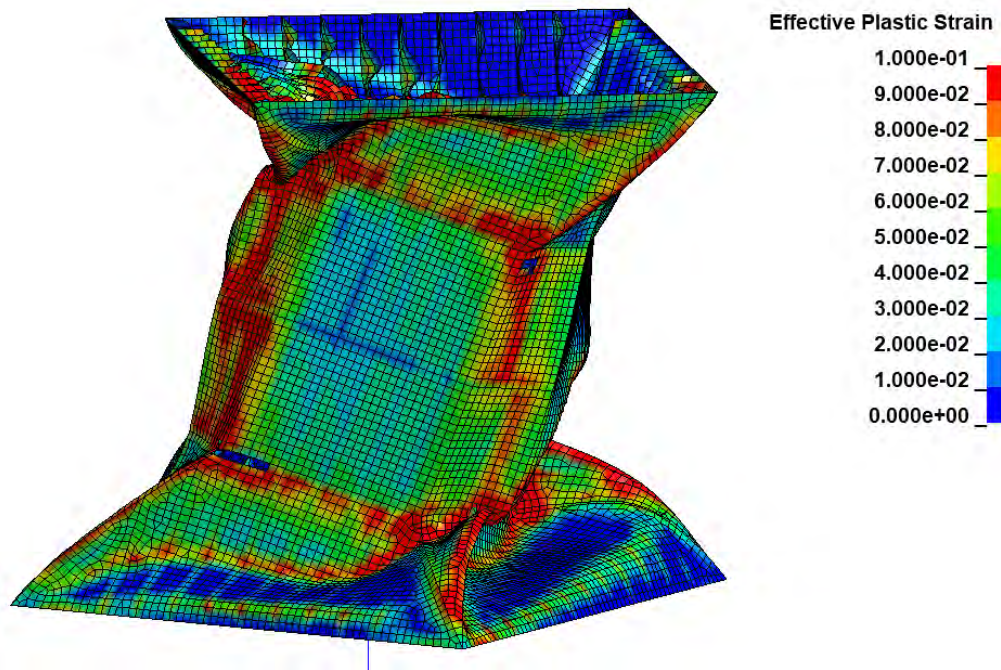


Figure 6-9 Deformation of column with fracture.

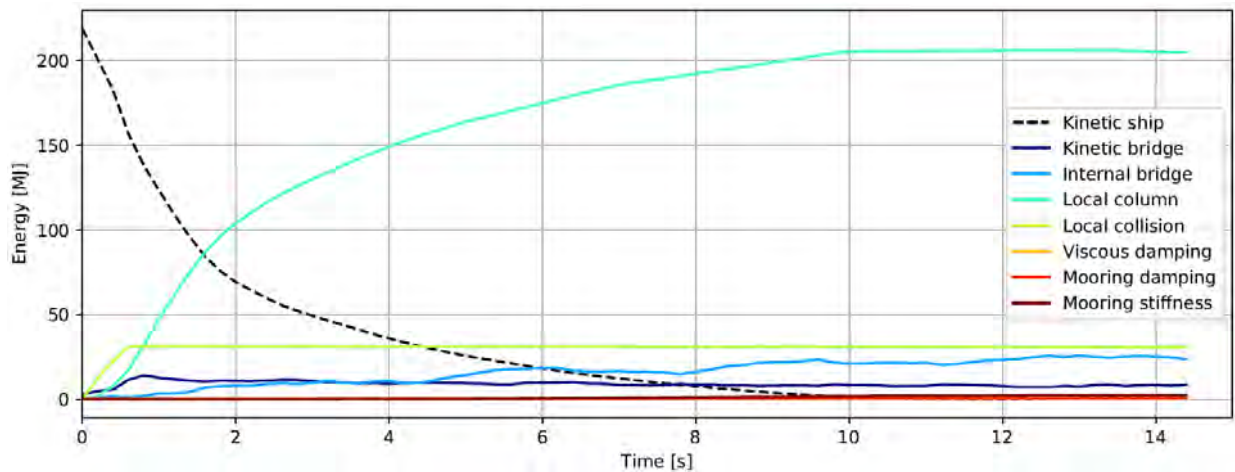


Figure 6-10 Energy balance and dissipation during the collision event.

6.2.3 Results (with further reinforcements)

Should the need arise when the revised ship collision scenarios become available, the response of the column could be further strengthened. Figure 6-11 shows the final deformations after impact, Figure 6-12 the torsional moment and Figure 6-13 the dissipated plastic strain energy vs. rotation of the column for the column models with varying strength. Increasing the column thickness is an effective measure to reduce the level of deformation, but it is not considered feasible to increase the column strength to a level without deformation without more drastic measures.

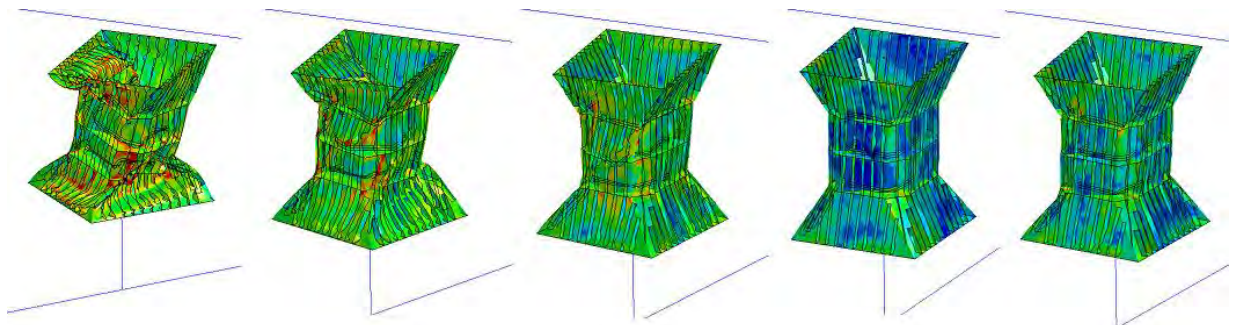


Figure 6-11 Final deformation of column for 40, 50, 60, and 80 mm shell thickness and 40 mm thickness with 50% energy (from left to right)

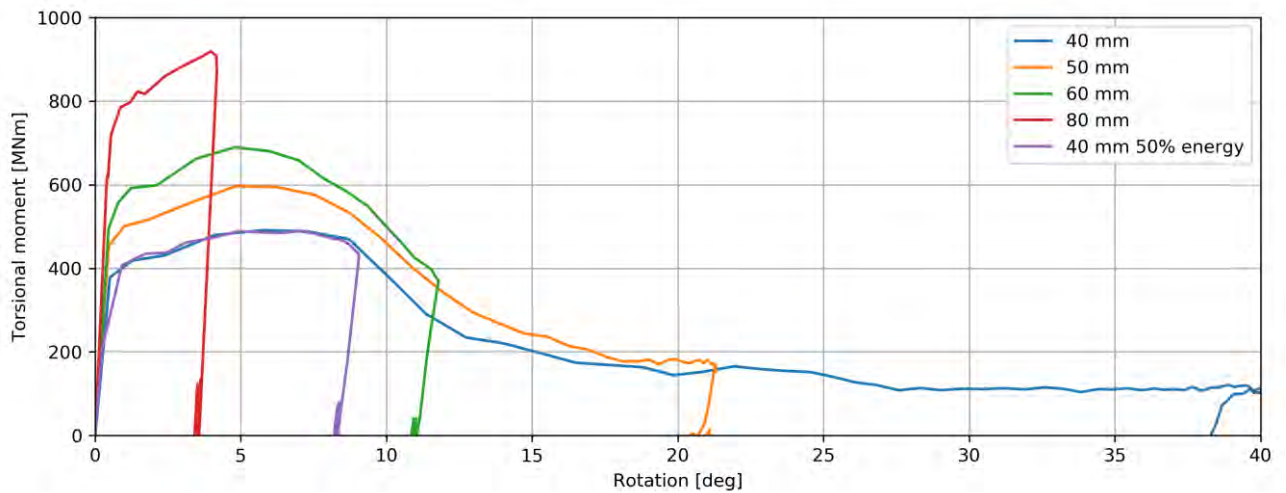


Figure 6-12 Torsional moment vs. column rotation for variations of column strength and impact energy.

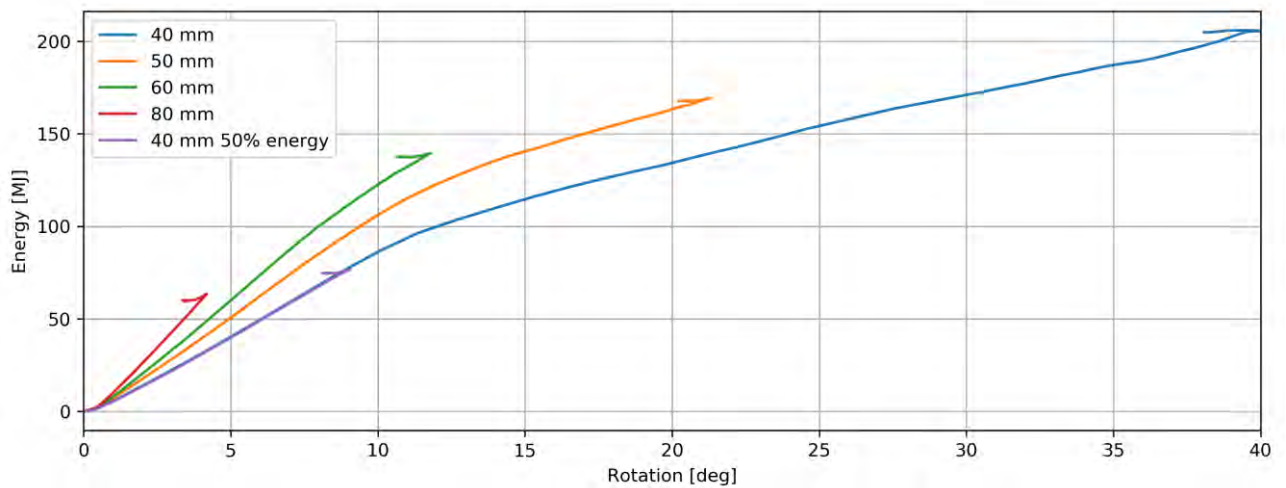


Figure 6-13 Dissipated plastic strain energy in the column vs. column rotation for variations of column strength and impact energy.

6.2.4 Discussion

Hydrodynamic response of the struck pontoon in yaw was not included in the global model as it initially was assumed that only small rotations would occur due to ship collisions. With the weak columns the rotation is significant; for the 25mm thickness the column is twisted 90 degrees in about 10 seconds. Including hydrodynamic response in yaw would have increased the resistance to rotation significantly, and thus shifted more of the damage from twisting of column to local damage in the pontoon and striking vessel. The results given in this section are thus conservative.

The base case column with 40 mm plate and with 50% of the impact energy shows approximately a 40% reduction in rotation compared to 100% impact energy, and this support the decision of keeping the 40 mm equivalent strength as the base case for the current phase.

To avoid overly thick plates it is recommended to reconsider the column geometry, at the expense of slightly increased wind loading and a more bulky aesthetic profile. See [25] for a discussion of more rational means of increasing the column strength based on the findings herein.

6.3 Bridge-girder damage

The bridge girder will get moderate local damage from a collision event to the bridge girder. For deckhouse collisions the local simulations so far indicate an indentation of up to two meters. Residual capacity checks from phase 3 indicate a 30% reduction in strong-axis and torsional moment capacity and a 15% reduction in weak-axis moment capacity, i.e. less than the load factor used for ULS capacity checks.

Global effects of ship collisions are limited to high strong-axis bending moments in each end (towards northern abutment and towards the tower in A2, and local capacity around supports in the tower and towards columns in the back span. The local support is deemed feasible to solve in local strength design and is not considered further. The bridge girder strength towards the Northern abutment was increased considerably to have higher capacity against global loads. If a ship collision (or an environmental load) should cause an exceedance of the capacity the bridge girder would simply buckle and likely not cause damage to the abutment

A mitigating factor to reduce the loads going into the Northern abutment is to consider a non-reinforced bridge girder and investigate the local plastic behavior during a global collision event. This may act as a weak link to limit the loads that are transferred to the abutment and should be investigated further during detail design when the risk analysis has been updated with new impact energies.

7 Sensitivity checks

It is of interest to evaluate the sensitivity to variations in the input parameters on the ship collision response.

7.1 Reduction of impact energy

Work on ship collision risk has continued in SVV throughout the project, and a suggestion of re-routing the shipping channels on the west side of the crossing is promising as a means to significantly reduce the risk of ship collisions. The corresponding reduction in collision energy has not yet been evaluated. A 50% energy reduction was assumed to investigate the sensitivity of the bridge response to energy reductions.

Figure 7-1 and Figure 7-2 shows the axial force and strong-axis bending moment for ship-pontoon collisions at varying impact angle with full energy and 50% of the energy as defined in the design basis. Approximately 20% reduction of bridge girder response can be observed when comparing the figures.

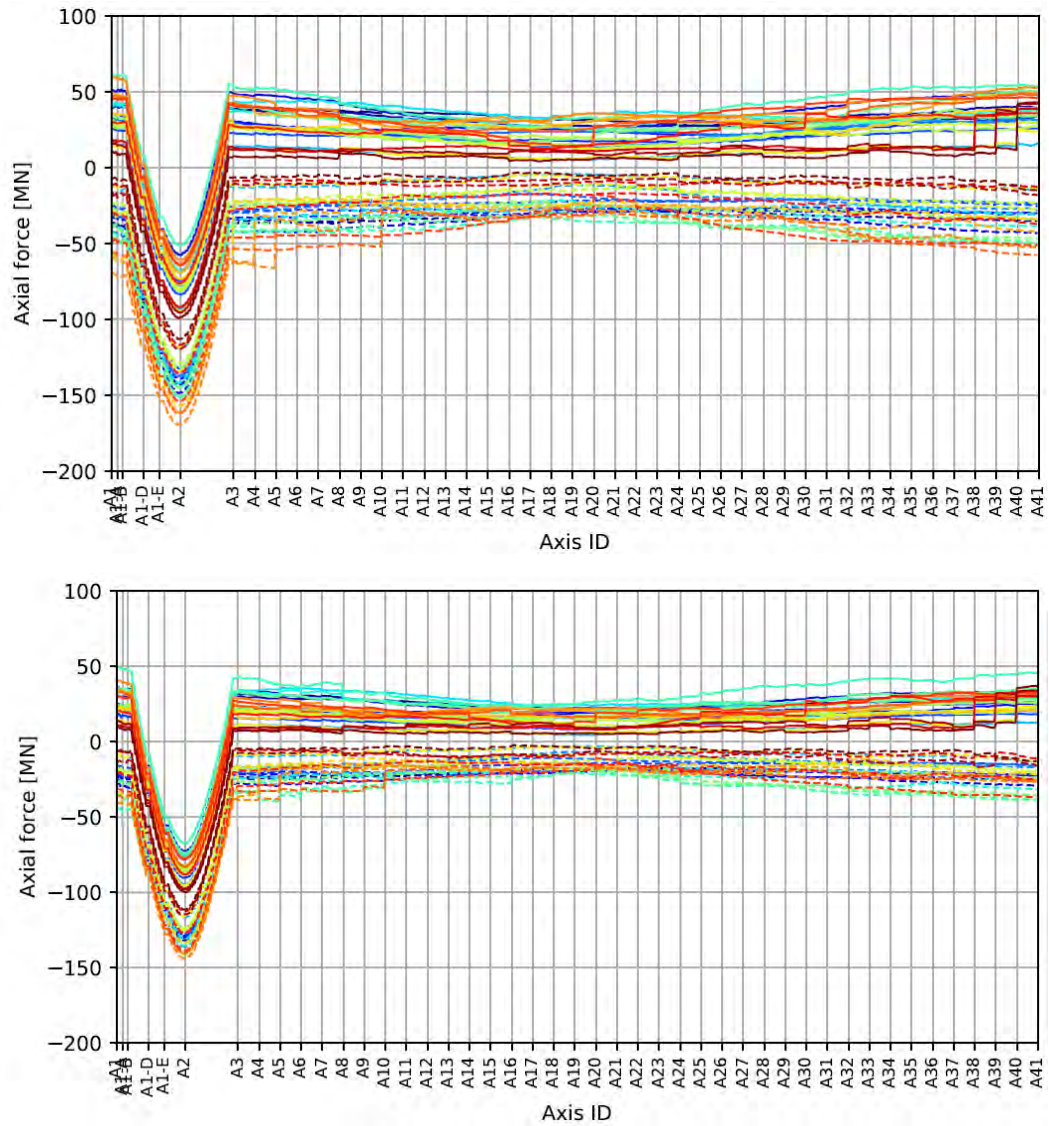


Figure 7-1 Bridge girder axial force for pontoon-ship collision with energy as pr. design basis (top) and 50% of the energy (bottom).

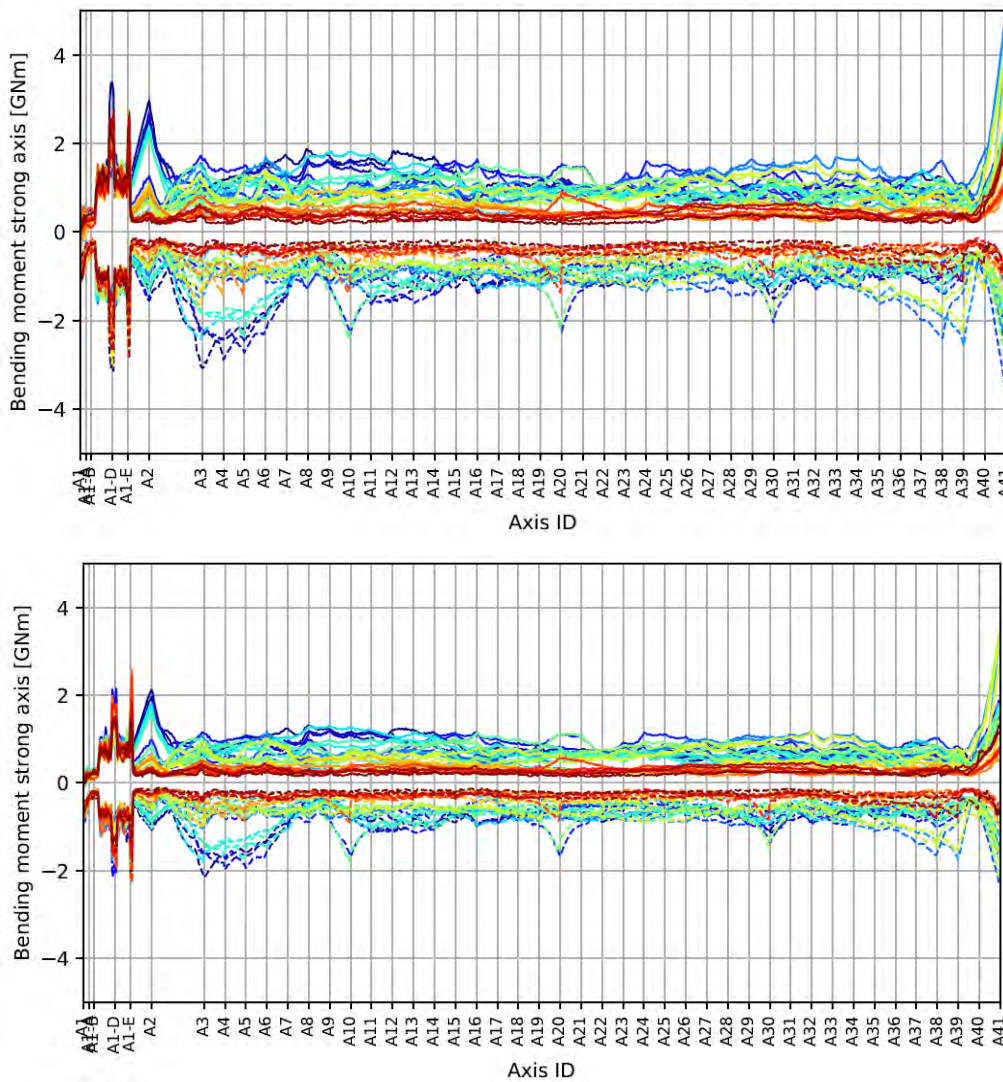


Figure 7-2 Bridge girder strong-axis bending moment for pontoon-ship collision with energy as pr. design basis (top) and 50% of the energy (bottom).

7.2 Increase of energy

Figure 7-3 and Figure 7-4 shows the axial force and strong-axis bending moment for pontoon collisions with 50% more energy than what's in the design basis. Only minor changes are seen to both response variables at either end, but some increase can be observed in the middle of the bridge. This corresponds well with the finding that the bridge is stiffness-dominated on either end and inertia-dominated towards the center. Increased energy only affects the inertia-dominated area.

Note that the local collision forces are not correctly represented for increased energies as the local simulations were stopped at around 200 MJ. If the energy increases significantly above those in the design basis the local simulations has to be updated in order to get reliable global results.

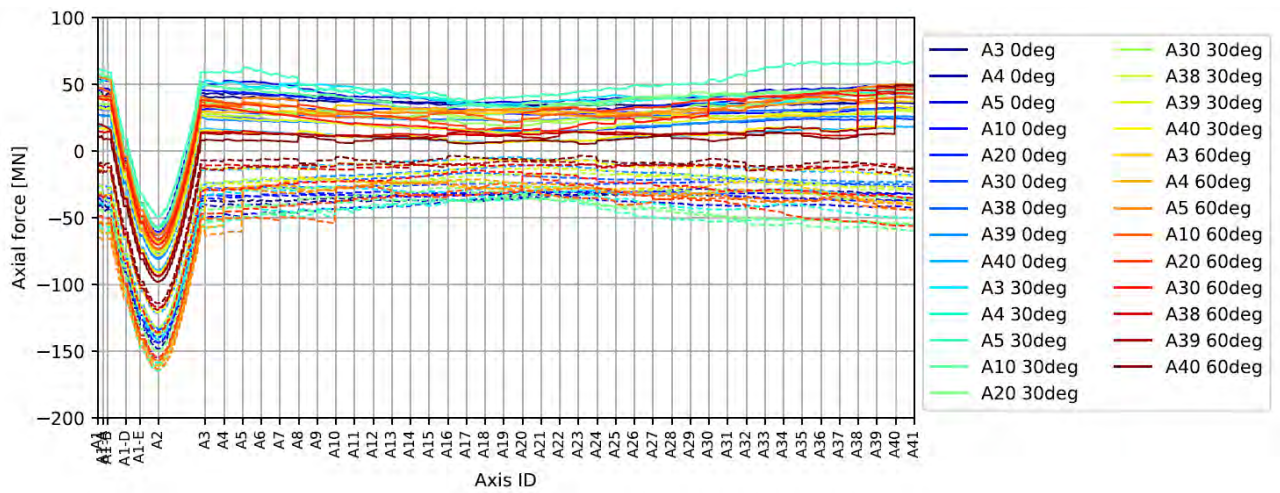


Figure 7-3 Bridge girder axial force for pontoon-ship collision with 50% increase of energy as pr. design basis.

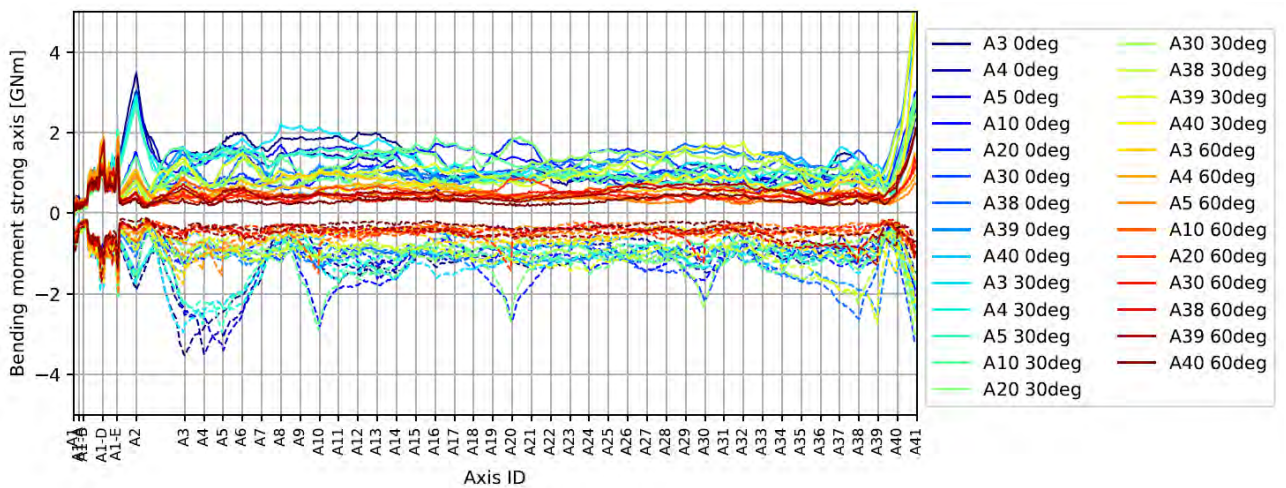


Figure 7-4 Bridge girder strong-axis bending moment for pontoon-ship collision with 50% increase of energy as pr. design basis.

8 Discussion and recommendations

The only damping sources that gives a significant contribution to the bridge response following an impact are viscous damping on pontoons and mooring lines, causing an improved response with more mooring. The effect of mooring damping is significant on the simulations and serves both to dissipate energy (and thereby stopping vibrations over some time) and to limit the peak deflections of the bridge girder directly after the impact. Comparison of global behavior in OrcaFlex and LS-DYNA reveal similar but not identical responses.

Local response was evaluated based on nonlinear finite element models with verified state-of-the-art material models following recommended guidelines for local response simulations. The resistance and resulting damage were verified for pontoon, column and bridge girder. The most severe damage to the bridge occurs in the pontoons and columns. Pontoon damage is acceptable in the sense of flooded volume whereas column damage is more challenging. Deckhouse collisions to the bridge girder was found to cause limited damage to the bridge girder itself, but high loads in the bridge abutments.

Pontoon collision and deckhouse collision cause a somewhat different response, with pontoon collisions giving higher torsional response in the bridge girder and deckhouse collisions a larger strong-axis bending moment response towards either end. For pontoon collisions the strong-axis bending moment is stiffness-dominated close to either end of the bridge, and there are only minor concept differences. For deckhouse collisions the southern scenarios are further out on the bridge, and the mooring stiffness contributes significantly to reduce peak loads towards the southern end. In the north high loads are observed for all concepts.

The bridge girder capacity is sufficient to avoid severe consequences of damage and shown to be robust in the post-damage phase (see [1]). However, the torsional resistance of the columns (for all pontoons, all concepts) will be dimensioned by ship collisions and should be a point of focus in further design development. If the ship impact energy is reduced compared to the current level in the upcoming risk analysis a column with stiffness equal to the narrow column geometry with 40 mm plate thickness is enough to have a reasonable but high plastic utilization of the column. However, if the impact energy is not reduced it is recommended to introduce a slight increase in the torsional resistance and to include stiffening members that behave well in a scenario with torsional deformation.

9 References

- [1] AMC, "SBJ-33-C5-AMC-90-RE-107 : Appendix G: Global Analyses - Response Rev. 0," 15.08.2019.
- [2] Statens Vegvesen, "SBJ-32-C4-SVV-90-BA-001 Design basis. Rev 0.," 19.11.2018.
- [3] C. Dørum, "304624-1-A-0028, Skipsstøt, varsel om endringer i design basis," SVV eRoom, 04.02.2019.
- [4] AMC, "SBJ-33-C5-AMC-26-RE-113 : Appendix M: Anchor systems Rev. 0," 15.08.2019.
- [5] AMC, "10205546-11-NOT-095 Rev1. Analytical mooring line damping," 2019.
- [6] AMC, "SBJ-33-C5-AMC-90-RE-100 : Concept evaluation - main report Rev. 0," 15.08.2019.
- [7] AMC, "SBJ-33-C5-AMC-90-RE-106 : Appendix F: Global Analyses - Modelling and assumptions Rev. 0," 15.08.2019.
- [8] AMC, "SBJ-33-C5-AMC-21-RE-108 : Appendix H: Global Analyses - Special studies Rev. 0," 15.08.2019.
- [9] T. Sarpkaya, "Separated Flow about Lifting Bodies and Impulsive flow about Cylinders," *AIAA Journal*, vol. 4, no. 3, pp. 414-420, 1966.
- [10] M. Storheim, "SBJ-20-C3-AAS-27-RE-002 K1 Ship Impact Report - Local. Rev. 0.," 2017.
- [11] M. Storheim and J. Amdahl, "On the sensitivity to work hardening and strain-rate effects in nonlinear FEM analysis of ship collisions", *Ship and Offshore Structures*, 2015.
- [12] "DNVGL RP-C208 : Determination of structural capacity by non-linear finite element analysis methods," DNVGL, Høvik, September 2016.
- [13] M. Storheim, H. Alsos and J. Amdahl, "Evaluation of nonlinear material behavior for offshore structures subjected to accidental actions," *Journal of Offshore Mechanics and Arctic Engineering*, vol. 140, 2018.
- [14] DNVGL, "DNVGL-OS-B101 - Metallic materials", DNV-GL, July 2015.
- [15] M. Storheim, Structural response in ship-platform and ship-ice collisions, PhD Thesis, Trondheim: Norwegian University of Science and Technology, 2016.
- [16] H. Alsos, O. Hopperstad, R. Törnqvist and J. Amdahl, "Analytical and numerical analyses of sheet metal instability using a stress based criterion," *International Journal of Solids and Structures*, vol. 45, no. 7, pp. 2042-2055, 2008.
- [17] A. H. A. Storheim, "A damage-based failure model for coarsely meshed shell structures", *International Journal of Impact Engineering*, no. 83, pp. 59-75, 2015.
- [18] M. Storheim, J. Amdahl and I. Martens, "On the accuracy of fracture estimation in collision analysis of ship and offshore structures," *Journal of Marine Structures*, vol. 44, pp. 254-287, 2015.
- [19] Handbook of stainless steel, Outokumpu - High performance stainless steel, 2013.
- [20] Y. Sha, I. F. Osvoll and J. Amdahl, "Ship-pontoon collision analysis of the floating bridge concepts for Bjørnafjorden," NTNU, Trondheim, 2018.
- [21] AMC, "10205546-13-NOT-087: Design of pontoons Rev. 0", 29.03.2019.
- [22] DNVGL, *DNVGL-RP-C204, Design against accidental loads*, 2017.
- [23] AMC, "10205546-11-RAP-165 :Appendix J: Ship collision Rev. 0," 29.03.2019.
- [24] AMC, "10205546-13-RAP-166 :Appendix K: Design of Floating Bridge Part Rev. 0," 28.03.2019.
- [25] AMC, "SBJ-33-C5-AMC-22-RE-111 : Appendix K: Design of Floating Bridge Part Rev. 0," 15.08.2019.
- [26] AMC, "10205546-11-NOT-076 AMC Status 2 - Plastic capacity of column," 29.03.2019.